TARGET IDENTIFICATION THEORY FOR SYNTHETIC APERTURE RADAR IMAGES USING PHYSICS-BASED SIGNATURES

by

CHEN-PANG YEANG

S.M., Massachusetts Institute of Technology, Cambridge, MA, USA
January 1996

B.S., National Taiwan University, Taipei, Taiwan
June 1992

Submitted to the Department of Electrical Engineering and Computer Science
in Partial Fulfillment of the Requirements for the Degree of

DOCTOR OF SCIENCE IN ELECTRICAL ENGINEERING

at the

MASSACHUSETTS INSTITUTE OF TECHNOLOGY

July 1999
[September 1999]

Signature of Author _____
Department of Electrical Engineering and Computer Science
July 14, 1999

Certified by _____
Jeffrey H. Shapiro
Julius A. Stratton Professor of Electrical Engineering
Thesis Supervisor

Accepted by _____
Arthur C. Smith
Chairman, Department Committee on Graduate Students

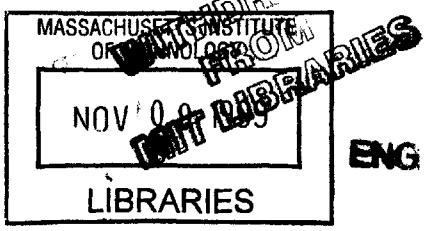

ENG

TARGET IDENTIFICATION THEORY FOR SYNTHETIC APERTURE RADAR IMAGES USING PHYSICS-BASED SIGNATURES

by

Chen-Pang Yeang

Submitted to the Department of Electrical Engineering and Computer Science
on July 14, 1999 in partial fulfillment of the requirements for the degree of
Doctor of Science in Electrical Engineering

ABSTRACT

This thesis develops a theory of target detection and classification from physics-based Synthetic Aperture Radar (SAR) signatures. The intermediate-frequency (IF) signal model consists of the return from a single or multiple-component target embedded in the clutter return from a random rough-surface reflector plus white Gaussian receiver noise. The target-return and clutter-return models are developed from electromagnetic theory. The modes of radar operation considered are stripmap and spotlight SARs. For a single-component target, we present adaptive-resolution processors created by varying the processing durations of the conventional chirp-compression stripmap-mode SAR processor and the conventional polar-formatting spotlight-mode SAR processor. We also develop the likelihood-ratio (optimum whitening-filter) target detectors for both stripmap- and spotlight-mode raw radar-return data. The Neyman-Pearson target-detection performance of the adaptive-resolution processors and the whitening-filter processors are compared. The signal and processor models for the single-component target are extended to multi-component targets. Likelihood-ratio detectors, sub-optimum detectors, generalized likelihood-ratio detectors, and approximate generalized likelihood-ratio detectors are constructed respectively, for the detection of multi-component targets with random phases, positions, amplitudes, and target pose. Approximate methods are proposed to calculate the receiver operating characteristics of these detection problems. The multi-component target detection performances for the whitening-filter processors and the conventional SAR processors are compared. Based on the theories and results from the study of SAR target detection problems, we present a preliminary performance analysis for the multi-component target classification problem.

Thesis Supervisor: Jeffrey H. Shapiro
Title: Julius A. Stratton Professor of Electrical Engineering

Acknowledgment

I cannot overemphasize the gratitude to my thesis supervisor Prof. Jeffrey H. Shapiro. His insistence on technical quality, mathematical rigor, physical insight, and connection with overarching problematics in the field of automatic target recognition not only extensively shaped the directions of this work, but also demonstrated to me a model of a great researcher and teacher. Such insistence is parallel with his warm personality and willingness to help. I would like to express my thanks to Prof. Alan S. Willsky and Prof. Jin Au Kong for their service on my thesis committee. Prof. Willsky gave me help in many aspects. The weekly seminar organized in his Stochastic Systems Group (SSG) was a valuable source for learning a broader/deeper theoretical and pragmatic context with respect to the research I have been conducting. Without the SSG computational facility, many numerical cases present in the thesis could not have been finished in time. While staying in Prof. Kong's Electromagnetic Wave Theory (EWT) group during my first two years in MIT, I was intensively trained on electromagnetic wave scattering and propagation theories. The parts related to EM scattering in this dissertation are fruits of this training. I also wish to thank Dr. John Fisher for participating in my thesis committee meeting. His suggestion regarding the multi-component target detection problems was very important for the last third of the dissertation.

It would be impossible to properly thank all the friends that have contributed to this dissertation. With some regrets, I will only pass regards to a few of them. Initiating the research project on SAR target recognition, my colleague Gilbert Leung laid a foundation for a physical understanding of adaptive-resolution processing upon which my work is built. I owe Gilbert a lot for fruitful discussions on research problems and warm friendship. Jeffrey Bounds, Phillip Nee, and Asuman Koksal were very excellent colleagues with sincere hearts. I also wish to show my appreciation to the SSG computer system administrator Andrew Kim, for his devoted effort on maintaining the network. My officemate Mohamud Jalal

Khan, senior Shih-En Shih, and classmates Tza-Jing Gung and Chen-Hsiang Yeang were great friends during my years in the MIT EECS department. Their friendship made me feel I was not left alone in a windowless chamber when I was depressed by bottlenecks on research or classes.

Finally, I wish to thank my father Chia-Chiu Yeang and mother Lan-Chun Hsu for their unreserved devotion to their children. Without their spiritual and material support, I could not sit here writing acknowledgment of my doctoral dissertation.

This research is supported from US Air Force Office of Scientific Research Grant F49620-96-1-0028.

To My Parents

Contents

List of Figures

List of Tables

Chapter 1

Introduction

1.1 Background

Radar has been a powerful sensor technology for both military and non-military purposes such as reconnaissance, remote sensing, positioning and navigation. The basic principle of radar is as follows. An electromagnetic wave propagates from the radar's transmitter to a distant object, where it is scattered and part of the wave propagates back to the radar's receiver. At the receiver, the returned waveform is processed to obtain information about the object such as its location, geometry, velocity, and composition.

The precision with which an object's position can be identified is restricted by radar resolution. For a diffraction-limited antenna, the spatial (cross-range) resolution is $\lambda_c L/a$, where λ_c is the carrier wavelength of the electromagnetic waveform, L is the target range, and a is the radius of the antenna aperture. For a pulsed radar, its range resolution is $c/4W$, where c is the speed of light, and W is the pulse bandwidth ($W = 1/2T$ for a transform-limited pulse of duration T). To improve the range resolution, a typical method is to increase the bandwidth of the transmitted pulse by modulating it with a frequency chirp [1-3]. To enhance the cross-range resolution, two approaches could be adopted: operating at shorter wavelengths, e.g. using a laser radar [4] in lieu of a microwave radar, or increasing the size of the "equivalent" antenna aperture via signal processing. The latter technique, known as Synthetic Aperture Radar (SAR) [5][6], is the subject area of this thesis.

The basic principle of synthetic aperture radar is to record the complete phase history of return signals as the radar antenna is moved along a predetermined path. Using the precise information about the radar antenna's path, the recorded phase history of return

signals is then coherently processed to produce a radar image with higher resolution than could otherwise be obtained. In this sense, the equivalent "synthetic" antenna aperture is the space the physical aperture sweeps out during the processing duration of the complete phase history. A SAR can be interpreted either as a radar system with a phased-array antenna or as a radar system in which the radar return contains a frequency chirp along the cross-range direction due to its time-dependent propagation delay [5]. From both perspectives, the enhanced spatial resolution is obtained via appropriate signal processing.

1.2 Related Work and Motivation

In recent years SAR has been used in detection and discrimination of man-made targets from natural background. A SAR-based Automated Target Recognition (ATR) system requires a fast and effective discriminator to suppress a vast amount of natural clutter, to detect the presence of a target, and to classify the type of target from its radar return [7]. Such a system relies on models for the different components of the radar return, namely, the returns from (different types of) artificial targets, natural clutter, and background noise. One typical approach is to model the target return as a parametrized deterministic signal pattern, and the clutter and noise as stochastic processes characterized by their statistics. In [8], the clutter and noise are modeled as Gaussian random processes with given covariance matrices, and the target return is modeled as a pre-specified spatio-temporal pattern multiplied by complex-amplitude parameters. In [9], the target return is composed of the contributions from several scattering centers. Each scattering-center component contains an amplitude and phase which are determined by the radar's carrier frequency and look angle plus the scattering centers' positions. The unwanted part of the radar return, i.e. the noise, is assumed to be a white-Gaussian process. In [10], the target signal is taken to be a Gaussian intensity function, the clutter a sinusoid with random phase, and the noise a Gaussian process.

Another approach for radar-signal modeling is to assume that the target return and the unwanted part (clutter plus noise) are random processes characterized by different statistics. In [11], the target return consisted of a deterministic part and a random part, with the latter coming from scattering-amplitude and scattering-center uncertainties. In [12], the radar signal is a target return multiplied by an uncorrelated speckle noise; the covariance matrices of the target return and the speckle noise are estimated by principal-component analysis. This approach also implies that different clutter types have different statistics. The work in [13] models the full polarimetric radar clutter as a product of a gamma-distributed textural variable and a Gaussian random vector whose covariance matrix is determined empirically. The numerical values for the covariance-matrix elements calculated from real SAR data are different for trees, shadows, grass, and mixed scrub.

The approaches mentioned above can also be applied to multiple radar images, i.e. to images of the same scene obtained from different sensors and/or at different resolutions. The signal model in [14] is similar to that in [8] except that an image point is a vector whose components represent sensor data collected at different bandwidths. In [15] and [16], radar images at different resolutions are modeled as Markov random fields, and the parameter values in their statistical models are used as a basis for classification or texture segmentation.

Recent studies on multiresolution radar images have revealed a promising potential for solving target identification problems. The work in [17] indicates that, from millimeter-wave SAR data, a processor based on an autoregressive model among multiresolution images provides a useful discriminant between natural clutter and man-made targets. In [18] it is demonstrated that, with ultra-wide-band foliage-penetrating SAR data, adaptive-resolution imaging can exploit the aspect-dependent reflectivity of man-made objects. In [19] it is shown that, based on the different variation-vs.-resolution patterns of targets and clutter, discrimination can be accomplished via adaptive multiresolution processing.

None of the above works is founded on a rigorous, physics-based theory that, taking into account the effects of the transmitter pulse shape, antenna beam pattern, free-space wave propagation, relates the radar return from targets and clutter to their respective physical characteristics in terms of an electromagnetic scattering model. In [1] and [2], the return signals corresponding to a spotlight-mode SAR and stripmap-mode SAR are constructed via a comprehensive consideration of radar-pulse transmission and propagation. The resultant return signal is formulated as a spatial integral of the Lambertian reflectivity pattern within the region of interest and the Green's function corresponding to the mode of radar operation. This approach, however, is not directly derived from a rigorous electromagnetic scattering theory, and therefore does not capture certain important features, such as aspect-angle dependence, in the return from a specular object. The work in [20] claims to build a physics-based ultra-wideband (UWB) radar return model of a specular target from the observed fact that an UWB pulse incident upon a flat reflector produces two return pulses, because of the discontinuities at the reflector's edges. This phenomenon is predictable from scattering theory. But using this phenomenology rather than electromagnetic scattering theory as a basis for constructing the signal model can fail to capture other significant features in the radar return. In [21][22], a UWB SAR target-return model is constructed using physical optics and the physical theory of diffraction. The pulse shape is considered via the UWB specification, and the antenna beam pattern could be incorporated by multiplying the return with a weighting function with respect to location. In [21] [22], however, the region of interest is only the parabolic trajectory corresponding to the footprint of a fixed target at the SAR image plane, rather than the whole two-dimensional image plane. In this sense, the processor is only one-dimensional, not two-dimensional. Moreover, the unwanted part of the radar signal does not include the clutter scattered from the environment. It only consists of white Gaussian noise.

To exploit the multiresolution characteristics in SAR imagery using a physics-based

approach seems promising. The mathematical formulation of the radar-return signal and chirp-compression processor in [3][4], together with a physical-optics model for the target scatterer were used in [6][23] to provide a first-principles analysis for discerning specular returns from diffuse returns in synthetic aperture radar imagery by means of their distinct multiresolution patterns. Because the scattering pattern of a specular reflector is directional rather than isotropic, its corresponding optimum processing duration should be shorter than that of a conventional chirp-compression processor. This verifies the empirical results from real SAR data that were reported in [18]. However, the scenario considered in [6][23] is restricted to a simple case: one-dimensional, continuous-wave, non-polarimetric, stripmap-mode, and single reflector only. To establish a comprehensive first-principles analysis for target identification in SAR imagery, a significant amount of work remains to be done.

Motivated by the work of [6][23], this thesis proposes to make a complete analysis for target detection from a physics-based model of SAR imagery. The operational conditions will be extended to a more realistic case: two-dimensional, chirp-pulse waveform, and full polarimetric data collection. The radar scenarios of interest include stripmap-mode and spotlight-mode SARs. The targets consist of a repertoire of geometrically-simple reflectors such as a specular mirror, a dihedral reflector, and a dielectric volume, and the clutter is assumed to originate from a reflecting rough surface. Both targets and clutter are modeled from electromagnetic scattering theory. The purpose of adopting electromagnetic theory is not to produce an accurate and comprehensive simulation of SAR images, but to provide a fundamental signal-model understanding for optimizing certain SAR signal-processing schemes. Both single reflector and multiple reflectors within a footprint area are considered. The observed multiresolution and adaptive-resolution features from the empirical studies are exploited for target recognition. In some cases, in which the optimum processors for target detection problems are available in analytical forms, their performances are compared with the performances of the multiresolution or adaptive-resolution processors.

1.3 Outline

The rest of this thesis is organized as follows. In Chapter 2, we construct the radar system model for a stripmap-mode, two-dimensional, pulse waveform, polarimetric SAR. The basic principle by which 2-D stripmap SAR gives imagery with enhanced resolution is presented. To build the radar return signature, models for the transmitted chirp-pulse waveform, the radar's antenna pattern, and free-space wave propagation are combined. The return from a target reflector is formulated in terms of the scattering coefficient derived from physical optics and physical theory of diffraction. A repertoire of geometrically-simple targets, including specular reflector, dihedral reflector, and dielectric volume, are considered. The radar clutter is modeled as the return from a random rough surface, as calculated from the Kirchhoff approximation [24] and incorporated into the return signal via the backpropagation formulation [3]. The receiver noise is modeled as a white Gaussian process.

In Chapter 3, we present an adaptive-resolution signal processing scheme for 2-D stripmap SAR imagery. The scheme is similar to the conventional 2-D stripmap SAR processor. It consists of chirp compression filters for both range and cross-range directions, however, in our adaptive-resolution scheme the processing durations for these filters are variable. Numerical calculations show that the adaptive-resolution signatures for different types of targets are different. For this adaptive-resolution processor, we also pose the target detection problem of deciding on the presence or absence of a simple reflector, with known geometry and location. For the same detection problem, the Neyman-Pearson optimum processor, composed of a whitening filter for clutter and noise and a matched filter corresponding to the filtered target-return, is also presented. Numerical values of signal-to-noise-plus-clutter-ratio (SNCR) for these two processors are compared. As was the case in the 1-D work of [6], our 2-D SAR formulation captures the broad-side flash phenomenon reported in [18], implying an optimum adaptive-resolution processing duration that is smaller than the full dwell time. There are some features, however, which are revealed in a our polarimetric 2-D SAR

model that are absent from the scalar 1-D SAR work. First, the dihedral reflector has an orientation-dependent polarimetric signature that is quite different from that of a specular reflector. Second, the dielectric volume has a range-spread return that is unlike those for the surface-reflector cases. Third, there is no operating regime in which the SNCR of the optimized adaptive-resolution receiver approximates that of the optimal, whitening-filter receiver.

In Chapter 4, we develop the single-component target detection theory for spotlight-mode SAR imagery. The fundamental principle for spotlight-mode SAR is first explained. Unlike the stripmap-mode SAR that exploits the time-dependent phase delays of radar returns along the cross-range direction, the spotlight-mode SAR imager interprets radar returns from different aspect angles as a tomographic rendition of the 2-D terrain-reflectivity profile. After a brief introduction of basic spotlight-mode SAR principles, we construct the radar return models. Similar to Chapter 2, the target return model is based on physical optics and geometric optics approximations of the electromagnetic scattering theory, the clutter's statistical model is the result of Kirchhoff approximation of random rough surface scattering, and the noise is modeled as white Gaussian. The repertoire of target reflectors is also identical to that considered in Chapter 2. Basically, the only essential difference between the stripmap-mode and spotlight-mode SAR radar return models lies in the antenna beam pattern along the cross-range direction. After the development of radar return models, we present two processor/detector models for the spotlight-mode SAR signal. The first one is the adaptive-resolution version of the conventional SAR processor, followed by a sampler and a threshold detector. To exploit the tomographic rendition of terrain reflectivity, the conventional spotlight-mode SAR processor is a de-chirped polar-formatted 2-D Fourier transformer [1]. The resolution adaptability allows us to adjust the radial (range) and angular (cross-range) sizes of the annular region prescribed by the polar formatter. The second processor is a Neyman-Pearson optimum processor, which is similar to the one

presented in Chapter 3. The performance analysis for these two types of processors are presented. First, we compare the cross-range and range image resolutions of the adaptive-resolution spotlight-mode SAR processor with the resolutions of the adaptive-resolution stripmap-mode SAR processor. Second, we numerically evaluate the SNCRs for these two processors and observe their variations with respect to different parameters. The salient features captured in the study of stripmap-mode SNCR in Chapter 3, such as the broadside flash of specular reflector, polarimetric effect of dihedral reflector, and frequency dispersion effect of dielectric volume, all appear in our results for spotlight-mode SAR. The cross-range processing durations for optimum SNCR are different for stripmap-mode and spotlight-mode operations due to their distinctive cross-range antenna beam patterns.

In Chapter 5, we extend the target detection theory for stripmap-mode and spotlight-mode SAR images from single-component targets to multi-component targets. A multi-component target is defined as a collection of simple reflectors distributed at different locations. Multi-component target is the norm in SAR ATR applications. To further embody the practicality, we model the multi-component targets with parameter uncertainties. In this chapter, four cases for uncertainties are considered: (i) the phase of return from every individual target component is random; (ii) the phase and location are random; (iii) the phase, location, and amplitude are random; (iv) the phase of return from every individual target component and the overall target pose are random. For each individual case, we develop a Neyman-Pearson processor followed by a likelihood-ratio, generalized likelihood-ratio, or other sub-optimum detectors. We also propose methods to calculate, either exactly or approximately, the numerical values of receiver operating characteristics for these detectors. The receiver operating characteristics for the conventional SAR detectors are also calculated. The detection performances of the likelihood-ratio based Neyman-Pearson detectors and the conventional SAR processors are compared.

In Chapter 6, we extend the binary target detectors developed in Chapter 5 to the

classifiers for a repertoire of multi-component targets. Based on the calculations of receiver operating characteristics for individual binary detection problems, we present a preliminary performance analysis for the likelihood-ratio-based target classifiers.

In Chapter 7, we wrap up with conclusions for the thesis. We point out the contributions made toward a fundamental understanding of the ultimate performance limits on SAR target detection, and we indicate areas for possible future research.

Chapter 2

2-D Stripmap SAR Signal Model

2.1 Basic Principle of 2-D SAR

The scenario for a two-dimensional stripmap-mode SAR is sketched in Figure 2.1. The radar antenna and receiver are mounted on an aircraft flying with velocity $\bar{v} = \hat{x}v$ at an altitude L m. Thus the position of the aircraft can be described by the vector $\bar{r}_t = \hat{x}vt + \hat{z}L$. The normal direction of the antenna aperture, $-\hat{z}' = -\hat{z}\sin(\psi) + \hat{y}\cos(\psi)$, is on the plane perpendicular to the velocity vector $\hat{x}$ and tilted downward from the horizontal direction $\hat{y}$ with angle ψ, making $L' = L/\sin(\psi)$ the range to the ground. As the aircraft flies, the footprint of the antenna beam swept along the ground is an elongated strip at distance $L/\tan\psi$ from the projection of aircraft trajectory and with width $\lambda_c L/d\sin(\psi)$, where d is radar's antenna diameter and λ_c is its wavelength.

The purpose of SAR is to improve the radar's spatial resolution. The fundamental principle of a 1-D CW synthetic aperture operation can be explained as follows [6]. For a continuous-wave downlooking radar imager, the Doppler-shift time history associated with the return from a point scatterer is a frequency chirp of rate $\dot{\nu}_D = -2v^2/\lambda_c L$. The time duration of the chirp, T, is the length of time during which the scatterer lies within the radar antenna beam; we shall presume far-field diffraction-limited operation, so that $T \approx \lambda_c L/vd$. Compressing this chirped radar return through a matched filter then yields a time-domain output waveform of duration x_{res}/v, where

$$x_{res} \approx \frac{v}{|\dot{\nu}_D|T} \approx \frac{d}{2} << \frac{\lambda_c L}{d}, \tag{2.1}$$

thus providing along-track (cross-range) spatial resolution that is much better than the diffraction-limited beamwidth of the real antenna aperture. For extended targets, the chirp

duration is determined by the target's scattering pattern; a large specular reflector will have a chirp duration much smaller than the dwell time, a fact which an optimum receiver for that target will exploit.

Similar to the 1-D SAR, the 2-D SAR also makes use of the radar-return chirp to enhance its resolution. However, there is an additional feature in the 2-D case. The 2-D SAR not only resolves the imagery in the cross-range direction ($\hat{x}$) but also in the range direction ($-\hat{z}'$). To accomplish this feature the transmitted waveform must be a train of repetitive pulses rather than a continuous wave. Thus the time-domain structure of this two-dimensional configuration consists of a discrete coordinate, m, along the cross-range direction which is the 2-D SAR counterpart of the continuous-time coordinate from the 1-D case, and a continuous coordinate, τ, along the range direction that corresponds to the time delay of the radar return [3]. The spatial resolution along the cross-range direction is achieved through the SAR operation similar to the one described in (1.1); the only difference is that the time coordinate in the 2-D case is discrete instead of continuous. However, the spatial resolution along the range direction is achieved by increasing the bandwidth of the individual radar pulse via chirp modulation rather than synthetic-aperture operation. As described in [4], two pulse-compressive filters are now employed in the receiver architecture: a discrete-time matched filter to form the synthetic aperture; and a continuous-time matched filter to realize the full range resolution capability of the individual chirped pulses. The flight geometry for the 2-D stripmap-mode SAR is illustrated in Figure 2.1.

2.2 Radar Target Return Model

The intermediate-frequency radar return model includes the transmitter model, propagation and scattering model, and receiver front-end model. A train of modulated radar pulses is generated at the transmitter. Each transmitted pulse propagates from the transmitting antenna to the target region where it is scattered (reflected) by the object and then

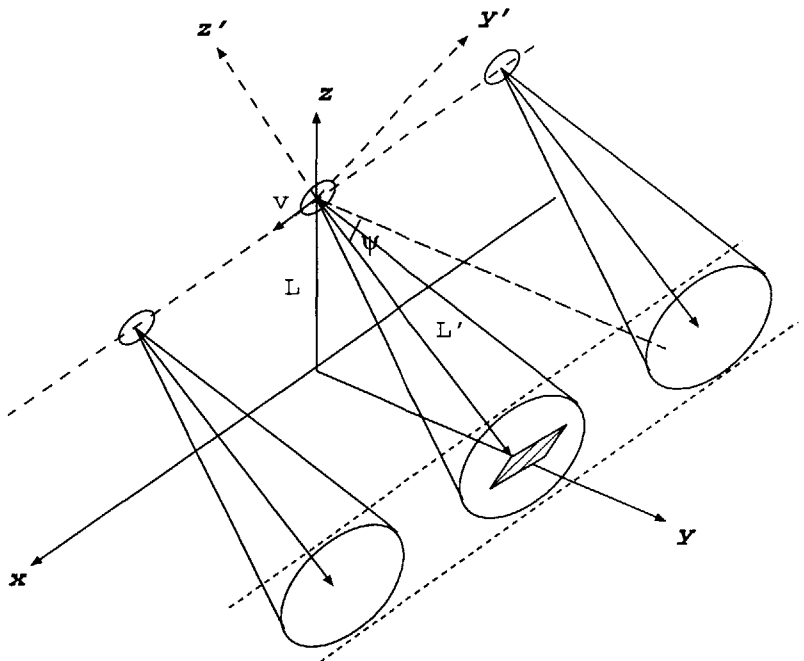

Figure 2.1 Flight geometry for a 2-D stripmap-mode SAR.

propagates back to the receiving antenna. The return pulse field is superimposed with the field of a superheterodyne local oscillator coherent with the transmitter but operated at an intermediate frequency (IF) offset from the transmitter carrier frequency. The resultant signal is passed through a bandpass filter to select the IF component. The block diagram for the construction of radar-return signal is shown in Figure 2.2.

The radar-return signal is a superposition of target return, clutter, and receiver noise. Since we are mainly interested in discriminating man-made objects from natural background, the target return is defined as the return from geometrically simple reflector(s), and the clutter is defined as the return from a random rough reflecting surface. The receiver noise is modeled as a white Gaussian random process.

2.2.1 Radar Transmitter Model

The transmitted signal is assumed to be a repetitive train of pulses with period T_s, complex envelope $p(t)$ and carrier angular frequency $\Omega_c\,\mathrm{s}^{-1}$ that is radiated from an aperture

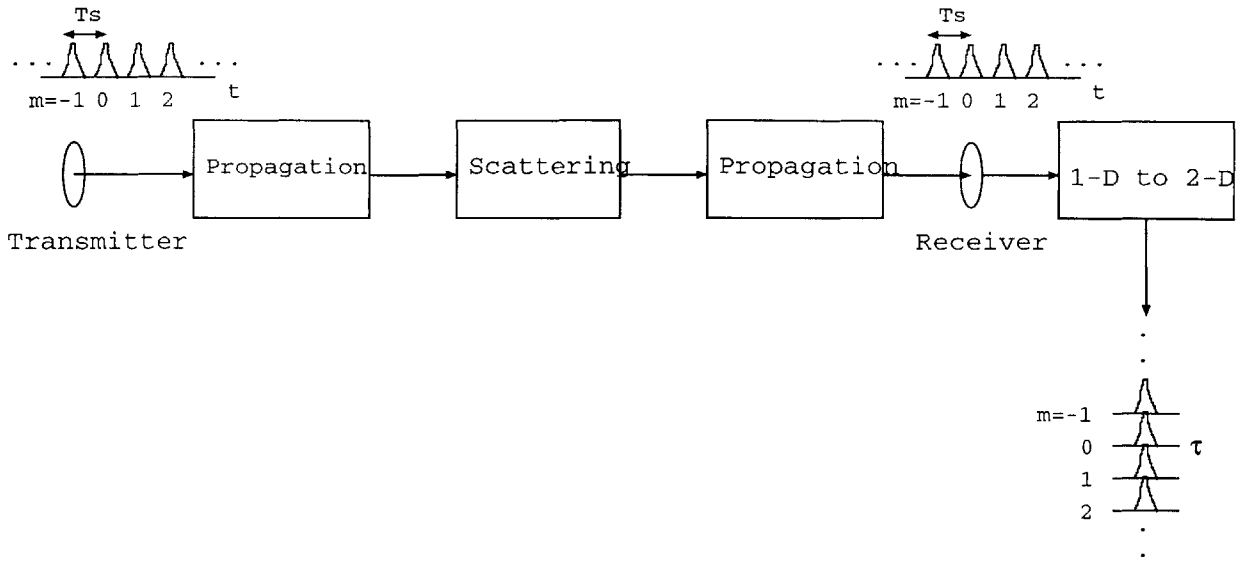

Figure 2.2 Radar return signal block diagram.

S_a. The resulting electric field on the surface of this aperture is

$$\bar{E}_a(\bar{r}_a, t) = \mathrm{Re}\left[\hat{u}_a\sqrt{\eta P_T}U_{ant}(\bar{r}_a)\sum_{m=-\infty}^{\infty} p(t - mT_s)e^{-i\Omega_c t}\right]. \tag{2.2}$$

In (2.2), $\bar{r}_a$ is the spatial coordinate of any point on the aperture S_a in the radar's rest-frame, whose origin is at the center of S_a. The vector $\hat{u}_a$, which must be orthogonal to the normal direction of S_a, represents the polarization of the transmitted field $\bar{E}_a$. In this study, we assume uniform polarization throughout the aperture, i.e. $\hat{u}_a$ = constant. P_T is the peak power of the transmitted field, and $\eta = \sqrt{\mu_0/\epsilon_0}$ is the natural impedance of free space. $U_{ant}(\bar{r}_a)$ is the stationary spatial antenna aperture pattern in the radar's rest-frame. We use an elliptical-Gaussian spatial pattern to model the finite aperture dimensions of the transmitter antenna [23].

$$U_{ant}(\bar{r}_a) = \sqrt{\frac{2}{\pi a_x a_y}}\exp[-(x_a/a_x)^2 - (y_a/a_y)^2], \tag{2.3}$$

where x_a is the coordinate in the along-track (cross-range) direction, y_a is the coordinate in the across-track (range) direction, a_x and a_y are the radii of S_a associated with the along-

track and across-track directions, respectively. We assume that the antenna aperture S_a does not appreciably truncate the Gaussian spatial pattern in (2.3), i.e.

$$\int\int_{S_a} d\bar{r}_a |U_{ant}(\bar{r}_a)|^2 \approx \int_{-\infty}^{\infty}\int_{-\infty}^{\infty} dx_a dy_a |U_{ant}(\bar{r}_a)|^2 = 1. \tag{2.4}$$

Thus, when we define the time-independent part of transmitted electric-field phasor $\bar{E}_a^0(\bar{r}_a) = \hat{u}_a\sqrt{\eta P_T}U_{ant}(\bar{r}_a)$, the associated Poynting vector satisfies the normalization condition:

$$\int\int_{S_a} d\bar{r}_a \frac{|\bar{E}_a^0(\bar{r}_a)|^2}{\eta} = P_T. \tag{2.5}$$

The complex envelope $p(t)$ is assumed to be a chirped Gaussian pulse with duration T_0 and chirp bandwidth W_0:

$$p(t) = \exp[-i\pi W_0 t^2/T_0 - 4(t/T_0)^2]. \tag{2.6}$$

From the equivalence principle [25], the electromagnetic field induced by the transmitted electric field $\bar{E}_a(\bar{r}_a, t)$ on the antenna surface S_a in (2.2) could be generated by an equivalent electric surface-current density $\bar{K}_a(\bar{r}_a, t)$ and zero magnetic surface-current density on S_a:

$$\begin{aligned}\bar{K}_a(\bar{r}_a, t) &= \frac{2}{\eta}\bar{E}_a(\bar{r}_a, t) \\ &= \mathrm{Re}\left\{\hat{u}_a\sqrt{\frac{8P_T}{\eta\pi a_x a_y}}\exp[-(x_a/a_x)^2 - (y_a/a_y)^2]\sum_{m=-\infty}^{\infty} p(t - mT_s)\exp(-i\Omega_c t)\right\}.\end{aligned} \tag{2.7}$$

2.2.2 Propagation

To simplify the propagation problem, we first consider the case of a single target located at $\bar{r}_p = \hat{y}L\cot\psi$ (see Figure 2.1). Throughout our work, we will neglect atmospheric effects and employ free-space propagation theory. From electromagnetic wave theory [25], the electric field $\bar{E}(\bar{r}, t)$ produced in free space by a monochromatic surface current density $\bar{K}(\bar{r}', t) = \mathrm{Re}\left[\bar{K}^0(\bar{r}')\exp(-i\Omega t)\right]$ distributed on the source surface S' can be calculated via the Green's-function formulation

$$\bar{E}(\bar{r}, t) \approx \mathrm{Re}\left[i\mu_0\Omega(\bar{\bar{I}} - \hat{r}\hat{r})\cdot\frac{e^{ikr}}{4\pi r}\int\int_{S'} d\bar{r}'\bar{K}^0(\bar{r}')\exp(-ik\hat{r}\cdot\bar{r}')\exp(-i\Omega t)\right] \tag{2.8}$$

under the far-field conditions $kr >> 1$, $ka^2/r << 1$. Here $r = |\bar{r}|$, $\hat{r} = \bar{r}/|\bar{r}|$, $\bar{r}'$ is the local coordinate of the surface S', $k = \Omega/c$ is the wave number (c is the speed of light), μ_0 is the free-space permeability, and a is the diameter of the surface S'. To render this far-field (Fraunhofer) approximation valid around the target located at $\bar{r}_p$ in our stripmap SAR, the preceding conditions become

$$kL' >> 1, \quad ka_x^2/L' << 1, \quad ka_y^2/L' << 1. \tag{2.9}$$

The surface current density $\bar{K}_a$ in (2.7) is not monochromatic. Thus the electromagnetic field $\bar{E}_i$ generated by $\bar{K}_a$ at far-field region is obtained by carrying out spectral analysis of (2.7) and employing (2.8) for every Fourier component of $\bar{K}_a$, namely,

$$\bar{E}_i(\bar{r},t) \approx \mathrm{Re}\{ \int_{-\infty}^{\infty} \frac{d\Omega}{2\pi} \sum_{m=-\infty}^{\infty} P(\Omega) e^{-i\Omega(t-mT_s)} i\mu_0(\Omega_c+\Omega) \sqrt{\frac{8P_T}{\eta\pi a_x a_y}} (\bar{\bar{I}} - \hat{r}\hat{r}) \frac{e^{i(k_c+k)r}}{4\pi r}$$

$$\cdot \hat{u}_a \int\int_{S_a} d\bar{r}_a \exp[-(x_a/a_x)^2 - (y_a/a_y)^2] \exp[-i(k_c+k)\hat{r}\cdot\bar{r}_a] \exp(-i\Omega_c t) \}, \tag{2.10}$$

where $k_c = \Omega_c/c$ is the wave number at the carrier frequency, and

$$\begin{aligned} P(\Omega) &= \int_{-\infty}^{\infty} dt\ p(t) e^{i\Omega t} \\ &= \sqrt{\frac{\pi}{i\pi W_0/T_0 + 4/T_0^2}} \exp[-\Omega^2/4(i\pi W_0/T_0 + 4/T_0^2)]. \end{aligned} \tag{2.11}$$

Equation (2.10) is the superposition of radar transmission fields at all frequencies. Each individual frequency component is, rather than a plane wave, a spherical wave $e^{i(k_c+k)r}/r$ modified by the antenna beam pattern $\int\int_{S_a} d\bar{r}_a \exp[-(x_a/a_x)^2 - (y_a/a_y)^2] \exp[-i(k_c+k)\hat{r}\cdot\bar{r}_a]$. However, in the far-field region around the target location $\bar{r}_p$, this field can be approximated by a plane wave with propagation direction $\hat{r}_i = (\bar{r}_p - \bar{r}_t)/|\bar{r}_p - \bar{r}_t|$, and amplitude and phase determined by (2.10). Thus the overall transmission field around the target center becomes

$$\bar{E}_i(\bar{r}'',t) \approx \mathrm{Re}\{ \int_{-\infty}^{\infty} \frac{d\Omega}{2\pi} \sum_{m=-\infty}^{\infty} P(\Omega) e^{-i\Omega(t-mT_s)} i\mu_0(\Omega_c+\Omega) \sqrt{\frac{P_T}{2\eta\pi^3 a_x a_y}} (\bar{\bar{I}} - \hat{r}_i\hat{r}_i) \frac{e^{i(k_c+k)r_i}}{4\pi r_i}$$

$$\cdot\hat{u}_a \int\int_{S_a} d\bar{r}_a \exp[-(x_a/a_x)^2-(y_a/a_y)^2]\exp[-i(k_c+k)\hat{r}_i\cdot\bar{r}_a]\exp[i(k_c+k)\hat{r}_i\cdot\bar{r}'']\exp(-i\Omega_c t)\ \},$$
(2.12)

where $\bar{r}'' = \bar{r} - \bar{r}_p$ is the local coordinate centered at $\bar{r}_p$, $\bar{r}_i = \bar{r}_p - \bar{r}_t$, $r_i = |\bar{r}_i|$. When the entire target is small enough to be within the Frauhofer region of the radar beam, equation (2.12) is an approximation for the transmission field around the whole target area. Under (2.12), the stripmap radar-return is non-negligible only within a cross-range region that is much smaller than the target range, namely,

$$vt/L' << 1. \tag{2.13}$$

Therefore we can use

$$\hat{r}_i \approx -\hat{z}' + \hat{x}vt/L', \tag{2.14}$$

and

$$r_i \approx L' + (vt)^2/2L', \tag{2.15}$$

to carry out the integral over S_a in (2.12), obtaining

$$\bar{E}_i(\bar{r}'',t) \approx \mathrm{Re}\{\int_{-\infty}^{\infty}\frac{d\Omega}{2\pi}\sum_{m=-\infty}^{\infty}P(\Omega)e^{-i\Omega(t-mT_s-L'/c)}i\mu_0(\Omega_c+\Omega)\sqrt{\frac{P_T a_x a_y}{2\eta\pi}}\frac{1}{L'}(\bar{\bar{I}}-\hat{r}_i\hat{r}_i)\cdot\hat{u}_a$$

$$\times\exp[ik_c(L'+(vt)^2/2L')]\exp[-((k_c+k)a_x vt)^2/4L'^2]\exp[i(k_c+k)\hat{r}_i\cdot\bar{r}'']\exp(-i\Omega_c t)\ \}. \tag{2.16}$$

2.2.3 Target Scattering

The return of the incident radar wave from a target can be modeled via scattering theory. Electromagnetic scattering theory indicates that, for an incident monochromatic plane wave with propagation direction $\hat{k}_i$, angular frequency Ω, and wave number $k = \Omega/c$, namely, $\bar{E}_i(\bar{r},t) = \mathrm{Re}\left\{\bar{E}_{i0}\exp[i(k\hat{k}_i\cdot\bar{r}-\Omega t)]\right\}$, the scattered wave in the far-field zone $kr >> 1$ is

$$\bar{E}_s(\bar{r},t) = \mathrm{Re}\left[\frac{e^{ikr}}{r}\bar{\bar{S}}(\hat{r},\hat{k}_i,\Omega)\cdot\bar{E}_{i0}e^{-i\Omega t}\right]. \tag{2.17}$$

Here $\bar{r}$ is in the local coordinate whose origin is at the object center, and $\bar{\bar{S}}(\hat{r}, \hat{k}_i; \Omega)$ is the object's bistatic scattering tensor as a function of the incident direction $\hat{r} = \bar{r}/|\bar{r}|$, scattering direction $\hat{r}$, and (angular) frequency Ω.

The incident radar pulse in (2.16) is a superposition of monochromatic plane waves. Therefore the field scattered from the target can be obtained by summing all the scattering fields corresponding to the individual monochromatic plane-wave components. The result is a superposition of spherical waves modulated by the scattering tensors:

$$\bar{E}_s(\bar{r}'', t) \approx \mathrm{Re}\{ \int_{-\infty}^{\infty} \frac{d\Omega}{2\pi} \sum_{m=-\infty}^{\infty} P(\Omega) e^{-i\Omega(t-mT_s-L'/c)} i\mu_0(\Omega_c+\Omega) \sqrt{\frac{P_T a_x a_y}{2\eta\pi L'^2}}\ \bar{\bar{S}}(\hat{r}'', \hat{r}_i; \Omega_c+\Omega)$$

$$\cdot(\bar{\bar{I}} - \hat{r}_i\hat{r}_i) \cdot \hat{u}_a \exp[ik_c(L' + (vt)^2/2L')] \exp[-((k_c+k)a_x vt)^2/4L'^2] \frac{e^{i(k_c+k)r''}}{r''} e^{-i\Omega_c t} \}. \quad (2.18)$$

Strictly speaking, for the synthetic aperture radar emitting a pulse at time t s toward a target a distance L' m away, the locus of the transmitter antenna, $\bar{r}_t = \hat{x}vt + \hat{z}L$, is different from that of the corresponding receiver antenna, $\bar{r}_{t+2L'/c} \approx \hat{x}v(t + 2L'/c) + \hat{z}L$. This is because it takes $2L'/c$ s for round-trip pulse propagation to occur. In this study, we assume that the bistatic angle between the transmitter, target, and receiver is extremely small, i.e., $v(2L'/c) << L'$, so that the scenario can be approximated as monostatic.

Only the scattered field in the vicinity of the receiver antenna enters into the calculation of the radar-return signal. Hence similar to the procedure in Section 2.2.2, we approximate the ensemble of spherical waves in (2.18) as an ensemble of plane waves. The radar-return field near the receiver antenna then becomes

$$\bar{E}_s(\bar{r}_c, t) \approx \mathrm{Re}\{ \int_{-\infty}^{\infty} \frac{d\Omega}{2\pi} \sum_{m=-\infty}^{\infty} P(\Omega) e^{-i\Omega(t-mT_s-2L'/c)} i\mu_0(\Omega_c+\Omega) \sqrt{\frac{P_T a_x a_y}{2\eta\pi}} \frac{1}{L'^2}$$

$$\times \bar{\bar{S}}(\hat{r}_s, \hat{r}_i; \Omega_c+\Omega) \cdot (\bar{\bar{I}} - \hat{r}_i\hat{r}_i) \cdot \hat{u}_a \exp[i2k_c(L' + (vt)^2/2L')]$$

$$\times \exp[-((k_c+k)a_x vt)^2/4L'^2] \exp[i(k_c+k)\hat{r}_s \cdot \bar{r}_c] \exp(-i\Omega_c t) \}, \quad (2.19)$$

where $\bar{r}_c$ is in the local coordinate with origin at the center of the receiver antenna aperture S_c, and the scattering direction satisfies

$$\hat{r}_s \approx -\hat{r}_i \approx \hat{z}' - \hat{x}vt/L', \tag{2.20}$$

according to the monostatic approximation and (2.14). To make the radar-return formulation in (2.19) symmetric, we define a "modified" scattering tensor $\bar{\bar{S}}'(\hat{r}_s, \hat{r}_i; \Omega_c + \Omega)$ such that

$$\frac{i(\Omega_c + \Omega)\mu_0}{4\pi}(\bar{\bar{I}} - \hat{r}_s\hat{r}_s) \cdot \bar{\bar{S}}'(\hat{r}_s, \hat{r}_i; \Omega_c + \Omega) = \bar{\bar{S}}(\hat{r}_s, \hat{r}_i; \Omega_c + \Omega), \tag{2.21}$$

and substitute (2.21) into (2.19). Thus the result becomes

$$\begin{aligned}\bar{E}_s(\bar{r}_c, t) \approx -\mathrm{Re}\{ \int_{-\infty}^{\infty} \frac{d\Omega}{2\pi} \sum_{m=-\infty}^{\infty} P(\Omega) e^{-i\Omega(t - mT_s - 2L'/c)} \mu_0^2 (\Omega_c + \Omega)^2 \sqrt{\frac{P_T a_x a_y}{32\eta\pi^3}} \frac{1}{L'^2} \\ (\bar{\bar{I}} - \hat{r}_s\hat{r}_s) \cdot \bar{\bar{S}}'(\hat{r}_s, \hat{r}_i; \Omega_c + \Omega) \cdot (\bar{\bar{I}} - \hat{r}_i\hat{r}_i) \cdot \hat{u}_a \exp[i2k_c(L' + (vt)^2/2L')] \\ \times \exp[-((k_c + k)a_x vt)^2/4L'^2] \exp[i(k_c + k)\hat{r}_s \cdot \bar{r}_c] \exp(-i\Omega_c t) \; \}. \end{aligned} \tag{2.22}$$

Notice that $\bar{\bar{S}}'(\hat{r}_s, \hat{r}_i; \Omega_c + \Omega)$ is the volume (or surface if the target is a perfect conductor) integral of $e^{-i(k_c+k)\hat{r}_s \cdot \bar{r}}$ times the induced volume (surface) current density over the target.

2.2.4 Receiver Front-End Model

The radar return is collected by a receiving antenna and downconverted to an intermediate frequency via a heterodyne process. We can represent the conversion of the field returned from the target, $\bar{E}_s(\bar{r}_c, t)$, to a front-end electronic signal, $y_{\text{front}}(t)$, by mixing with a virtual local-oscillator surface current density, $\bar{K}_c(\bar{r}_c, t)$, on the receiver antenna aperture S_c. Thus,

$$y_{\text{front}}(t) = \int\int_{S_c} d\bar{r}_c \bar{K}_c(\bar{r}_c, t) \cdot \bar{E}_s(\bar{r}_c, t). \tag{2.23}$$

The local-oscillator surface current density $\bar{K}_c$ is assumed to be a CW field with carrier frequency $\Omega_c - \Omega_{\text{IF}}$ and the same spatial beam pattern as the transmitted surface current

density $\bar{K}_a$, namely,

$$\bar{K}_c(\bar{r}_c,t) = \mathrm{Re}\left\{\hat{u}_c\sqrt{\frac{8P_{LO}}{\eta\pi a_x a_y}}\exp[-(x_c/a_x)^2-(y_c/a_y)^2]\exp[-i(\Omega_c+\Omega_{\mathrm{IF}})t]\right\}, \tag{2.24}$$

where $\hat{u}_c$ is the polarization of the local oscillator field.

Because of the mixing operation, the front-end signal $y_{\mathrm{front}}(t)$ contains an RF component with carrier frequency $2\Omega_c-\Omega_{\mathrm{IF}}$ and an IF component with carrier frequency Ω_{IF}. To extract the IF component, the front-end signal is passed through an IF bandpass filter with center frequency Ω_{IF}. From (2.23), it can be shown that, $y_{\mathrm{IF}}(t)$, the IF component of $y_{\mathrm{front}}(t)$, is

$$y_{\mathrm{IF}}(t) = \frac{1}{2}\mathrm{Re}\left[\int\int_{S_c} d\bar{r}_c\bar{\mathrm{K}}_c^*(\bar{r}_c,t)\cdot\bar{\mathrm{E}}_s(\bar{r}_c,t)\right], \tag{2.25}$$

where $*$ denotes complex conjugate, $\bar{\mathrm{K}}_c(\bar{r}_c,t)$ is the phasor of the CW field $\bar{K}_c(\bar{r}_c,t)$, and $\bar{\mathrm{E}}_s(\bar{r}_c,t)$ is the "time-dependent" phasor of the pulse field $\bar{E}_s(\bar{r}_c,t)$. These phasors satisfy the following relations:

$$\bar{K}_c(\bar{r}_c,t) = \mathrm{Re}\left\{\bar{\mathrm{K}}_c(\bar{r}_c,t)\exp[-i(\Omega_c+\Omega_{\mathrm{IF}})t]\right\}, \tag{2.26}$$

$$\bar{E}_s(\bar{r}_c,t) = \mathrm{Re}\left[\bar{\mathrm{E}}_s(\bar{r}_c,t)\exp(-i\Omega_c t)\right]. \tag{2.27}$$

The phasor (complex envelope) $y(t)$ of the IF signal $y_{\mathrm{IF}}(t)$ satisfies the relation $y_{\mathrm{IF}}(t) = \mathrm{Re}\left[y(t)e^{-i\Omega_{\mathrm{IF}}t}\right]$. From (2.22), (2.24), (2.25), we have that:

$$\begin{aligned} y(t) \approx & -\int_{-\infty}^{\infty}\frac{d\Omega}{2\pi}\sum_{m=-\infty}^{\infty}P(\Omega)e^{-i\Omega(t-mTs-2L'/c)}\mu_0^2(\Omega_c+\Omega)^2 \\ & \times\frac{\sqrt{P_T P_{LO}}a_x a_y}{4\pi\eta L'^2}\exp[i2k_c(L'+(vt)^2/2L')]\exp[-((k_c+k)a_x vt)^2/2L'^2] \\ & \hat{u}_c\cdot(\bar{\bar{I}}-\hat{r}_s\hat{r}_s)\cdot\bar{\bar{S}}'(\hat{r}_s,\hat{r}_i;\Omega_c+\Omega)\cdot(\bar{\bar{I}}-\hat{r}_i\hat{r}_i)\cdot\hat{u}_a, \end{aligned} \tag{2.28}$$

where $\hat{r}_i$ and $\hat{r}_s$ are obtained from (2.14) and (2.20), respectively.

The radar return in (2.28) is a train of pulses separated by T_s s. Because the returns associated with two adjacent pulses are ordinarily non-overlapping, we can reformulate $y(t)$

as a two-dimensional signal $r(m,\tau)$, using the discrete index m to represent the pulse number, and the continuous time τ to span the interval $(-T_s/2, T_s/2]$. That is,

$$y(t) \approx \sum_{m=-\infty}^{\infty} r(m, t - mT_s - 2L'/c), \tag{2.29}$$

where

$$\begin{aligned} r(m,\tau) \approx & -\int_{-\infty}^{\infty} \frac{d\Omega}{2\pi} P(\Omega) e^{-i\Omega\tau} \mu_0^2 (\Omega_c + \Omega)^2 \frac{\sqrt{P_T P_{LO}} a_x a_y}{4\pi\eta L'^2} \exp[i2k_c(L' + (mvT_s)^2/2L')] \\ & \times \exp[-((k_c + k)a_x mvT_s)^2/2L'^2]\ \hat{u}_c \cdot (\bar{\bar{I}} - \hat{r}_s\hat{r}_s) \\ & \cdot \bar{\bar{S}}'(\hat{z}' + \hat{x}mvT_s/L', -\hat{z}' - \hat{x}mvT_s/L'; \Omega_c + \Omega) \cdot (\bar{\bar{I}} - \hat{r}_i\hat{r}_i) \cdot \hat{u}_a. \end{aligned} \tag{2.30}$$

Also notice, in (2.28) and (2.30), that the polarimetric signature that is embedded in the scattering function can be exploited by choosing different incident ($\hat{u}_a$) and receiving ($\hat{u}_c$) polarizations. In what follows, we will define the aircraft flight direction $\hat{x}$ to be vertical polarization, and the direction $\hat{y}'$, which is orthogonal to $\hat{x}$ and the antenna's nominal direction $\hat{z}'$, to be horizontal polarization. In all cases we will consider the HH, VV, and HV components of the radar return; VH, being identical to HV because of reciprocity, will not be explicitly treated. We shall use the boldface symbol to denote the fully polarimetric return signal, namely,

$$\mathbf{r}(m,\tau) = \begin{bmatrix} r_{HH}(m,\tau) \\ r_{VV}(m,\tau) \\ r_{HV}(m,\tau) \end{bmatrix}. \tag{2.31}$$

The formulation in (2.30) describes the radar return from a scatterer at the scene center $(x,y,z) = (0, L'\cos(\psi), 0)$. When the scatterer is located at $(x,y,z) = (\Delta_x, \Delta_y + L\cot(\psi), 0)$ away from the scene center, its radar return can still be calculated by the same method. In this case, the target's location offset changes the incident and scattering directions which modify the antenna beam patterns and scattering coefficient in (2.30). The location offset also causes additional phase delay. Taking these effects into account, we can extend (2.30) to the case when the target position is $(\Delta_x, \Delta_y + L\cot(\psi), 0)$ away from the scene center with the following result:

$$r(m,\tau) \approx -\int_{-\infty}^{\infty} \frac{d\Omega}{2\pi} P(\Omega) e^{-i\Omega[\tau - 2\Delta_y \cos(\psi)/c]} \mu_0^2(\Omega_c+\Omega)^2 \frac{\sqrt{P_T P_{LO}} a_x a_y}{4\pi\eta L'^2}$$
$$\times \exp\{i2k_c[L' + \Delta_y\cos(\psi) + (\Delta_y \sin(\psi))^2/2L']\} \exp[ik_c(mvT_s - \Delta_x)^2/L']$$
$$\times \exp[-((k_c+k)a_x(mvT_s-\Delta_x))^2/2L'^2] \exp[-((k_c+k)a_y\Delta_y\sin(\psi))^2/2L'^2]$$
$$\hat{u}_c \cdot \bar{\bar{S}}'\left(\frac{\hat{z}'L' + \hat{x}mvT_s/L' - \hat{x}\Delta_x - \hat{y}\Delta_y}{|\hat{z}'L' + \hat{x}mvT_s/L' - \hat{x}\Delta_x - \hat{y}\Delta_y|}, \frac{-\hat{z}'L' - \hat{x}mvT_s/L' - \hat{x}\Delta_x - \hat{y}\Delta_y}{|\hat{z}'L' + \hat{x}mvT_s/L' - \hat{x}\Delta_x - \hat{y}\Delta_y|}; \Omega_c+\Omega\right) \cdot \hat{u}_a \quad (2.32)$$

where $\Delta_x << L'$ and $\Delta_y << L'$. In contrast to (2.30), it is clear in (2.32) that additional phase factor and different antenna beam patterns and scattering coefficient are incorporated. Since the location offset is much smaller than the slant range L', the incident and scattering directions are still approximately orthogonal to the plane of antenna aperture. Thus $(\bar{\bar{I}} - \hat{r}_i\hat{r}_i) \cdot \hat{u}_a$ and $(\bar{\bar{I}} - \hat{r}_s\hat{r}_s) \cdot \hat{u}_c$ in (2.30) are approximated by $\hat{u}_a$ and $\hat{u}_c$, respectively.

2.3 Target Model

In this study, we consider several types of objects with simple geometry and material composition, including a specular reflector, a dihedral reflector, and a dielectric volume. The radar return signal in (2.30) is related to the target object through the modified scattering tensor $\bar{\bar{S}}'$. Hence target modeling reduces to calculating this scattering tensor. The target types of interest are sketched in Figure 2.3.

2.3.1 Specular Reflector

The specular reflector we shall model is a flat plate with a perfectly conducting surface. Its bistatic scattering tensor can be calculated, in the physical optics limit, by assuming that the induced surface current density on the plate is $\bar{K} = 2\hat{n}_{sb} \times \bar{H}_i$, where $\hat{n}_{sb}$ is the surface normal and $\bar{H}_i$ is the incident magnetic field. We will consider a square reflector, with sides of length $2\rho_t$, and surface normal $\hat{n}_{sb} = \hat{x}\sin(\theta_{sb})\cos(\phi_{sb}) + \hat{y}\sin(\theta_{sb})\sin(\phi_{sb}) + \hat{z}\cos(\theta_{sb})$, where θ_{sb} and ϕ_{sb} are polar and azimuthal angles. When the reflector's normal direction lines

• Specular Reflector:

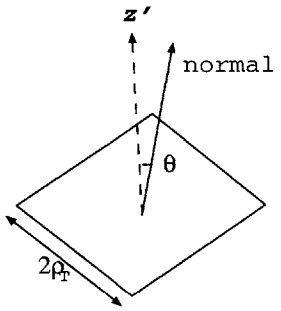

• Dihedral Reflector:

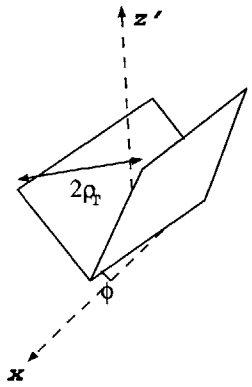

• Dielectric Volume:

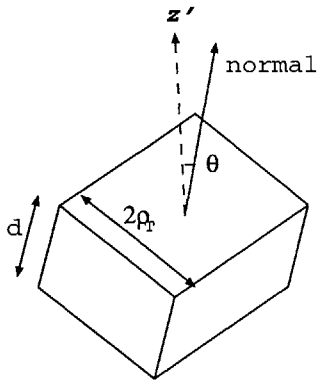

• Extended Rough Surface:

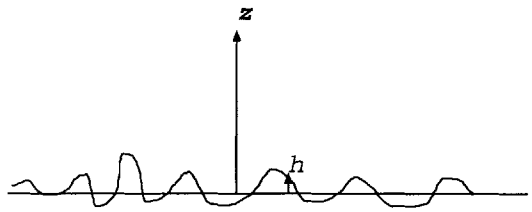

Figure 2.3 Types of targets.

up with the antenna aperture's normal direction, we have $\theta_{sb} = \pi/2 - \psi$, $\phi_{sb} = -\pi/2$. Thus the modified dyadic scattering tensor in (2.30) under the physical optics approximation is

$$\begin{aligned}
&\bar{\bar{S}}'(\hat{z}' + \hat{x}mvT_s/L', -\hat{z}' - \hat{x}mvT_s/L'; \Omega_c + \Omega) \\
&\approx \frac{2}{\eta}[\hat{r}_i\hat{n}_{sb} - (\hat{r}_i \cdot \hat{n}_{sb})\bar{\bar{I}}]\ 4\rho_t^2\ \mathrm{sinc}[(\Omega_c + \Omega)\alpha_{xb}\rho_t/c]\ \mathrm{sinc}[(\Omega_c + \Omega)\alpha_{yb}\rho_t/c], \qquad (2.33)
\end{aligned}$$

where

$$\alpha_{xb} = -\frac{2mvT_s}{L'}\sin(\phi_{sb}) - 2\cos(\psi)\cos(\phi_{sb}), \qquad (2.34)$$

and

$$\alpha_{yb} = -\frac{2mvT_s}{L'}\cos(\theta_{sb})\cos(\phi_{sb}) + 2\cos(\psi)\cos(\theta_{sb})\sin(\phi_{sb}) + 2\sin(\psi)\sin(\theta_{sb}). \qquad (2.35)$$

Substituting (2.33) into (2.30), we find that the 2-D polarimetric radar return from this target is

$$\begin{aligned}
\mathbf{r}(m,\tau)_{\text{specular}} \approx -\int_{-\infty}^{\infty} &\frac{d\Omega}{2\pi}P(\Omega)e^{-i\Omega\tau}\frac{\sqrt{P_T P_{LO}}(\Omega_c + \Omega)^2 a_x a_y}{2\pi c^2 L'^2}\ e^{i2k_c L'} \\
&\times \exp[(ik_c/L' - (k_c + k)^2 a_x^2/2L'^2)(mvT_s)^2]\ 4{\rho_t}^2(\hat{z}' \cdot \hat{n}_{sb}) \\
&\times \mathrm{sinc}[(\Omega_c + \Omega)\alpha_{xb}\rho_t/c]\ \mathrm{sinc}[(\Omega_c + \Omega)\alpha_{yb}\rho_t/c] \begin{bmatrix} 1 \\ 1 \\ 0 \end{bmatrix}. \qquad (2.36)
\end{aligned}$$

Equation (2.36) implicitly assumes that when the target at $\hat{y}L\cot\psi$ is within the antenna-beam footprint, $\hat{r}_s = -\hat{r}_i$ is approximately orthogonal to $\hat{u}_a$ and $\hat{u}_c$.

2.3.2 Dihedral Reflector

The dihedral reflector we shall consider consists of two perfectly-conducting rectangular plates 1 and 2 whose edges meet at a right angle. The orientation of this dihedral is defined by two unit vectors: the dihedral axis, $\hat{n}_{\text{axis}}$, is the intersecting edge of the two plates, and the normal axis, $\hat{n}_{\text{face}}$, is perpendicular to $\hat{n}_{\text{axis}}$ and bisects the 90° angle formed by two plates. Four terms in the reflected field from this dihedral are significant: specular reflection from plate 1 to the radar; specular reflection from plate 2 to the radar; double reflection

from plate 1 to plate 2 to the radar; and double reflection from plate 2 to plate 1 to the radar. To calculate these terms, we parallel the approach in [26]. The two single-reflection terms are obtained as was done in the specular reflector case. The two double-reflection terms are obtained by using geometric optics to calculate the reflection from the field from the first plate to the second. This field is then used as the incident wave for calculating the double-reflection contribution to the radar return via the physical optics approximation.

The complete analytic form of the scattering tensor of a dihedral reflector is presented in Appendix A. Here we will limit ourselves to noting two interesting points. The first concerns shadowing. Previous treatments of dihedral reflectors treat them as point scatterers when they are irradiated by plane waves whose propagation directions are perpendicular to $\hat{n}_{\text{axis}}$. This is justified from geometric optics in that every incident plane wave is reflected back to exactly the opposite direction. However, when calculating the double-reflection terms in our scattering model, the field incident on the second plate is a piece of plane wave—due to the geometric optics approximation—but it does not irradiate the entire area of the second plate because of shadowing. The higher the look angle with respect to $\hat{n}_{\text{face}}$ is, the larger the shadow area is, therefore the smaller the monostatic scattering coefficient becomes. As a result, the dihedral is not rigorously a point scatterer. The second point arises when the direction that bisects the dihedral, $\hat{n}_{\text{face}}$ is parallel to $\hat{z}'$ and the antenna position is near its $m = 0$ location. Under these conditions, the two double-reflection terms are approximately proportional to $\exp[-((k_c + k)l_z \cos(\phi)/2L')^2 (mvT_s)^2]$, where ϕ is the angle between $\hat{x}$ and dihedral axis. This implies that the duration (in the cross-range direction) of the radar return from a dihedral varies with the orientation of that target in a manner previously reported in [23].

2.3.3 Dielectric Volume

The dielectric volume we shall study is a rectangular-parallelepiped body filled with

homogeneous dielectric material of relative permittivity ϵ_r. To calculate the scattering coefficient of a dielectric volume, we first calculate the electric and magnetic fields inside the medium—from the infinite-layer approximation—and then obtain the induced current density from the internal field. Finally, the scattered field is found from the induced current by using the dyadic Green's function approach, cf. [27]. The complete analytical formulation of the scattering tensor of a dielectric volume is presented in Appendix B. The geometry of the dielectric volume has no intrinsic difference from that of our specular reflector. Its radar return is different, however, from that of the specular reflector, because the resonant structure of the dielectric body gives a range-dependent signature that the perfectly-conducting (surface-reflecting) mirror does not.

2.4 Clutter Model

Clutter typically refers to the radar return from anything other than the desired target. In this study, the only component other than the single target that contributes to the radar return will be assumed to be reflection from an infinite rough ground surface. To calculate this clutter return, we use a backpropagation formulation [3]. The backpropagation formulation for the radar return is based on the reciprocity of the free-space dyadic Green's function and the condition of narrow bandwidth. A complete derivation of the backpropagation formulation is provided in Appendix C. From Appendix C and using (2.24) to show that $\bar{\mathrm{K}}_c$ is real, we find that the complex envelope of the IF waveform due to clutter can be expressed as follows:

$$y(t) = \frac{1}{2}\int\int_{S_c} d\bar{r}_c \bar{\mathrm{K}}_c^*(\bar{r}_c, t) \cdot \bar{\mathrm{E}}_s(\bar{r}_c, t)$$

$$\approx \int\int_{S_b} d\bar{r}_b \left[\bar{\mathrm{K}}_s(\bar{r}_b, t - L'/c) \cdot \bar{\mathrm{E}}_c^b(\bar{r}_b, t - L'/c) - \bar{\mathrm{N}}_s(\bar{r}_b, t - L'/c) \cdot \bar{\mathrm{H}}_c^b(\bar{r}_b, t - L'/c)\right], \quad (2.37)$$

where S_b is the ground surface, $\bar{\mathrm{E}}_c^b$ and $\bar{\mathrm{H}}_c^b$ are backpropagated electric and magnetic fields generated from the local oscillator surface current density $\bar{\mathrm{K}}_c$, and $\bar{\mathrm{K}}_s$ and $\bar{\mathrm{N}}_s$ are the equivalent electric and magnetic surface current densities induced by the incident radar wave.

Note that the local oscillator current density is CW, having only harmonic time-dependence. Therefore its backpropagated fields $\bar{\mathrm{E}}_c^b$ and $\bar{\mathrm{H}}_c^b$ are identical to the forward-propagated fields $\bar{\mathrm{E}}_c$ and $\bar{\mathrm{H}}_c$.

The surface current densities $\bar{\mathrm{K}}_s$ and $\bar{\mathrm{N}}_s$ in (2.37) do not imply that the rough surface is a perfect conductor. They are "equivalent" surface current densities representing the rough-surface scattering effect in the sense that the scattered field $\bar{\mathrm{E}}_s$ from the surface can be expressed in terms of $\bar{\mathrm{K}}_s$ and $\bar{\mathrm{N}}_s$ via Huygens' principle,

$$\bar{\mathrm{E}}_s(\bar{r},t) = \int_{-\infty}^{\infty} \frac{d\Omega}{2\pi} e^{-i\Omega t} \int\int_{S_b} d\bar{r}_b \{\, i\mu_0(\Omega_c+\Omega)\bar{\bar{G}}(\bar{r},\bar{r}_b;\Omega_c+\Omega)\cdot[\hat{n}_b(\bar{r}_b)\times\bar{\bar{\mathrm{H}}}(\bar{r}_b,\Omega)]$$

$$+\nabla\times\bar{\bar{G}}(\bar{r},\bar{r}_b;\Omega_c+\Omega)\cdot[\hat{n}_b(\bar{r}_b)\times\bar{\bar{\mathrm{E}}}(\bar{r}_b,\Omega)]\,\}, \tag{2.38}$$

where $\hat{n}_b(\bar{r}_b)$ is the normal vector of the rough surface at $\bar{r}_b$, $\bar{\bar{\mathrm{E}}}(\bar{r}_b,\Omega)$ and $\bar{\bar{\mathrm{H}}}(\bar{r}_b,\Omega)$ are the Fourier components of the time-dependent phasors $\bar{\mathrm{E}}(\bar{r}_b,t)$ and $\bar{\mathrm{H}}(\bar{r}_b,t)$ at frequency Ω, that is,

$$\bar{\bar{\mathrm{E}}}(\bar{r}_b,\Omega) = \int_{-\infty}^{\infty} dt\bar{\mathrm{E}}(\bar{r}_b,t)e^{i\Omega t}, \tag{2.39}$$

$$\bar{\bar{\mathrm{H}}}(\bar{r}_b,\Omega) = \int_{-\infty}^{\infty} dt\bar{\mathrm{H}}(\bar{r}_b,t)e^{i\Omega t}, \tag{2.40}$$

and the surface current densities are

$$\bar{\mathrm{K}}_s = \hat{n}_b \times \bar{\mathrm{H}}_s, \tag{2.41}$$

$$\bar{\mathrm{N}}_s = -\hat{n}_b \times \bar{\mathrm{E}}_s. \tag{2.42}$$

Therefore, calculating the current excited on the rough surface is equivalent to solving a rough-surface scattering problem.

To facilitate a simple, analytical construction of a clutter model, we solve the rough surface scattering problem via the Kirchhoff approximation presented in [24], which computes the scattered field from an arbitrary point on the rough surface by using Snell's law with respect to the plane tangential to the surface point of interest. Substituting the electric and

magnetic surface current densities $\bar{K}_s$ and $\bar{N}_s$ obtained from the Kirchhoff approximation into (2.37), we get the following expression for the IF complex envelope of the clutter return from the rough surface,

$$y(t) = \int_{-\infty}^{\infty} \frac{d\Omega}{2\pi} e^{-i\Omega(t-L'/c)} \int\int_{S_b} d\bar{r}_b \bar{E}_c^b(\bar{r}_b) \cdot \frac{1}{\eta} \{ [-(\hat{n}_b(\bar{r}_b) \cdot \hat{r}_i)\ \hat{q}_i(\bar{r}_b)\ \hat{q}_i(\bar{r}_b)\ (1 - R_h(\bar{r}_b, \Omega_c + \Omega))$$
$$+ (\hat{n}_b(\bar{r}_b) \times \hat{q}_i(\bar{r}_b))\ \hat{p}_i(\bar{r}_b)\ (1 + R_v(\bar{r}_b, \Omega_c + \Omega))]$$
$$+ \bar{\bar{r}}_i \cdot [\ (\hat{n}_b(\bar{r}_b) \cdot \hat{r}_i)\ \hat{q}_i(\bar{r}_b)\ \hat{p}_i(\bar{r}_b)\ (1 - R_v(\bar{r}_b, \Omega_c + \Omega))$$
$$+ (\hat{n}_b(\bar{r}_b) \times \hat{q}_i(\bar{r}_b))\ \hat{q}_i(\bar{r}_b)\ (1 + R_h(\bar{r}_b, \Omega_c + \Omega))] \} \cdot \bar{\bar{E}}_a(\bar{r}_b, \Omega), \tag{2.43}$$

In (2.43) the dyad $\bar{\bar{r}}_i$ is defined such that for any vector $\bar{A}$, $\hat{r}_i \times \bar{A} = \bar{A} \cdot \bar{\bar{r}}_i$. The vectors $\hat{p}_i(\bar{r}_b)$ and $\hat{q}_i(\bar{r}_b)$ are the localized vertical and horizontal polarizations with respect to the incident vector $\hat{r}_i$ at $\bar{r}_b$ on the rough surface S_b (see Figure 2.4). In other words, $\hat{q}_i(\bar{r}_b) = \hat{n}_b(\bar{r}_b) \times \hat{r}_i$, $\hat{p}_i(\bar{r}_b) = \hat{n}_b(\bar{r}_b) \times \hat{q}_i(\bar{r}_b)$. $R_h(\bar{r}_b, \Omega_c + \Omega)$ and $R_v(\bar{r}_b, \Omega_c + \Omega)$ are the horizontally and vertically polarized reflection coefficients at location $\bar{r}_b$ and frequency $\Omega_c + \omega$. From Snell's law,

$$R_h(\bar{r}_b, \Omega_c + \Omega) = \frac{\cos(\theta_l)(\bar{r}_b) - \sqrt{\epsilon_{r1}(\Omega_c + \Omega) - \sin^2\theta_l(\bar{r}_b)}}{\cos(\theta_l)(\bar{r}_b) + \sqrt{\epsilon_{r1}(\Omega_c + \Omega) - \sin^2\theta_l(\bar{r}_b)}}, \tag{2.44}$$

$$R_v(\bar{r}_b, \Omega_c + \Omega) = \frac{\epsilon_{r1}(\Omega_c + \Omega)\cos(\theta_l)(\bar{r}_b) - \sqrt{\epsilon_{r1}(\Omega_c + \Omega) - \sin^2\theta_l(\bar{r}_b)}}{\epsilon_{r1}(\Omega_c + \Omega)\cos(\theta_l)(\bar{r}_b) + \sqrt{\epsilon_{r1}(\Omega_c + \Omega) - \sin^2\theta_l(\bar{r}_b)}}, \tag{2.45}$$

where $\theta_l(\bar{r}_b)$ is the angle between $\hat{r}_i$ and $\hat{n}_b(\bar{r}_b)$, $\epsilon_{r1}(\Omega_c + \Omega)$ is the relative permittivity of the medium below the rough surface S_b at frequency $\Omega_c + \omega$ (see Figure 2.4). Here the relative permittivity is assumed to be independent of position within a local region. On a coarser scale, the relative permittivity could be different in different regions since the terrain texture is not homogeneous in general.

The term in braces between the transmitter forward propagating field and the receiver backpropagation field in the integrand of (2.43) corresponds to the effect of rough-surface reflection. In general, it is a complicated dyadic factor depending on the dielectric constant and the orientation of the local surface tangent. For a given surface profile, it requires an

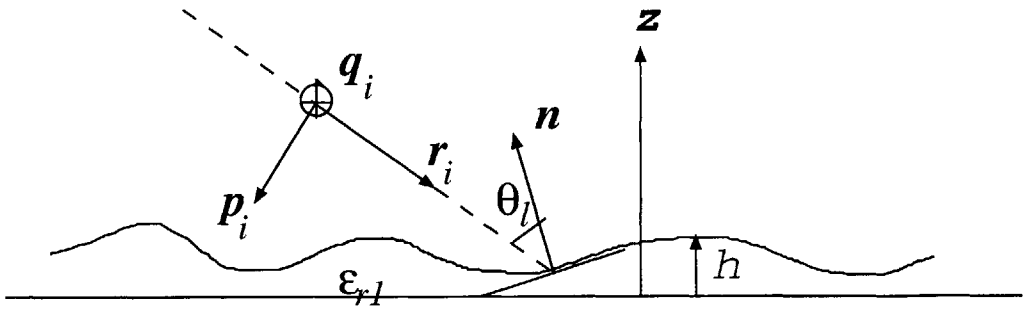

Figure 2.4 Local incident angle and polarization vectors for the rough surface.

intensive amount of computation to obtain this factor. Moreover, in a real situation it is almost impossible to get the exact profile of terrain surface. Therefore, for practical reasons, we adopt a generic, quasi-phenomenological approach based on (2.43) to model the effect of rough-surface reflection. Assume the rough surface S_b in concern is defined by a surface height profile h, namely, $z_b = -h(x_b, y_b)$. Then the generic clutter model is constructed as follows.

First, for the rough surface S_b, we introduce a dyadic reflector tensor $\bar{\bar{R}}(\bar{r}_b, \Omega_c + \Omega)$ to represent the term in braces in the integrand of (2.43). Second, we project the domain of the surface integral in (2.43) from S_b to the $z_b = 0$ plane. Thus the integrand of the surface integral over $z_b = 0$ plane becomes the product of the transmitter forward propagating field at $z_b = 0$, the dyadic reflection tensor $\bar{\bar{R}}$, the receiver backpropagation field at $z_b = 0$, and the Jacobian corresponding to the domain conversion from S_b to $z_b = 0$ plane, and the round-trip phase delay corresponding to the wave propagation of the transmitter and receiver fields between S_b and $z_b = 0$ plane. The Jacobian is $1/\cos(\zeta(x_b, y_b))$ where $\zeta(x_b, y_b)$ is the angle between $\hat{z}$ and n_b at (x_b, y_b). Third, we apply (2.16) for the forward propagating transmitter field and the receiver backpropagation field at $z_b = 0$, and assume that: (i) the curvature of the surface S_b is small enough that the variation of the Jacobian over (x_b, y_b)

can be neglected; (ii) the relative permittivity of the medium below the surface is almost a constant over the bandwidth of the radar pulse so that the reflection tensor $\bar{\bar{R}}$ is frequency-independent; and (iii) the bandwidth of the radar pulse does not resolve the surface height, i.e., that $|h| << cT_0/2(T_0W_0+1)$. Then the polarimetric 2-D clutter return from a rough surface becomes:

$$\begin{aligned}\mathbf{r}_{\text{clutter}}(m,\tau) \approx & -\frac{\sqrt{P_T P_{LO}}\Omega_c^2 a_x a_y}{2\pi c^2 L'^2} e^{i2k_c L'} \sin(\psi) \int_{-\infty}^{\infty}\int_{-\infty}^{\infty} dx_b dy_b p(\tau - 2y_b\cos(\psi)/c) \\ & \times \exp[(ik_c/L' - k_c^2 a_x^2/2L'^2)(x_b - mvT_s)^2]\ \exp[(ik_c/L' - k_c^2 a_y^2/2L'^2)y_b^2\sin^2(\psi)] \\ & \times \exp[i2k_c[y_b\cos(\psi) + h(x_b,y_b)\sin(\psi)]] \begin{bmatrix} R_{HH}(x_b,y_b) \\ R_{VV}(x_b,y_b) \\ R_{HV}(x_b,y_b) \end{bmatrix}, \end{aligned} \tag{2.46}$$

where R_{HH}, R_{VV}, and R_{HV} are the HH, VV, and HV components of the dyadic reflection tensor $\bar{\bar{R}}$.

Equation (2.46) describes the radar return from a deterministic rough surface. As a practical matter, it is too complicated to pursue the deterministic approach in detail, so we shall model $h(x_b,y_b)$, $R_{HH}(x_b,y_b)$, $R_{VV}(x_b,y_b)$ and $R_{HV}(x_b,y_b)$ as stochastic processes. Paralleling the work in [3][4] we define a field transition coefficient:

$$\mathbf{T}(x_b,y_b) = \exp[i2k_c h(x_b,y_b)\sin(\psi)] \begin{bmatrix} R_{HH}(x_b,y_b) \\ R_{VV}(x_b,y_b) \\ R_{HV}(x_b,y_b) \end{bmatrix}. \tag{2.47}$$

Assuming that $\sqrt{\langle h^2\rangle} >> \lambda_c$, and that the reflection coefficients $R_{\alpha\beta}$ are independent of the surface height profile h, we can take $\mathbf{T}$ to be a zero-mean, circulo-complex, white, vector-Gaussian random process, fully characterized by

$$\begin{aligned}\langle \mathbf{T}(x_b,y_b)\mathbf{T}^\dagger(x_b',y_b')\rangle = & \frac{\lambda_c^2}{\sin^2(\psi)}\delta(x_b - x_b')\delta(y_b - y_b') \\ \times & \begin{bmatrix} \langle|R_{HH}(x_b,y_b)|^2\rangle & \langle R_{HH}(x_b,y_b)R_{VV}^*(x_b,y_b)\rangle & \langle R_{HH}(x_b,y_b)R_{HV}^*(x_b,y_b)\rangle \\ \langle R_{HH}^*(x_b,y_b)R_{VV}(x_b,y_b)\rangle & \langle|R_{VV}(x_b,y_b)|^2\rangle & \langle R_{HV}^*(x_b,y_b)R_{VV}(x_b,y_b)\rangle \\ \langle R_{HH}^*(x_b,y_b)R_{HV}(x_b,y_b)\rangle & \langle R_{VV}^*(x_b,y_b)R_{HV}(x_b,y_b)\rangle & \langle|R_{HV}(x_b,y_b)|^2\rangle \end{bmatrix}. \end{aligned} \tag{2.48}$$

Note that the correlation matrix in (2.48) includes the polarimetric behavior of the clutter return, which can depend significantly on the geographic region under inspection. In this paper we shall assume there is a statistically-uniform terrain texture within the radar footprint. Therefore the correlation matrix in (2.48) is approximately independent of x_b and y_b. Empirical work [13] suggests that: all the off-diagonal components in (2.48) are insignificant except for the HH×VV terms; the HH×HH and VV×VV terms are approximately equal; and the strength of HV×HV term is significantly smaller than that of HH×HH term, unless multiple scattering is prominent. Thus, in our radar clutter model, we use

$$\langle \mathbf{T}(x_b, y_b)\mathbf{T}^\dagger(x_b', y_b')\rangle = \frac{\lambda_c^2}{\sin^2(\psi)}\delta(x_b - x_b')\delta(y_b - y_b')\begin{bmatrix} 1 & \rho & 0 \\ \rho^* & 1 & 0 \\ 0 & 0 & \epsilon \end{bmatrix}, \tag{2.49}$$

where $0 < |\rho| < 1$ and $0 < \epsilon < 1$.

A diffuse target is modeled as a finite square piece of the rough surface with sides of length $2\rho_t$. Hence, referring to (2.46), (2.47), the 2-D radar return from a diffuse target becomes

$$\begin{aligned}\mathbf{r}_{\text{diffuse}}(m,\tau) \approx -\frac{\sqrt{P_T P_{LO}}\Omega_c^2 a_x a_y}{2\pi c^2 L'^2} e^{i2k_c L'} \sin(\psi) \int_{-\rho_t}^{\rho_t}\int_{-\rho_t}^{\rho_t} dx_b dy_b p(\tau - 2y_b\cos(\psi)/c) \\ \times \exp[(ik_c/L' - k_c^2 a_x^2/2L'^2)(x_b - mvT_s)^2]\ \exp[(ik_c/L' - k_c^2 a_y^2/2L'^2)y_b^2\sin^2(\psi)] \\ \times \exp[i2k_c y_b\cos(\psi)]\mathbf{T}(x_b, y_b)\end{aligned} \tag{2.50}$$

In Chapter 3 we will use the model described in (2.50) to demonstrate that the radar return from a diffuse target is much more isotropic than that from a specular reflector.

2.5 Noise Model

Noise refers to the contamination of the radar return by the receiver system at the front end. Typically, this is thermal noise, and has a white spectrum. In this paper, the receiver noise $\mathbf{r}_{\text{noise}}(m,\tau)$ is assumed to be a zero-mean, circulo-complex, vector-Gaussian stochastic

process that is white in all its domains, viz., its discrete-time index, m, its continuous-time parameter, τ, and its vector (polarimetric) domain. Thus it is completely characterized by the following correlation matrix,

$$\langle \mathbf{r}_{\text{noise}}(m,\tau)\mathbf{r}^{\dagger}_{\text{noise}}(m',\tau')\rangle = N_0\delta[m-m']\delta(\tau-\tau')\begin{bmatrix}1&0&0\\0&1&0\\0&0&1\end{bmatrix}. \tag{2.51}$$

Both of the unwanted components of the radar return, the clutter and the noise, are stochastic in our model. Since the receiver noise and the radar clutter have completely different physical origins, we assume that they are statistically independent of each other.

Chapter 3

Performance of 2-D Stripmap SAR

3.1 Stripmap SAR Processor Models

To get useful information from the radar return modeled in the previous chapter requires the use of appropriate signal processing. In this chapter, two types of SAR image processing systems are considered: an adaptive-resolution processor and a whitening-filter processor. System models for these two processors are described here.

3.1.1 Adaptive-Resolution Processor

Figure 3.1 shows the architecture for our adaptive-resolution 2-D SAR processor. The incoming radar return is passed through chirp compression filters in both the cross-range (discrete-time) and range (continuous-time) domains. The output from these chirp compression filters is then video detected to form a radar intensity image. The impulse responses for the chirp compression filters are

$$h_1[m] = \exp[(-ik_c/L' - k_c^2 a_x^2 \kappa^2/2L'^2)(mvT_s)^2] \quad \text{and} \quad h_2(\tau) = \exp[(i\pi W_0/T_0 - 4\nu^2/T_0^2)\tau^2]. \tag{3.1}$$

A conventional 2-D SAR processor uses chirp-compression filters $h_1[m]$ and $h_2(\tau)$ arranged—by setting $\kappa = \nu = 1$—to be matched filters for the radar return from a point scatterer. As noted earlier, an extended specular target can have a very different return duration than that from a point scatterer. Thus our adaptive-resolution processor will be optimized over κ and ν to achieve best detection performance for such an extended target. We will use $\mathbf{l}^{\mathrm{AR}}_{\mathrm{target}}(m,\tau)$, $\mathbf{l}^{\mathrm{AR}}_{\mathrm{clutter}}(m,\tau)$, and $\mathbf{l}^{\mathrm{AR}}_{\mathrm{noise}}(m,\tau)$ to denote target-return, clutter, and noise outputs,

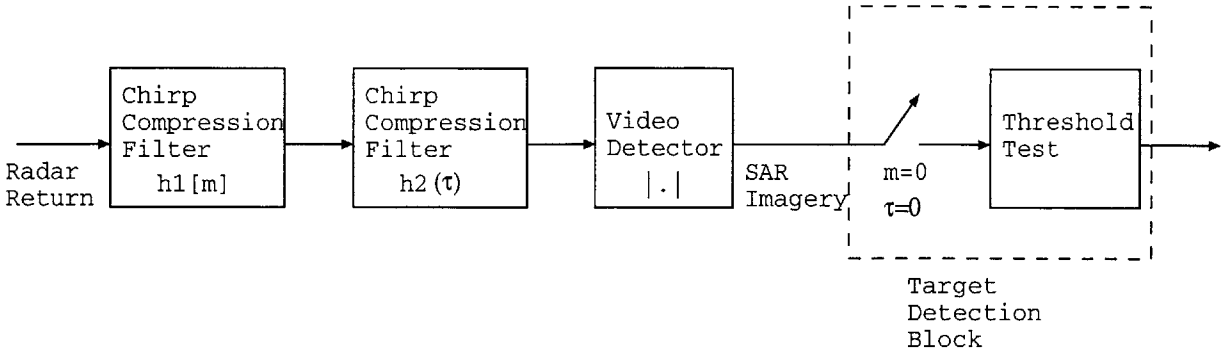

Figure 3.1 Block diagram of adaptive-resolution 2-D SAR processor.

respectively, from the adaptive-resolution chirp-compression filters in (3.1). They are given by

$$\begin{aligned} \mathbf{l}^{\mathrm{AR}}_{\mathrm{component}}(m,\tau) &= h_2(\tau) * h_1[m] * \mathbf{r}_{\mathrm{component}}(m,\tau) \\ &= \sum_{m'=-\infty}^{\infty} h_1[m-m'] \int_{-\infty}^{\infty} d\tau' h_2(\tau-\tau') \mathbf{r}_{\mathrm{component}}(m',\tau'), \end{aligned} \tag{3.2}$$

where $*$ denotes convolution, and "component" could be target, clutter, or noise.

3.1.2 Whitening Processor

Optimized adaptive-resolution processing, of the type just described, can enhance SAR image resolution. However, for binary detection of a deterministic target return embedded in stochastic clutter and noise, the optimum Neyman-Pearson processing scheme uses a filter to whiten the clutter-plus-noise component of the IF waveform, followed by a matched filter corresponding to the target-return waveform passed through the whitening filter, followed in turn by video detection, sampling, and a threshold test. This processing architecture is shown in Figure 3.2.

The form of the whitening filter is determined by the covariance function of the clutter-plus-noise component of the radar return's IF complex envelope. Because the clutter and

the noise are independent, their overall covariance function is the sum of their individual covariance functions. The covariance of the receiver noise is given in (2.50). From (2.46), (2.47), and (2.49), the covariance of the radar clutter can be calculated. The resulting covariance function of the clutter-plus-noise component $\mathbf{r}_v$ is:

$$\langle \mathbf{r}_v(m,\tau)\mathbf{r}_v^\dagger(m',\tau')\rangle = N_0\delta[m-m']\delta(\tau-\tau')\begin{bmatrix}1&0&0\\0&1&0\\0&0&1\end{bmatrix}$$
$$+P_0\exp[-B_0(A_0\tau^2+C_0\tau'^2-2\tau\tau')]\exp[-D_0(m-m')^2]\begin{bmatrix}1&\rho&0\\\rho^*&1&0\\0&0&\epsilon\end{bmatrix}, \tag{3.3}$$

where

$$P_0 = \left(\frac{\Omega_c a_x a_y}{cL'^2}\right)^2 P_T P_{LO}\pi\sqrt{\frac{1}{[32\cos^2(\psi)/c^2T_0^2+k_c^2a_y^2\sin^2(\psi)/L'^2](k_c^2a_y^2/L'^2)}},$$
$$A_0 = 1+\frac{k_c^2a_y^2\sin^2(\psi)/L'^2}{(-i\pi W_0/T_0+4/T_0^2)(4\cos^2(\psi)/c^2)},$$
$$B_0 = \frac{[(4/T_0^2)^2+(\pi W_0/T_0)^2](4\cos^2(\psi)/c^2)}{32\cos^2(\psi)/T_0^2c^2+k_c^2a_y^2\sin^2(\psi)/L'^2},$$
$$C_0 = 1+\frac{k_c^2a_y^2\sin^2(\psi)/L'^2}{(i\pi W_0/T_0+4/T_0^2)(4\cos^2(\psi)/c^2)},$$
$$D_0 = \frac{v^2T_s^2}{k_c^2a_x^2/L'}[(k_c^2a_x^2/2L'^2)^2+(k_c/L')^2]. \tag{3.4}$$

From (3.3) we see that the clutter $\mathbf{r}_{\text{clutter}}(m,\tau)$ is stationary with respect to the discrete cross-range coordinate m, a result consistent with the work in [6][23], but it is non-stationary with respect to the continuous range coordinate τ, unless $A_0 = C_0 = 1$. To derive the whitening-filter impulse response for the non-stationary process $\mathbf{r}_v(m,\tau)$, one may employ the Karhunan-Loeve expansion of (3.4). However, the functional form of the non-stationary whitening filter is cumbersome and difficult to calculate. To avoid its direct manipulation in our performance calculations we will come up with a simpler form by imposing constraints on the radar parameters. It can be shown that when $(1/4)\tan^2(\psi)(k_ca_y/L')^2(cT_0)^2 << 1$, the

parameters A_0 and C_0 in (3.4) are approximately equal to 1, hence the $\mathbf{r}_v(m,\tau)$ covariance function in (3.3) is approximately stationary. Combining this condition with the Fraunhofer far-field limit $k_c a_x^2/L' << 1$, (3.3) reduces to:

$$\langle \mathbf{r}_v(m,\tau)\mathbf{r}_v^\dagger(m',\tau')\rangle = N_0\delta[m-m']\delta(\tau-\tau')\begin{bmatrix}1&0&0\\0&1&0\\0&0&1\end{bmatrix}$$

$$+P\exp[-A(\tau-\tau')^2]\exp[-B(m-m')^2]\begin{bmatrix}1&\rho&0\\\rho^*&1&0\\0&0&\epsilon\end{bmatrix}, \tag{3.5}$$

where

$$P = \left(\frac{\Omega_c a_x a_y}{cL'^2}\right)^2 P_T P_{LO}\pi\frac{L'cT_0}{4\sqrt{2}\cos(\psi)k_c a_x},$$
$$A = \frac{1}{8}\left[\left(\frac{4}{T_0}\right)^2 + (\pi W_0)^2\right],$$
$$B = \left(\frac{vT_s}{a_x}\right)^2. \tag{3.6}$$

Note that $(1/4)\tan^2(\psi)(k_c a_y/L')^2(cT_0)^2 << 1$ is not an unreasonable assumption for a typical SAR system. For example, in Lincoln Lab's ADTS, the slant range $L' \approx 7000$ m, the antenna beamwidth $1/(k_c a_y) \approx \pi/90$, and the pulse width T_0 is of the same order of the reciprocal bandwidth, 1/600 MHz [28]. Hence $(k_c a_y/L')(cT_0) \approx 1/486 << 1$ for this system.

Let us define the shift-invariant covariance function $\mathbf{K}_{vv}(m,\tau) = \langle \mathbf{r}_v(m+m',\tau+\tau')\cdot \mathbf{r}_v^\dagger(m',\tau')\rangle$, and define the Fourier transform of $\mathbf{K}_{vv}(m,\tau)$ to be $\mathbf{S}_{vv}(\omega,\Omega)$, where

$$\mathbf{S}_{vv}(\omega,\Omega) = \sum_{m=-\infty}^{\infty} e^{-i\omega m}\int_{-\infty}^{\infty} d\tau e^{i\Omega\tau}\mathbf{K}_{vv}(m,\tau), \tag{3.7}$$

and ω, Ω are frequencies associated with the discrete and continuous time coordinates, m and τ, respectively. To whiten the spectrum in (3.7), the frequency response of the whitening filter $\mathbf{H}_w(\omega,\Omega)$ must satisfy the following relation:

$$\mathbf{H}_w(\omega,\Omega)\cdot\mathbf{S}_{vv}(\omega,\Omega)\cdot\mathbf{H}_w^\dagger(\omega,\Omega) = \mathbf{I}, \tag{3.8}$$

where $\mathbf{I}$ is the 3×3 identity matrix. In other words, the filter $\mathbf{H}_w(\omega, \Omega)$ whitens the stochastic signal $\mathbf{v}$ in the discrete cross-range coordinate, continuous range coordinate, and polarimetric domains. Plugging (3.5) and (3.7) into (3.8), the frequency response of the whitening filter $\mathbf{H}_w(\omega, \Omega)$ can be obtained. The result is

$$\mathbf{H}_w(\omega,\Omega) = \begin{bmatrix} \frac{\rho^*/\sqrt{2}|\rho|}{\sqrt{N_0+(1+|\rho|)\alpha(\omega,\Omega)}} & \frac{1/\sqrt{2}}{\sqrt{N_0+(1+|\rho|)\alpha(\omega,\Omega)}} & 0 \\ \frac{-\rho^*/\sqrt{2}|\rho|}{\sqrt{N_0+(1-|\rho|)\alpha(\omega,\Omega)}} & \frac{1/\sqrt{2}}{\sqrt{N_0+(1-|\rho|)\alpha(\omega,\Omega)}} & 0 \\ 0 & 0 & \frac{1}{\sqrt{N_0+(1+\epsilon\alpha(\omega,\Omega))}} \end{bmatrix}, \tag{3.9}$$

where

$$\alpha(\Omega,\omega) = P\sqrt{\frac{\pi}{A}}e^{-\Omega^2/4A}\sum_{m=-\infty}^{\infty} e^{-i\omega m}e^{-Bm^2}. \tag{3.10}$$

Let the impulse response of the whitening filter, which is the inverse Fourier transform of $\mathbf{H}_w(\omega, \Omega)$, be $\mathbf{h}_w(m, \tau)$. Then the impulse response of the matched filter $\mathbf{h}_M(m, \tau)$ is the transpose conjugate, time reverse of the receiver front-end target waveform passed through the whitening filter, namely,

$$\begin{aligned} \mathbf{h}_M^\dagger(-m,-\tau) &= \mathbf{h}_w(m,\tau) * \mathbf{r}_{\text{target}}(m,\tau) \\ &= \sum_{m'=-\infty}^{\infty}\int_{-\infty}^{\infty} d\tau' \mathbf{h}_w(m-m',\tau-\tau')\cdot\mathbf{r}_{\text{target}}(m',\tau'). \end{aligned} \tag{3.11}$$

Note that the whitening-filter output is a 3×1 vector, whereas the matched-filter impulse response is a 1×3 vector. Hence the matched-filtered radar signal is a scalar, unlike the output from the adaptive-resolution processor, which is rather a 1×3 polarimetric vector. The scalar output components of target return, clutter, and noise after the whitening filter and the matched filter are

$$l_{\text{component}}^{\text{white}}(m,\tau) = \mathbf{h}_M(m,\tau) * \mathbf{h}_w(m,\tau) * \mathbf{r}_{\text{component}}(m,\tau), \tag{3.12}$$

for "component" = target, clutter, and noise.

The whitening-filter processor is seldom as practical as the adaptive-resolution processor; it requires exact knowledge of the clutter and noise statistics, as well as the waveforms

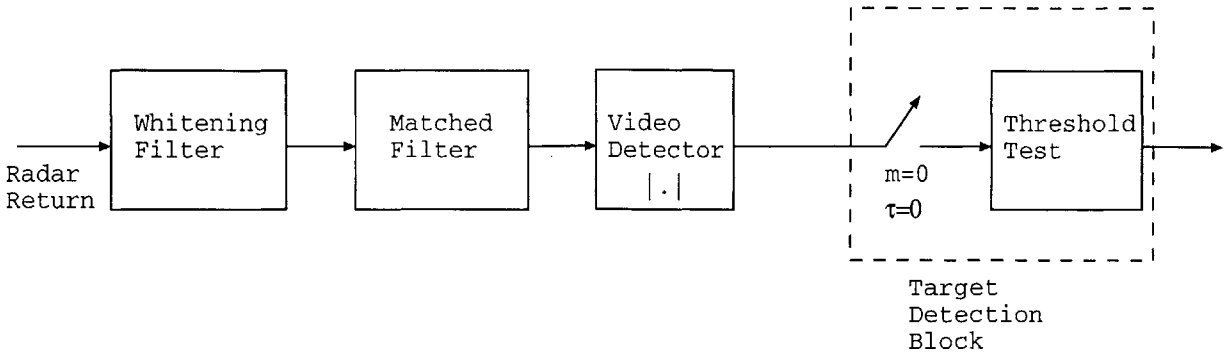

Figure 3.2 Block diagram of whitening-filter processor.

scattered from the target types of interest. Nevertheless, the whitening-filter processor is conceptually important in that it is the Neyman-Pearson optimum processor for the target detection problem. As such, its receiver operating characteristic—its detection vs. false-alarm probability behavior—bounds the performance of any realizable processor. By comparing the detection performance of a adaptive-resolution processor with that of a whitening processor, we can have a better idea about how far the adaptive-resolution processor's detection performance is from the ultimate theoretical limit. By comparing the detection performance of the optimized adaptive-resolution processor with its conventional-processor ($\kappa = 1, \nu = 1$) limit, we can learn how important it is to treat extended targets differently from point scatterers.

3.2 Performance Analysis

We now explore the performance of the adaptive-resolution SAR processor under several interesting operating conditions. We begin by studying its SAR-imagery spatial resolution as we vary the processing durations for the cross-range and range filters. Then we formulate a likelihood-ratio test for the associated target detection problem and show that its

performance is totally characterized by the signal-to-noise-plus-clutter-ratio (SNCR). Finally, we present numerical results comparing the SNCRs of the adaptive-resolution and whitening-filter processors.

3.2.1 Spatial Resolution Behavior

For a target located at a known position $(x, y, z) = (0, L/\tan(\psi), 0)$ on the ground, the intensity image produced by our adaptive-resolution processor has its maximum value at $m = \tau = 0$. Let us define the image resolution in the cross-range (range) direction as the width of the region around $\tau = 0$ (around cross-range $m = 0$) within which the intensity exceeds $1/e$ of the peak value. Figure 3.3 shows numerical results for these resolutions as functions of the processing duration parameters, κ and ν. Five target types are considered: specular reflector; dihedral reflector with orientation angle $\phi = 0°$; dihedral reflector with orientation angle $\phi = 90°$; diffuse target; and dielectric volume with relative permittivity $\epsilon_r = 10 + i5$. All targets have the same geometric size. The diffuse-target image is defined as the ensemble average of the processor output intensity based on the statistics of the clutter.

Several interesting features are revealed in Figure 3.3. First, the cross-range adaptive-resolution signatures of the specular reflector and the diffuse target are different, and this difference is accentuated as the processing duration decreases, i.e., as κ increases. For sufficiently large κ the spatial resolution of the diffuse target is much larger than that of the specular reflector. This behavior is easily explained. When the processing duration is very short the cross-range component of radar return undergoes almost no pulse compression, so its SAR image is nearly return-duration limited. The coherent scattering structure of a specular reflector produces a strongly directional reflected beam, whereas the diffuse target scatters into the hemisphere. The resulting difference in target-return durations accounts for the resolution difference seen in Figure 3.3.

The second interesting feature in Figure 3.3 is the orientation-angle dependence of the

dihedral reflector's adaptive-resolution signature. When the dihedral axis lines up with direction, $\hat{y}$, its spatial-resolution behavior is very close to that of the diffuse target, whereas when its axis lines up with the aircraft-flight direction, $\hat{x}$, its spatial-resolution behavior is like that of the specular reflector. This trend is also consistent with our physical intuition. When the dihedral axis lines up with $\hat{y}$, the dihedral looks like an isotropic scatterer insofar the cross-range direction is concerned so a strong return is observed from every direction. When the dihedral axis lines up with $\hat{x}$, such isotropy is not present, hence the cross-range behavior of the scattering pattern is similar to that of the specular reflector.

The final feature worth noting about Figure 3.3 is that the cross-range behavior of the dielectric volume is very close to that of the specular reflector. This phenomenon can be explained by recalling that the scattering coefficient depends on the incident/scattering directions and the frequency. Roughly speaking, the direction dependence of the scattering coefficient determines the cross-range behavior, whereas its frequency dependence determines the range behavior. Typically these two dependences are coupled. However, when the radar bandwidth is much smaller than the carrier frequency, the space and frequency dependent terms are approximately separable. For the dielectric volume, the direction-dependent part of the scattering coefficient is almost identical to that of the specular reflector. Therefore the cross-range spatial resolutions of these two target types are quite similar.

Spatial resolution behavior in the range direction is different from what we have just discussed for the cross-range direction. Although there are differences in the range-direction spatial resolutions among our various target types, the differences are not very large. This indicates that, over the radar's pulse bandwidth, the frequency dependences of the target scattering coefficients are all quite similar.

3.2.2 Target Detection Problem

Suppose that a single target may or may not be located at $(x, y, z) = (0, L/\tan(\psi), 0)$,

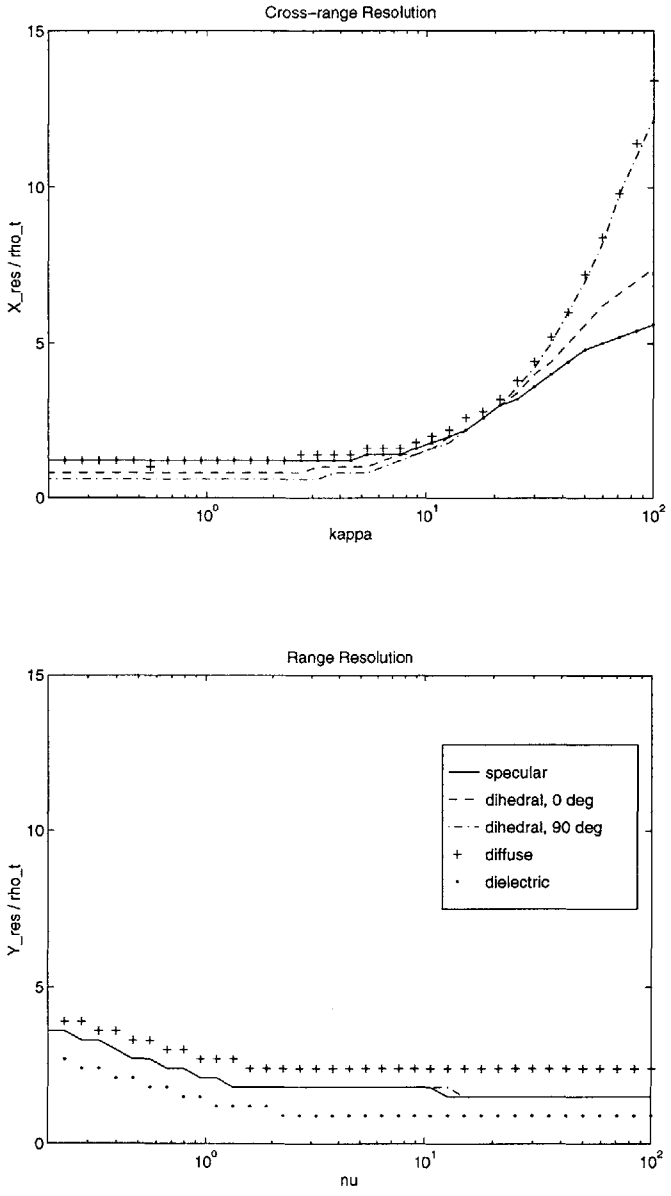

Figure 3.3 SAR imagery spatial resolutions as functions of chirp-compression filter durations. The calculations assume $k_c a_x^2/2L' = 0.004$, $\rho_t/a_x = 5.0$, $\Omega_c/2\pi = 10\,\text{GHz}$, $T_0 = 0.05\,\mu\text{s}$, $W_0 = 10\,\text{MHz}$, and $\epsilon_r = 10.0 + i5.0$.

on top of a clutter-generating rough-surface ground. Thus, the IF complex envelope at the input to either the Figure 3.1 or Figure 3.2 processor is

$$\mathbf{r}(m,\tau) = \mathbf{r}_{\text{clutter}}(m,\tau) + \mathbf{r}_{\text{noise}}(m,\tau), \tag{3.13}$$

when the target is absent (hypothesis H_0), or it is

$$\mathbf{r}(m,\tau) = e^{i\phi_r}\mathbf{r}_{\text{target}}(m,\tau) + \mathbf{r}_{\text{clutter}}(m,\tau) + \mathbf{r}_{\text{noise}}(m,\tau), \tag{3.14}$$

when the target is present (hypothesis H_1). Here, ϕ_r is an uniformly-distributed random phase representing the incoherence of target return with respect to the clutter and noise, and the target is a known choice from our set of possibilities: specular reflector, dihedral reflector of known orientation, or dielectric volume.

For both the adaptive-resolution (Figure 3.1) and the whitening-filter (Figure 3.2) processing architectures, we wish to optimize Neyman-Pearson detection performance, viz., we wish to maximize the detection probability

$$P_D = \Pr(\text{say}H_1 \mid H_1\text{true}), \tag{3.15}$$

at a prescribed false-alarm probability,

$$P_F = \Pr(\text{say}H_1 \mid H_0\text{true}). \tag{3.16}$$

It is known [29] that the threshold tests shown in Figure 3.1 and Figure 3.2 are indeed the optimum post-filter decision rules, for the hypothesis test specified above, and that the Figure 3.2 system is the optimum processing of the raw data specified in (3.13) and (3.14). Moreover, the receiver operating characteristic—the P_D vs. P_F curve traced out as the threshold is increased from zero to infinity—for either of these tests takes the following simple form,

$$P_D = Q(\sqrt{2 \cdot \text{SNCR}}, \sqrt{-2\ln(P_F)}), \tag{3.17}$$

where

$$Q(\alpha,\beta) = \int_{\beta}^{\infty} dz z \exp(-\alpha^2/2 - z^2/2) I_0(\alpha z), \tag{3.18}$$

is Marcum's Q function, $I_0(x) = \int_0^{2\pi} (d\psi/2\pi) e^{x\cos(\psi)}$ is the zeroth-order modified Bessel function, and SNCR is the signal-to-noise-plus-clutter ratio of the processor under consideration. As indicated in (3.17) and (3.18), the P_D-P_F curve is parametrized by the SNCR value. Hence the performance of the binary target detection problem is fully characterized by this parameter.

The SNCR in (3.17) and (3.18) is defined as the signal-to-noise-plus-clutter after the processor. For the adaptive-resolution processor, the SNCR has three polarimetric components, HH, VV, and HV, since the processor output is a 3×1 vector, hence,

$$\mathrm{SNCR}^{\mathrm{AR},\alpha\beta} = \frac{\left| l_{\mathrm{target}}^{\mathrm{AR},\alpha\beta}(m=0,\tau=0) \right|^2}{\langle \left| l_{\mathrm{clutter}}^{\mathrm{AR},\alpha\beta}(m=0,\tau=0) \right|^2 \rangle + \langle \left| l_{\mathrm{noise}}^{\mathrm{AR},\alpha\beta}(m=0,\tau=0) \right|^2 \rangle}, \tag{3.19}$$

where $\alpha\beta$ = HH, VV, HV. For the whitening-filter processor, the SNCR has only one component since the processor output is a scalar, hence

$$\mathrm{SNCR}^{\mathrm{white}} = \frac{\left| l_{\mathrm{target}}^{\mathrm{white}}(m=0,\tau=0) \right|^2}{\langle \left| l_{\mathrm{clutter}}^{\mathrm{white}}(m=0,\tau=0) \right|^2 \rangle + \langle \left| l_{\mathrm{noise}}^{\mathrm{white}}(m=0,\tau=0) \right|^2 \rangle}. \tag{3.20}$$

3.2.3 Signal-to-Noise-plus-Clutter-Ratio

In this subsection, we will compare numerical SNCR values for our adaptive-resolution (AR) processor and the optimum whitening-filter processor. The parameter values used in our computations are given in Table 3.1. These parameters are not based on any real SAR imaging system, but they are not far from the specification of such a system. Compared with the Lincoln Laboratory 35 GHz airborne SAR imaging system [28], our radar carrier frequency is lower (35 GHz vs. 10 GHz), bandwidth is smaller (600 MHz overall bandwidth vs. 10 MHz chirp bandwidth), and slant range is about the same (7000 m vs. 7070 m). The cross-range and range resolutions for the Lincoln Laboratory system are both 0.3 m. When

Flight Parameters	Radar Parameters	Reflector Parameters
aircraft altitude $L = 5000\,\mathrm{m}$	antenna radii $a_x = a_y = 1\,\mathrm{m}$	target radii $\rho_t = 1.5\,\mathrm{m}$
aircraft speed $v = 100\,\mathrm{m/s}$	Tx and LO powers $P_T = P_{LO} = 1\,\mathrm{W}$	relative permittivity $\epsilon_r = 10 + i5$
slant angle $\psi = 45°$	radar frequency $f_c = \Omega_c/2\pi = 10\,\mathrm{GHz}$	HV clutter strength $\epsilon = 0.2$
	pulse-repetition period $T_s = 10\,\mathrm{ms}$	HH×VV correlation $\rho = 0.57$
	pulse width $T_0 = 0.05\,\mu\mathrm{s}$	
	chirp bandwidth $W_0 = 10\,\mathrm{MHz}$	

Table 3.1 Table of parameter values for SNCR calculations.

the target is a point scatterer and $\kappa = \nu = 1$, the parameter set in Table 3.1 implies a 1 m cross-range resolution width and 16.1 m range resolution for stripmap-mode operation, and 0.7 m cross-range resolution and 19.1 m range resolultion for spotlight-mode operation.

3.2.3.1 Adaptive-Resolution Processor

Figure 3.4 illustrates the variation of the specular reflector's SNCR with respect to processing durations. In this figure, CNR is the clutter-to-noise spectrum ratio at zero frequency. The two panels on the left in Figure 3.4 are under clutter-dominant conditions (SNCR $\approx$ SCR, where SCR is the signal-to-clutter ratio) whereas the two on the right are under noise-dominant conditions (SNCR $\approx$ SNR, where SNR is the signal-to-noise ratio). The top two panels in Figure 3.4 show the cross-range-processing duration behavior, and the two lower panels give the range-processing duration behavior. For the cross-range features, different curves represent different antenna aperture sizes. All the curves shown are for HH polarization, because the VV values turned out to be very close to the HH, and the HV values were negligible.

Figure 3.4 makes it clear that the clutter-dominated regime is very different from the noise-dominated regime. This is because the clutter has a colored-noise spectrum that is quite different from the white spectrum of the receiver noise. When noise dominates, the SNCR is a unimodal function of κ, with a maximum $\kappa = \kappa_{\text{opt}}$. This optimum κ value best matches the duration of the cross-range processor to the radar return from the target. The return duration for the specular reflector is shorter than that for the isotropic/diffuse target, hence $\kappa_{opt} > 1$ for the specular reflector. If we presume the return beam to be approximately a Gaussian pattern, we can show that $\kappa_{opt} \approx \sqrt{1 + 2\rho_t^2/a_x^2}$.

Turning now to the range-processing duration behavior in the noise-dominant regime, we see from Figure 3.4 that the SNCR value is unimodal in ν, with an optimum value fixed at unity. The optimum ν value does not change because the shape of each individual radar pulse is unaffected by surface reflection from the specular reflector. Figure 3.4 also shows that in the noise-dominant regime the SNCR is independent of chirp bandwidth W_0.

Figure 3.5 illustrates the orientation-angle dependence of the SNCR for a dihedral mirror. The orientation angle, ϕ, is the angle between the dihedral axis and $\hat{x}$. The most significant feature in Figure 3.5 is the polarimetric effect. The SNCR values for HH and VV are almost identical. They both have local maxima at $\phi = 0°$ and $\phi = 90°$, as well as minima at $\phi = 45°$. Unlike the specular reflector case, the SNCR values for HV do not vanish. With respect to orientation angle, their behavior is opposite to that of HH and VV: at $\phi = 0°$ and $\phi = 90°$ local minima occur, at $\phi = 45°$ a maximum occurs. Such ϕ-dependent characteristics are generated by the double-reflection terms of the dihedral mirror's scattering function. As the dihedral axis is rotated, the polarization of the doubly-reflected electromagnetic field rotates twice as fast. At $\phi = 45°$, the rotation is 90°, hence the cross-polarized component, HV, becomes much stronger than the co-polarized components, HH and VV. The different patterns of SNCR variation at different polarizations implies that the full polarimetric information is essential to the detection and recognition of a dihedral mirror (or other types of targets

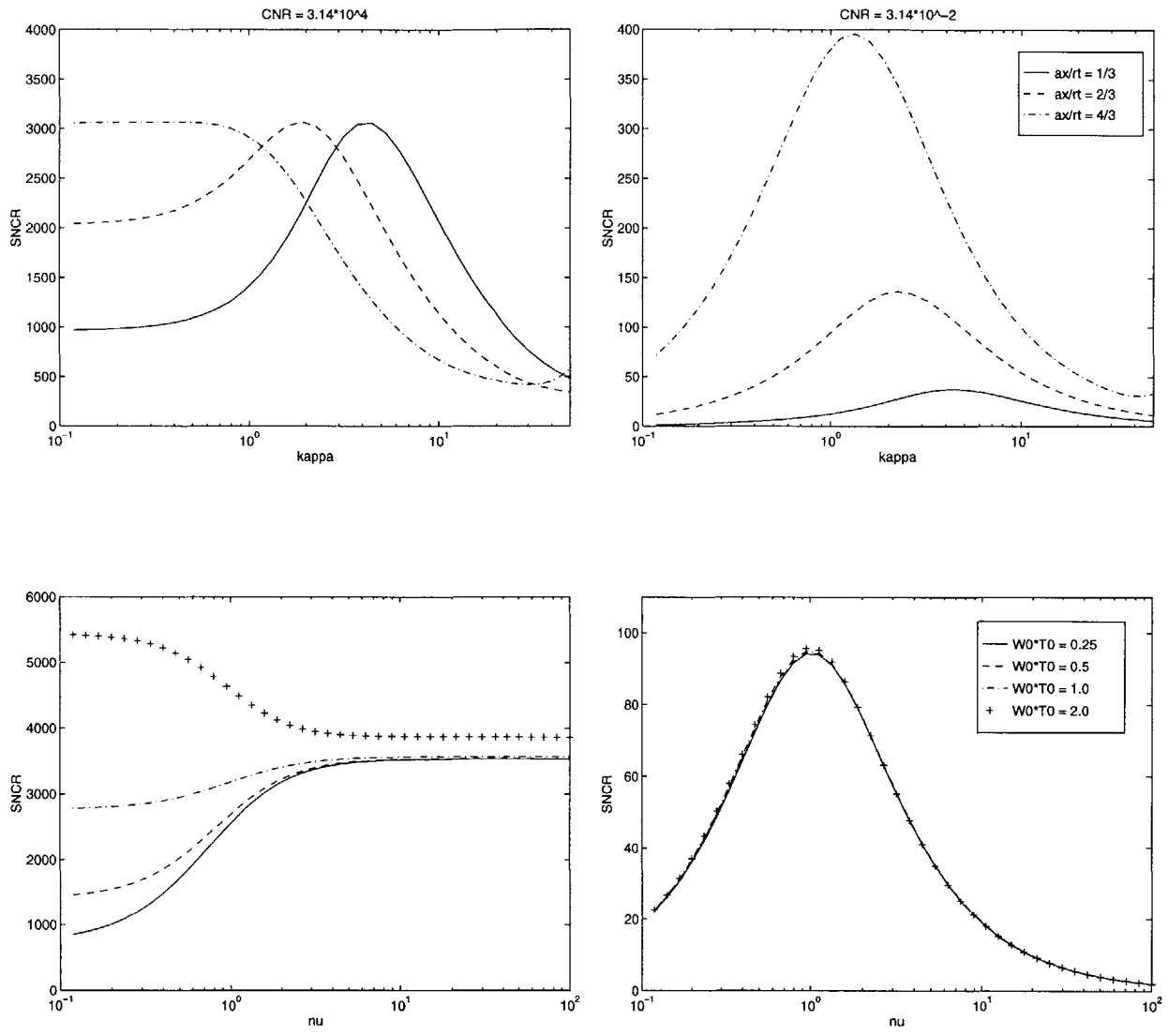

Figure 3.4 SNCR vs. chirp-compression filter durations: AR processor, specular reflector. Upper panels have $\nu = 1$; lower panels have $\kappa = 1$.

involving multiple scattering).

The dihedral's orientation affects its return-beam pattern too. Figure 3.6 illustrates the variation of a dihedral reflector's SNCR with respect to κ when the noise dominates the clutter. At the three orientation angles $\phi = 0°, 45°, 90°$, the SNCR variations are similar to each other, as well as to their counterparts for a specular reflector. However the optimum κ values are different for different ϕ: the larger ϕ is, the smaller κ_{opt} becomes. This is because the scattering beamwidth of a dihedral mirror in the cross-range direction is a function of its orientation angle. The larger ϕ is, the closer its scattering pattern is to being isotropic, hence the longer its return duration. By treating the scattering coefficient of dihedral mirror as approximately Gaussian, the optimum κ can be taken to be $\kappa_{opt} \approx \sqrt{1 + (\rho_t^2/a_x^2)\cos^2(\phi)}$. Notice that even though the return-beam pattern for a dihedral reflector at $\phi = 90°$ is very close to isotropic, it is not identical to that of an isotropic scatterer. The radar return is not equally strong at all look angles. At large look angles, more dramatic shadowing is encountered, and hence the radar return becomes weaker. So a directional scattering beam pattern still exists for a dihedral oriented at 90°. This effect becomes significant when the antenna footprint is large enough to irradiate the target at a look angle that is well off the slant direction: at $\phi = 90°$ with $a_x/\rho_t = 1/3$, Figure 3.6 shows that κ_{opt} differs significantly from unity.

Figure 3.7 illustrates the dielectric volume's SNCR variations with respect to κ and ν when the noise dominates the clutter. The κ-dependent features here are identical to those seen for the specular reflector: the optimum κ values are the same, and the SNCR values for different aperture sizes are in the same proportion. The ν-dependent behavior is different, however, from the previous (surface-scattering) cases. The radar return from a dielectric volume has a SNCR that decreases with increasing chirp bandwidth W_0. These results are consistent with the comments made in Section 2.3.3. The cross-range beam pattern of the radar return from a dielectric volume is the same as that of a specular reflector. Volume

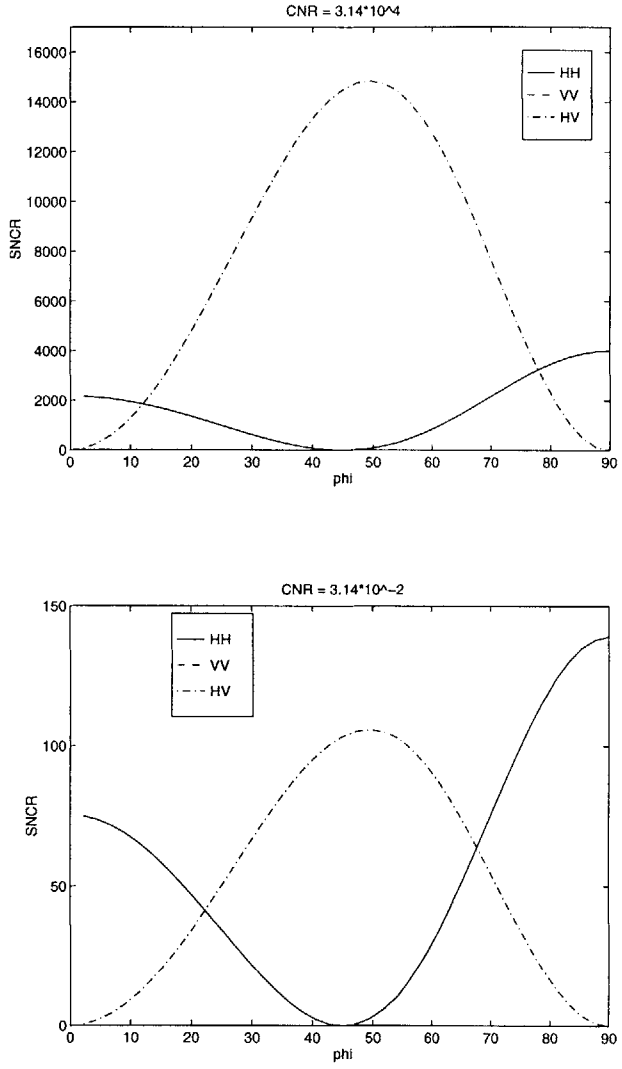

Figure 3.5 SNCR vs. orientation angle: AR processor, dihedral reflector, $\kappa = \nu = 1$; clutter dominant for the upper panel and noise dominant for the lower panel.

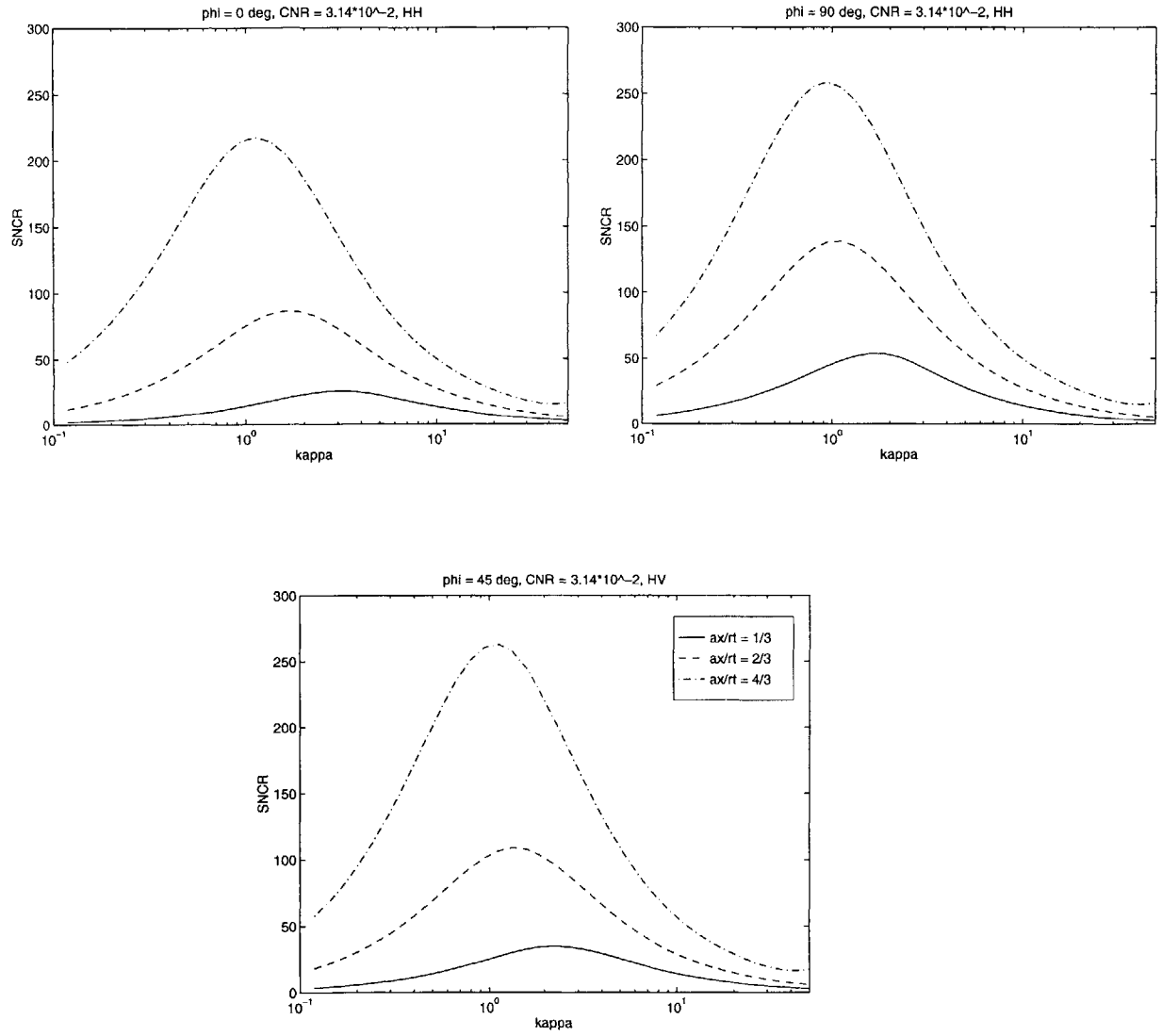

Figure 3.6 SNCR vs. cross-range chirp-compression filter duration: AR processor, dihedral reflector, $\nu = 1$, noise dominant; the upper left panel has dihedral orientation angle $\phi = 0°$, upper right panel has $\phi = 90°$, lower panel has $\phi = 45°$.

scattering, however, disperses individual radar pulses, and this effect becomes more serious with increasing pulse bandwidth.

3.2.3.2 Whitening Processor

Here we shall compare the SNCR values for the AR processor with those for the optimum, whitening-filter processor. Note for the parameters in Table 3.1, the value

$$(1/4)\tan^2(\psi)(k_c a_y/L')^2(cT_0)^2 \approx \pi^2/200 << 1.$$

Hence the clutter is approximately stationary, and the whitening filter in (3.9) can be applied.

By construction, the clutter-plus-noise part of whitening filter's output has a white spectrum. Thus, the SNCR value for the whitening-filter processor in (3.20) reduces to the "energy" of the impulse response of the matched filter described in (3.11):

$$\begin{aligned}\mathrm{SNCR}_{\mathrm{white}} &= \sum_{m=-\infty}^{\infty}\int_{-\infty}^{\infty} d\tau \mathbf{h}_M(-m,-\tau)\cdot\mathbf{h}_M^{\dagger}(-m,-\tau) \\ &= \int_{-\pi}^{\pi}\frac{d\omega}{2\pi}\int_{-\infty}^{\infty}\frac{d\Omega}{2\pi}\mathbf{R}_{\mathrm{target}}^{\dagger}(\omega,\Omega)\cdot\mathbf{H}_w^{\dagger}(\omega,\Omega)\cdot\mathbf{H}_w(\omega,\Omega)\cdot\mathbf{R}_{\mathrm{target}}(\omega,\Omega), \qquad (3.21)\end{aligned}$$

where $\mathbf{R}_{\mathrm{target}}(\omega,\Omega)$ is the 2-D Fourier transform of $\mathbf{r}_{\mathrm{target}}(m,\tau)$, and the equality is derived from (3.11) and Parseval's theorem. Plugging the whitening filter from (3.9) into (3.21), we obtain:

$$\mathrm{SNCR}_{\mathrm{white}} \approx \int_{-\infty}^{\infty}\frac{d\Omega}{2\pi}\int_{-\infty}^{\infty}\frac{d\omega}{2\pi}\left[\frac{(N_0+\alpha)(|S_{HH}|^2+|S_{VV}|^2)-2\mathrm{Re}[\alpha\rho S_{HH}^* S_{VV}]}{[N_0+(1+|\rho|)\alpha][N_0+(1-|\rho|)\alpha]}+\frac{|S_{HV}|^2}{N_0+\epsilon\alpha}\right], \qquad (3.22)$$

where S_{uv} is the target-return spectrum for input and output polarizations u and v, respectively.

If we approximate the variations of the target return along the range and cross-range directions by Gaussian shapes, then the two filters $h_1[m]$ and $h_2(\tau)$ in the κ-ν-optimized AR

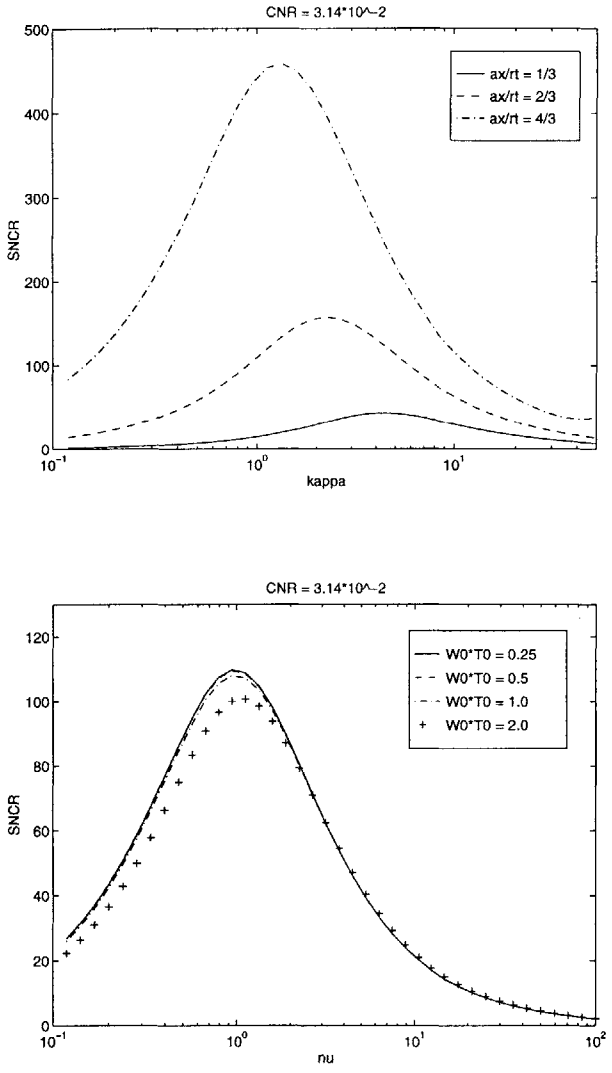

Figure 3.7 SNCR vs. chirp-compression filter durations: AR processor, dielectric volume, noise dominant. Top panel has $\nu = 1$; lower panel has $\kappa = 1$.

processor are the matched filters for the target return waveform. By Parseval's theorem, the SNCR for the κ-ν-optimized AR processor is approximately.

$$\mathrm{SNCR}_{\mathrm{AR}}^{uv} \approx \frac{\left[\int_{-\infty}^{\infty}\frac{d\Omega}{2\pi}\int_{-\infty}^{\infty}\frac{d\omega}{2\pi}|S_{uv}|^2\right]^2}{\int_{-\infty}^{\infty}\frac{d\Omega}{2\pi}\int_{-\infty}^{\infty}\frac{d\omega}{2\pi}|S_{uv}|^2(N_0+\alpha c_{uv})}, \tag{3.23}$$

where c_{uv} is reflection-coefficient covariance between polarizations u and v, which is the $u-v$ element of the matrix in (2.49).

Several significant aspects can be discerned from (3.22) and (3.23). In the noise-dominant regime, i.e., when $N_0 >> \alpha(\Omega,\omega)$ for all (Ω,ω), we see that $\mathrm{SNCR}_{\mathrm{white}}$ reduces to the sum of target-return energies over all three polarizations divided by the noise spectrum N_0, whereas $\mathrm{SNCR}_{\mathrm{AR}}$ becomes the target-return energy at a specific polarization divided by the noise spectrum. Therefore $\mathrm{SNCR}_{\mathrm{white}}/\mathrm{SNCR}_{\mathrm{AR}}$ becomes a polarimetric-effect-dependent constant. Regardless of the polarimetric effect, $\mathrm{SNCR}_{\mathrm{AR}}$ in this case has reached its upper bound.

When we are not in the noise-dominant regime, the relationship between $\mathrm{SNCR}_{\mathrm{white}}$ and $\mathrm{SNCR}_{\mathrm{AR}}$ is more complicated, and the AR processor might not be able to achieve the optimum, white-noise limit. Figure 3.8 plots the numerical results for $\mathrm{SNCR}_{\mathrm{white}}/\mathrm{SNCR}_{\mathrm{AR}}$ versus CNR for different target types. All the curves in Figure 3.8 have a similar trend: $\mathrm{SNCR}_{\mathrm{white}} >> \mathrm{SNCR}_{\mathrm{AR}}$ prevails when clutter dominates. As the white-noise spectrum is increased, however, the performance gap between the optimum processor and the AR processor decreases. Eventually, the noise-dominant regime is reached and $\mathrm{SNCR}_{\mathrm{white}}/\mathrm{SNCR}_{\mathrm{AR}}$ becomes independent of CNR and equal to 2 for the specular reflector, the dielectric volume, and the dihedral reflector at $\phi = 0°$ and $90°$, and equal to one for the dihedral reflector at $\phi = 45°$.

The work of [6] on 1-D SAR showed that when the size of a specular target becomes much larger than the antenna aperture $\mathrm{SNCR}_{\mathrm{white}}/\mathrm{SNCR}_{\mathrm{AR}} \approx 1$ prevails regardless of the clutter strength. The reason this occurs in 1-D SAR is that a very large specular reflector

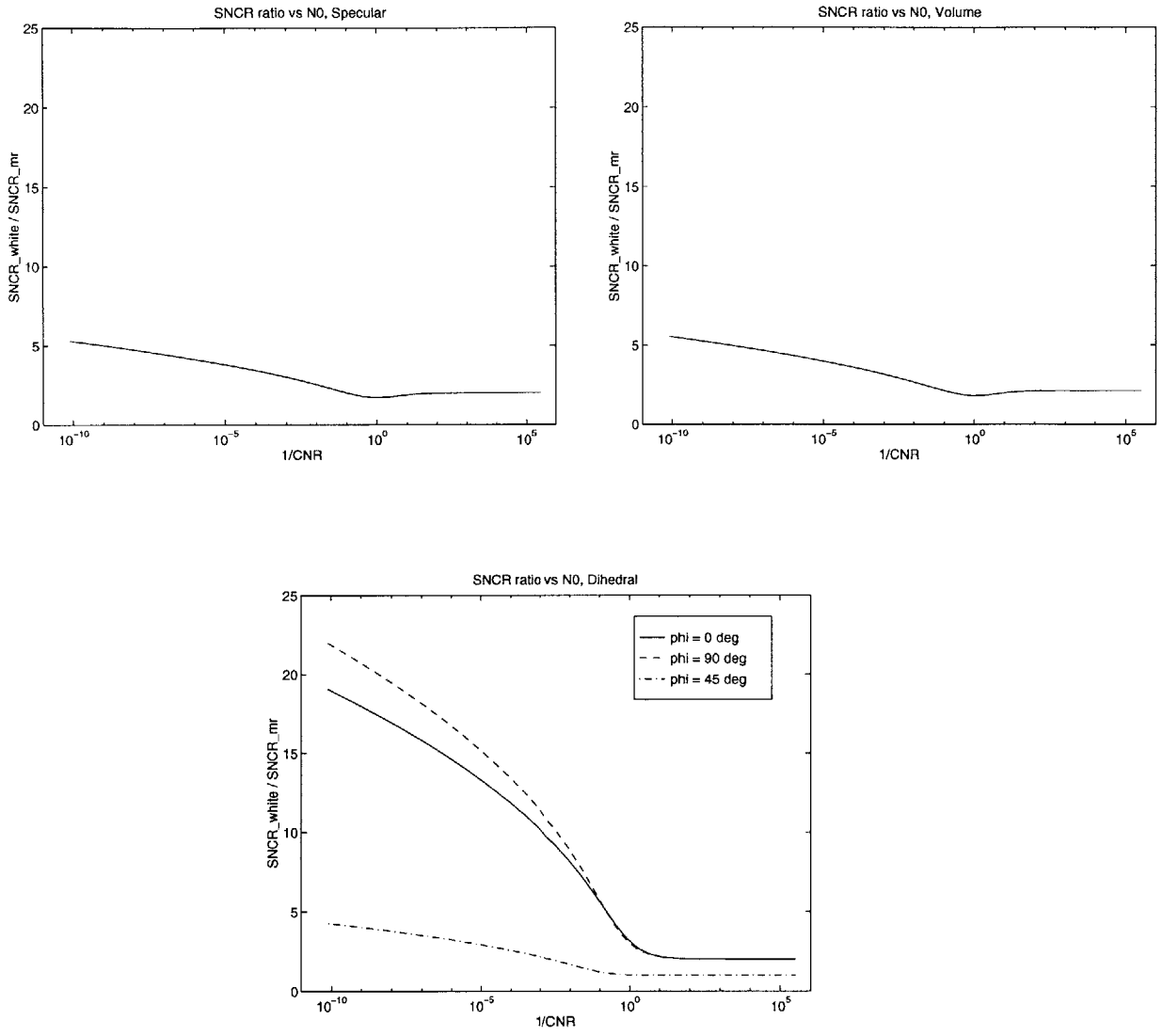

Figure 3.8 $\mathrm{SNCR_{white}/SNCR_{AR}}$ vs. CNR. For the AR processor, $\kappa = [1 + 2\rho_t^2/a_x^2]^{1/2}$, for the specular reflector and the dielectric volume, and $\kappa = [1 + (\rho_t^2/a_x^2)\cos^2(\phi)]^{1/2}$ for the dihedral reflector; $\nu = 1$ in all cases. The chosen polarimetric component is HH for the specular reflector, the dielectric volume, the dihedral reflector at $\phi = 0°$ and $90°$, and is HV for the dihedral reflector at 45°. Upper left panel: specular reflector, upper right panel: dielectric volume, lower panel: dihedral reflector.

produces a very short duration return. Over the small chirp bandwidth associated with such a short-duration return the clutter spectrum is almost white, so the whitening filter is superfluous and the optimum receiver is the duration-optimized AR processor.

Our analysis shows that the preceding result of [6] does not extend to 2-D SAR. The most critical difference between the 1-D and 2-D configurations is that the latter has two frequencies—ω and Ω—representing variations along the cross-range and the range directions. Having a large specular target indeed renders the clutter spectrum flat within the narrow ω-bandwidth of that target's short-duration return. But the Ω-bandwidth of the target, which is not significantly altered by target size, is still comparable to the Ω-bandwidth of the clutter. So the clutter spectrum cannot be approximated as white within the 2-D bandwidth of the target return, hence omitting the whitening filter inevitably leads to sub-optimum detection performance. Figure 3.9 plots $\mathrm{SNCR}_{\mathrm{white}}/\mathrm{SNCR}_{\mathrm{AR}}$ versus target size. Increasing target size does reduce $\mathrm{SNCR}_{\mathrm{white}}/\mathrm{SNCR}_{\mathrm{AR}}$ to some extent, but this improvement is limited by CNR. The minimum $\mathrm{SNCR}_{\mathrm{white}}/\mathrm{SNCR}_{\mathrm{AR}}$ is not always optimum (2 or 1, depending on polarimetric condition). The larger CNR is, the higher the minimum $\mathrm{SNCR}_{\mathrm{white}}/\mathrm{SNCR}_{\mathrm{AR}}$ value becomes.

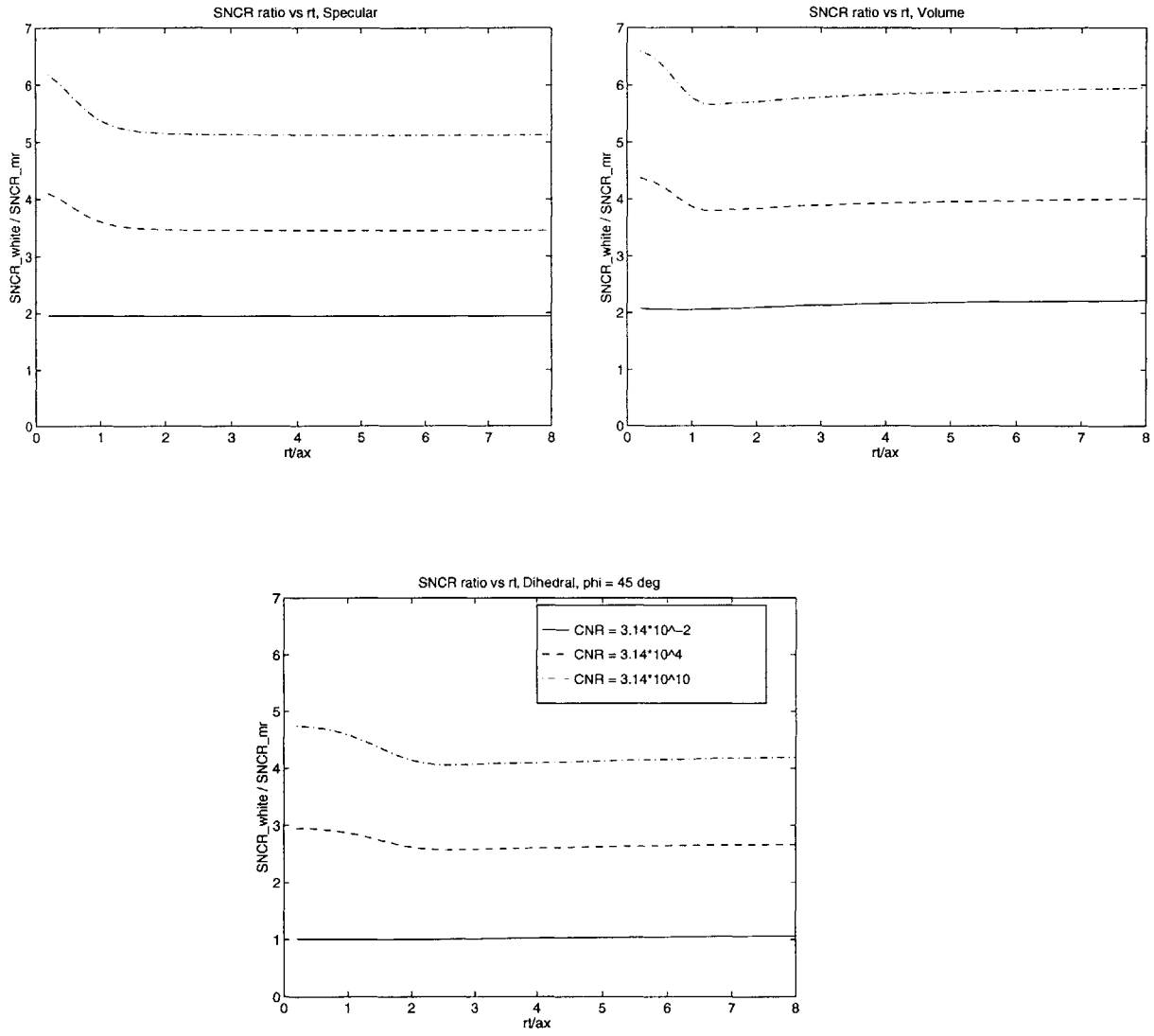

Figure 3.9 $\mathrm{SNCR_{white}/SNCR_{AR}}$ vs. target size. The choices of κ, ν and polarimetric components are the same as in Figure 3.8. Upper left panel: specular reflector, upper right panel: dielectric volume, lower panel: dihedral reflector.

Chapter 4

2-D Spotlight SAR: Signal Model and Performance Analysis

4.1 The Basic Principle of Spotlight-Mode SAR

From the viewpoint of antenna synthesis, increasing the time duration over which a coherent radar-return is available from a target improves the resolution that can be achieved. In stripmap-mode SAR, the dwell time of a target in the radar footprint area is restricted by the antenna beam width. This implies that the resolution length after synthetic aperture formation cannot be smaller than the size of the real antenna aperture [23]. To release this resolution limitation, a different mode of synthetic aperture operation— spotlight-mode SAR— has been developed.

In spotlight-mode SAR, the antenna beam "spotlights" a fixed region all the time. In other words, its footprint area on the ground is kept approximately stationary, rather than allowed to sweep along an elongated strip as in the case of the stripmap-mode SAR. Figure 4.1 illustrates the physical scenario of a 2-D spotlight-mode SAR. Comparing Figure 4.1 with Figure 2.1, almost all the aspects of the two modes of SAR operations are identical: the aircraft is flying along a linear path at a constant altitude, the radar mounted on the aircraft is continually transmitting discrete pulses toward the region of interest on the ground, and so on. The only difference is the normal direction of antenna aperture. For stripmap-mode operation, the normal direction of antenna aperture is fixed at $-\hat{z}'$. For spotlight-mode operation, on the other hand, the normal direction of antenna aperture is adjusted along the flight path to constantly point toward the region centered at $(x, y, z) = (0, L\cot(\psi), 0)$. More explicitly, the antenna normal direction for the mth pulse is $(-\hat{z}' - \hat{x}mvT_s/L')/\sqrt{1 + (mvT_s/L')^2}$.

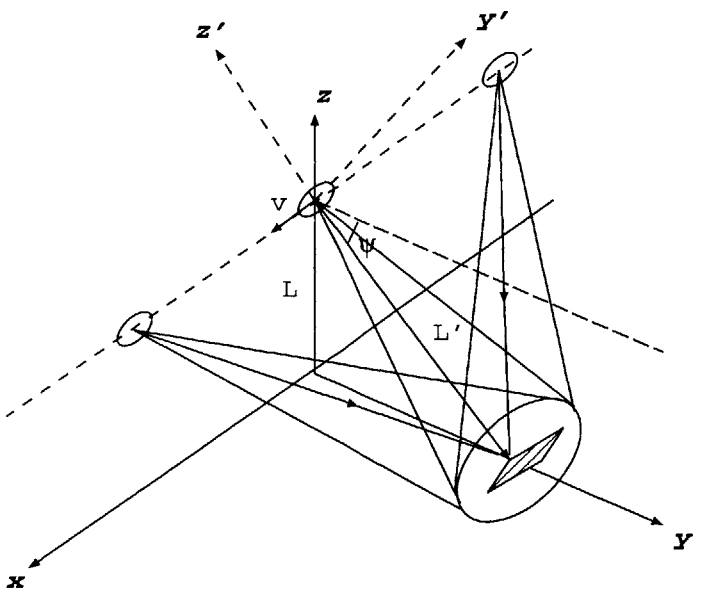

Figure 4.1 Flight geometry for a 2-D spotlight-mode SAR.

The principal advantage of spotlight-mode SAR over conventional stripmap-mode SAR is its enhanced resolution. In stripmap-mode operation, the duration that a region of interest is illuminated is at most the antenna-beam size divided by the speed of the aircraft. Extending the synthetic-aperture formation (signal processing duration) beyond this limit does not improve the image resolution. In contrast, in the spotlight-mode operation, the duration that a region of interest is illuminated can be arbitrarily long in principle. Therefore, in the ideal situation, phase information from every aspect angle concerning a region of interest can be collected and integrated via SAR operation. This implies that the resolution size of a spotlight-mode SAR image can be very small, provided the signal processing duration is very large. Because of this characteristic, the processing duration of a spotlight-mode SAR is often longer than that of a stripmap-mode SAR. In reality, the choice of arbitrarily long processing duration does not guarantee an arbitrarily fine resolution. The aspect-angle dependence of the terrain reflectivity in the region of interest restricts the image resolution.

A 2-D spotlight-mode SAR image is often interpreted as a tomographic rendition of

the 2-D terrain-reflectivity profile. The conventional processor for 2-D spotlight-mode SAR data is designed based on such tomographic signal model. Typically, it consists of: a phase modulator that compensates for the quadratic phase term with respect to cross range and de-chirps the chirped pulse of the radar return; a sampler that discretizes the "short" time along the range direction; a polar formatter that arranges the sampled data in an annular domain; and a 2-D inverse Fourier transformer applied to the annular domain [1][5]. In this Fourier transformer, the radial and angular resolutions are determined by the processing durations along the range and cross-range directions. Therefore, in a manner similar to the one we used for stripmap-mode SAR, we will define an adaptive-resolution processor for the spotlight-mode SAR to be a conventional spotlight-mode SAR processor containing a 2-D inverse Fourier transformer with variable processing durations along both range and cross-range directions. Similarly, we will define a whitening processor for the spotlight-mode SAR to consist of a whitening filter that whitens the spectrum of clutter plus noise, followed by a matched filter for the waveform of the target-return.

In this chapter, we will explore the same topics that we considered in the last two chapters, for the 2-D spotlight-mode SAR. First, we will construct the radar return signal models for the spotlight-mode SAR scenario. The radar signals of interest include the returns from a target with simple geometry and constitution, clutter from rough surface scattering, and noise, and once again the models are derived from electromagnetic propagation and scattering theories. Second, we will lay out the detailed descriptions for the adaptive-resolution processor and the whitening processor. Third, we will present numerical performance-analysis results, including resolution and binary detection performance (which is completely characterized by SNCR, the signal-to-noise-plus-clutter ratio). The variations of SNCR with respect to different parameters are compared. All these variation conditions are identical to those set out in Chapter 3 for the stripmap-mode SAR. Hence we can directly compare the performance (SNCR) of these two modes of SAR operations.

4.2 Radar Return Model

Similar to the stripmap-mode SAR, the intermediate-frequency radar return model of the spotlight-mode SAR consists of the transmitter model, the propagation and scattering model, and the receiver front-end model. A train of discrete radar pulses is generated at the transmitter. Each pulse is propagated toward the objects to be observed, scattered or reflected, and propagated back to the radar receiver. The return pulse is mixed with a superheterodyne local oscillator field, and the resultant signal is passed through an IF bandpass filter. Such process is identical to the one depicted in Figure 2.2.

The radar return signal of a spotlight-mode SAR also includes three components: target return, clutter which is the return from the rough ground surface, and receiver noise which is modeled as a white Gaussian random process. The repertoire of targets considered in this chapter is identical to that in Chapter 2: a specular mirror, a dihedral mirror with different directions for its axis, and a dielectric volume.

The transmitted radar signal is assumed to be a train of chirped pulses with period T_s, and the complex envelope of each individual pulse, $p(t)$, is described by (2.6). The field distribution pattern on the antenna aperture is modeled as an elliptical Gaussian, as that in (2.3). Thus the effective surface current density $\bar{K}_a(\bar{r}_a, t)$ can be described by (2.7).

For the surface current density of the transmitted antenna aperture given by (2.7), the incident electric field $\bar{E}_i$ around the scene center on the ground is approximated by (2.12). To further approximate the formulation in (2.12), we have to bear in mind two significant differences between stripmap-mode operation and spotlight-mode operation. First, the surface integral over S_a in (2.12) represents the antenna beam factor along the direction of wave propagation from the transmitter antenna aperture to the scene center. For stripmap-mode operation, the antenna normal direction is fixed at $-\hat{z}'$, which implies the local coordinate $\bar{r}_a$ does not depend on time. But the incident direction toward the scene center, $\hat{r}_i$, varies

with time (pulse number) (see (2.14)). So $\hat{r}_i \cdot \bar{r}_a$ in (2.12) is a function of time. This result gives a time (pulse number)-dependent antenna beam factor $\exp[-((k_c + k)a_x vt)^2/4L'^2]$ for the incident electric field around the scene center, as indicated in (2.16). For spotlight-mode operation, the antenna normal direction follows the scene center as the aircraft flies. Hence the normal direction of $\bar{r}_a$ is parallel to the incident direction toward the scene center, $\hat{r}_i$. The quantity $\hat{r}_i \cdot \bar{r}_a$ is therefore equal to 0, which implies the antenna beam factor in the incident field is 1 rather than $\exp[-((k_c + k)a_x vt)^2/4L'^2]$. Second, since the antenna aperture direction of a stripmap-mode SAR is fixed along the path, the radar return is non-negligible only within a cross-range distance much smaller than the range distance. Thus the range distance $r_i = \sqrt{L'^2 + (vt)^2}$ can be approximated by its first-order expansion $L' + (vt)^2/2L'$ for the phase terms, and its zeroth-order expansion L' for the amplitude terms. (Equations (2.13) to (2.15) describe this approximation condition.) However, for a spotlight-mode SAR, the antenna beam can illuminate the region of interest throughout the flight path. Thus the radar return is not necessarily negligible when the antenna aperture is far away from its nominal ($t = 0$) position. Therefore, the approximation formulations in (2.14) and (2.15) cannot be applied. We should retain the definitional formulation $r_i = \sqrt{L'^2 + (vt)^2}$.

The scattering field from a target located at the scene center can also be calculated from the incident field in (2.16) and electromagnetic scattering theory by following the procedures in Section 2.2.3. Similar to (2.22), the resultant scattering field is represented in terms of the incident field and the bistatic scattering tensor.

The receiver front-end model is identical to the one in Section 2.2.4. The returned electrical field $\bar{E}_s$ is mixed with a CW heterodyne local oscillator surface current density $\bar{K}_c$, which is modeled by (2.24). The resultant signal is then passed through an IF filter to extract its IF component. Finally, the complex envelope of the IF signal, $y(t)$, is reformulated as a two-dimensional signal $r(m, \tau)$, using the discrete index to represent pulse number, and the continuous time τ to denote the time delay along the range direction. Following the

same convention of transmitting and receiving polarizations as that in Section 2.2.4, the fully polarimetric 2-D radar returns $r_{HH}(m,\tau)$, $r_{VV}(m,\tau)$, and $r_{HV}(m,\tau)$ can be defined.

Based on the above discussion, we now present our formulations for the 2-D spotlight-mode radar return signals corresponding to target return, clutter, and noise. The target return is the radar-return signal from a target with simple geometry or composition: a specular mirror, a dihedral mirror, or a dielectric volume. The location of the target is assumed known. Therefore the antenna beam can be adjusted such that the target is at the scene center $(x,y,z) = (0, L'\cos(\psi), 0)$. Thus target return is then as follows:

$$\mathbf{r}_{\text{target}}(m,\tau) \approx -\int_{-\infty}^{\infty} \frac{d\Omega}{2\pi} P(\Omega) e^{-i\Omega\tau} \mu_0^2 (\Omega_c+\Omega)^2 \frac{\sqrt{P_T P_{LO}} a_x a_y}{4\pi\eta[L'^2+(mvT_s)^2]} \exp[i2k_c\sqrt{L'^2+(mvT_s)^2}]$$

$$\times \exp\{i2(\Omega/c)\sqrt{L'^2+(mvT_s)^2}\}\mathbf{U}_c \cdot \bar{\bar{S}}'\left(\frac{\hat{z}'L'+\hat{x}mvT_s/L'}{|\hat{z}'L'+\hat{x}mvT_s/L'|}, \frac{-\hat{z}'L'-\hat{x}mvT_s/L'}{|\hat{z}'L'+\hat{x}mvT_s/L'|}; \Omega_c+\Omega\right)\cdot \mathbf{U}_a, \tag{4.1}$$

where

$$\mathbf{U}_a = \begin{bmatrix} \hat{u}_H \\ \hat{u}_V \\ \hat{u}_H \end{bmatrix}; \quad \mathbf{U}_c = \begin{bmatrix} \hat{u}_H \\ \hat{u}_V \\ \hat{u}_V \end{bmatrix}, \tag{4.2}$$

are the tensors associated with the polarizations of the transmitted field and the receiver local oscillator field.

The modified scattering tensors $\bar{\bar{S}}'$ of the specular mirror, the dihedral mirror, and the dielectric volume are given by (2.33), (A.35), and (B.15), respectively, because the incident and scattering directions are independent of the SAR operation mode.

When the target center is not exactly located at the scene center, the formulation in (4.1) has to be slightly modified in two aspects. First, the distance between the target and the antenna aperture is different. Therefore the phase delay must be changed accordingly. Second, the scene center is equivalent to the peak position of the spotlight-mode SAR's antenna beam pattern. So when the target location deviates from the scene center, its radar return experiences an attenuated antenna beam factor. For a target located at $(x,y,z) =$

$(\Delta_x, \Delta_y + L\cot(\psi), 0)$, the radar return is therefore

$$
\begin{aligned}
\mathbf{r}_{\text{target}}(m,\tau) \approx & -\int_{-\infty}^{\infty} \frac{d\Omega}{2\pi} P(\Omega) e^{-i\Omega\tau} \mu_0^2 (\Omega_c+\Omega)^2 \frac{\sqrt{P_T P_{LO}} a_x a_y}{4\pi\eta[L'^2+(mvT_s)^2]} \\
& \times \exp[i2k_c\sqrt{(L'+\Delta_y\cos(\psi))^2+(mvT_s-\Delta_x)^2+(\Delta_y\sin(\psi))^2}] \\
& \times \exp\{i2(\Omega/c)\sqrt{(L'+\Delta_y\cos(\psi))^2+(mvT_s-\Delta_x)^2+(\Delta_y\sin(\psi))^2}\} \\
& \times \exp\left\{-\frac{[(k_c+k)]^2 {a_x}^2}{2[L'^2+(mvT_s)^2]} \frac{L'^2}{L'^2+(mvT_s)^2}[\Delta_x+(mvT_s\cos(\psi)/L')\Delta_y]^2\right\} \\
& \times \exp\left\{-\frac{[(k_c+k)]^2 {a_y}^2}{2[L'^2+(mvT_s)^2]}[\Delta_y\sin(\psi)]^2\right\} \\
& \times \mathbf{U}_c \cdot \tilde{\bar{S}}'\left(\frac{\hat{z}'L'+\hat{x}mvT_s/L'-\hat{x}\Delta_x-\hat{y}\Delta_y}{|\hat{z}'L'+\hat{x}mvT_s/L'-\hat{x}\Delta_x-\hat{y}\Delta_y|}, \frac{-\hat{z}'L'-\hat{x}mvT_s/L'-\hat{x}\Delta_x-\hat{y}\Delta_y}{|\hat{z}'L'+\hat{x}mvT_s/L'-\hat{x}\Delta_x-\hat{y}\Delta_y|}; \Omega_c+\Omega\right)\cdot\mathbf{U}_a.
\end{aligned}
\tag{4.3}
$$

Notice here the propagation distance is $\sqrt{(L'+\Delta_y\cos(\psi))^2+(mvT_s-\Delta_x)^2+(\Delta_y\sin(\psi))^2}$ rather than $\sqrt{L'^2+(mvT_s)^2}$. The beam factors along two orthogonal directions of the antenna aperture plane, $\exp\{-\frac{[(k_c+k)]^2 {a_x}^2}{2[L'^2+(mvT_s)^2]}\frac{L'^2}{L'^2+(mvT_s)^2}[\Delta_x+(mvT_s\cos(\psi)/L')\Delta_y]^2\}$, and $\exp\{-\frac{[(k_c+k)]^2 {a_y}^2}{2[L'^2+(mvT_s)^2]}[\Delta_y\sin(\psi)]^2\}$, are obtained by measuring the target location's offset from the antenna normal direction. This shows that when the target location is not exactly at the scene center, the antenna beam factor is not invariant with respect to the pulse number in a strict sense: the spotlight region moves slightly relative to the target.

Clutter is modeled as the radar return from a random rough ground surface. Equation (2.46) gives the formulation for the clutter of a stripmap-mode SAR. Paralleling our development of (2.30), the clutter can be interpreted as the sum of contributions from all points on the ground plane, whose scattering coefficients are proportional to the local reflectivities. Following the reasoning used in Section 2.4, we can obtain the spotlight-mode radar clutter as the sum of contributions from all individual points on the ground plane, where each point-contribution is calculated by (4.3). Thus the clutter of a spotlight-mode SAR is

$$
\mathbf{r}_{\text{clutter}}(m,\tau) \approx -\frac{\sqrt{P_T P_{LO}}\Omega_c^2 a_x a_y}{2\pi c^2 L'^2}\zeta_m \int_{-\infty}^{\infty}\int_{-\infty}^{\infty} dx_b\, dy_b
$$

$$\times \exp\{i2k_c\sqrt{(L'+y_b\cos(\psi))^2+(mvT_s-x_b)^2+(y_b\sin(\psi))^2}\}$$

$$\times p[\tau-(2/c)\sqrt{(L'+y_b\cos(\psi))^2+(mvT_s-x_b)^2+(y_b\sin(\psi))^2}]$$

$$\times \exp\{-\frac{{k_c}^2{a_x}^2}{2[L'^2+(mvT_s)^2]}\frac{L'^2}{L'^2+(mvT_s)^2}[x_b+(mvT_s\cos(\psi)/L')y_b]^2\}$$

$$\times \exp\{-\frac{{k_c}^2{a_y}^2}{2[L'^2+(mvT_s)^2]}[y_b\sin(\psi)]^2\}\exp[i2k_ch(x_b,y_b)\zeta_m]\begin{bmatrix}R_{HH}(x_b,y_b)\\R_{VV}(x_b,y_b)\\R_{HV}(x_b,y_b)\end{bmatrix}, \qquad (4.4)$$

where $\zeta_m = L/\sqrt{[L\csc(\psi)]^2+(mvT_s)^2}$. Here R_{HH}, R_{VV} and R_{HV} are the HH, VV, and HV components of the dyadic reflection tensor. The ground surface is assumed to be random. So the reflection tensor and the surface height h are random Gaussian processes. Following (2.47), we can define a transition tensor $\mathbf{T}$, whose statistics are given by (2.49).

The receiver noise of the spotlight-mode SAR return is modeled as a zero-mean, circulo-complex, Gaussian stochastic process that is white in range-time, cross-range-time, and polarimetric domains. Its correlation matrix is given by (2.51). The random noise is assumed to be independent of the random clutter.

4.3 Spotlight SAR Processor Models

In this chapter, we consider two types of SAR processors that deal with the 2-D radar-return signal from spotlight-mode operation: an adaptive-resolution processor, and a whitening-filter processor. The first one extends the standard polar-formatting-Fourier-transform spotlight-mode SAR processor to different resolutions via a technique similar to the one adopted in Section 3.1.1: varying the processing durations of the 2-D Fourier transformer. The second one, as the optimum binary detector, applies a whitening filter to whiten the unwanted part of the radar return (clutter plus noise), and a matched filter corresponding to the shape of the target return. In this section, we will introduce the system model of the standard spotlight-mode SAR processor, as well as the two processor schemes of concern.

4.3.1 Standard Spotlight-mode SAR Processor

Depending upon different interpretations for the 2-D radar returned signal of the spotlight-mode operation, different synthetic aperture processors are designed. A standard way of interpreting the radar return is to conceive it as a convolved form of the 2-D Fourier transform of the terrain reflectivity profile, namely, the tomographic rendition of the terrain-reflectivity distribution [1][5]. So the task of the processor is to convert the radar-return signal into a straight-forward 2-D Fourier transform of the terrain reflectivity, and carry out the inverse Fourier transform to recover the reflectivity profile.

Figure 4.2 illustrates the block diagram of a standard spotlight-mode SAR processor [5]. The radar-return signal is first multiplied by a complex waveform to de-chirp along both the range and cross-range directions. The de-chirped signal, which is still continuous for the range-time, is sampled to become a discrete-time signal in both directions. The sampled signal is then rearranged by a polar formatter, and passed through a 2-D discrete Fourier transformer. We will justify this SAR processor by demonstrating that for a target located $\hat{x}\Delta_x + \hat{y}\Delta_y$ away from the scene center, the processor produces sharply-peaked image at $\hat{x}\Delta_x + \hat{y}\Delta_y$.

For a target located $\hat{x}\Delta_x + \hat{y}\Delta_y$ away from the scene center, the spotlight-mode radar-return signal is given by (4.3). Assume that the bandwidth of the transmitted pulse is narrow enough to neglect the frequency dispersion effect in the antenna beam factors and the scattering tensor. In other words, we assume that these factors are all approximately functions of the carrier frequency only. Thus we can take these factors out of the frequency integral, and what is left inside the integral is just the spectrum of the transmitted pulse with a phase shift proportional to time. Therefore,

$$\mathbf{r}_{\text{target}}(m,\tau) \approx -\mu_0^2 {\Omega_c}^2 \frac{\sqrt{P_T P_{LO}} a_x a_y}{4\pi\eta[L'^2 + (mvT_s)^2]}$$
$$\times \mathbf{U}_c \cdot \bar{\bar{S}}'\left(\frac{\hat{z}'L' + \hat{x}mvT_s/L' - \hat{x}\Delta_x - \hat{y}\Delta_y}{|\hat{z}'L' + \hat{x}mvT_s/L' - \hat{x}\Delta_x - \hat{y}\Delta_y|}, \frac{-\hat{z}'L' - \hat{x}mvT_s/L' - \hat{x}\Delta_x - \hat{y}\Delta_y}{|\hat{z}'L' + \hat{x}mvT_s/L' - \hat{x}\Delta_x - \hat{y}\Delta_y|}; \Omega_c\right) \cdot \mathbf{U}_a$$

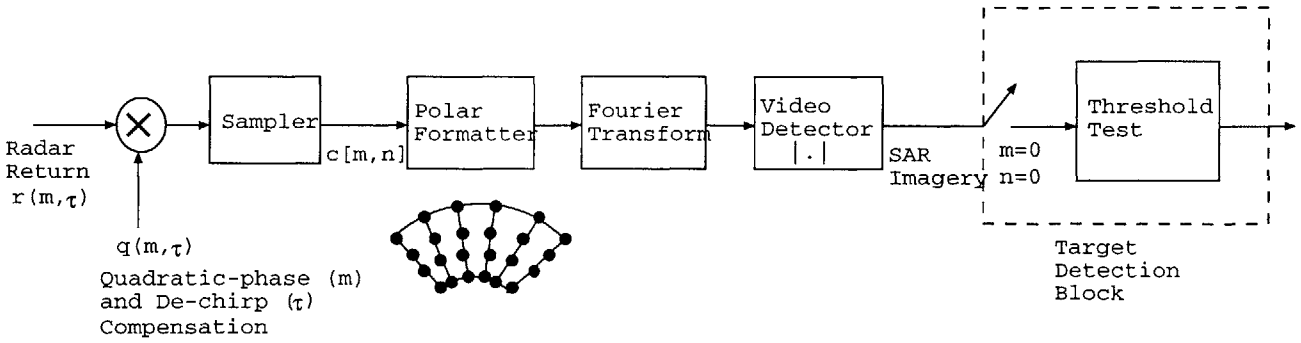

Figure 4.2 Standard spotlight-mode SAR processor.

$$\times \exp\{-\frac{{k_c}^2 {a_x}^2}{2[L'^2 + (mvT_s)^2]} \frac{L'^2}{L'^2 + (mvT_s)^2}[\Delta_x + (mvT_s\cos(\psi)/L')\Delta_y]^2\}$$

$$\times \exp\{-\frac{{k_c}^2 {a_y}^2}{2[L'^2 + (mvT_s)^2]}[\Delta_y \sin(\psi)]^2\}$$

$$\times \exp[i2k_c\sqrt{(L' + \Delta_y\cos(\psi))^2 + (mvT_s - \Delta_x)^2 + (\Delta_y\sin(\psi))^2}]$$

$$\times p[\tau - (2/c)\sqrt{(L' + \Delta_y\cos(\psi))^2 + (mvT_s - \Delta_x)^2 + (\Delta_y\sin(\psi))^2}], \tag{4.5}$$

where $p(\tau) = \exp[-i\pi(W_0/T_0)\tau^2 - (4/{T_0}^2)\tau^2]$.

In (4.5), the phase terms that correspond to the frequency chirps along the cross-range and range directions vary with the pulse number m. A basic principle of spotlight-mode SAR processing is to calibrate the phase such that when the target is at the scene center the phase shift, similar to the antenna beam pattern, is independent of the pulse number. Therefore a de-chirping waveform

$$q_{\text{ref}}(m,\tau) = \exp[-i2k_c\sqrt{L'^2 + (mvT_s)^2}]\exp[i\pi(W_0/T_0)(\tau - (2/c)\sqrt{L'^2 + (mvT_s)^2})^2] \tag{4.6}$$

is mixed with the returned signal in (4.5). The result is denoted by $\mathbf{r}_{\text{target}}^{\text{dechirp}}(m,\tau)$, where

$$\mathbf{r}_{\text{target}}^{\text{dechirp}}(m,\tau) = q_{\text{ref}}(m,\tau) \times \mathbf{r}_{\text{target}}(m,\tau). \tag{4.7}$$

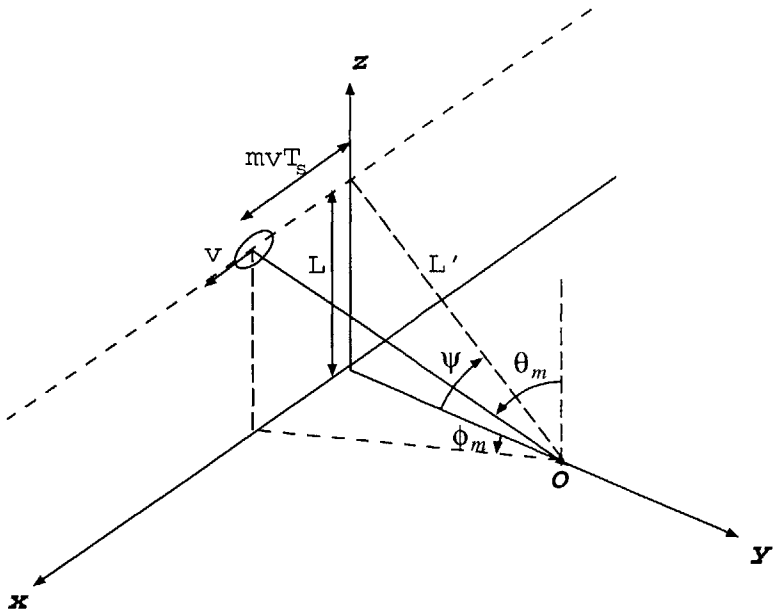

Figure 4.3 The geometric denotations of θ_m and ϕ_m.

Following the convention of spotlight-mode SAR processing, we define two angles and use them to represent the de-chirped signal in (4.7). They are

$$\theta_m \equiv \tan^{-1}\left[\frac{\sqrt{(mvT_s)^2 + (L\cot(\psi))^2}}{L}\right], \quad \phi_m \equiv \tan^{-1}\left[\frac{mvT_s}{L\cot(\psi)}\right]. \tag{4.8}$$

Both of these two angles have geometric connotations. The elevation angle θ_m denotes the angle between the vertical axis ($\hat{z}$) and the slant-range vector (with respect to the scene center), while the azimuth angle ϕ_m denotes the angle between the broadside axis ($\hat{y}$) and the direction projected from the slant-range vector onto the ground plane. Both angles are functions of the pulse number m since the slant-range vector is dependent upon the aircraft position. The geometric scenario for θ_m and ϕ_m is illustrated in Figure 4.3.

The equivalent synthetic aperture of a spotlight-mode SAR can be larger than that of a stripmap-mode SAR, because the spotlight-mode dwell time for a fixed region is not restricted by the size of antenna beamwidth. However, this does not mean that the spotlight-mode synthetic aperture will be arbitrarily large. In particular, it is still reasonable to assume

that $m_a v T_s << L'\cos(\psi)$, where $-m_a/2 \leq m \leq m_a/2$ is the discrete processing duration. So, for the 2-D signals within the domain of concern, we can approximate the slant range $\sqrt{(L'+\Delta_y\cos(\psi))^2+(mvT_s-\delta_x)^2+(\Delta_y\sin(\psi))^2}$ by its first-order expansion:

$$\sqrt{(L'+\Delta_y\cos(\psi))^2+(mvT_s-\delta_x)^2+(\Delta_y\sin(\psi))^2}$$

$$\approx \sqrt{L'^2+(mvT_s)^2}+\sin(\theta_m)[\Delta_y\cos(\phi_m)-\Delta_x\sin(\phi_m)]. \tag{4.9}$$

Plugging (4.9) into the 2-D radar return (4.5) and mixing with the reference waveform (4.6), we get two phase factors in the de-chirped signal (4.7). They correspond to the radar carrier and the frequency chirp of the transmitted pulse, respectively,

$$\exp\{i2k_c[\sqrt{(L'+\Delta_y\cos(\psi))^2+(mvT_s-\delta_x)^2+(\Delta_y\sin(\psi))^2}-\sqrt{L'^2+(mvT_s)^2}]\}$$

$$\approx \exp\{i2k_c\sin(\theta_m)[\Delta_y\cos(\phi_m)-\Delta_x\sin(\phi_m)], \tag{4.10}$$

$$\exp\{-i\frac{\pi W_0}{T_0}[(\tau-\frac{2}{c}\sqrt{(L'+\Delta_y\cos(\psi))^2+(mvT_s-\Delta_x)^2+(\Delta_y\sin(\psi))^2})^2$$
$$-(\tau-\frac{2}{c}\sqrt{L'^2+(mvT_s)^2})^2]\}$$
$$\approx \exp\{i\pi(W_0/T_0)(4/c)[\tau-(2/c)\sqrt{L'^2+(mvT_s)^2}]^2\sin(\theta_m)[\Delta_y\cos(\phi_m)-\Delta_x\sin(\phi_m)]\}, \tag{4.11}$$

where, in addition to (4.9), we have neglected quadratic terms involving Δ_x and Δ_y [5].

The de-chirped signal $\mathbf{r}_{\text{target}}^{\text{dechirp}}(m,\tau)$ is passed through a sampler to discretize the continuous range-time τ with a sampling period T_r. Thus the output $\mathbf{c}_{\text{target}}[m,n]$ is

$$\mathbf{c}_{\text{target}}[m,n] \equiv \mathbf{r}_{\text{target}}^{\text{dechirp}}(m, nT_r+(2/c)\sqrt{L'^2+(mvT_s)^2})$$
$$\approx -\mu_0^2{\Omega_c}^2\frac{\sqrt{P_T P_{LO}}a_x a_y}{4\pi\eta[L'^2+(mvT_s)^2]}\exp\{-\frac{{k_c}^2{a_x}^2L'^2}{2[L'^2+(mvT_s)^2]}[\Delta_x+(mvT_s\cos(\psi)/L')\Delta_y]^2\}$$
$$\times\exp\{-\frac{{k_c}^2{a_y}^2}{2[L'^2+(mvT_s)^2]}[\Delta_y\sin(\psi)]^2\}$$
$$\times\mathbf{U}_c\cdot\bar{\bar{S}}'(\frac{\hat{z}'L'+\hat{x}mvT_s/L'-\hat{x}\Delta_x-\hat{y}\Delta_y}{|\hat{z}'L'+\hat{x}mvT_s/L'-\hat{x}\Delta_x-\hat{y}\Delta_y|},\frac{-\hat{z}'L'-\hat{x}mvT_s/L'-\hat{x}\Delta_x-\hat{y}\Delta_y}{|\hat{z}'L'+\hat{x}mvT_s/L'-\hat{x}\Delta_x-\hat{y}\Delta_y|};\Omega_c)\cdot\mathbf{U}_a$$

$$\times \exp\{-(4/T_0^2)[nT_r - (2/c)\sin(\theta_m)(-\Delta_x \sin(\phi_m) + \Delta_y \cos(\phi_m))]^2\}$$

$$\times \exp\{i(2/c)[\Omega_c + 2\pi(W_0/T_0)nT_r]\sin(\theta_m)[-\Delta_x \sin(\phi_m) + \Delta_y \cos(\phi_m)]\}. \quad (4.12)$$

Notice the sampler not only discretizes the range-time τ but it also adds a time shift $(2/c)\sqrt{L'^2 + (mvT_s)^2}$ to each individual pulse, to compensate for the propagation delay between the antenna aperture and the scene center.

The signal $\mathbf{c}_{\text{target}}[m,n]$ exists only within a limited region of m and n. For the cross-range index m, $\mathbf{c}_{\text{target}}[m,n]$ is restricted to $-m_a/2 \leq m \leq m_a/2$, where m_a is the processing duration of the synthetic aperture operation; namely, $m_a v T_s$ is the size of synthetic aperture. As indicated above, we assume that the processing duration m_a is small enough that $m_a v T_s/(L'\cos(\psi)) << 1$ holds. Thus the scattering tensor and the inverse-square distance factor in (4.12) are approximately constants within the processing duration. For the range index n, $\mathbf{c}_{\text{target}}[m,n]$ is restricted by the pulse envelope. Suppose the Gaussian envelope in (4.12) is replaced by an unit-height rectangular envelope with width T_0, then the region of n in which $\mathbf{c}_{\text{target}}[m,n]$ is appreciable is approximately $-(T_0/2T_r) + (2/cT_r)\sin(\theta_m)(\sqrt{2}L'/k_c a_y) \leq n \leq (T_0/2T_r) - (2/cT_r)\sin(\theta_m)(\sqrt{2}L'/k_c a_y)$ (a_y is the antenna aperture size along range direction). We also approximate the two Gaussian antenna beam patterns in (4.12) by unit-height rectangular patterns (namely, 1 when the target is located within the antenna beam footprint area, and 0 when it is out of the footprint area), and assume that (Δ_x, Δ_y) is within this footprint. So both factors are equal to 1.

Based on these assumptions, the sampled signal $\mathbf{c}_{\text{target}}[m,n]$ can be represented in a very simple form:

$$\mathbf{c}_{\text{target}}[m,n] \approx -\mu_0^2 {\Omega_c}^2 \frac{\sqrt{P_T P_{LO}} a_x a_y}{4\pi\eta L'^2} \mathbf{U}_c \cdot \bar{\bar{S}}'(\hat{z}', -\hat{z}'; \Omega_c) \cdot \mathbf{U}_a$$
$$\times \exp\{i(2/c)[\Omega_c + 2\pi(W_0/T_0)nT_r]\sin(\theta_m)[-\Delta_x \sin(\phi_m) + \Delta_y \cos(\phi_m)]\}. \quad (4.13)$$

The points (m,n) at which $\mathbf{c}_{\text{target}}$ does not vanish form a rectangular array in the 2-D

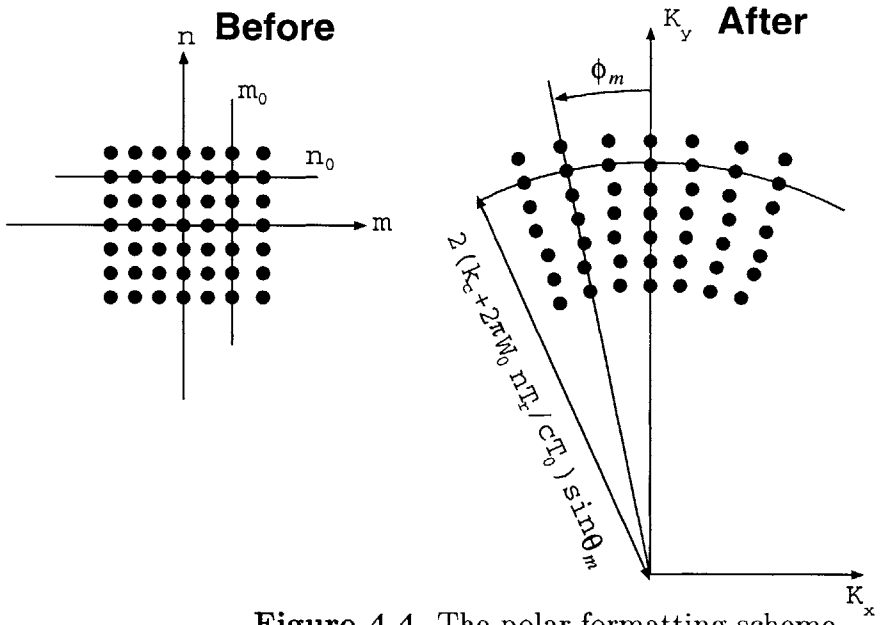

Figure 4.4 The polar formatting scheme.

plane. Different points on a line of constant m represents different discrete samples of the range time at a fixed cross-range index. However, (4.13) indicates it is more advantageous to rearrange this array in a polar format. To be specific, we define

$$K[m,n] \equiv (2/c)[\Omega_c + 2\pi(W_0/T_0)nT_r]\sin(\theta_m),$$

$$K_x[m,n] \equiv K[m,n]\sin(-\phi_m), \qquad K_y[m,n] \equiv K[m,n]\cos(-\phi_m), \tag{4.14}$$

and map the point (m,n) on the 2-D plane where the x and y coordinates are $K_x[m,n]$ and $K_y[m,n]$. As indicated in Figure 4.4, this mapping is equivalent to rearranging the constant-m points from a vertical line to a radial line from origin, tilted angle $-\phi_m$ with respect to the vertical axis (a line of constant ϕ_m). In the terminology of spotlight-mode SAR processing, such arrangement is called "polar formatting" [5]. When m_a is small, $\sin(\theta_m)$ in (4.14) is approximately equal to $\cos(\psi)$ over the whole region of interest. Thus the distance between two sample points along a line of constant ϕ_m is almost a constant, and the region mapped from a rectangular domain of (m,n) is annular.

After polar formatting, the the sampled signal $\mathbf{c}_{\text{target}}$ in (4.13) becomes $d_{\text{target}}[K_x, K_y]$, which can be interpreted as discrete samples of a 2-D complex waveform on the $K_x - K_y$ plane:

$$\mathbf{d}_{\text{target}}[K_x, K_y] \approx -\mu_0^2 {\Omega_c}^2 \frac{\sqrt{P_T P_{LO}} a_x a_y}{4\pi\eta {L'}^2} \mathbf{U}_c \cdot \bar{\bar{S}}'(\hat{z}', -\hat{z}'; \Omega_c) \cdot \mathbf{U}_a \exp[iK_x\Delta_x + iK_y\Delta_y]. \quad (4.15)$$

The formulation of the polar formatted signal $\mathbf{d}_{\text{target}}$ in (4.15) is simple and desirable: the target reflectivity is proportional to its amplitude, while the information of the target position appears as phase modulation. If we consider the radar return from a terrain in which every point contributes, then the polar formatted signal in (4.15) becomes exactly the Fourier integral (sum) of the terrain reflectivity profile. Hence, the most straightforward method to recover the reflectivity profile from the polar formatted signal is to carry out the inverse Fourier transform.

The polar formatted signal in (4.15) is passed through a discrete 2-D Fourier transformer:

$$\mathbf{l}_{\text{target}}(x, y) \equiv \sum_{K_x} \sum_{K_y} \mathbf{d}_{\text{target}}[K_x, K_y] \exp[-iK_x x - iK_y y]. \quad (4.16)$$

Thus the output $\mathbf{l}_{\text{target}}$ has a sharp peak at the position $(x, y) = (\Delta_x, \Delta_y)$ whose amplitude is proportional to the target reflectivity. The actual resolution of this output image (the width of the peak) is determined by the size of the annular (K_x, K_y) region in Figure 4.4. If $m_a v T_s / L' \cos(\psi) << 1$ and $2\pi W_0 << \Omega_c$, then the annular region is approximately a rectangular window with lengths $(2\Omega_c/c)(m_a v T_s/L')$ and $4\pi W_0 \cos(\psi)/c$ along the horizontal and vertical directions, respectively. It can be shown [1] that the resolution widths of the output image along the horizontal and vertical directions are $1/(2\Omega_c/c)(m_a v T_s/L')$ and $c/4\pi W_0 \cos(\psi)$, respectively. It is clear that the cross-range (horizontal) resolution is controlled by the synthetic aperture processing duration m_a, and the range (vertical) resolution is controlled by the chirp bandwidth W_0. Thus, it is preferable to increase m_a and W_0 to obtain an image with finer resolution. However, it is not possible to increase m_a indefinitely. As indicated above, an important assumption under the working principle of the

standard spotlight-mode SAR processor is that m_a is small enough to ensure that the dechirped, sampled, delay compensated radar signal $\mathbf{c}_{\text{target}}[m, n]$ in (4.12) can be interpreted as a polar-formatted 2-D Fourier transform of the target scattering tensor. This requires that the scattering tensor and the inverse-square distance factor be invariant with the cross-range index m, which is true only for small enough m_a.

In a real SAR processor, more elaborate schemes such as interpolation-FFT and convolution-backprojection [1][5][30] are often implemented to carry out the 2-D discrete Fourier transform in (4.16). The idea under most of these schemes is preparing the data in a form more germane to the Fast Fourier Transform algorithm and hence taking advantage of the computational efficiency of the FFT. But all of these schemes involve subtle numerical issues. In this chapter, we directly carry out the 2-D Fourier transform in (4.16) instead of adopting any elaborate scheme, because the principal purpose of this thesis is not to analyze the performance of a particular system, but to achieve fundamental understanding of SAR performance limitations.

4.3.2 Adaptive-Resolution Processor

The image resolution of a standard spotlight-mode SAR processor is determined by the size of the annular region over which the Fourier transform is carried out. In Section 4.3.1, we mentioned that the angular width of the annular region is determined by the processing duration along the cross-range direction, and the radial width is determined by the width of the radar pulse as well as the length of the antenna footprint along the range direction. The former is a free variable, while the latter is fixed by the radar front-end system. Thus compared with the standard stripmap-mode SAR processor that fixes the processing durations of the chirp compression filters along the cross-range and range directions, the standard spotlight-mode SAR processor has one more degree of freedom. This is because the dwell period of a target under the spotlight is not restricted by the size of antenna beam.

The idea of the adaptive-resolution spotlight-mode SAR processor is similar to the one for the corresponding stripmap-mode SAR in Section 3.1.1: we adopt the architecture of a standard SAR processor described in Section 4.3.1, but vary the cross-range processing duration (angular width of the annular region) and the range processing duration (radial width of the annular region). To be specific, let the cross-range index m of the discrete de-chirped signal $\mathbf{c}_{\text{target}}$ chosen for further processing be from $-m_a/2$ to $m_a/2$, and let the range index n for further processing be from $-n_a/2$ to $n_a/2$. Thus m_a and n_a represent the cross-range and range processing durations, respectively. To be consistent with the notation in (3.1), we define

$$m_a \equiv \frac{2\sqrt{2}L'}{\kappa k_c a_x v T_s}, \qquad n_a \equiv \frac{T_0}{\nu T_r}. \tag{4.17}$$

Thus for the same κ and ν, the processing durations of the adaptive-resolution stripmap-mode SAR and the spotlight-mode SAR processors are identical. The case $\kappa = \nu = 1$ corresponds to the conventional spotlight-mode SAR processor.

We can obtain the output image of the adaptive-resolution SAR processor by plugging the radar return (4.3), (4.4) or (2.51) into the processor. For the radar return from a target located (Δ_x, Δ_y) from the scene center, the output image is

$$\begin{aligned}
\mathbf{l}_{\text{target}}(x,y) \approx & \sum_{m=-m_a/2}^{m_a/2} \sum_{n=-n_a/2}^{n_a/2} \exp(-iK_x[m,n]x - iK_y[m,n]y) \times (-1)\frac{\sqrt{P_T P_{LO}}a_x a_y {\mu_0}^2}{4\pi\eta[L'^2 + (mvT_s)^2]} \\
& \times \exp\{i2k_c \sin(\theta_m)[\Delta_y \cos(\phi_m) - \Delta_x \sin(\phi_m)]\} \exp[i\pi(W_0/T_0)(nT_r)^2] \\
& \times \int_{-\infty}^{\infty} \frac{d\Omega}{2\pi} \sqrt{\frac{\pi}{i\pi W_0/T_0 + 4/{T_0}^2}} \exp[-\Omega^2/4(i\pi W_0/T_0 + 4/{T_0}^2)](\Omega_c + \Omega)^2 \\
& \times \exp\left\{-\frac{(k_c+k)^2 {a_x}^2}{2L'^2}\frac{[\Delta_x + \Delta_y \cos^2(\psi)\tan(\phi_m)]^2}{[1+\cos^2(\psi)\tan(\phi_m)]^2}\right\} \\
& \times \exp\left\{-\frac{(k_c+k)^2 {a_y}^2}{2L'^2}\frac{[\Delta_y \sin(\psi)]^2}{[1+\cos^2(\psi)\tan(\phi_m)]}\right\} \\
& \times \mathbf{U}_c \cdot \bar{\bar{S}}'\left(\frac{\hat{z}'L' + \hat{x}mvT_s/L' - \hat{x}\Delta_x - \hat{y}\Delta_y}{|\hat{z}'L' + \hat{x}mvT_s/L' - \hat{x}\Delta_x - \hat{y}\Delta_y|}, \frac{-\hat{z}'L' - \hat{x}mvT_s/L' - \hat{x}\Delta_x - \hat{y}\Delta_y}{|\hat{z}'L' + \hat{x}mvT_s/L' - \hat{x}\Delta_x - \hat{y}\Delta_y|}; \Omega_c + \Omega\right) \cdot \mathbf{U}_a,
\end{aligned} \tag{4.18}$$

where $K_x[m,n]$ and $K_y[m,n]$ are defined by (4.14), θ_m ϕ_m are defined by (4.8). Similarly, the output image of a clutter return is

$$\mathbf{l}_{\text{clutter}}(x,y) \approx \sum_{m=-\frac{m_a}{2}}^{\frac{m_a}{2}} \sum_{n=-\frac{n_a}{2}}^{\frac{n_a}{2}} \int_{-\infty}^{\infty}\int_{-\infty}^{\infty} dx_b\, dy_b\, (-1)\frac{\sqrt{P_T P_{LO}}a_x a_y {\Omega_c}^2}{2\pi c^2 {L'}^2}$$

$$\times \exp\{-i\frac{2}{c}[\Omega_c + 2\pi(W_0/T_0)nT_r]\sin(\theta_m)[(x-x_b)\sin(-\phi_m) + (y-y_b)\cos(-\phi_m)]\}$$

$$\times \exp\left\{-\frac{{k_c}^2{a_x}^2}{2{L'}^2}\frac{[x_b + y_b\cos^2(\psi)\tan(\phi_m)]^2}{[1+\cos^2(\psi)\tan(\phi_m)]^2}\right\}\exp\left\{-\frac{{k_c}^2{a_y}^2}{2{L'}^2}\frac{[y_b\sin(\psi)]^2}{[1+\cos^2(\psi)\tan(\phi_m)]}\right\}$$

$$\times \exp\{-(4/{T_0}^2)[nT_r - (2/c)\sin(\theta_m)[x_b\sin(-\phi_m) + y_b\cos(-\phi_m)]]^2\}\cos(\theta_m)\mathbf{T}(x_b,y_b), \tag{4.19}$$

where the statistics of the transition matrix $\mathbf{T}(x_b,y_b)$ are given by (2.49). The output image corresponding to the receiver noise is

$$\mathbf{l}_{\text{noise}}(x,y) \approx \sum_{m=-\frac{m_a}{2}}^{\frac{m_a}{2}} \sum_{n=-\frac{n_a}{2}}^{\frac{n_a}{2}} \exp\{-i\frac{2}{c}[\Omega_c + 2\pi(W_0/T_0)nT_r]\sin(\theta_m)[x\sin(-\phi_m) + y\cos(-\phi_m)]\}$$

$$\times \exp\{-i2k_c\sqrt{{L'}^2 + (mvT_s)^2}\}\exp[i\pi(W_0/T_0)[(nT_r)^2]\mathbf{r}_{\text{noise}}(m, nT_r + (2/c)\sqrt{{L'}^2 + (mvT_s)^2}), \tag{4.20}$$

where the correlation function of the discretized white-Gaussian receiver noise $\mathbf{r}(m,n)$ is

$$\langle \mathbf{r}_{\text{noise}}(m,n)\mathbf{r}^{\dagger}_{\text{noise}}(m',n')\rangle \approx N_0\delta[m-m']\delta[n-n']\frac{1}{T_r}\begin{bmatrix}1&0&0\\0&1&0\\0&0&1\end{bmatrix}. \tag{4.21}$$

Equation (4.21) is derived by plugging the approximation

$$\delta(nT_r) \approx \frac{1}{T_r}\delta[n] \tag{4.22}$$

into (2.51).

Notice that when $x = y = 0$, the target component of the output from the adaptive-resolution spotlight SAR processor is approximately the sum (integral) of the de-chirped radar return over the given processing durations (see (4.18)). If the processing durations m_a

and n_a are chosen to match the dwell durations of the target return along the cross-range and range directions, then this result is approximately equal to the output of the (original) target return from a matched filter sampled at $m = \tau = 0$. In addition, for a white input noise, the intensities from an adaptive-resolution processor and from a matched-filter processor are both proportional to the processing durations. So the adaptive-resolution spotlight SAR processor with properly chosen processing durations is equivalent to the matched-filter processor at the sampled point corresponding to the scene center: $m = n = 0$.

4.3.3 Whitening Processor

As indicated in Section 3.1.2, for binary detection of a deterministic target return embedded in random clutter and noise, the optimum Neyman-Pearson processor is the whitening processor. The architecture of a spotlight-mode whitening processor is depicted in Figure 4.5. It is essentially the same structure as the stripmap-mode whitening processor illustrated in Figure 3.2: a filter that whitens the stochastic clutter and noise; a matched filter corresponding to the target-return waveform after the whitening filter; a video detector; and a detection block. The differences between the spotlight-mode and stripmap-mode whitening processors lie in the time-shift compensation at the spotlight-mode front-end, and the sample impulse responses of the whitening filter and the matched filter.

The impulse response of the whitening filter is determined by the covariance function of clutter-plus-noise at the receiver front-end. For convenience, we compensate the parabolic time-shift of the IF complex envelope of radar return first:

$$\tilde{\mathbf{r}}(m, \tau) \equiv \mathbf{r}[m, \tau + (2/c)\sqrt{L'^2 + (mvT_s)^2}]. \tag{4.23}$$

The compensated complex envelope $\tilde{\mathbf{r}}(m, \tau)$ contains three components: target return $\tilde{\mathbf{r}}_{\text{target}}(m, \tau)$, clutter $\tilde{\mathbf{r}}_{\text{clutter}}(m, \tau)$, and noise $\tilde{\mathbf{r}}_{\text{noise}}(m, \tau)$. Since clutter is independent of noise, the covariance function of clutter-plus-noise is the sum of the two individual covariance functions. The noise $\mathbf{r}_{\text{noise}}(m, \tau)$ is a circulo-complex zero-mean Gaussian process that

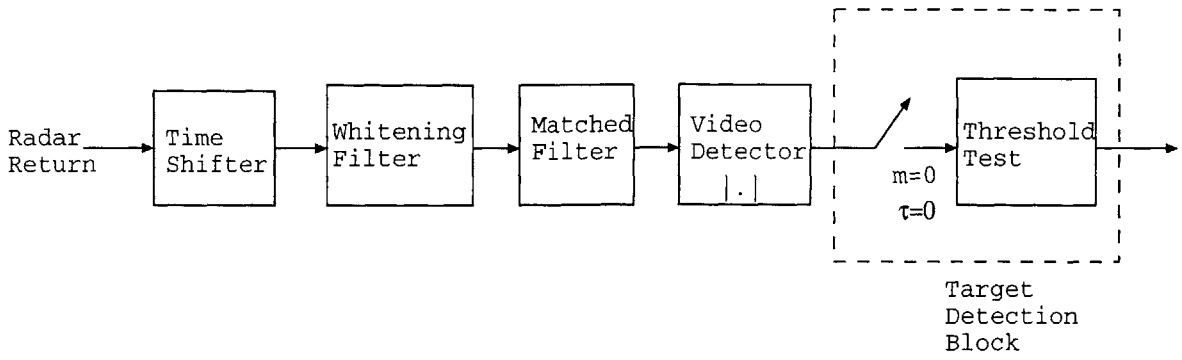

Figure 4.5 The spotlight-mode whitening-filter processor.

is white in all domains. It can be shown that the time-compensated noise $\tilde{\mathbf{r}}_{\text{noise}}(m,\tau)$ is also a circulo-complex zero-mean white Gaussian process. Thus the covariance function of $\tilde{\mathbf{r}}_{\text{noise}}(m,\tau)$ is also described by (2.51). From (4.4), (2.47), (2.49), and the definition (4.23), we can calculate the covariance function of the time-compensated clutter $\tilde{\mathbf{r}}_{\text{clutter}}(m,\tau)$. Hence we obtain the following covariance function for the time-compensated clutter-plus-noise, $\tilde{\mathbf{r}}_v(m,\tau) \equiv \tilde{\mathbf{r}}_{\text{clutter}}(m,\tau) + \tilde{\mathbf{r}}_{\text{noise}}(m,\tau)$:

$$\langle \mathbf{r}_v(m,\tau)\mathbf{r}_v^\dagger(m',\tau')\rangle = N_0\delta[m-m']\delta(\tau-\tau')\begin{bmatrix}1&0&0\\0&1&0\\0&0&1\end{bmatrix} + P_0\exp[-B_0(A_0\tau^2 + C_0\tau'^2 - 2\tau\tau')]$$

$$\times \exp\{-(vT_s/a_x)^2[(1-ik_ca_x^2/L')m^2 + (1+ik_ca_x^2/L')m'^2 - 2mm']\}\begin{bmatrix}1&\rho&0\\\rho^*&1&0\\0&0&\epsilon\end{bmatrix}, \quad (4.24)$$

where P_0, A_0, B_0, and C_0 are described by (3.4). Comparing the covariance function of clutter-plus-noise in (4.24) with that in (3.3), we find that the τ-dependences of the stripmap-mode clutter and the spotlight-mode clutter are identical, as are their amplitudes and reflectivity matrices. But their m-dependences are different. The stripmap-mode clutter is stationary with respect to the cross-range index m. The spotlight-mode SAR, due to its cross-range-independent antenna footprint pattern, has a non-stationary clutter with respect

to m. However, as can be seen from (4.24), as long as the radar is operated at the Fraunhofer far-field range such that $k_c a_x^2/L' << 1$, the non-stationarity of the spotlight-mode clutter with respect to m can be neglected. Thus the covariance function of clutter-plus-noise for the spotlight-mode SAR is approximately equal to that of the stripmap-mode SAR in (3.3). Similarly, we can impose the constraint $(1/4)\tan^2(\psi)(k_c a_y/L')^2(cT_0)^2 << 1$ to achieve the clutter-plus-noise stationary with respect of the range-time τ. Therefore, the covariance function of clutter-plus-noise for the spotlight-mode SAR is also described by (3.5) and (3.6). This conclusion reveals that different modes of directing the antenna beam patterns cause only minor difference to the statistics of the random components at radar return, which can be ignored when the radar is operated at the far-field region with respect to the area of interest.

Because the covariance function of the clutter-plus-noise for the spotlight-mode SAR is governed by (3.5), the whitening filter for the spotlight-mode SAR is identical to the whitening filter for the stripmap-mode SAR, which is described by (3.9) and (3.10). In addition, we can define the impulse of the spotlight-mode matched filter by following (3.11):

$$\begin{aligned}\mathbf{h}_M^{\dagger}(-m,-\tau) &\equiv \mathbf{h}_w(m,\tau) * \tilde{\mathbf{r}}_{\text{target}}(m,\tau) \\ &= \sum_{m'=-\infty}^{\infty} \int_{-\infty}^{\infty} d\tau' \mathbf{h}_w(m-m',\tau-\tau') \cdot \tilde{\mathbf{r}}_{\text{target}}(m',\tau'). \end{aligned} \tag{4.25}$$

Thus the scalar output components of target return, clutter, and noise after the whitening filter and the matched filter are

$$l_{\text{component}}^{\text{white}}(m,\tau) = \mathbf{h}_M(m,\tau) * \mathbf{h}_w(m,\tau) * \tilde{\mathbf{r}}_{\text{component}}(m,\tau), \tag{4.26}$$

for "component" = target, clutter, and noise.

4.4 Performance Analysis

In this section, we present numerical performance results for the spotlight-mode adaptive-resolution processor and the whitening-filter processor under certain interesting operating

conditions. First, we examine the spatial-resolution variations of the images formed by the adaptive-resolution spotlight SAR processor as its cross-range and range processing durations are changed. These results are compared with their counterparts generated by the adaptive-resolution stripmap SAR processor, which were presented in Section 3.2.1. Second, the signal-to-noise-plus-clutter-ratio (SNCR) corresponding to the sampled output of the adaptive-resolution processor and the whitening-filter processor are presented. The SNCR behaviors are also compared with those of the stripmap SAR processors given earlier in Section 3.2.3.

4.4.1 Spatial Resolution Behavior

For a target at the scene center $(x, y, z) = (0, L/\tan(\psi), 0)$, the intensity image produced by the adaptive-resolution spotlight SAR processor, $\mathrm{I}_{\mathrm{target}}(x, y)$ (see (4.16)), has its maximum value at $x = y = 0$. Following the definition in Section 3.2.1, the image resolution in the cross-range (range) direction is the width of the region around $y = 0$ ($x = 0$) within which the intensity exceeds $1/e$ of its peak value. Figure 4.6 shows numerical results for these resolutions as functions of the processing-duration parameters, κ and ν. The same five target types from Section 3.2.1 are considered here: specular reflector; dihedral reflector with orientation angle $\phi = 0°$; dihedral reflector with orientation angle $\phi = 90°$; diffuse target; and dielectric volume with relative permittivity $\epsilon_r = 10 + i5$. All targets have the same geometric size. The diffuse-target image is defined as the ensemble average of the processor output intensity based on the statistics of finite-size clutter.

Some interesting characteristics can be seen in the numerical results in Figure 4.6. First, unlike the adaptive-resolution behavior of stripmap-mode SAR, the spotlight-mode SAR's cross-range resolution length at lower processing duration ($\kappa > 1$) is the same for all the targets we have considered. On the other hand, when the processing duration is long enough ($\kappa < 1$), significant differences in cross-range resolution for different targets become appar-

ent. As κ approaches 0, the cross-range resolution lengths all converge to constant values. Similar to the stripmap-mode SAR, these finest resolution lengths depend on target type and, in a decreasing order, are as follows: specular mirror/dielectric volume, diffuse target, dihedral with 0° orientation angle, and dihedral with 90° orientation angle. The cross-range resolution behavior of a dielectric volume is identical to that of a specular reflector. This can be explained, as we did in Section 3.2.1, by the approximate identity of the scattering beam patterns of the specular reflector and the dielectric volume. Moreover, the cross-range resolution behaviors of dihedral reflectors with various orientation angles are also different. As indicated in Section 3.2, dihedral reflectors with different orientation angles generate scattering beam patterns of different sizes. Within $[0°, 90°]$, the larger the orientation angle is, the wider the beam pattern is. Thus in terms of return duration, a dihedral reflector with large orientation angle is equivalent to a flat reflector with smaller size. In short, the finest cross-range resolution length decreases with decreasing equivalent target size.

Similar to the stripmap-mode SAR, the range-resolution behavior of spotlight-mode SAR images throughout all the range processing durations do not have significant target-type differences. This is shown in the lower panel of Figure 4.6. However, the variation trends are different for the two modes of SAR operation. For the stripmap-mode SAR, the resolution length decreases with decreasing processing duration (increasing ν) under our current choice of time-bandwidth product $W_0T_0 = 0.5$. On the other hand, for the spotlight-mode SAR, the resolution length associated with the same time-bandwidth product increases with decreasing processing duration.

Analytical forms for the target-return image resolution lengths of the adaptive-resolution SAR processing can be obtained via the following approximation procedure. Let us consider, for simplicity, a specular reflector with edge length $2\rho_t$ located at the scene center. We neglect the $m-$dependence of the $1/r$ amplitude-attenuation term, assume the radar pulse has a narrow-bandwidth such that $\Omega_c + \Omega \approx \Omega_c$ in the Green's function, and approximate the sinc

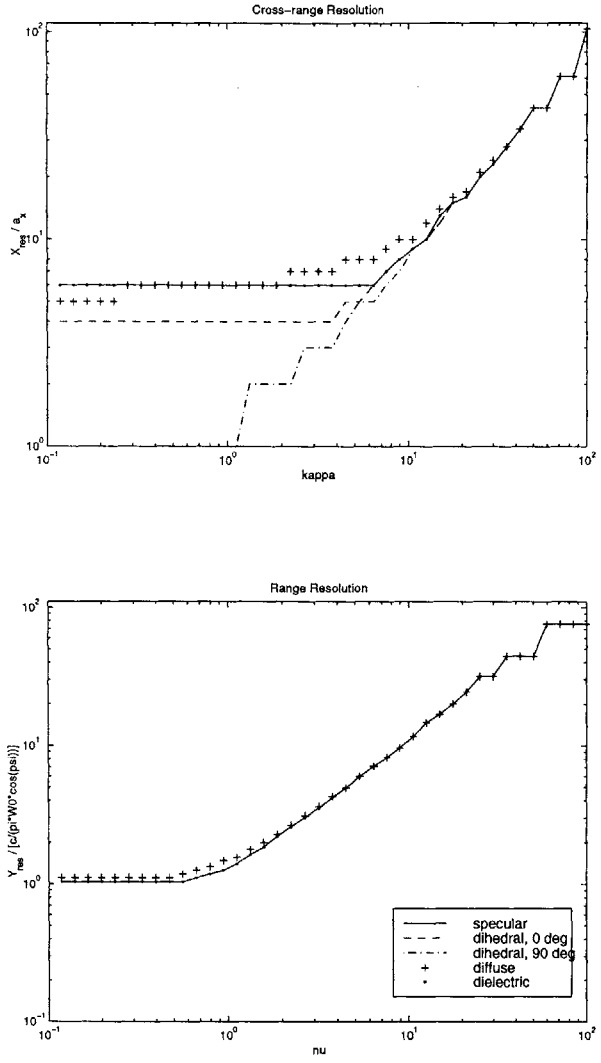

Figure 4.6 SAR imagery spatial resolutions as functions of the chirp-compression filter durations. The calculations assume $k_c a_x^2/2L' = 0.004$, $\rho_t/a_x = 5.0$, $\Omega_c/2\pi = 10\,\text{GHz}$, $T_0 = 0.05\,\mu\text{s}$, $W_0 = 10\,\text{MHz}$, and $\epsilon_r = 10.0 + i5.0$.

waveform in the target scattering pattern by a Gaussian waveform. Then the co-polarized radar target return takes the simple approximation form,

$$r_{\text{target}}(m,\tau) \approx Ae^{-[k_c^2(2\rho_t^2+a_x^2)/2L'^2](mvT_s)^2} e^{i(k_c/L')(mvT_s)^2} e^{(-i\pi W_0/T_0-4/T_0^2)\tau^2} \quad \text{stripmap}$$

$$r_{\text{target}}(m,\tau) \approx Ae^{-(k_c^2\rho_t^2/L'^2)(mvT_s)^2} e^{i(k_c/L')(mvT_s)^2} e^{(-i\pi W_0/T_0-4/T_0^2)\tau^2} \quad \text{spotlight,} \qquad (4.27)$$

where A is a proportionality constant. According to Section 3.1.1, the adaptive-resolution stripmap-mode SAR processor consists of duration-variable chirp-compression filters along the cross-range and range directions. Thus the output stripmap-mode SAR image is

$$l_{\text{target}}(m,\tau) \approx A \sum_{m'=-\infty}^{\infty} e^{-(k_c^2 a_x^2 \kappa^2/2L'^2)[(m-m')vT_s]^2} e^{i(k_c/L')[(m-m')vT_s]^2} e^{-[k_c^2(2\rho_t^2+a_x^2)/2L'^2](m'vT_s)^2}$$

$$\times e^{i(k_c/L')(m'vT_s)^2} \int_{-\infty}^{\infty} d\tau' e^{(i\pi W_0/T_0-4\nu^2/T_0^2)(\tau-\tau')^2} e^{(-i\pi W_0/T_0-4/T_0^2)\tau'^2}. \qquad (4.28)$$

In (4.28), the Gaussian integral over τ can be carried out analytically. Also, the m-summation can be approximated by another Gaussian integral. Converting the pulse widths into length units (meters), we obtain the resolution lengths along the cross-range and range directions:

$$x_{\text{res}} \approx \sqrt{\frac{a_x^2(1+\kappa^2)/2+\rho_t^2}{1+(k_c a_x^2/2L')^2\kappa^2(1+2\rho_t^2/a_x^2)}}$$

$$y_{\text{res}} \approx \frac{c}{\pi W_0 \cos(\psi)} \sqrt{\frac{1+\nu^2}{1+(4\nu/\pi W_0 T_0)^2}}. \qquad (4.29)$$

On the other hand, according to Section 4.3.2, the adaptive-resolution spotlight-mode SAR processor de-chirps the target return in (4.27) and carries out the polar-formatted Fourier transform of the de-chirped return. Thus the output spotlight-mode SAR image is

$$l_{\text{target}}(x,y) \approx Ae^{-i2k_c\cos(\psi)y} \sum_{m=-m_a/2}^{m_a/2} e^{i(2k_c/L')(mvT_s)x} e^{-(k_c^2\rho_t^2/L'^2)(mvT_s)^2}$$

$$\times \sum_{n=-n_a/2}^{n_a/2} e^{-i[4\pi W_0\cos(\psi)/cT_0](nT_r)y} e^{-(4/T_0^2)(nT_r)^2}. \qquad (4.30)$$

In (4.30), the summations over m and n can be approximated by integrals with finite upper and lower limits. To get analytical results, the "hard limit" of the integrand, corresponding to the upper and the lower bounds, are replaced by the Gaussian-shaped factors. Thus the amplitude of the output image $l_{\text{target}}(x, y)$ is also Gaussian in terms of both x and y. Plugging (4.17) into the integrals, we can obtain the resolution lengths along the cross-range and range directions in length units (meters):

$$x_{\text{res}} \approx \sqrt{\kappa^2 a_x^2/2 + \rho_t^2}$$

$$y_{\text{res}} \approx \frac{c}{\pi W_0 \cos(\psi)} \sqrt{1 + \nu^2}. \tag{4.31}$$

Figure 4.7 compares the analytical and numerical results for the stripmap- and spotlight-mode SAR image resolution lengths of a specular reflector. As illustrated in the figures, the approximation formulae (4.29) and (4.31) have good agreement with the numerical results.

Some interesting features of the spatial resolution behaviors obtained from Figure 3.3 and Figure 4.6 can be well explained by using the approximate formulae. First, the cross-range resolution lengths for stripmap-mode and spotlight-mode SARs exhibit a significant difference in (4.29) and (4.31) when the processing duration is very small. When κ goes to infinity, x_{res} for the stripmap SAR in (4.29) approaches a constant value $(2L'/k_c a_x)\sqrt{1/2 + \rho_t^2/a_x^2}$, which corresponds to the dwell duration of the target return determined by the target scattering beam pattern and the antenna beam pattern. As we explained in Section 3.2.1, this result is a natural consequence of using a chirp-compression filter with infinitely small processing duration such that its output is actually the unprocessed radar return. However, when κ goes to infinity, x_{res} for the spotlight SAR in (4.31) increases with κ to infinity, which is much longer than x_{res} for the stripmap SAR. Moreover, at large κ, x_{res} in (4.31) is totally dominated by the term $\kappa^2 a_x^2/2$, and thus independent of ρ_t. Therefore, unlike the stripmap SAR whose cross-range resolution length at large κ is proportional to the radar return dwell duration and hence largely affected by the target scattering pattern, the cross-

range resolution length for the spotlight-mode SAR at large κ is determined only by the processing duration. This is because the spotlight-mode SAR processor (along the cross-range direction) is not a chirp-compression filter for the chirped radar return but rather a Fourier transformer for the de-chirped radar return. The waveform of the de-chirped radar return is indeed determined by the target size. However, when the processing duration (which sets the domain for the Fourier integral) is very small, the de-chirped radar return is approximately a constant, hence the shape of its waveform is irrelevant. The width of the pulse after Fourier transformation is totally determined by the processing duration. The smaller the duration is, the larger the width is.

Now consider what happens when the processing duration becomes large. In this limit x_{res} of the spotlight SAR has a stronger dependence on ρ_t than does x_{res} of the stripmap SAR. From (4.29) and (4.31), when κ goes to 0 the value of x_{res} approaches $\sqrt{a_x^2/2 + \rho_t^2}$ and ρ_t for the stripmap and spotlight SAR, respectively. This explains why the quasi-isotropic scatterer—a dihedral reflector with 90° orientation angle—has a significantly smaller resolution length for the spotlight SAR than it does for the stripmap SAR.

Equations (4.29) and (4.31) also explain the opposite variation trends for the stripmap and spotlight SARs' range resolution behaviors. For the stripmap SAR, y_{res} in (4.29) is proportional to $\sqrt{(1+\nu^2)/(1+(4/\pi W_0 T_0)^2\nu^2)}$, so that the time-bandwidth product W_0T_0 plays a key role. When the factor $4/\pi W_0T_0$ exceeds 1, y_{res} decreases with ν; when $4/\pi W_0T_0$ is less than 1, y_{res} increases with ν. Figures 3.3 and 4.6 assume $W_0T_0 = 0.5$, so the factor $4/\pi W_0T_0$ is greater than 1, and hence y_{res} decreases with increasing ν. For the spotlight SAR, on the other hand, the y_{res} in (4.31) is proportional to $\sqrt{1+\nu^2}$, which is independent of the time-bandwidth product. Therefore the spotlight SAR's y_{res} always increases with increasing ν. This is because the frequency chirp of the radar return is compensated via the de-chirping process of the spotlight SAR processor. Thus the parameter W_0 does not have any effect except in proportionally determining the processing duration of the Fourier

transform. For the pulse waveform after the Fourier transformer, the smaller the processing duration is, the larger the resolution length is.

4.4.2 Signal-to-Noise-plus-Clutter-Ratio

It is shown in Section 3.2.2 that for a stripmap SAR single-target binary-detection problem, the receiver operating characteristic is completely characterized by the signal-to-noise-plus-clutter-ratio (SNCR). It is a straightforward exercise to extend this conclusion to the same problem of a spotlight SAR. So in this section, we study the numerical SNCR values for the adaptive-resolution processor and the whitening-filter processor of spotlight SAR. The parameters values used in computations are in Table 3.1.

4.4.2.1 Adaptive-Resolution Processor

Figure 4.8 illustrates the variation of the specular reflector's SNCR with respect to processing durations. In this figure, CNR is the clutter-to-noise spectrum ratio at zero frequency. The two panels on the left in Figure 4.8 are under clutter-dominant conditions (SNCR $\approx$ SCR, where SCR is the signal-to-clutter ratio) whereas the two on the right are under noise-dominant conditions (SNCR $\approx$ SNR, where SNR is the signal-to-noise ratio). The top two panels in Figure 4.8 show the cross-range-processing duration behavior, and the two lower panels give the range-processing duration behavior. For the cross-range features, different curves represent different antenna aperture sizes. All the curves shown are for HH polarization.

Similar to what we saw in Figure 3.4, Figure 4.8 makes it clear that the clutter-dominated regime is very different from the noise-dominated regime. This is because the clutter has a colored-noise spectrum that is quite different from the white spectrum of the receiver noise. As we described in Section 4.3.2, for the sample point at the scene center, the

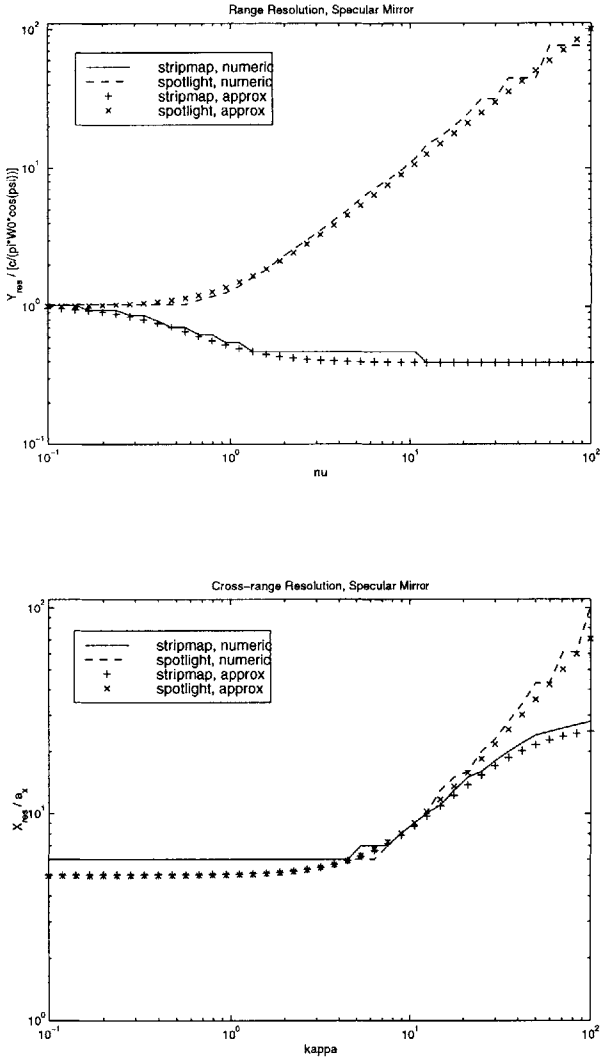

Figure 4.7 Comparison of numerical and analytical SAR imagery spatial resolutions of a specular reflector. The parameter values are identical to those in Figure 3.3.

adaptive-resolution processor with proper processing durations approximates a matched-filter processor. Therefore when noise dominates, the SNCR is a unimodal function of κ, with a maximum $\kappa = \kappa_{\text{opt}}$. This optimum κ value best matches the duration of the cross-range processor to the radar return from the target. If we presume the return beam to be approximately a Gaussian pattern, we can show that $\kappa_{opt} \approx \sqrt{2}\rho_t/a_x$. Compared with κ_{opt} of the stripmap SAR, $\sqrt{1 + 2\rho_t^2/a_x^2}$ in Figure 3.4, the optimum κ of the spotlight SAR lacks a term 1 within the square root; this 1 corresponds to the cross-range antenna beam pattern of the stripmap mode.

The SNCR behaviors with respect to varying range-processing duration in the spotlight-SAR case is quite similar to what we have previously seen in the stripmap-SAR case. In the clutter-dominant regime, both Figure 3.4 and Figure 4.8 indicate that the SNCR values increases with increasing chirp bandwidth W_0. In the noise-dominant regime, we see from Figure 4.8 that the SNCR value is, like Figure 3.4, unimodal in ν, with an optimum value fixed at unity. The optimum ν value does not change because the shape of each individual radar pulse is unaffected by surface reflection from the specular reflector. Figure 4.8 also shows that in the noise-dominant regime the SNCR is independent of chirp bandwidth W_0.

The curves of SNCR versus processing duration parameters in Figure 4.8 are not as smooth as those in Figure 3.4: in the former there are some bumps and apparent discontinuities. The reason is that the adaptive-resolution spotlight SAR processor, unlike the stripmap SAR processor, cannot continuously vary its processing durations. As indicated in Section 4.3.2, the processing durations of the spotlight SAR processor are the integers m_a and n_a that define the domain of the 2-D discrete Fourier transform. The parameters m_a and n_a are inversely proportional to κ and ν (see (4.17)). However, whereas κ and ν can be varied continuously, the parameters that actually control the processing durations, m_a and n_a, can be only varied discretely since they are integers. So the SNCR is not smoothly changed with the parameters κ and ν. The discretization effect becomes more significant

when m_a and n_a are small, or equivalently, when κ and ν are large.

Figure 4.9 illustrates the orientation-angle dependence of the SNCR for a dihedral reflector. The orientation angle, ϕ, is the angle between the dihedral axis and $\hat{x}$. The most significant feature in Figure 4.9 is the polarimetric effect. The SNCR values for HH and VV are almost identical. They both have local maxima at $\phi = 0°$ and $\phi = 90°$, as well as minima at $\phi = 45°$. The SNCR values for HV do not vanish. With respect to orientation angle, their behavior is opposite to that of HH and VV: at $\phi = 0°$ and $\phi = 90°$ local minima occur, at $\phi = 45°$ a maximum occurs. Similar to the case of stripmap SAR in Figure 3.5, such ϕ-dependent characteristics are generated by the double-reflection terms of the dihedral reflector's scattering function. Thus, no matter what mode the SAR operation is, the different patterns of SNCR variation at different polarizations imply that the full polarimetric information is essential to the detection and recognition of a dihedral reflector (or other types of targets involving multiple scattering).

The dihedral reflector's orientation affects its return-beam pattern too. Figure 4.10 illustrates the variation of a dihedral reflector's SNCR with respect to κ when the noise dominates the clutter. At the three orientation angles $\phi = 0°, 45°, 90°$, the SNCR variations are similar to each other, as well as to their counterparts for a specular reflector. However the optimum κ values are different for different ϕ: the larger ϕ is, the smaller κ_{opt} becomes. This is because the scattering beamwidth of a dihedral reflector in the cross-range direction is a function of its orientation angle. The larger ϕ is, the closer its scattering pattern is to being isotropic, hence the longer its return duration. By treating the dihedral reflector's scattering coefficient as approximately Gaussian, the optimum κ can be shown to be $\kappa_{opt} \approx \rho_t / a_x \cos(\phi)$. Compared with the stripmap SAR counterparts in Figure 3.6, the most significant difference occurs when $\phi = 90°$. For the spotlight SAR, the approximate formula suggests that $\kappa_{\text{opt}} = 0$ at $\phi = 90°$, which implies the SNCR value is monotonically decreasing with κ. This result explains why the curves in the second panel of Figure 4.10 are

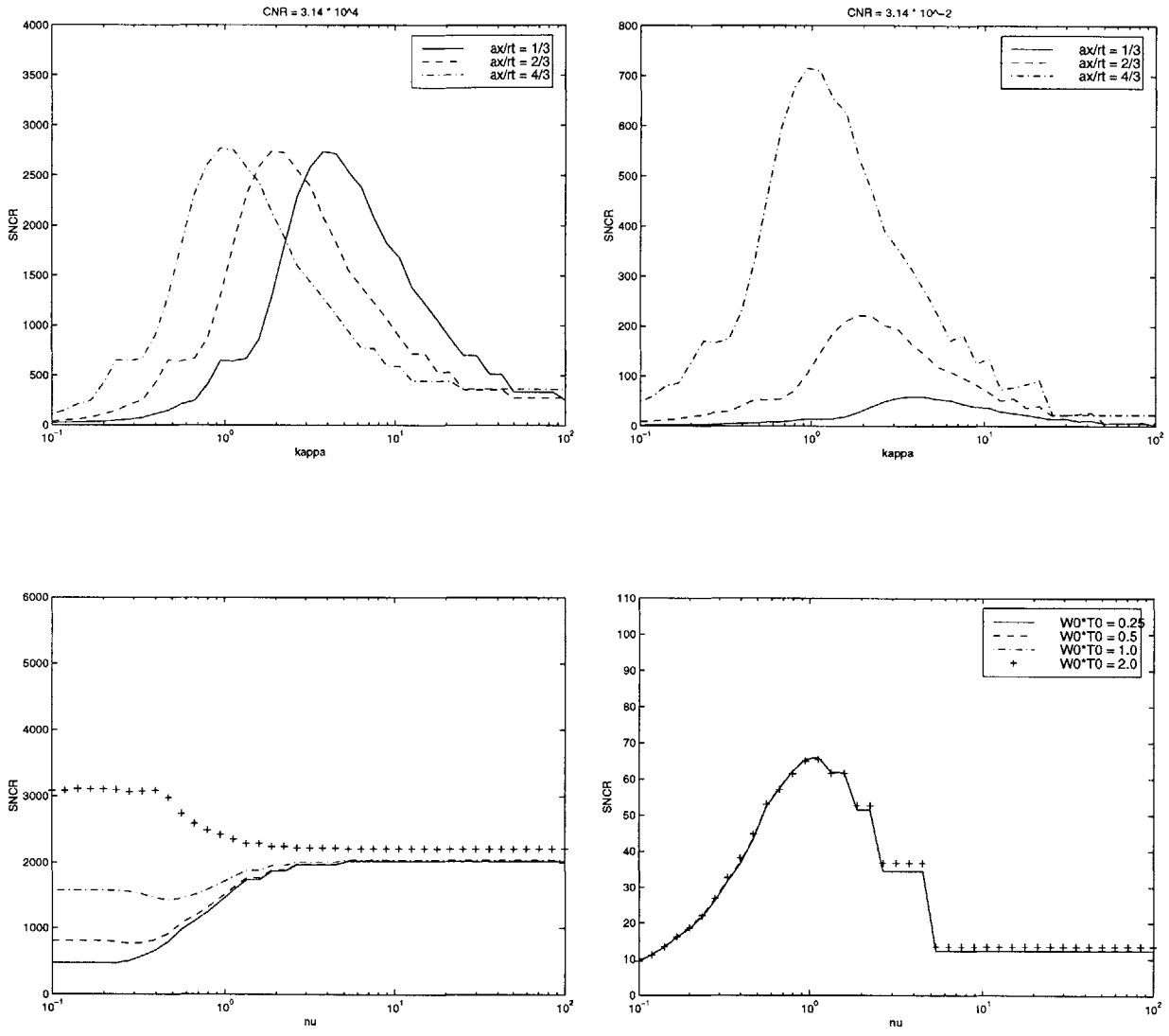

Figure 4.8 SNCR vs. chirp-compression filter durations: AR processor, specular reflector. Upper panels have $\nu = 1$; lower panels have $\kappa = 1$.

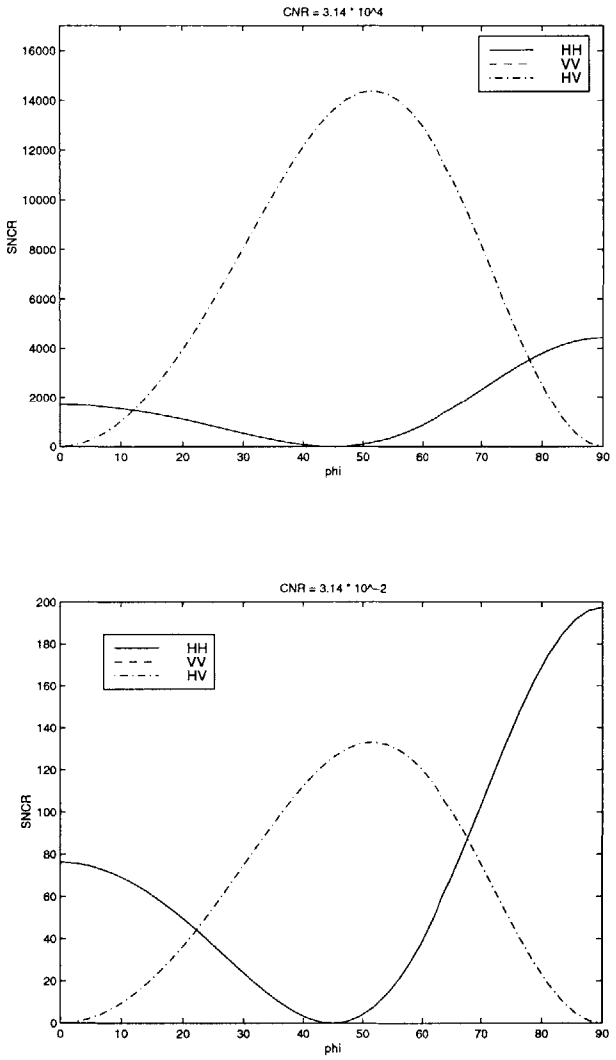

Figure 4.9 SNCR vs. orientation angle: AR processor, dihedral reflector, $\kappa = \nu = 1$.

monotonic rather than unimodal. In Section 3.2.3.1, we observed that a dihedral reflector with 90°-orientation angle is not an ideal isotropic scatterer. So the corresponding optimum κ should be larger than 0, and the SNCR curve also has to be unimodal. We cannot observe unimodal SNCR curves in the second panel of Figure 4.10 since the peak is beyond the lower limit of $\kappa = 0.1$.

Figure 4.11 illustrates the dielectric volume's SNCR variations with respect to κ and ν when the noise dominates the clutter. The κ-dependent features here are identical to those seen for the specular reflector: the optimum κ values are the same, and the SNCR values for different aperture sizes are in the same proportion. The ν-dependent behavior is different from the surface-scattering cases. The radar return from a dielectric volume has a SNCR that decreases with increasing chirp bandwidth W_0. We have explained the same phenomena for the stripmap SAR in Section 3.2.3: the cross-range beam pattern of the radar return from a dielectric volume is the same as that of a specular reflector; volume scattering, however, disperses individual radar pulses, and this effect becomes more serious with increasing pulse bandwidth.

For both stripmap-mode operation and spotlight-mode operation, the SNCRs for the adaptive-resolution processors are robust with respect to target size. Suppose we do not know the exact target size and hence choose a mismatched cross-range processing duration based on the incorrect information we have on target size. When the target-size error is not too large, the output SNCR would not deviate too much from the maximum value. Take the specular reflector with $\rho_t/a_x = 1.5$ as an example. The optimum κ is $\sqrt{1 + 2\rho_t^2/a_x^2}$ for stripmap-mode operation and $\sqrt{2}\rho_t/a_x$ for spotlight-mode operation. When we replace ρ_t in these optimum κ values by $0.8\rho_t$ or $1.2\rho_t$, the mismatched SNCR values are only 5% less than the SNCR peak values (see to Figures 3.4 and 4.8). So the mismatched SNCR deviation is not very sensitive to the information of target size.

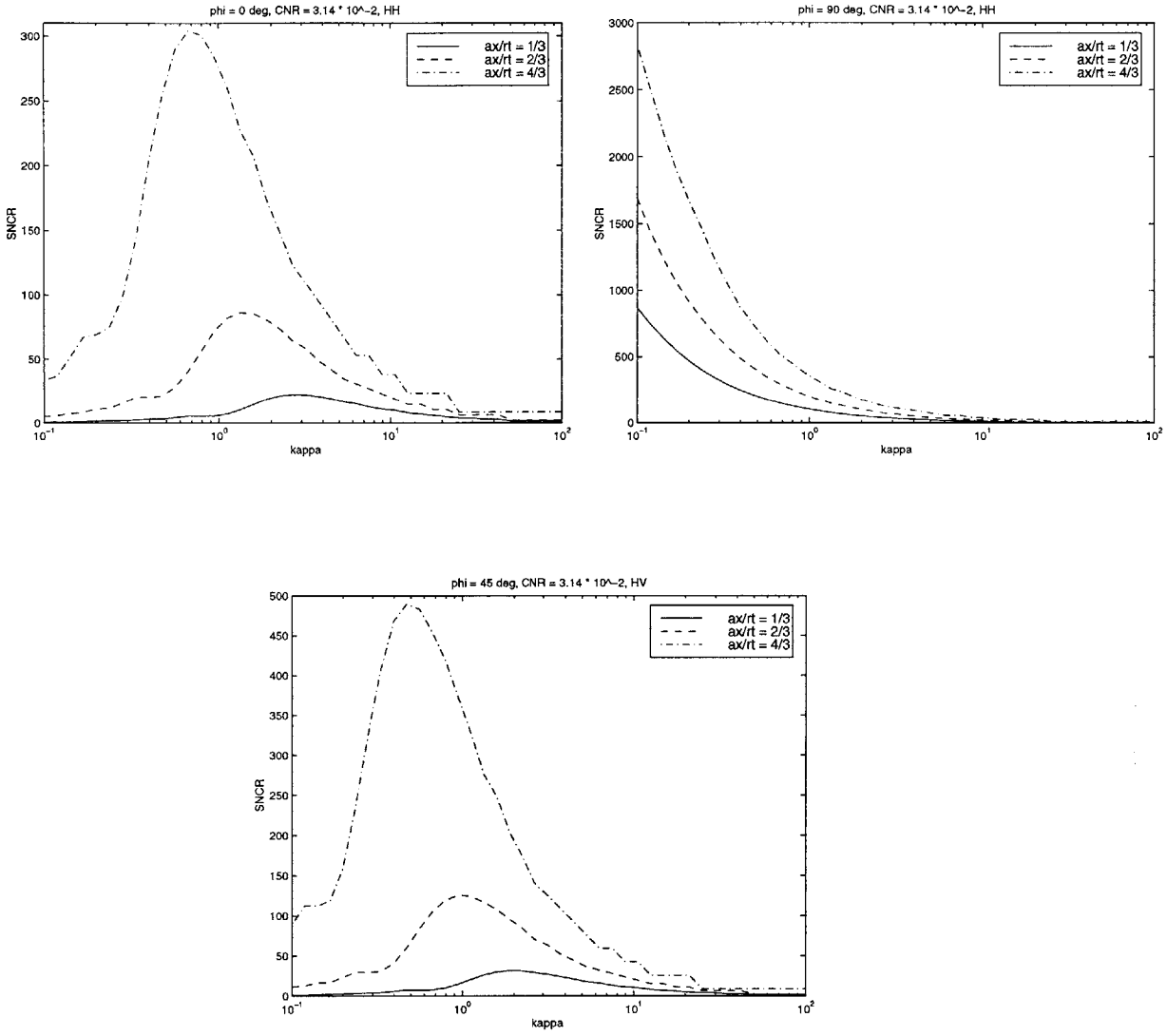

Figure 4.10 SNCR vs. cross-range chirp-compression filter duration: AR processor, dihedral reflector, $\nu = 1$, noise dominant.

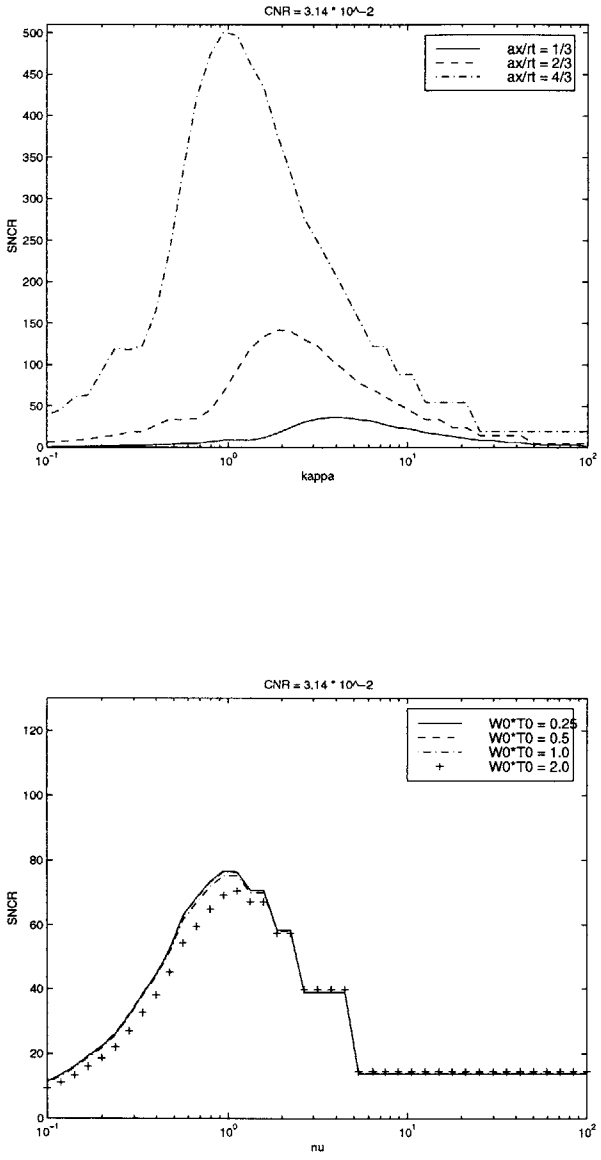

Figure 4.11 SNCR vs. chirp-compression filter durations: AR processor, dielectric volume, noise dominant. Top panel has $\nu = 1$; lower panel has $\kappa = 1$.

4.4.2.2 Whitening Processor

Here we shall compare the SNCR values for the AR processor with those for the optimum, whitening-filter processor. Note for the parameters in Table 3.1, we have that

$$(1/4)\tan^2(\psi)(k_c a_y/L')^2(cT_0)^2 \approx \pi^2/200 << 1.$$

Hence the clutter is approximately stationary (see Section 4.3.3), and the whitening filter in (3.9) can be applied.

By construction, the clutter-plus-noise part of the whitening filter's output has a white spectrum. Thus, the SNCR value for the whitening-filter processor in (3.20) reduces to the "energy" of the impulse response of the matched filter described in (4.25). Following a procedure similar to the one used in Section 3.2.3.2, we can obtain a formula for the SNCR of the spotlight SAR whitening-filter processor which is identical in structure to the one described by (3.22). The only difference is that for stripmap and spotlight SARs, the target-return spectra with respect to the cross-range time index are different.

From the discussion in Section 4.3.2, it is clear that the adaptive-resolution processor whose processing durations match the (cross-range and range) dwell durations are approximately identical to the matched-filter processor at the sample point corresponding to the scene center. Moreover, for both stripmap and spotlight SAR, the noise-component output from the adaptive-resolution processor is roughly proportional to the cross-range and range processing durations. Thus, the approximate SNCR formulation (3.23) also applies to the spotlight-mode SAR when noise dominates over clutter. The clutter return can be thought of as the sum of target returns contributed from all possible locations on the ground. For those contributions not from the scene center, the output of the stripmap SAR adaptive-resolution processor does not resemble that of the spotlight SAR adaptive-resolution processor. Therefore, the sampled outputs of clutter are different for different modes of SAR operation.

Several significant SNCR aspects observed in the case of stripmap SAR also appear in the case of spotlight SAR. In the noise-dominant regime, we see from (3.22) and (3.23) that $\text{SNCR}_{\text{white}}$ reduces to the sum of target-return energies over all three polarizations divided by the noise spectrum N_0, whereas SNCR_{AR} becomes the target-return energy at a specific polarization divided by the noise spectrum. Therefore $\text{SNCR}_{\text{white}}/\text{SNCR}_{\text{AR}}$ becomes a polarimetric-effect-dependent constant. Regardless of the polarimetric effect, SNCR_{AR} in this case has reached its upper bound. The relationship between $\text{SNCR}_{\text{white}}$ and SNCR_{AR} is more complicated out of the noise-dominant regime. Here the adaptive-resolution processor is not able to achieve the optimum, white-noise limit. Figure 4.12 plots our numerical results for $\text{SNCR}_{\text{white}}/\text{SNCR}_{\text{AR}}$ versus CNR for different target types. All the curves in Figure 4.12 have a similar trend: $\text{SNCR}_{\text{white}} >> \text{SNCR}_{\text{AR}}$ prevails when clutter dominates. As the white-noise spectrum is increased, the performance gap between the optimum processor and the adaptive-resolution processor decreases. Eventually, the noise-dominant regime is reached and $\text{SNCR}_{\text{white}}/\text{SNCR}_{\text{AR}}$ becomes independent of CNR and equal to 2 for the specular reflector, the dielectric volume, and the dihedral reflector at $\phi = 0°$ and $90°$, and equal to 1 for the dihedral reflector at $\phi = 45°$. These trends are exactly the same as those of the stripmap SAR in Figure 3.8. Comparing Figure 4.12 with Figure 3.8, there are two main differences. First, the SNCRs in both cases decrease with increasing noise level, but the values at the clutter-dominant side are quite different. As we have explained, this is because the clutter outputs from the stripmap SAR and spotlight SAR adaptive-resolution processors are different. Second, at the noise-dominant side, the SNCR values in Figure 4.12 are slightly higher than those in Figure 3.8. This is because the spotlight SAR adaptive-resolution processor is only an approximate matched-filter processor for the target return from the scene center. The processing durations of the processor match the dwell durations of the target return, but the return waveform is not precisely matched in the processor. In particular, the target return waveform is Gaussian with respect to the range time index and a sinc function with respect to the cross-range time index, whereas the adaptive-resolution

spotlight SAR processor uses rectangular windows to limit the processing durations in both range and cross-range directions. The adaptive-resolution stripmap SAR processor matches the target return waveform better because the impulse responses of both range and cross-range chirp-compression filters are shaped by Gaussian functions. So the adaptive-resolution spotlight SAR processor is less optimum than is the corresponding stripmap SAR processor.

Figure 4.13 plots $\mathrm{SNCR_{white}/SNCR_{AR}}$ versus target size. The trends are similar to those indicated in the stripmap-SAR case in Figure 3.9. When noise does not dominate over clutter, increasing target size reduces $\mathrm{SNCR_{white}/SNCR_{AR}}$ to some extent. This improvement is limited by CNR. The minimum $\mathrm{SNCR_{white}/SNCR_{AR}}$ is not always optimum (2 or 1, depending on polarimetric condition). The larger CNR is, the higher the minimum $\mathrm{SNCR_{white}/SNCR_{AR}}$ value becomes. When noise dominates over clutter, the ratio $\mathrm{SNCR_{white}/SNCR_{AR}}$ is approximately invariant with target size.

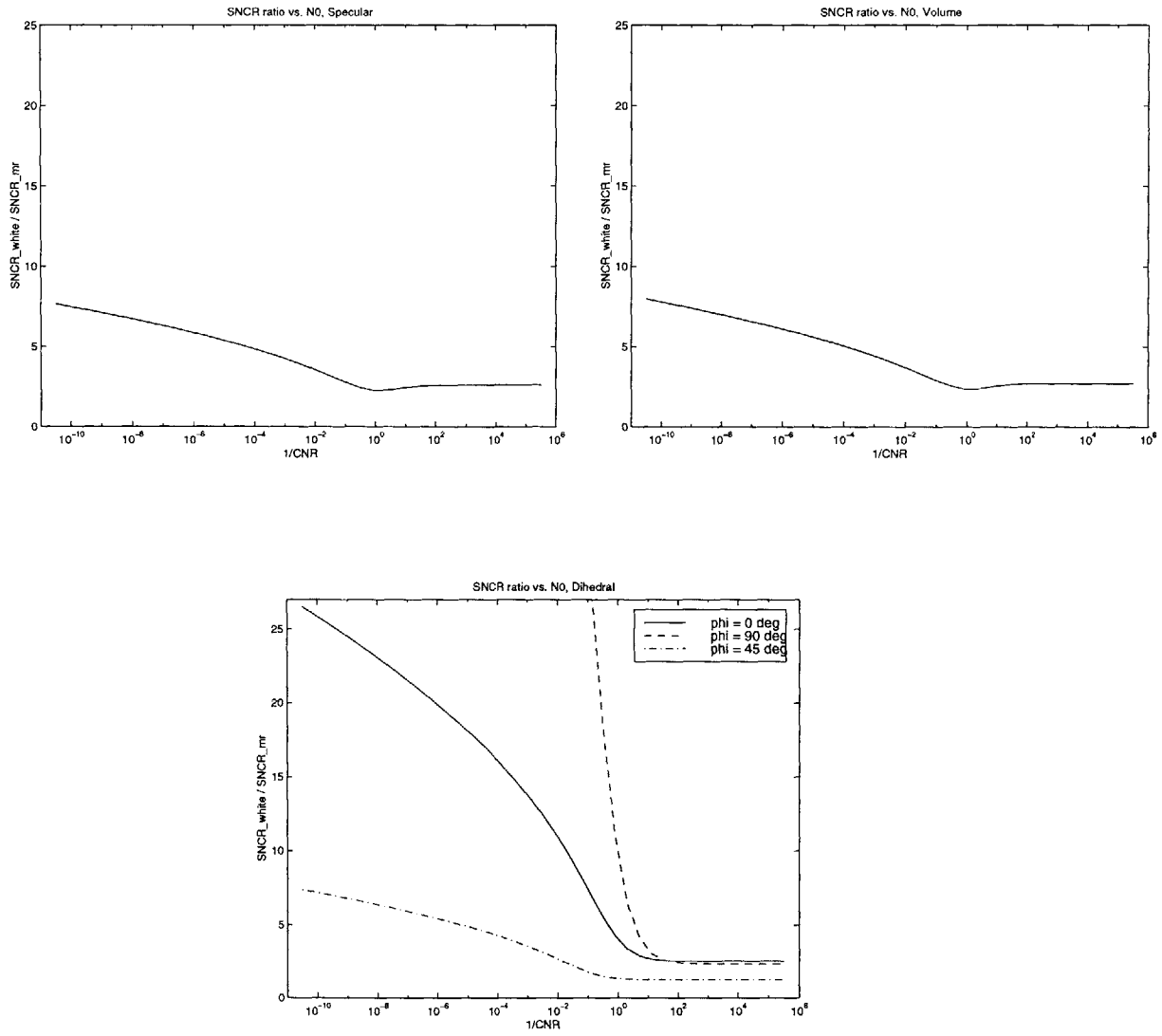

Figure 4.12 $\mathrm{SNCR}_{\mathrm{white}}/\mathrm{SNCR}_{\mathrm{AR}}$ vs. CNR. For the AR processor, $\kappa = \sqrt{2}\rho_t/a_x$, for the specular reflector and the dielectric volume, and $\kappa = \rho_t/a_x \cos(\phi)$ for the dihedral reflector; $\nu = 1$ in all cases. The chosen polarimetric component is HH for the specular reflector, the dielectric volume, the dihedral reflector at $\phi = 0°$ and 90°, and is HV for the dihedral reflector at 45°.

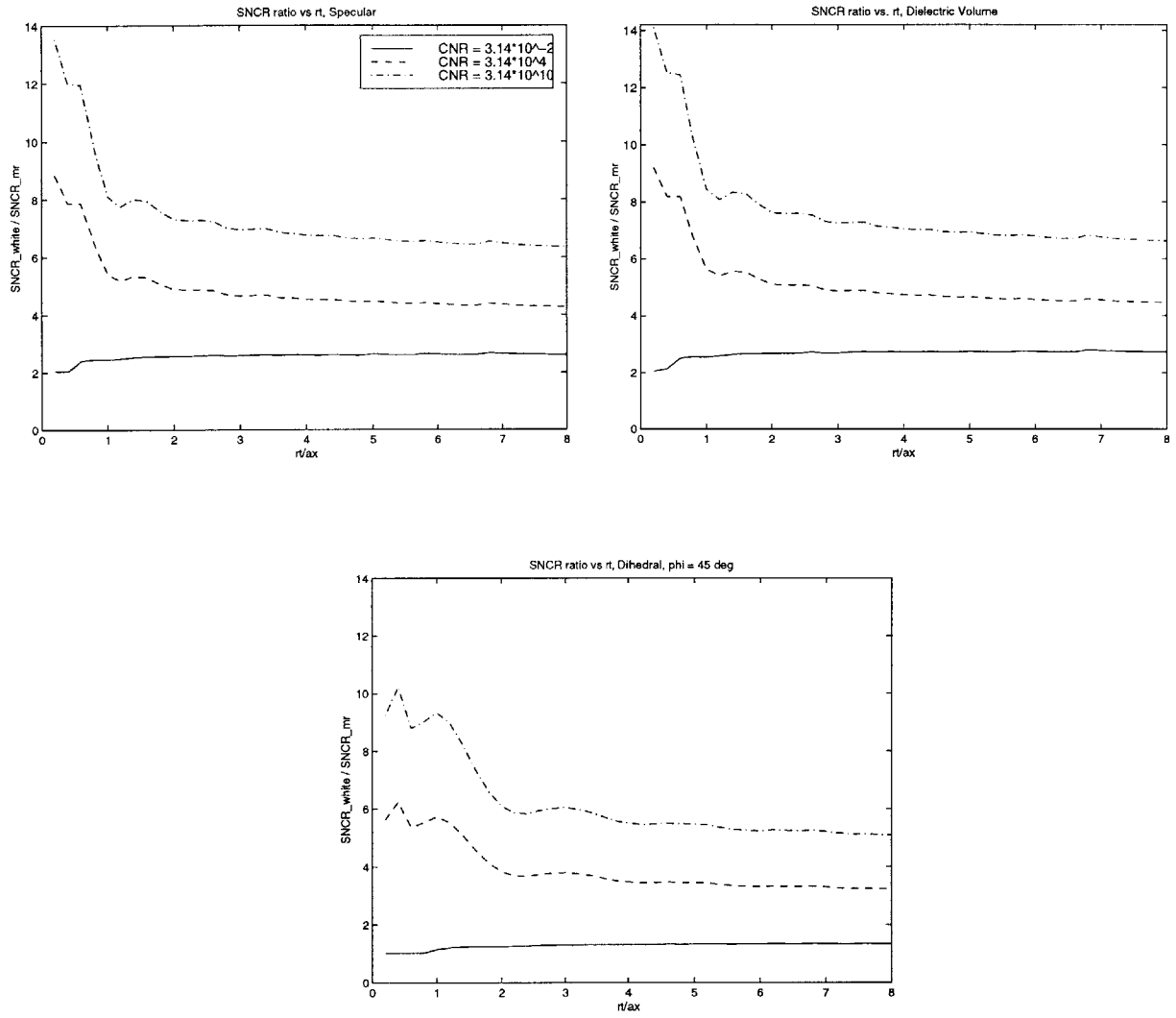

Figure 4.13 $\mathrm{SNCR_{white}/SNCR_{AR}}$ vs. target size. The choices of κ, ν and polarimetric components are the same as in Figure 3.8.

Chapter 5

Multi-Component Target Detection Problems

5.1 From Single-Component to Multi-Component Targets

The previous chapters have laid out the foundation for a target-detection theory for stripmap-mode and spotlight-mode synthetic aperture radar imagery. In these chapters, however, we only considered the case of a single simple reflector (specular, dihedral reflector or dielectric volume) on the ground plane. In real SAR campaigns, there are usually more than one target on the whole image plane, or even within the radar footprint area. Moreover, real targets such as tanks are composed of many smaller reflectors. For detecting and recognizing such realistic targets, the extension of the theoretical treatment to the case of multiple reflectors is necessary.

A multi-component target is defined as a collection of simple reflectors located at different positions. The radar-return signal from a single reflector located at $(\Delta_x, \Delta_y, 0)$ with respect to the scene center can be obtained from (2.31) (stripmap-mode) or (4.3) (spotlight-mode). Suppose we neglect the multiple scattering of electromagnetic waves among different reflectors, then the radar-return signal from a multi-component target is the sum of the contributions from all its individual reflectors. On the other hand, the clutter and noise components in the radar return are unaltered by the change of target. Hence the extension of the radar-return signals in Chapter 2 and Chapter 4 to the case of multi-component targets is straightforward.

Our theoretical treatment of SAR imagery consists of three aspects: the radar-return signal model; the processing for recognizing targets from the imagery; and the quantitative

as well as qualitative performances analysis for these processors. As noted above, the radar-return models developed for single-component targets can be easily extended to the case of multi-component targets. However, extending our target detection/classification schemes and the associated performance analyses is not so straightforward. We can demonstrate the involved nature of such extension from an example: the 2-D stripmap-mode SAR image after passing the radar return through the adaptive-resolution chirp compression filters specified in (3.1). Consider the same 2-D stripmap SAR scenario as the one described by the flight and radar parameters in Table 3.1. Suppose the multi-component target consists of three reflectors with center positions $(\Delta_x, \Delta_y) = (0,0), (-7,-3), (5,-4)$ on the ground. All the reflectors are assumed to be specular mirrors of the same size: $\rho_t = 1.5$ m. The normal directions of the three reflector plates are all parallel to $\hat{z}'$, the nominal direction for the target at $(\Delta_x, \Delta_y) = (0,0)$. The SAR image of this multi-component target after the adaptive-resolution chirp-compression filters thus can be computed by following Section 3.1.1 for each reflector. Figure 5.1 plots the computed intensities (on a linear scale) for the 2-D SAR images of the three-reflector scenario. The three panels correspond to different processing durations for the cross-range chirp-compression filter $h_1[m]$: $\kappa = 1,\ 10,\ 100$. The range chirp-compression filter $h_2(\tau)$ is set to the full dwell time, namely, $\nu = 1$, for the three cases. Neither clutter nor noise is present in the radar return.

When $\kappa = 1$, Figure 5.1 shows that the three reflectors can be fully resolved along the cross-range direction. As the processing duration for $h_1[m]$ decreases, the resolution becomes coarser, hence the SAR image of an individual reflector is blurred over a wider area, which is consistent with the results in Section 3.2.1. However, the multi-component SAR images have a new feature that cannot be captured by the single-reflector theory developed in Chapters 2, 3, and 4. From Figure 5.1, we observe that at coarser resolutions the overall intensity image is not the superposition of the intensity images corresponding to individual reflectors. For example, at $\kappa = 100$ the SAR image is not composed of three

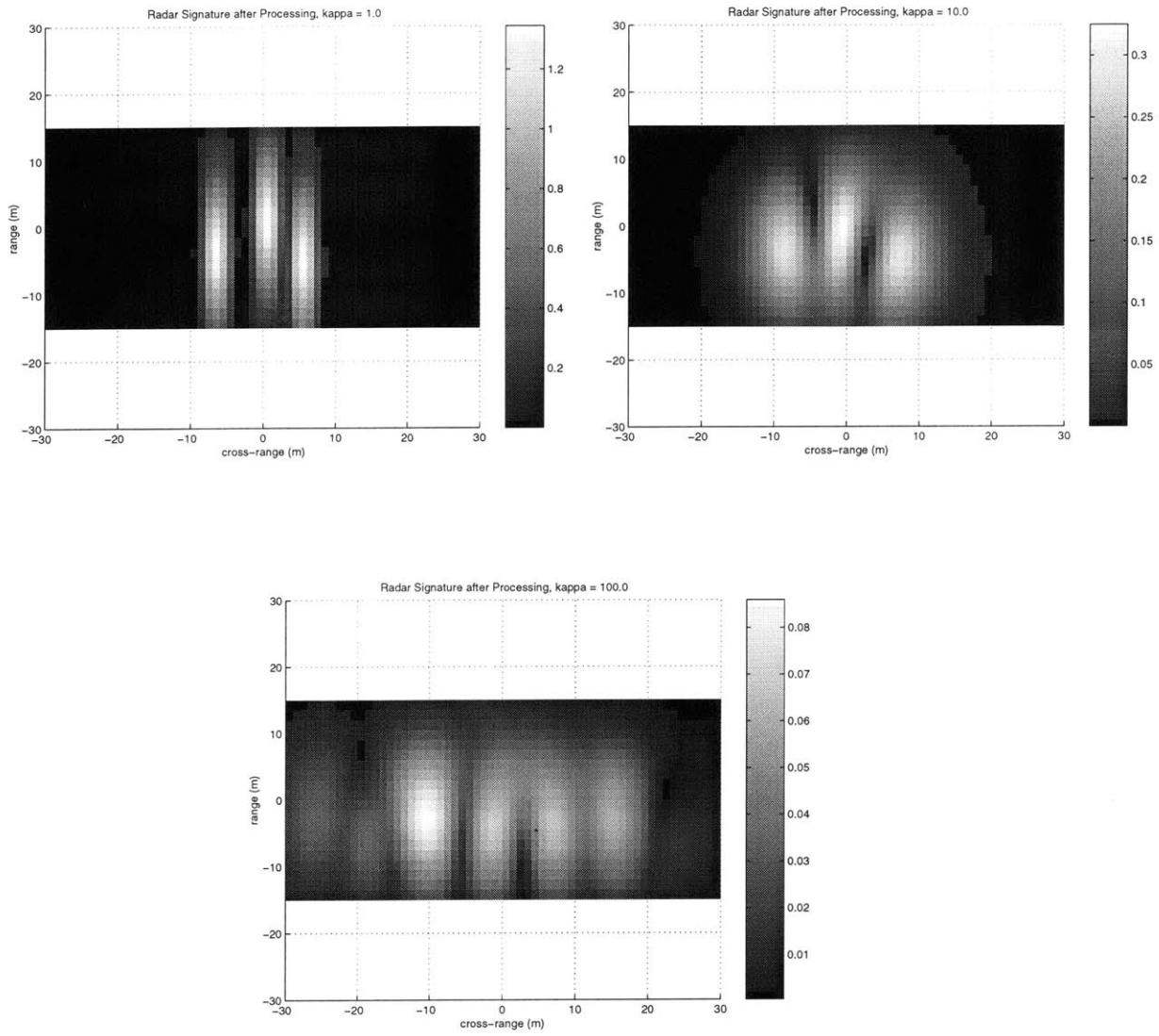

Figure 5.1 2-D SAR images for a multi-component target. The three reflectors have the same size $\rho_t = 1.5$ m and the same normal direction $\hat{z}'$. Their center locations are $(\Delta_x, \Delta_y) = (0,0), (-7,-3), (5,-4)$. For the image at top left, top right, and bottom, κ is 1, 10, 100, respectively; $\nu = 1$ for the three cases. The polarization is HH.

overlapping blurred spots. Instead, it is a pattern with a pronounced periodic variation along the cross-range direction. This is because the overall radar return is the coherent sum of its individual reflector components. The phases of the individual return components are different, because their different spatial locations lead to different propagation delays. Hence when the resolution is coarse enough such that different reflector images overlap, they interfere with one another.

The results in Figure 5.1 have an interesting implication. In Section 3.2.1 and Section 4.4.1, we have shown that the variations of image resolution with respect to processing durations are different for different types of reflectors. Thus the SAR image multi-resolution behavior may be used to classify the type of a single-component target. However, when a multi-component target is present, the image patterns from individual components might be mixed with one another rather than distinctively superimposed when the resolution (processing duration) is low. Therefore, the low-resolution part of the multi-resolution image repertoire of an individual target component, that is used to classify the reflector type, is not available.

The low-resolution image, such as the one indicated in the last panel of Figure 5.1, can also be interpreted as the original radar return (in terms of cross-range direction) before synthetic-aperture operation. The interference pattern appearing in this unprocessed radar-return signal is determined by the relative phases of all the individual target components. Such phases are functions of a variety of radar, propagation, and target factors, such as the radar carrier frequency, target-component positions, atmospheric disturbances, target scattering cross section, and the jittering motion of the antenna platform. In order to plot Figure 5.1, we assume all these factors are given. However, in real applications, it is not practical to make this assumption. As a matter of fact, when dealing with the radar images of real-world multi-component targets, we not only lack complete information about the relative phase of each component, but also about some other parameters such as the

position of each target component, the pose/orientation of the whole target geometry, the scattering amplitude from each component, etc. In other words, if we want to come up with a multi-component target detection/recognition scheme for SAR images, it is essential to make such scheme able to handle the uncertainties in some parameters of the radar-return model.

This chapter is devoted to the multi-component target detection problems for stripmap- and spotlight-mode SAR images. As a detection problem, it is still a binary hypothesis test: determine whether a (known) multi-component target is present or absent from the given radar image corrupted with clutter and noise. Complete information about the multi-component target includes the geometric type, size, material constitution, orientation, and center location of each reflector, and the phase of the radar return from each reflector. On the one hand, a useful target detection scheme does not have to take all of these parameters as given. Furthermore, a feasible detection scheme may not be able to afford dealing with the variations of all parameters at once. In this chapter, we choose to investigate four cases: the phase of each target component is random; the phase and reflector location of each target component are random; the phase, location, and scattering amplitude of each target component are random; and the target pose is random.

The rest of this chapter is organized as follows. In Sections 5.2 through 5.5, we develop detectors for uncertain-parameter multi-component targets based on the output images from the whitening-filter Neyman-Pearson processors described in Sections 3.1.2 and 4.3.3. In Section 5.2, we come up with a likelihood-ratio detection scheme which is Neyman-Pearson optimum, a sum-amplitude detection scheme, and a sum-amplitude-square detection scheme for a multi-component target with random phases. The receiver operating characteristics of these detectors are computed and compared. In Section 5.3, we come up with a generalized likelihood-ratio test for a multi-component target with random phases and positions. To compute the probability of detection and the probability of false alarm for this detector

requires work on the level-crossing problem for a 2-D random field. We develop an approximate formula for calculating this probability, and verify its validity with Monte Carlo simulations. In Section 5.4, we develop an approximate generalized likelihood-ratio detector for a multi-component target with random phases, positions, and scattering amplitudes. Its receiver operating characteristic is evaluated by applying the 2-D level-crossing theory presented in the previous section. In Section 5.5, we also propose a generalized likelihood-ratio detector for a multi-component target with random pose. A finite-bin approximation to the random-field level-crossing problem is used to evaluate its receiver operating characteristic. In Section 5.6, we impose the detection schemes for a multi-component target with any of the four uncertainty types, as developed in Section 5.2 through 5.5, onto the output image of the conventional SAR processor. Target detection performances are evaluated and compared with their whitening-filter-processor counterparts.

The aim of this chapter is not to develop a sophisticated, comprehensive, and powerful target detector capable of recognizing realistic man-made targets in SAR applications with good performance. Instead, it tries to quantify, from a fundamental-principles viewpoint, the target-detection performance advantage of multiresolution/adaptive-resolution processors as compared to conventional SAR imagers. Thus the multi-component target models chosen to investigate in this chapter do not have to be as complicated as a real-world object, such as a tank or truck. They could be simple, but embody the characteristics that highlight the performance differences between single-component and multi-component targets as well as the differences between conventional SAR full-resolution processing and multiresolution/adaptive-resolution processing.

5.2 Multi-Component Target Detection with Unknown Phases

5.2.1 Detection Schemes

To derive the optimum detector for a multi-component target with unknown component phases, we start from a simplified scenario. We consider the case of a scalar 1-D radar-return $r(t)$ from a multi-component target that is corrupted by a zero-mean unit-spectrum white Gaussian noise $w(t)$. Thus the complex envelope at the input to the detector is

$$r(t) = w(t), \tag{5.1}$$

when the target is absent (hypothesis H_0), or it is

$$r(t) = \sum_{m=1}^{M} e^{i\phi_m} s_m(t - t_m) + w(t), \tag{5.2}$$

when the target is present (hypothesis H_1). Here, the target contains M components. The complex envelope $s_m(t)$ is the radar-return waveform from the type of reflector corresponding to the m-th component of the target when it is located at the scene center; its time delay t_m is determined by the actual location of this component. The phases ϕ_m from $m = 1$ to M are mutually independent random variables and uniformly distributed within $[0, 2\pi)$. They represent the incoherence of each target-component with respect to other components as well as the noise.

In order to obtain a tractable solution to the multi-component target detection problem, we shall assume, in all that follows, that the physical separation between any two reflectors i and j is large enough to yield

$$\int_{-\infty}^{\infty} dt s_i^*(t - t_i) s_j(t - t_j) \approx 0. \tag{5.3}$$

Thus the waveforms $s_1(t - t_1)$, $s_2(t - t_2)$, ...,$s_M(t - t_M)$ are mutually orthogonal, hence we can use them as basis functions for a series expansion of the radar return $r(t)$. The binary

detection problem for continuous waveforms depicted in (5.1) and (5.2) can reduced to an equivalent binary detection problem for random vectors:

$$H_0: \quad \mathbf{r} = \mathbf{w}, \tag{5.4}$$

$$H_1: \quad \mathbf{r} = \mathbf{s} + \mathbf{w}, \tag{5.5}$$

where $\mathbf{r} = [r_1, r_2, ..., r_M]^T$, $\mathbf{w} = [w_1, w_2, ..., w_M]^T$, $\mathbf{s} = [e^{i\phi_1}s_1, e^{i\phi_2}s_2, ..., e^{i\phi_M}s_M]^T$,

$$r_m = \int_{-\infty}^{\infty} dt s_m^*(t - t_m) \cdot r(t), \tag{5.6}$$

$$s_m = \int_{-\infty}^{\infty} dt s_m^*(t - t_m) \cdot s_m(t - t_m), \tag{5.7}$$

$$w_m = \int_{-\infty}^{\infty} dt s_m^*(t - t_m) \cdot w(t). \tag{5.8}$$

The random variable r_m is the projection of the radar-return signal $r(t)$ onto the basis function $s_m(t-t_m)$. Because the noise $w(t)$ is zero-mean white Gaussian with unit spectrum, the random variable w_m is zero-mean complex-Gaussian with variance

$$< |w_m|^2 >= E_m = \int_{-\infty}^{\infty} dt s_m^*(t) \cdot s_m(t). \tag{5.9}$$

Here E_m is the energy of the m^{th}-component return.

The optimum detection scheme for the binary hypothesis test problem described in (5.4) and (5.5) is a likelihood-ratio test [29]. Under our orthogonality-condition assumption, the Gaussian random variables w_1, w_2, ..., w_M are mutually independent, thus the random variables r_1, r_2, ..., r_M are also conditionally independent under both H_0 and H_1. The joint probability density function of the random vector $\mathbf{r}$ under H_0 or condition H_1 can therefore be represented as the product of the marginal probability density functions for the individual components [29]:

$$p_{\mathbf{r}|H_0}(r_1, r_2, ..., r_M|H_0) = \prod_{m=1}^{M} \frac{1}{\pi E_m} \exp[-|r_m|^2/E_m], \tag{5.10}$$

$$p_{\mathbf{r}|H_1}(r_1, r_2, ..., r_M|H_1) = \prod_{m=1}^{M} \frac{1}{\pi E_m} \exp[-|r_m|^2/E_m - E_m] I_0(2|r_m|), \tag{5.11}$$

where I_0 is the zeroth-order modified Bessel function described in Section 3.2.2. Thus the likelihood ratio is

$$l(\mathbf{r}) = \frac{p_{\mathbf{r}|H_1}(r_1, r_2, ..., r_M|H_1)}{p_{\mathbf{r}|H_0}(r_1, r_2, ..., r_M|H_0)} = \prod_{m=1}^{M} \exp[-E_m] I_0(2|r_m|). \tag{5.12}$$

The Neyman-Pearson optimum detection scheme for the binary hypothesis test problem is a threshold detector based on the likelihood ratio, which can be simplified to

$$\prod_{m=1}^{M} I_0(2|r_m|) \underset{\text{say } H_0}{\overset{\text{say } H_1}{\gtrless}} \beta, \tag{5.13}$$

where β is the threshold.

The optimum detection scheme (5.13) involves the computation of Bessel functions, which may not be easy to accomplish by traditional analog radar devices. For many radar systems, the sub-optimal sum-amplitude detection scheme

$$\sum_{m=1}^{M} 2|r_m| \underset{\text{say } H_0}{\overset{\text{say } H_1}{\gtrless}} \gamma, \tag{5.14}$$

or sum-amplitude-square detection scheme

$$\sum_{m=1}^{M} 2|r_m|^2 \underset{\text{say } H_0}{\overset{\text{say } H_1}{\gtrless}} \alpha, \tag{5.15}$$

are more frequently used [31].

Since we already have the conditional probability density functions ((5.1)) and (5.11)), the receiver operating characteristics for these three types of detectors can be obtained. For each of these detectors, the probability of detection (P_D) is calculated by integrating $p_{\mathbf{r}|H_1}(r_1, r_2, ..., r_M|H_1)$ over the $\mathbf{r}$-domains in which the scaled likelihood ratio (5.13), the sum-amplitude (5.14), and the sum-amplitude-square (5.15) exceed the thresholds β,

γ and α, respectively. Similarly, the probability of false alarm (P_F) is calculated by integrating $p_{\mathbf{r}|H_0}(r_1, r_2, ..., r_M|H_0)$ over the $\mathbf{r}$-domains where the scaled likelihood ratio, the sum-amplitude, or the sum-amplitude-square exceeds its respective threshold. Making use of the monotonic property of $I_0(2|r_m|)$, $|r_m|$, and $|r_m|^2$ with respect to $|r_m|$, we can obtain the following multiple-integral expressions for P_D and P_F. For the likelihood-ratio detector, we get

$$P_D = \Pr(\text{say}H_1 \mid H_1\text{true}) = \int\int ... \int_{\prod_{m=1}^{M} I_0(2|r_m|)\geq\beta} d\mathbf{r}\ p_{\mathbf{r}|H_1}(r_1, r_2, ..., r_M|H_1)$$

$$= 1 - \int_0^{[I_0^{-1}(\beta)]^2/4E_1} du_1\ e^{-u_1-E_1} I_0(\sqrt{4E_1u_1}) \int_0^{[I_0^{-1}(\beta/I_0(\sqrt{4E_1u_1}))]^2/4E_2} du_2\ e^{-u_2-E_2} I_0(\sqrt{4E_2u_2})$$

$$.... \int_0^{[I_0^{-1}(\beta/\prod_{m=1}^{M-1} I_0(\sqrt{4E_mu_m}))]^2/4E_M} du_M\ e^{-u_M-E_M} I_0(\sqrt{4E_Mu_M}), \tag{5.16}$$

$$P_F = \Pr(\text{say}H_1 \mid H_0\text{true}) = \int\int ... \int_{\prod_{m=1}^{M} I_0(2|r_m|)\geq\beta} d\mathbf{r}\ p_{\mathbf{r}|H_0}(r_1, r_2, ..., r_M|H_0)$$

$$= 1 - \int_0^{[I_0^{-1}(\beta)]^2/4E_1} du_1\ e^{-u_1} \int_0^{[I_0^{-1}(\beta/I_0(\sqrt{4E_1u_1}))]^2/4E_2} du_2\ e^{-u_2}$$

$$.... \int_0^{[I_0^{-1}(\beta/\prod_{m=1}^{M-1} I_0(\sqrt{4E_mu_m}))]^2/4E_M} du_M\ e^{-u_M}. \tag{5.17}$$

For the sum-amplitude detector, we get

$$P_D = \Pr(\text{say}H_1 \mid H_1\text{true}) = \int\int ... \int_{\sum_{m=1}^{M} 2|r_m|\geq\gamma} d\mathbf{r}\ p_{\mathbf{r}|H_1}(r_1, r_2, ..., r_M|H_1)$$

$$= 1 - \int_0^{\gamma^2/4E_1} du_1\ e^{-u_1-E_1} I_0(\sqrt{4E_1u_1}) \int_0^{[\gamma-\sqrt{4E_1u_1}]^2/4E_2} du_2\ e^{-u_2-E_2} I_0(\sqrt{4E_2u_2})$$

$$.... \int_0^{[\gamma-\sum_{m=1}^{M-1}\sqrt{4E_mu_m}]^2/4E_M} du_M\ e^{-u_M-E_M} I_0(\sqrt{4E_Mu_M}), \tag{5.18}$$

$$P_F = \Pr(\text{say}H_1 \mid H_0\text{true}) = \int\int ... \int_{\sum_{m=1}^{M} 2|r_m|\geq\gamma} d\mathbf{r}\ p_{\mathbf{r}|H_0}(r_1, r_2, ..., r_M|H_0)$$

$$= 1 - \int_0^{\gamma^2/4E_1} du_1\ e^{-u_1} \int_0^{[\gamma-\sqrt{4E_1u_1}]^2/4E_2} du_2\ e^{-u_2} .... \int_0^{[\gamma-\sum m=1^{M-1}\sqrt{4E_mu_m}]^2/4E_M} du_M\ e^{-u_M}. \tag{5.19}$$

For the sum-amplitude-square detector, we get

$$P_D = \Pr(\text{say}H_1 \mid H_1\text{true}) = \int\int ... \int_{\sum_{m=1}^{M} 2|r_m|^2\geq\alpha} d\mathbf{r}\ p_{\mathbf{r}|H_1}(r_1, r_2, ..., r_M|H_1)$$

$$= 1 - \int_0^{\alpha/4E_1} du_1\ e^{-u_1-E_1} I_0(\sqrt{4E_1u_1}) \int_0^{[\alpha-4E_1u_1]/4E_2} du_2\ e^{-u_2-E_2} I_0(\sqrt{4E_2u_2})$$

$$.... \int_0^{[\alpha-\sum_{m=1}^{M-1} 4E_mu_m]/4E_M} du_M\ e^{-u_M-E_M} I_0(\sqrt{4E_Mu_M}), \tag{5.20}$$

$$P_F = \Pr(\text{say}H_1 \mid H_0\text{true}) = \int\int ... \int_{\sum_{m=1}^{M} 2|r_m|^2 \geq \alpha} d\mathbf{r}\ p_{\mathbf{r}|H_0}(r_1, r_2, ..., r_M|H_0)$$

$$= 1 - \int_0^{\alpha/4E_1} du_1\ e^{-u_1} \int_0^{[\alpha-4E_1u_1]/4E_2} du_2\ e^{-u_2} .... \int_0^{[\alpha-\sum m=1^{M-1} 4E_mu_m]/4E_M} du_M\ e^{-u_M}. \tag{5.21}$$

The above detection schemes for the 1-D radar signals can be extended to the 2-D polarimetric radar-signal models developed in Chapter 2 and Chapter 4. But in order to directly apply them, two conditions have to be satisfied. First, the 2-D radar return should be shift invariant with respect to reflector location. If the shift-invariance condition holds, then we can use the radar-return waveform from the reflector located at scene center as the matched-filter impulse response for that same reflector at any location– the only difference would be the sampling time (m, τ). Otherwise we have to construct different matched filters for the same reflector at different locations, which turns out to be intractable. Based on the radar-signal models in Chapters 2 and 4, we can show that this time-shift condition approximately holds for the 2-D radar return. Here, we consider a simple example: a square specular mirror with edge length $2\rho_t$. Suppose that: (i) the radar-pulse bandwidth is much smaller than the carrier frequency so that frequency dispersion can be neglected; (ii) the scattering pattern is approximately Gaussian; and (iii) the size of the synthetic aperture is much smaller than the slant range L'. Then the HH-polarized radar return from the reflector at scene center is approximately

$$Ke^{(ik_c/L'-k_c^2\rho_t^2/L'^2)(mvT_s)^2} e^{-k_c^2a_x^2/2L'^2(mvT_s)^2]} \exp[(-i\pi W_0/T_0-4/T_0^2)\tau^2 \tag{5.22}$$

for the stripmap-mode (see (2.30)), and

$$Ke^{(ik_c/L'-k_c^2\rho_t^2/L'^2)(mvT_s)^2} e^{(-i\pi W_0/T_0-4/T_0^2)\tau^2} \tag{5.23}$$

for the spotlight-mode (see (4.1)), where K is a proportionality constant. Similarly, when the reflector is located $(\Delta_x, \Delta_y, 0)$ from the scene center, where Δ_x and Δ_y are much smaller

than L', the HH-polarized radar return is approximately

$$Ke^{ik_c/L'(\Delta_y \sin(\psi))^2} e^{i2k_c\Delta_y \cos(\psi)} e^{(ik_c/L' - k_c^2\rho_t^2/L'^2)(mvT_s - \Delta_x)^2}$$

$$\times e^{-k_c^2 a_x^2/2L'^2 (mvT_s - \Delta_x)^2} e^{(-i\pi W_0/T_0 - 4/T_0^2)(\tau - 2\Delta_y \cos(\psi)/c)^2} \tag{5.24}$$

for the stripmap-mode (see (2.32)), and

$$Ke^{ik_c/L'(\Delta_y \sin(\psi))^2} e^{i2k_c\Delta_y \cos(\psi)} e^{(ik_c/L' - k_c^2\rho_t^2/L'^2)(mvT_s - \Delta_x)^2}$$

$$\times e^{(-i\pi W_0/T_0 - 4/T_0^2)(\tau - 2\Delta_y \cos(\psi)/c)^2} \tag{5.25}$$

for the spotlight-mode (see (4.3)). The phase factor $\exp[ik_c/L'(\Delta_y \sin(\psi))^2] \exp[i2k_c\Delta_y \cos(\psi)]$ can be incorporated into the random phase associated with the reflector. Thus the binary hypothesis testing problem for the 2-D radar return from an M-component target is as follows:

When the target is absent (hypothesis H_0) we observe

$$\mathbf{r}(m,\tau) \approx \mathbf{r}_{\text{clutter}}(m,\tau) + \mathbf{r}_{\text{noise}}(m,\tau) \tag{5.25}$$

and when the target is present (hypothesis H_1) we observe

$$\mathbf{r}(m,\tau) \approx \sum_{i=1}^{M} e^{j\tilde{\phi}_i} \mathbf{r}_i(m - m_i, \tau - \tau_i) + \mathbf{r}_{\text{clutter}}(m,\tau) + \mathbf{r}_{\text{noise}}(m,\tau) \tag{5.26}$$

In (5.25) and (5.26): $\{\phi_i\}$ are independent identically distributed (iid) random variables that are uniformly distributed over $[0, 2\pi)$; r_i is radar-return from the i^{th} component at scene center; and $(m_i, \tau_i) = (\Delta_x^i/vT_s, 2\Delta_y^i \cos(\psi)/c)$ when the i^{th} component is located at (Δ_x^i, Δ_y^i). Notice that for the binary hypothesis testing problem in (5.25) and (5.26), the unwanted part of the radar return is not white. Therefore in order to apply the detection schemes in (5.13), (5.14) and (5.15), we have to pass the radar return through the whitening filter.

The second condition for the extension of 2-D detection scheme is the orthogonality condition. Its specific form is as follows: for two different target components i and j,

their locations $(\Delta_x^i, \Delta_y^i) = (m_i v T_s, c\tau_i/2\cos(\psi))$ and $(\Delta_x^j, \Delta_y^j) = (m_j v T_s, c\tau_j/2\cos(\psi))$ are sufficiently far apart to satisfy

$$\sum_m \int d\tau \; \mathbf{s}_i^\dagger(m - m_i, \tau - \tau_i) \cdot \mathbf{s}_j(m - m_j, \tau - \tau_j) \approx 0, \tag{5.27}$$

where $\mathbf{s}_i(m, \tau)$ is the output of whitening filter with input $\mathbf{r}_i(m, \tau)$.

Figure 5.2 sketches the block diagrams of the optimum, sum-amplitude, and sum-amplitude-square detectors. Notice that the projection of the radar-return signal onto a basis function is accomplished by passing the signal through a matched filter and sampling the output at proper time. The probability of detection and probability of false alarm for these 2-D detectors can still be calculated by applying (5.16) through (5.21), with the i^{th} component's energy E_i computed by integrating the squared signal amplitude over the range-time τ, and then summing the result over the cross-range time m, and the polarization possibilities.

5.2.2 Performance Analysis

In this section, we present receiver operating characteristics for the likelihood-ratio, sum-amplitude, and sum-amplitude-square detectors for two simple multi-component targets. The first target of concern consists of three identical square specular reflectors at different locations. The center locations of the three reflectors with respect to scene center are $(\Delta_x, \Delta_y) = (0, 0), (-7, -3), (5, -5)$ (in units of meters). For all target components, the half length of each square reflector plate, ρ_t, is 0.5 m, and the plate's normal direction is $\hat{z}'$. The second target we will consider consists of two identical square specular reflectors and a square dihedral reflector. The center locations of the two specular reflectors are $(0, 0)$ and $(-7, -3)$ respectively, and the center location of the dihedral reflector is $(5, -5)$. The shape and orientation of the specular reflectors are the same as those in the first example. The edge length of the dihedral reflector is $\sqrt{2}\rho_t$ where $\rho_t = 0.5$m. The dihedral axis is on the plane perpendicular to the slant range direction $\hat{z}'$. The angle between the dihedral axis and

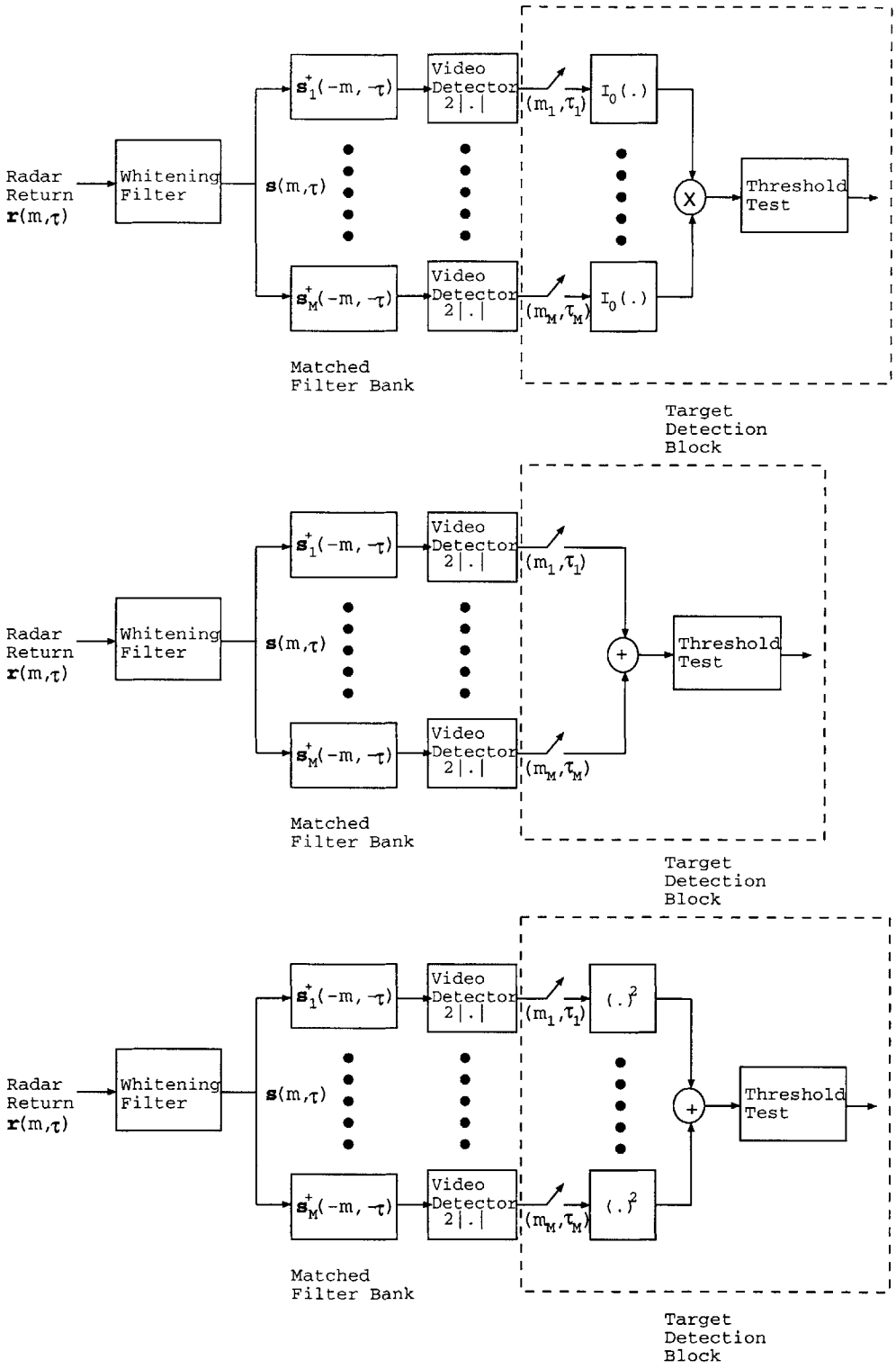

Figure 5.2 Multi-component target detectors; in order from top to bottom: likelihood-ratio (optimum), sum-amplitude, and sum-amplitude-square detectors.

flight direction $\hat{x}$, ϕ, is 45°. Throughout this chapter, the other parameters are chosen as follows: the chirp bandwidth $W_0 = 200$ MHz, the clutter-to-noise-ratio CNR $= 3.14 \times 10^{-2}$ (noise dominant), and all the remaining parameter values are the same as those in Table 3.1.

Using the preceeding parameter values we have obtained numerical values for the resolution lengths associated with the individual target components. For spotlight-mode operation, we found the image resolution lengths of the specular component after the whitening and matched filters were approximately 1.00 m (cross-range) and 1.06 m (range). For the dihedral component, the spotlight-mode image resolution lengths were the same: 1.00 m (cross-range) and 1.06 m (range). For stripmap-mode operation, the image resolution lengths of the specular component were 1.25 m (cross-range) and 1.06 m (range), as were the image resolution lengths of the dihedral component. Thus for the center locations we have chosen, there is no overlap between the image resolution regions of the three target components. Therefore, the orthogonality condition (5.27) holds.

Figure 5.3 plots the receiver operating characteristics of the likelihood-ratio, sum-amplitude, and sum-amplitude-square detectors for the first target example. Figure 5.4 plots the receiver operating characteristics of the same three detectors for the second target example. Each figure includes both stripmap-mode and spotlight-mode results. Note that Figures 5.3 and 5.4 are plotted on probability-paper axes to permit accurate display of both high (near unity) and low (near zero) probability values. A couple of interesting trends can be observed from these figures. First, for the same target, spotlight-mode operation has better detection performance than does stripmap-mode operation. The reason is obvious, if we inspect the numerical SNCR values for the individual target components. For target 1, the SNCR's at the matched-filter outputs for the reflectors at $(0,0), (-7,-3), (5,-5)$ are 10.70, 10.08, 10.24 for spotlight-mode, and 6.24, 6.21, 6.21 for stripmap-mode operation. For target 2, the SNCR's at the matched-filter outputs for the reflectors at $(0,0), (-7,-3), (5,-5)$ are

10.70, 10.08, 3.21 for spotlight-mode, and 6.24, 6.21, 1.73 for stripmap-mode operation. The spotlight-mode target return has higher SNCR values than the stripmap-mode target return for all individual components. Therefore the $P_D - P_F$ curves for spotlight-mode operation go deeper into the desirable ($P_D = 1$, $P_F = 0$) upper left-hand corner region than do the curves for stripmap-mode operation. The physical reason behind this behavior is also clear: because spotlight-mode operation illuminates the target for a longer time duration than does stripmap-mode operation, its post-filter signal strengths are correspondingly higher.

Furthermore, when we contrast the $P_D - P_F$ curves of the two different targets under the same mode of SAR operation, we see that the first target yields better detection performance than does the second target. Again, this phenomenon is a consequence of the individual SNCR values reported in last paragraph. The first two components of both targets are identical. For the target dimensions and orientations we have chosen, the third component of the second target (dihedral) has a smaller SNCR value than that of the first component (specular reflector). So the detection performance associated with the second target is inferior to that of the first target.

Finally, in these two examples, the receiver operating characteristics of the likelihood-ratio, sum-amplitude, and sum-amplitude-square detectors are nearly identical. As we have demonstrated in Section 5.2.1, the likelihood-ratio detector is also the Neyman-Pearson optimum detector. So in these two examples our two simpler but sub-optimal detectors are actually very close to the optimum performance limit. Such observation cannot be rigorously extended to the conclusion that the sum-amplitude and sum amplitude-square detectors *per se* are close approximations to the Neyman-Pearson optimum detector for all possible multi-component targets. Nevertheless, there is a high-SNCR justification for the near-equivalence of the likelihood-ratio detector and the sum-amplitude detector. The likelihood-ratio from Section 5.2.1 involves the zeroth-order modified Bessel function I_0, which can be approximated by an exponential function ($I_0(x) \approx e^x$) when the SNCR value

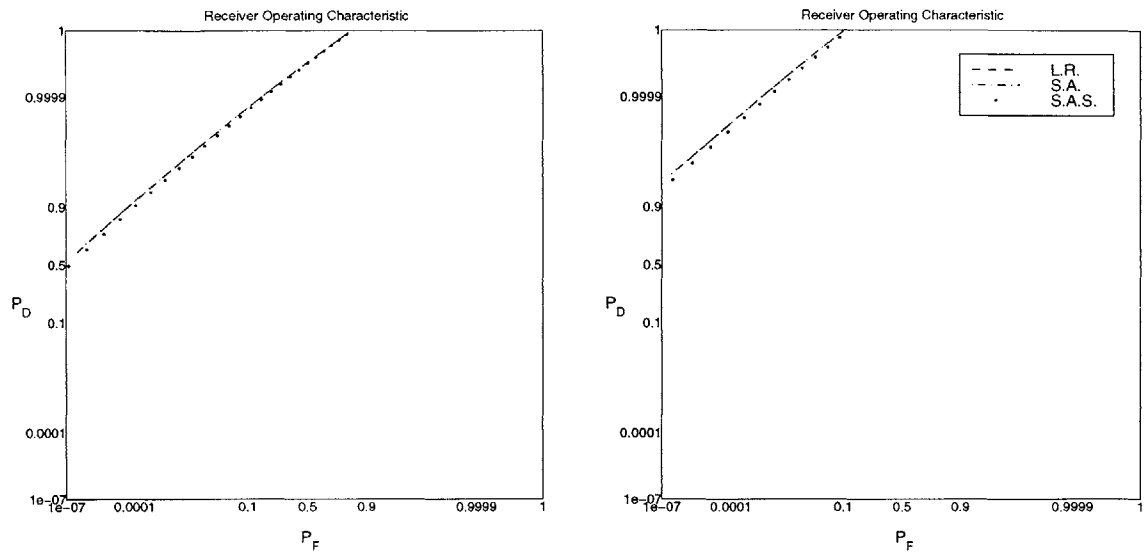

Figure 5.3 Receiver operating characteristics: Neyman-Pearson processor, multi-component target with random phases, 3 specular reflectors. Left panel is stripmap-mode operation; right panel is spotlight-mode operation.

is high. Applying this approximation reduces the likelihood-ratio detector to the sum-amplitude detector.

5.3 Multi-Component Target Detection with Unknown Phases and Positions

In this section, we consider a multi-component target whose component phases and locations are randomly and independently varied. Similar to what was done in Section 5.2.1, we develop the target detector from the 1-D radar model. The binary hypothesis testing problem for the scalar 1-D radar return is as follows. We observe

$$r(t) = w(t), \tag{5.28}$$

when the target is absent (hypothesis H_0), and we observe

$$r(t) = \sum_{m=1}^{M} e^{i\phi_m} s_m(t - t_m) + w(t), \tag{5.29}$$

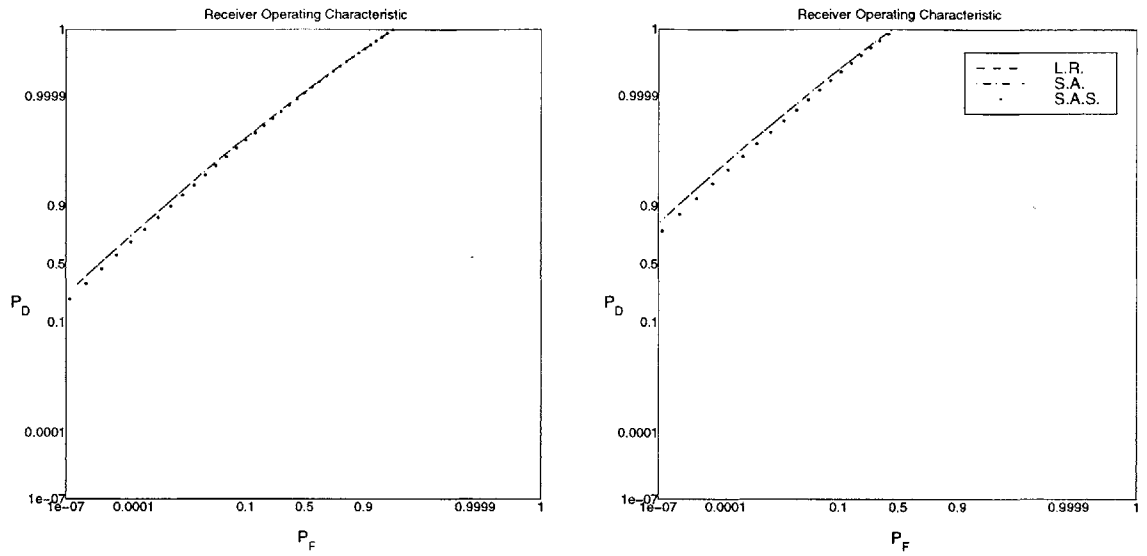

Figure 5.4 Receiver operating characteristics: Neyman-Pearson processor, multi-component target with random phases, 2 specular plus 1 dihedral reflector. Left panel is stripmap-mode operation; right panel is spotlight-mode operation.

when the target is present (hypothesis H_1). Equations (5.28) and (5.29) are identical to (5.1) and (5.2) except for one aspect: the pulse delay time of the m^{th} component t_m, which corresponds to the component's center location, is now taken to be random. The random variables t_1, ..., t_M are assumed mutually independent, and each t_m is uniformly distributed within $[t_m^0 - T_m/2, t_m^0 + T_m/2]$. This position randomness models the variability or unavailability of exact knowledge about some aspects of a real-world target reflector constellation.

5.3.1 Detection Scheme

When the delay times in (5.29) are random variables, it is difficult to write down the likelihood ratio for the binary hypothesis testing problem. However, it is possible (and useful) to formulate the generalized likelihood ratio and develop a detector scheme on that basis [21]. Here we follow the approach of [21] to derive a generalized likelihood-ratio detector scheme for the target with random component-phases and component-positions. First, suppose that the orthogonality condition (5.3) continues to hold over the entire range of delay-time

uncertainty. Then, for a specific realization of the pulse delay times $(t_1, ..., t_M)$, one can write down the likelihood ratio from (5.6), (5.7), and (5.12):

$$l(\mathbf{r}; t_1, ..., t_M) = \frac{p_{\mathbf{r}|H_1}(r_1, r_2, ..., r_M|H_1; t_1, ..., t_M)}{p_{\mathbf{r}|H_0}(r_1, r_2, ..., r_M|H_0; t_1, ..., t_M)}$$

$$= \prod_{m=1}^{M} \exp\left[-\int_{-\infty}^{\infty} dt s_m^*(t) \cdot s_m(t)\right] I_0\left(2\left|\int_{-\infty}^{\infty} dt s_m^*(t - t_m) \cdot r(t)\right|\right). \tag{5.30}$$

For a given radar return $r(t)$, the likelihood ratio is a function of t_1,... ,t_M. One can obtain the maximum-likelihood estimate of these parameters from the radar return:

$$\begin{bmatrix} \hat{t}_1 \\ \cdot \\ \cdot \\ \hat{t}_M \end{bmatrix} = \arg \max_{t_1 \in [t_1^0 - T_1/2, t_1^0 + T_1/2], ..., t_M \in [t_M^0 - T_M/2, t_M^0 + T_M/2]}$$

$$\left[\prod_{m=1}^{M} \exp\left[-\int_{-\infty}^{\infty} dt s_m^*(t) \cdot s_m(t)\right] I_0\left(2\left|\int_{-\infty}^{\infty} dt s_m^*(t - t_m) \cdot r(t)\right|\right)\right], \tag{5.31}$$

where $\hat{t}_1$, ..., $\hat{t}_M$ are the maximum-likelihood estimate. The generalized likelihood ratio is defined as the likelihood ratio when the maximum-likelihood estimates are plugged into the unknown parameters. Plugging (5.31) into (5.30), we have that:

$$\text{GLR} = l(\mathbf{r}; \hat{t}_1, ..., \hat{t}_M)$$

$$= \max_{t_1, ..., t_M} \left[\prod_{m=1}^{M} \exp\left[-\int_{-\infty}^{\infty} dt s_m^*(t) \cdot s_m(t)\right] I_0\left(2\left|\int_{-\infty}^{\infty} dt s_m^*(t - t_m) \cdot r(t)\right|\right)\right], \tag{5.32}$$

where we abbreviate $\max_{t_1 \in [t_1^0 - T_1/2, t_1^0 + T_1/2], ..., t_M \in [t_M^0 - T_M/2, t_M^0 + T_M/2]}$ as $\max_{t_1, ..., t_M}$.

The generalized-likelihood-ratio detector based on (5.32) can be written in the following form:

$$\max_{t_1, ..., t_M} \left[\prod_{m=1}^{M} I_0\left(2\left|\int_{-\infty}^{\infty} dt s_m^*(t - t_m) \cdot r(t)\right|\right)\right] \underset{\text{say } H_0}{\overset{\text{say } H_1}{\gtrless}} \beta \tag{5.33}$$

where β is the threshold. Furthermore, since the zeroth-order modified Bessel function is positive with positive argument and t_1, ..., t_M are mutually independent variables, maximizing the overall product of I_0's in (5.33) is equivalent to maximizing the individual I_0's

in the product. Hence the generalized-likelihood-ratio detector becomes

$$\prod_{m=1}^{M} \max_{t_m} \left[I_0 \left(2 \left| \int_{-\infty}^{\infty} dt s_m^*(t - t_m) \cdot r(t) \right| \right) \right] \underset{\text{say } H_0}{\overset{\text{say } H_1}{\gtrless}} \beta. \tag{5.34}$$

The form of the GLR detector is similar to the LR detector depicted in (5.13), except that in the GLR detector the value used to compare the threshold is maximized over the region of delay-time uncertainty. This operation can be achieved by inserting a duration-limited peak detector after video detection of the output from each individual matched filter.

Similar to Section 5.2.1, the detection problem for a multi-component target with unknown phases and positions can be extended to 2-D polarimetric radar signals. The formulation for the binary hypothesis test is almost identical to (5.25) and (5.26), except the time-shifts m_i and τ_i for each component are now random variables, rather than known constants, because each component center-location (Δ_x^i, Δ_y^i) is now uniformly distributed within its given uncertainty area. The GLR detector for the 1-D signal case can also be extended to a detector for the 2-D radar return. For the 2-D GLR detector, the whitening filter and the matched filter all operate on both range and cross-range times, and the peak detector exploits the maximum signal amplitude within the given 2-D uncertainty area rather than a 1-D interval. Figure 5.5 sketches the block diagram of the generalized-likelihood-ratio detector.

5.3.2 Receiver Operating Characteristic Evaluation

To calculate the detection and false-alarm probabilities for the 1-D generalized-likelihood-ratio detector, we define

$$x_m \equiv \max_{t_m \in [t_m^0 - T_m/2, t_m^0 + T_m/2]} \left| 2 \int_{-\infty}^{\infty} dt \; s_m^*(t - t_m) \cdot r(t) \right| \tag{5.35}$$

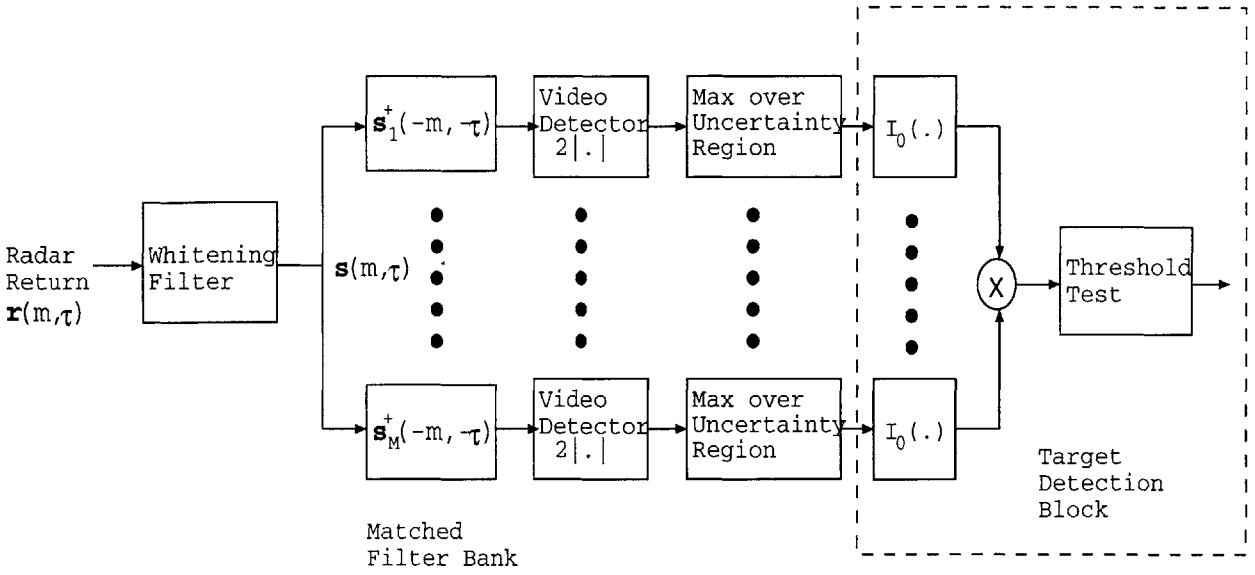

Figure 5.5 Generalized-likelihood-ratio detector for the multi-component target with unknown phases and positions.

for $m = 1, ..., M$. Because of the orthogonality condition that the target components satisfy, the $x_1, ..., x_M$ are conditionally independent, given either H_0 or H_1. The probability of detection is therefore (see (5.16))

$$\begin{aligned} P_D &= \Pr(\text{say} H_1 \mid H_1 \text{true}) \\ &= 1 - \int_0^{I_0^{-1}(\beta)} dy_1 \; p_{x_1|H_1}(y_1|H_1) \int_0^{I_0^{-1}(\beta/I_0(y_1))} dy_2 \; p_{x_2|H_1}(y_2|H_1) .... \\ &\quad \times \int_0^{I_0^{-1}(\beta/\prod_{m=1}^{M-1} I_0(y_m))} dy_M \; p_{x_M|H_1}(y_M|H_1), \end{aligned} \tag{5.36}$$

and the probability of false alarm is (see (5.17))

$$\begin{aligned} P_F &= \Pr(\text{say} H_1 \mid H_0 \text{true}) \\ &= 1 - \int_0^{I_0^{-1}(\beta)} dy_1 \; p_{x_1|H_0}(y_1|H_0) \int_0^{I_0^{-1}(\beta/I_0(y_1))} dy_2 \; p_{x_2|H_0}(y_2|H_0) .... \\ &\quad \times \int_0^{I_0^{-1}(\beta/\prod_{m=1}^{M-1} I_0(y_m))} dy_M \; p_{x_M|H_0}(y_M|H_0). \end{aligned} \tag{5.37}$$

The conditional probability density functions $p_{x_m|H_0}(y_m|H_0)$ and $p_{x_m|H_1}(y_m|H_1)$ can be obtained by taking the derivatives of the conditional cumulative probability functions; in other

words,

$$p_{x_m|H_0}(y_m|H_0) = \frac{d}{dy_m} \Pr\{x_m \le y_m|H_0\}$$

$$= \frac{d}{dy_m} \Pr\left\{ \max_{t_m \in [t_m^0 - T_m/2, t_m^0 + T_m/2]} \left| 2\int_{-\infty}^{\infty} dt\ s_m^*(t - t_m) \cdot w(t) \right| \le y_m \right\}, \tag{5.38}$$

$$p_{x_m|H_1}(y_m|H_1) = \frac{d}{dy_m} \Pr\{x_m \le y_m|H_1\}$$

$$= \frac{d}{dy_m} \Pr\left\{ \max_{t_m \in [t_m^0 - T_m/2, t_m^0 + T_m/2]} \left| 2\int_{-\infty}^{\infty} dt\ s_m^*(t - t_m) \cdot [\sum_{i=1}^{M} e^{i\phi_i} s_i(t - t_i) + w(t)] \right| \le y_m \right\}. \tag{5.39}$$

The receiver operating characteristic for the 2-D generalized likelihood-ratio detector can also be calculated by applying (5.36) through (5.39) by replacing the integral over t by an integral over τ followed by summations over m and polarization, and then performing the maximization operations over the 2-D uncertainty areas rather than 1-D uncertainty intervals.

The calculation of the conditional cumulative probability functions in (5.38) and (5.39) is not as straightforward as what has been done in Section 5.2.1, because it involves the level-crossing theory for a complex random field. As implied by (5.38) and (5.39), to obtain P_D and P_F for the 1-D (2-D) detection problem it suffices to solve the following general level-crossing problem: for a complex 1-D (2-D) random process $z(t)$ ($z(m, \tau)$) with a given covariance function and a fixed threshold level a, what is the probability that $|z(t)|$ ($|z(m, \tau)|$) is smaller than a for all the t (m, τ) within a known interval (area). For the problem of concern in this Section, the random process is the output signal from the matched filter (corresponding to an individual component) of the generalized-likelihood-ratio detector. When the target is absent, this random process is approximately stationary; when the target is present, it is non-stationary. As a result we ought to consider the level-crossing problems for H_0 and H_1 separately.

5.3.2.1 1-D Level-Crossing Theory

The level-crossing theory for a 1-D stationary random process has been intensively studied. Helstrom [31] and Bello [32] have provided lists of relevant literature citations. Siegert presented a general solution for the first-passage-time probability density of a real Markov process $r(t)$, which is defined as minus the time derivative of the probability $P(T;a)$ that $r(t)$ is below the threshold a throughout the interval [33]. It turns out that the Laplace transform of the first-passage-time probability density with a given initial condition $r(0) = r_0$ is the ratio of the Laplace transform of $r(t)$'s transition probability density functions at initial condition $r(0) = r_0$ to the corresponding transform at initial condition $r(0) = a$. For a real-valued Gauss-Markov process, or a complex-valued Gauss-Markov process with mutually independent real and imaginary parts, analytical expressions for the first-passage-time probability density can be obtained from Siegert's theory [34-36] when the process's autocovariance function is a two-sided exponential.

In general, the exact analytical solution for the probability $P(T;a)$ of a non-Markov stationary process $r(t)$ is not available. However, Rice has demonstrated that when the threshold level a is much larger than the root-mean-square of the process and the interval duration T is much greater than the correlation time of the process, $P(T;a)$ can be approximated by a simple formula [31][37]. The basic idea of this approach is to calculate the average rate at which the stochastic process crosses the threshold level from below, and then to use this rate to obtain the probability $P(T;a)$. When the interval duration T is much longer than the correlation time, the process has negligible correlation with its initial value and initial time derivative throughout most of the duration-T interval. So $P(T;a)$ is almost independent of the initial condition. Thus one can define an average rate $\lambda(a)$ as the average number of $r(t)$ upward crossings of the level a per unit time. For a stationary process, such rate is independent of time. Furthermore, when the threshold level is very high, upward crossings are rare events. Their occurrences are very far apart hence they can be taken to be

statistically independent. Thus the number of upward crossings in an interval of duration T, $n(T;a)$ can be modeled as a Poisson process [38]. The probability $P(T;a)$ that the process is below the threshold level a throughout an interval of duration T, is then equivalent to the probability that a Poisson-distributed variable with mean $\lambda(a)$ is zero, i.e.,

$$P(T;a) \approx e^{-\lambda(a)T}. \tag{5.40}$$

Equation (5.40) reduces the computation of $P(T;a)$ to the calculation of the crossing rate $\lambda(a)$ of the stochastic process. For a stationary process $r(t)$, Rice proposed the following approximate formula for $\lambda(a)$ [37]:

$$\lambda(a) \approx \int_0^\infty d\dot{r}\ p(a,\dot{r}), \tag{5.41}$$

where $\dot{r} = dr/dt$ and $p(r,\dot{r})$ is the joint probability density function of r and $\dot{r}$.

The task of obtaining $P(T;a)$ is to evaluate the integral in (5.41). Suppose the complex random process of concern is a Gaussian process $z(t) = x(t)+iy(t)$, with covariance functions

$$< z(t)z^*(t') >= u(t-t'), \qquad < z(t)z(t') >= 0. \tag{5.42}$$

Then $x(t)$ and $y(t)$ are independent Gaussian processes with the same covariance function $u(t)/2$. Whenever $|z(t)|$ is above (below) the threshold level a, we have that $r(t) = [x(t)]^2 + [y(t)]^2$ is also above (below) the threshold level a^2. Notice that r, the sum of the squares of two independent identically distributed Gaussian processes has a chi-square distribution, and the conditional density for $\dot{r}$, which is equal to $2x\dot{x} + 2y\dot{y}$, is Gaussian given x and y. One can then use these facts along with the Bayes rule to derive the joint probability density function $p(r,\dot{r})$, and hence obtain $\lambda(a)$ via (5.41). It can be shown that [31]

$$\lambda(a) \approx \beta \left[\frac{a^2}{\pi u(0)}\right]^{1/2} \exp\left[-\frac{a^2}{\pi u(0)}\right], \tag{5.43}$$

where

$$\beta^2 = \frac{|u''(0)|}{|u(0)|} \tag{5.44}$$

and $u''(t) = d^2u/dt^2$. The time-domain representation of β can be converted to a frequency-domain representation:

$$\beta^2 = \frac{\left|\int_{-\infty}^{\infty} d\Omega\ \Omega^2 U(\Omega)\right|}{\left|\int_{-\infty}^{\infty} d\Omega\ U(\Omega)\right|}, \tag{5.45}$$

where $U(\Omega)$ is the Fourier transform of $u(t)$. Notice that $1/\beta$ is, in essence, the correlation time of the process. When the covariance $u(t) = Ae^{-(t/t_l)^2}$, β is equal to $\sqrt{2}/t_l$.

To sum up, for a zero-mean circulo-complex Gaussian process $z(t)$ with covariance function $u(t)$, the probability $P(T;a)$ that $|z(t)|$ is below a threshold level a throughout an interval with duration T is approximately

$$P(T;a) \approx \exp\left\{-\beta T\sqrt{\frac{a^2}{\pi u(0)}}\exp\left[-\frac{a^2}{u(0)}\right]\right\} \tag{5.46}$$

when $\beta T >> 1$ and $a^2 >> u(0)$, where

$$\beta^2 = \frac{|u''(0)|}{|u(0)|} = \frac{\left|\int_{-\infty}^{\infty} d\Omega\ \Omega^2 U(\Omega)\right|}{\left|\int_{-\infty}^{\infty} d\Omega\ U(\Omega)\right|}. \tag{5.47}$$

5.3.2.2 Resolution-Bin Model

There is another approach to approximate the value of $P(T;a)$. In the laser-radar literatures, it is a common practice to apply the resolution-bin model to calculate the level-crossing probabilities [39]. The basic idea is to divide the interval of concern, $[0,T]$, into a sequence of N resolution bins with center locations t_1, t_2, ..., t_N, where the bin size is on the order of the correlation time for the random process under consideration. Then it is reasonable to approximate the probability that the real random process $r(t)$ is smaller than a within the whole interval $[0,T]$ by the joint probability that $r(t_1) < a$, $r(t_2) < a$, ..., and $r(t_N) < a$. Furthermore, if the bin size is not significantly smaller than the correlation length, then the random variables $r(t_1)$, $r(t_2)$, ..., $r(t_N)$ can be taken, approximately, to be statistically independent. The joint level-crossing probability is then the product of level-crossing probabilities for each individual sample point. For a stationary random process, $r(t_1)$, $r(t_2)$,

...., and $r(t_N)$ have the same probability density function. The resulting joint level-crossing probability is then the N^{th} power of a sample point's level-crossing probability. In other words,

$$P(T;a) = \Pr\{r(t) < a; 0 \le t \le T\} \approx \Pr\{r(t_1) < a \ \& \ r(t_2) < a \ \& \ .... \ \& \ r(t_N) < a\}$$

$$\approx \prod_{i=1}^{N} \Pr\{r(t_i) < a\} = [\Pr\{r(t_i) < a\}]^N. \tag{5.48}$$

For a zero-mean circulo-complex Gaussian process $z(t)$ with covariance function $u(t)$, the approximate probability $P(T;a)$ that $|z(t)| < a$ within $[0,T]$ can also be obtained from the resolution bin model via (5.48). To calculate the probability that $|z(t_i)| < a$, the chi-square distribution is applied. The result of the probability $P(T;a)$ is

$$P(T;a) \approx \{1 - \exp\left[-\frac{a^2}{u(0)}\right]\}^{T/t_{bin}}, \tag{5.49}$$

where t_{bin} is the bin duration. Notice that (5.49) gives a different formula for $P(T;a)$ than the analytical result in (5.46).

The validity of the resolution-bin approach depends on two conditions. The first is that a sample point chosen a priori from a bin interval can well represent the level-crossing characteristic of the whole bin interval, i.e., if any point within the bin exceeds the threshold level, it must be almost the case that the chosen sample point exceeds the threshold level as well. The second is that the correlation among the sample points representing different resolution bins is small. Both conditions are determined by the size of the bin t_{bin}. The analytical form of the optimum t_{bin} that best fits (5.49) to the actual level-crossing probability is not available. But one can obtain its approximate numerical value by fitting (5.49) to the level-crossing probability from Monte Carlo simulations.

We have two reasons for presenting the resolution-bin approach for the level-crossing problem. First, the result from the resolution-bin approximation can be very useful when the duration of the uncertainty interval T is not much longer than the correlation length of the

random process; this is a case in which the analytical level-crossing theory is not applicable. Second, in the limit when the interval duration is much longer than the correlation time, so that the analytical formula (5.46) is more accurate than the approximate result (5.49), the resolution-bin approach *per se* provides an interpretation for (5.46) that is important to our extension of level-crossing theory from 1-D to 2-D. The approach we will take is a Markovian representation of the level-crossing probability. Suppose the interval $[0, T]$ is divided into a sequence of bins $I_1 = [0, t_{bin}]$, $I_2 = [t_{bin}, 2t_{bin}]$, ..., $I_N = [(N-1)t_{bin}, T]$, where the bin size t_{bin} is identical to the correlation time of the random process and $N = T/t_{bin}$. Then, via Bayes' rule, the level-crossing probability $P(T; a)$ can be represented as the following product of conditional probabilities:

$$\begin{aligned} P(T;a) &= \Pr\{|z(t)| < a : 0 \le t \le T\} = \Pr\{|z(t)| < a : t \in I_1 \ \& \ t \in I_2 \ \& \ .... \ \& \ t \in I_N\} \\ &= \Pr\{|z(t)| < a : t \in I_1\} \times \Pr\{|z(t)| < a : t \in I_2 \mid |z(t)| < a : t \in I_1\} \\ &\times \Pr\{|z(t)| < a : t \in I_3 \mid |z(t)| < a : t \in I_1 \ \& \ t \in I_2\} \times ..... \\ &\times \Pr\{|z(t)| < a : t \in I_N \mid |z(t)| < a : t \in I_1 \ \& \ .... \ \& \ t \in I_{N-1}\}. \end{aligned} \tag{5.50}$$

Because each bin's duration is one correlation time, the behavior of the random process within bin I_i is almost statistically independent of the behaviors within any other bins except I_{i-1} and I_{i+1}. Therefore, the Bayesian representation (5.50) can be rewritten in a more concise form:

$$P(T;a) \approx \Pr\{|z(t)| < a : t \in I_1\} \cdot \prod_{i=1}^{N-1} \Pr\{|z(t)| < a : t \in I_{i+1} \mid |z(t)| < a : t \in I_i\}. \tag{5.51}$$

When the random process is stationary, the conditional probability $\Pr\{|z(t)| < a : t \in I_{i+1} \mid |z(t)| < a : t \in I_i\}$ is the same for all bins. Thus

$$P(a;T) \approx \Pr\{|z(t)| < a : t \in I_1\} \cdot [\Pr\{|z(t)| < a : t \in I_{i+1} \mid |z(t)| < a : t \in I_i\}]^{N-1}. \tag{5.52}$$

When the interval T is much longer than the correlation length, $P(a;T)$ in (5.52) is dominated by the $(N-1)^{th}$ power of the conditional probability. the contribution of $\Pr\{|z(t)| <$

$a : t \in I_1\}$ is unimportant. Thus we can approximate $\Pr\{|z(t)| < a : t \in I_1\}$ by $\Pr\{|z(t)| < a : t \in I_{i+1} \mid |z(t)| < a : t \in I_i\}$, and get

$$P(a;T) \approx [\Pr\{|z(t)| < a : t \in I_{i+1} \mid |z(t)| < a : t \in I_i\}]^N. \tag{5.53}$$

Equation (5.53) indicates that an approximate evaluation of the probability that $|z(t)| < a$ within an interval with long duration T follows fairly easily from knowledge of the conditional probability that $|z(t)| < a$ within a correlation time, given the fact that $|z(t)| < a$ prevailed within the preceding correlation time. The formulation from analytical level-crossing theory (5.46) implies that

$$\Pr\{|z(t)| < a : t \in I_{i+1} \mid |z(t)| < a : t \in I_i\} \approx \exp\left\{-\beta t_{corr}\sqrt{\frac{a^2}{\pi u(0)}}\exp\left[-\frac{a^2}{u(0)}\right]\right\}, \tag{5.54}$$

where t_{corr} is the correlation time of $z(t)$. For simplicity, we use $\Pr\{I_{i+1}|I_i\}$ to denote the probability in (5.54). Similarly, we use $\Pr\{t_i\}$ to denote the probability that $|z(t_i)| < a$, where t_i is the midpoint of I_i. The chi-square density of $|z|$ implies that

$$\Pr\{t_i\} = 1 - \exp\left[-\frac{a^2}{u(0)}\right]. \tag{5.55}$$

When the probability of crossing from below is very low ($a^2 >> u(0)$),

$$\Pr\{t_i\} = \exp\left\{\log\left[1 - \exp\left[-\frac{a^2}{u(0)}\right]\right]\right\} \approx \exp\left\{\exp\left[-\frac{a^2}{u(0)}\right]\right\}. \tag{5.56}$$

Comparing (5.56) with (5.54), a simple relation between $\Pr\{t_{i+1}\}$ and $\Pr\{I_{i+1}|I_i\}$ can be obtained when $a^2 >> u(0)$,

$$\Pr\{I_{i+1}|I_i\} \approx [\Pr\{t_{i+1}\}]^{\beta t_{corr}\sqrt{a^2/\pi u(0)}}. \tag{5.57}$$

This relation will be the basis for our extension of 1-D level-crossing theory to the 2-D problem.

5.3.2.3 2-D Level-Crossing Theory

The level-crossing problem whose solution determines the SAR receiver operating characteristics we need in this chapter is 2-D rather than 1-D. For simplicity, let us at first assume that both the range-time index and the cross-range-time index of the radar return signal are continuous. So in order to evaluate P_F, we need to solve the following problem. For a stationary zero-mean circulo-complex Gaussian process $z(x, y)$ with covariance function $u(x, y)$, what is the probability $P(A; a)$ that $|z(x, y)|$ is below a threshold level a for all (x, y) within a 2-D region A. To simplify the derivation, we assume that A is a rectangular region $A = \{(x, y) : 0 \leq x \leq X, 0 \leq y \leq Y\}$.

Some prior work has been done on the theory of level crossing for a 2-D random field [32]. Longuet-Higgins analyzed a variety of geometrical characteristics of a 2-D Gaussian stationary random field, such as the average of number of zero crossings along a line, the average length per unit area of contours generated by some fixed level of the field, and the average number density of relative maxima, minima, saddle points [40]. Kessler and Freund studied the probability density of level crossings along specific directions in an isotropic 2-D Gaussian random field [41]. Adler and Hasofer defined the excursion set associated with a random field in a multi-dimensional space, and constructed the characteristic of the excursion set, which is related to its number of connected components. Cast into the 1-D case, such characteristic represents the number of crossings from below [42]. However, to the author's knowledge, no prior studies provide a direct answer to the probability of level crossings of the 2-D circulo-complex Gaussian random process within a given area.

In this Section, we propose formulations to evaluate the 2-D level-crossing probability. The formulations are derived from heuristic extension of the 1-D level-crossing theories presented in Section 5.3.2.1 and Section 5.3.2.2, and are verified by comparing with the results from Monte Carlo simulations. We consider first the case in which X and Y are much longer than the $x-$ and $y-$ correlation lengths of the random process. The basic

idea is similar to the discussion at the end of Section 5.3.2.2. As indicated in Figure 5.6, the rectangular uncertainty area A is divided into a sequence of strips $\{J_i\}_{i=1}^{N}$, where $J_i = \{(x,y) : (i-1)x_{corr} \leq x \leq ix_{corr}, 0 \leq y \leq Y\}$, and x_{corr} is the correlation length of $z(x,y)$ along the x-direction. Following the argument given in Section 5.3.2.2, the probability that $|z(x,y)|$ is below the level a within the whole region of A can be approximated by a product of conditional probabilities:

$$P(a;X,Y) \approx [\Pr\{|z(x,y)| < a : (x,y) \in J_{i+1} \mid |z(x,y)| < a : (x,y) \in J_i\}]^{N_x}, \tag{5.58}$$

where $N_x = X/x_{corr}$. Also, the conditional probability $\Pr\{|z(x,y)| < a : (x,y) \in J_{i+1} \mid |z(x,y)| < a : (x,y) \in J_i\}$ may be obtained via a formulation similar to that used for its 1-D counterpart. In (5.57), the conditional probability that the amplitude of the 1-D random process is smaller than a level within a bin interval, given the fact that it is below the level within the previous bin interval, is a function of the probability that the amplitude is smaller than the level at the center point of the bin interval under consideration. Here we argue that the same relation holds for a 2-D random field. In other words,

$$\Pr\{J_{i+1}|J_i\} \approx [\Pr\{x_{i+1}\}]^{\beta_x x_{corr}\sqrt{a^2/\pi u(0,0)}}, \tag{5.59}$$

In (5.59), $\Pr\{J_{i+1}|J_i\} \equiv \Pr\{|z(x,y)| < a : (x,y) \in J_{i+1} \mid |z(x,y)| < a : (x,y) \in J_i\}$, $\Pr\{x_{i+1}\} \equiv \Pr\{|z(x,y)| < a : x = (i-1/2)x_{corr}, 0 \leq y \leq Y\}$, and

$$\beta_x^2 = \frac{|u_{xx}(0,0)|}{|u(0,0)|}, \tag{5.60}$$

where $u_{xx}(x,y) = (\partial^2/\partial x^2)u(x,y)$. Notice that $\Pr\{x_{i+1}\}$ is the probability of no crossing from below along a line parallel to y axis with length Y. Such probability can also be calculated from the analytical formula (5.46). Hence

$$\Pr\{x_{i+1}\} \approx \exp\left\{-\beta_y Y\sqrt{\frac{a^2}{\pi u(0,0)}}\exp\left[-\frac{a^2}{u(0,0)}\right]\right\}, \tag{5.61}$$

where

$$\beta_y^2 = \frac{|u_{yy}(0,0)|}{|u(0,0)|}, \tag{5.62}$$

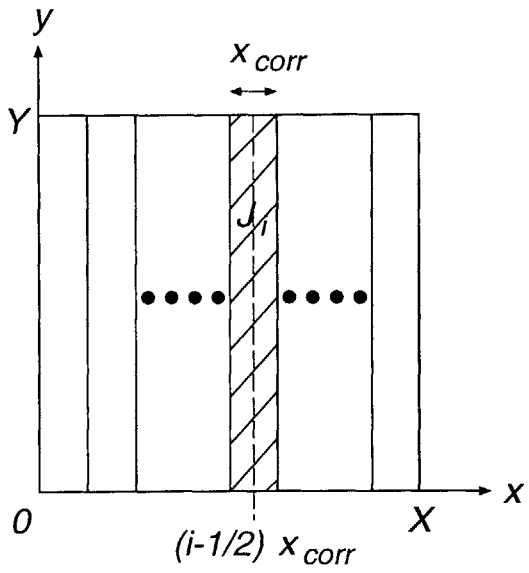

Figure 5.6 The strip-bin division of the uncertainty area for the 2-D random field.

for $u_{yy}(x,y) = (\partial^2/\partial y^2)u(x,y)$. Plugging (5.61) into (5.59) and then (5.59) into (5.58), we have a formula for the 2-D level-crossing probability:

$$P(a;X,Y) \approx \exp\left\{-\beta_x\beta_y XY\frac{a^2}{\pi u(0,0)}\exp\left[-\frac{a^2}{u(0,0)}\right]\right\}. \tag{5.63}$$

Equation (5.63) is a consistent formulation for the 2-D level-crossing probability in two senses. First, equation (5.57) asserts that the "interval probability" p_i (the conditional probability that a random process is below the threshold level within an interval) and the "point probability" p_p (the probability that it is below the threshold level at a point) have a power relation $p_i = p_p^Q$. It can be shown that the same power relation would hold for the "strip probability" p_s (the conditional probability that it is below the threshold level within a strip) and the "line probability" p_l (the probability that it is below the threshold level along a line) if the relations between p_s and p_i and between p_l and p_p are identical power-law forms, namely, $p_s = p_i^R$ and $p_l = p_p^R$. From the 1-D level-crossing theory, p_l and p_p satisfy this power-law condition. We may also argue that the same relation must be approximately true for p_s and p_i, because a strip can be conceived as a collection of intervals and a line as a collection of points. Second, if we derive the 2-D level-crossing probability from the

conditional probabilities of the strips along the x direction, the result would be identical to the one in (5.63). As a matter of fact, (5.63) suggests that the probability is function of the area of the uncertainty region; the direction of the vector $\hat{x}X + \hat{y}Y$ should be unimportant.

When the dimensions of the uncertainty region is not much larger than the correlation lengths of the random process, the formula (5.63) does not apply. In this case, the level-crossing probability is approximated by the resolution-bin approach, where the 1-D bin interval is replaced by the 2-D cell area. From (5.49), it can be shown that

$$P(X, Y; a) \approx \{1 - \exp\left[-\frac{a^2}{u(0,0)}\right]\}^{XY/x_{bin}y_{bin}}, \tag{5.64}$$

where x_{bin} and y_{bin} are bin sizes along x and y directions.

We verified our 2-D level-crossing probability formulas (5.63) and (5.64) by comparing them with the results from Monte Carlo simulations. The parameters chosen for the simulations were as follows. The complex stationary 2-D random field $z(x, y)$ was modeled as a zero-mean, circulo-complex Gaussian process with a Gaussian-shaped, separable covariance function

$$< z(x,y)z^*(x',y') >= u(x-x', y-y') = A\exp[-(x-x')^2/x_l^2]\exp[-(y-y')^2/y_l^2], \tag{5.65}$$

where $x_l = x_{corr}/2$ and $y_l = y_{corr}/2$ are the half correlation lengths. The correlation lengths along the two orthogonal directions were assumed to be equal, and sampling periods $x_l/10$ along the x direction and $y_l/10$ along the y direction were used. The edge lengths of the uncertainty region, namely X and Y, were also assumed to be identical. The number of realizations for the profiles of $z(x, y)$ was 1000. To generate a realization of $z(x, y)$, we first generated a complex Gaussian random profile whose value at each point on the 2-D plane was uncorrelated with its value at any other point (i.e., a white-Gaussian process), and then passed this 2-D signal through a shaping filter to form a 2-D signal with the prescribed spectrum (the Fourier transform of (5.65)). The white Gaussian complex random profile

was generated by independently producing the complex value at each point from magnitude and phase random variables that followed Rayleigh and uniform distributions, respectively. The fraction of realizations whose maximum $|z(x,y)|$ within the uncertainty region exceeded different threshold levels were then recorded, for comparison with our theoretical work.

Figure 5.7 plots the probability of level-crossing versus the threshold level for different sizes of the uncertainty region. In the figure, the Monte Carlo simulation results are compared with the values from formulations (5.63) and (5.64). For a covariance function with a separable and Gaussian form in (5.65), we find that (5.63) can be written as

$$P(a;X,Y) \approx \exp\left\{-\frac{X}{x_l}\frac{Y}{y_l}\frac{2a^2}{\pi u(0,0)}\exp\left[-\frac{a^2}{u(0,0)}\right]\right\}. \tag{5.66}$$

For the curves corresponding to (5.64), the bin sizes are identical along x and y directions, and optimized to get the best fit for the Monte Carlo simulation results. The four panels of the figure correspond to the cases when $X/x_l = Y/y_l = 2.0$, 4.0, 8.0 and 16.0. In other words, the edge length is one, two, four, and eight times the correlation length. From Figure 5.7, it is clear that (5.63), as an extension of the 1-D level-crossing theory to the 2-D cases, reasonably matches the Monte Carlo simulation results when the probability of crossing-from-below is not too large. Therefore, (5.63) is a valid formula for 2-D level-crossing probability. When the size of the uncertainty region becomes smaller, it is the optimized resolution-bin approximation (5.64) that has a better fit to the simulation results. Figure 5.8 plots the optimized bin size of (5.64) for different sizes of uncertainty region, and Figure 5.9 plots the average error of the 2-D level-crossing formula (5.63) and resolution-bin formula (5.64) with respect to the Monte Carlo simulation results for different sizes of uncertainty region. From the figure, when $X/x_l = Y/y_l$ is equal to or smaller than 1, (5.63) has a significantly higher error compared with (5.64). Therefore, in the rest of this thesis, we will apply (5.63) when the edge length of the uncertainty region is larger than the correlation length, and (5.64) when the edge length of the uncertainty region is less than the correlation length.

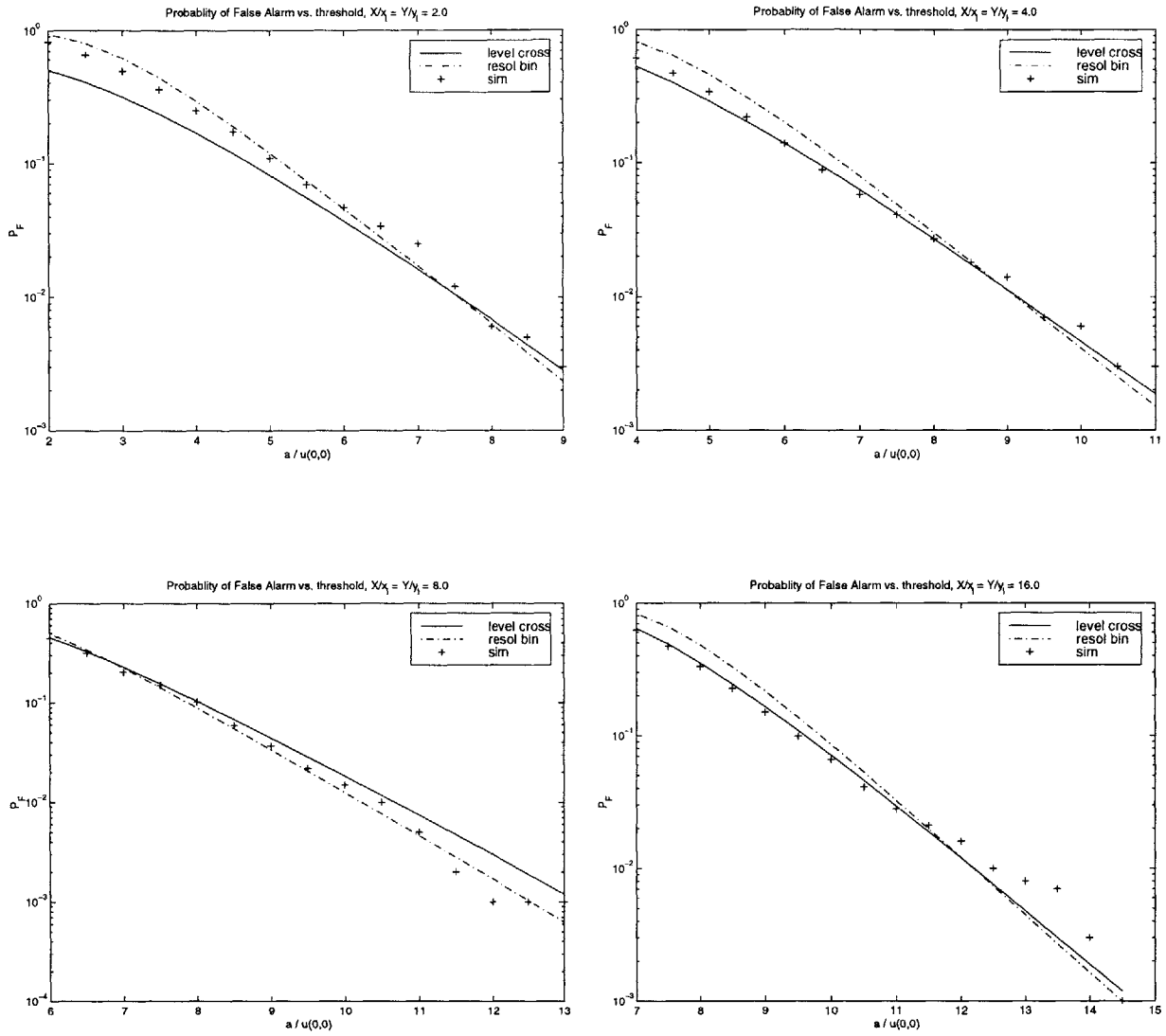

Figure 5.7 Comparison of the Monte Carlo simulation results with the 2-D level-crossing formulations (5.63) and (5.64). The covariance function of the complex random process is described in (5.65). The panels from top to bottom: $X/x_l = Y/y_l = 2.0$, 4.0, 8.0 16.0. For each panel, the horizontal axis stands for the threshold level, and the vertical axis stands for the probability that the intensity of the complex random process exceeds the threshold (in log scale). Notice that the bin sizes of (5.64) along x and y directions are equal and optimized to fit the simulation results.

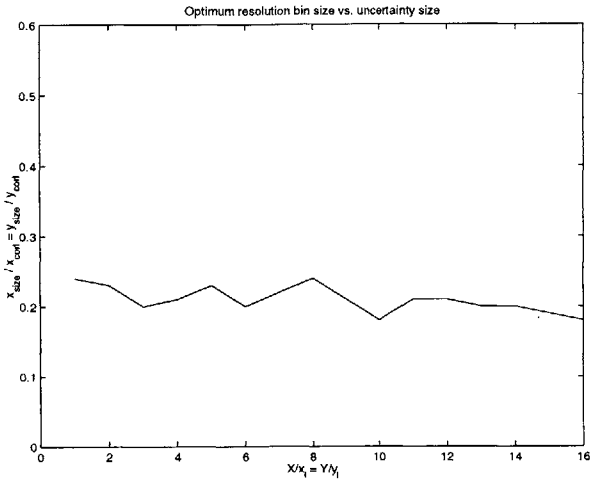

Figure 5.8 The optimized bin size of (5.64) for fitting the simulation results versus the size of uncertainty region.

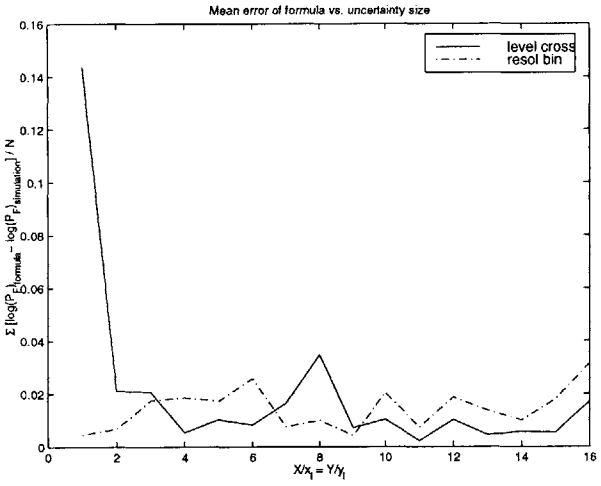

Figure 5.9 The average errors of (5.63) and (5.64) with respect to the Monte Carlo simulation results versus the size of uncertainty region. The average error is defined as the mean of the difference for the log of probability from simulation and the log of probability from formula.

5.3.2.4 Evaluation of P_D

The analytical level-crossing theory associated with the calculation of P_D is more difficult to obtain, since the random process of concern is not stationary when the target return is present. However, when the signal-to-noise-plus-clutter-ratio is high, a simple approximation can be applied to evaluate P_D: the probability that the maximum intensity of the output within the uncertainty region exceeds the threshold level is equal to the probability of detection for the same threshold level and the same target return with known position [31]. The justification for this approximation is as follows. When a strong target return is present, the peak value of the output from each component's matched filter occurs at a position very close to the true position of this component. When such peak is well above the threshold level and the noise fluctuation is much smaller than the peak strength, it is unlikely that the noise will cause the output to fall below the threshold level. In other words, once the output maximum within the uncertainty region exceeds the threshold level, its sample at the target's true position must also exceed this level. Therefore, we can directly apply (5.16) to calculate P_D.

5.3.3 Performance Analysis

In this section, we present the receiver operating characteristic for detecting targets with independent component-position uncertainties. The multi-component targets of concern are similar to those described in Section 5.2.2. But here the center location of every target component is not deterministic and exactly known. Instead, it is uniformly distributed within a given uncertainty region. To be more specific, the first target consists of three identical square specular reflectors each with edge length $2\rho_t$, and the second target consists of two identical square specular reflectors each with edge length $2\rho_t$ and a square dihedral reflector with edge length $\sqrt{2}\rho_t$, where $\rho_t = 0.5$ m. For both targets, the center locations of the first, second, and third components are uniformly distributed within given square uncertainty

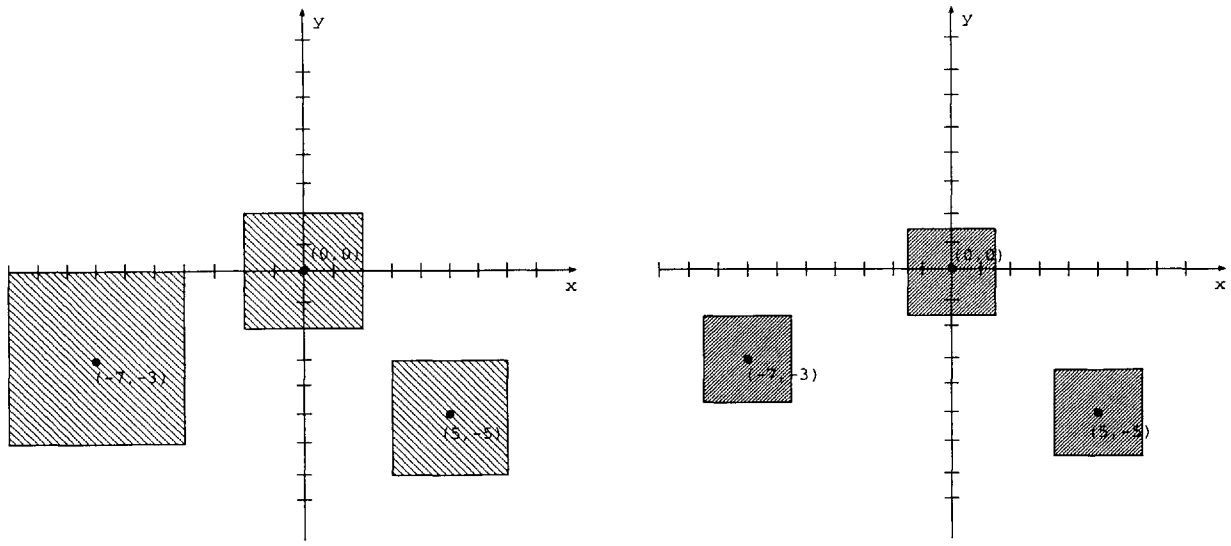

Figure 5.10 Specifications for the uncertainty-region geometries. Left panel: uncertainty specification 1. Right panel: uncertainty specification 2. Notice that $(0, 0)$ is the scene center of the antenna footprint area. The aircraft flies along the x direction.

regions centered at $(0, 0), (-7, -3), (5, -5)$ with respect to scene center. In this section, we consider two sets of specifications for the dimensions of these uncertainty regions. In the first set, the edge lengths of the square uncertainty regions for components 1, 2, and 3 are 4 m, 6 m, and 4 m, respectively. In the second set, the edge lengths of the square uncertainty regions for components 1, 2, and 3 are 3 m, 3 m, and 3 m, respectively. Figure 5.10 plots these two uncertainty specifications. All the other parameter values, including target component orientations, signal-to-noise-plus-clutter-ratio, flight parameters, and radar parameters, are the same as those specified in Section 5.2.2.

For both specifications in Figure 5.10, the separations among the uncertainty regions of the three components are large enough that the minimum possible distance between any pair of components still exceeds the sum of the half-resolution lengths of their corresponding image spots after the matched filters. In other words, the output image spots still do not overlap, even though their locations are allowed to vary within different uncertainty regions. Therefore, the orthogonality condition (5.27) still applies. Furthermore, in Figure 5.10, the

dimensions of the uncertainty regions along both x and y directions are more than twice the correlations lengths of the random field after the matched filter, which are the image resolution lengths of the corresponding target components. Therefore we use the 2-D level-crossing formula (5.63) to calculate the probability of false alarm.

Figure 5.11 plots the receiver operating characteristics of the likelihood-ratio detectors for the first example target. Figure 5.12 plots the receiver operating characteristics of the same detectors for the second example target. Again, in each figure, both the results from stripmap-mode and spotlight-mode operations are presented. There are three curves in each panel, corresponding to the behavior of the likelihood-ratio detector for the multi-component target with no position uncertainty, the generalized likelihood-ratio detector for the multi-component target with position uncertainty specification 1 in Figure 5.10, and the generalized likelihood-ratio detector for the multi-component target with position uncertainty specification 2 in Figure 5.10. The numerical results in Figures 5.11 and 5.12 are consistent with intuition: (i) when the precise information on the target components' locations is lost, the detection performance of the generalized likelihood-ratio detector is degraded; (ii) the larger the uncertainty regions are, the greater this degradation becomes. In addition, we see that the ROC curves in Figures 5.11 and 5.12 that correspond to the stripmap-mode and spotlight-mode operations have different slopes. This is a consequence of different target-return spectra (along the cross-range direction) between the two synthetic-aperture operations.

5.4 Multi-Component Target Detection with Unknown Phases, Positions, and Amplitudes

In this section, we consider a multi-component target where the phases, locations, and scattering amplitudes of individual components are randomly and independently varied. Similar to Section 5.3.1, we develop a generalized likelihood-ratio target detector for this

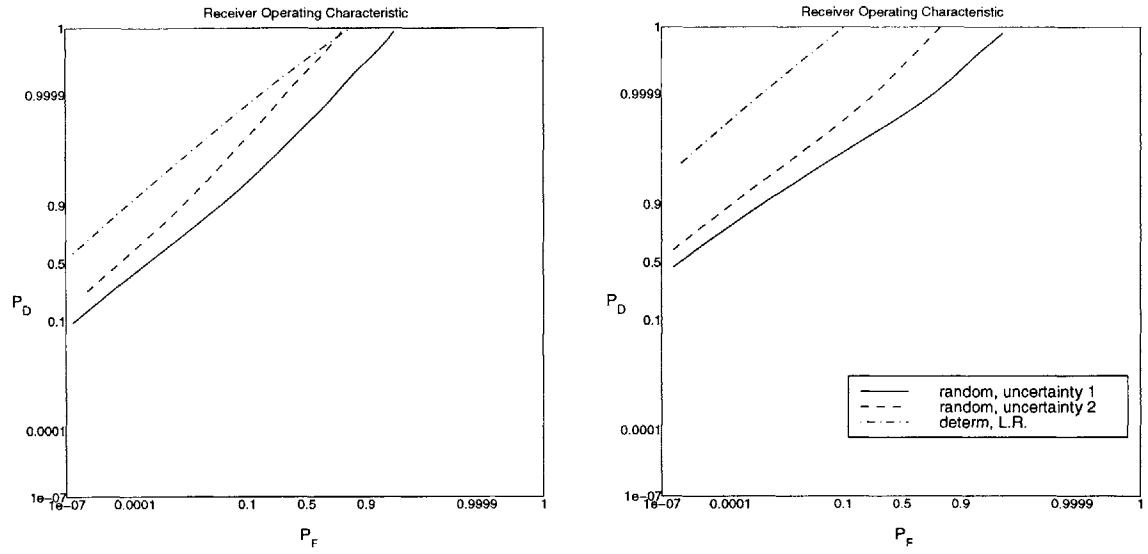

Figure 5.11 Receiver operating characteristics: 3 specular reflectors; likelihood-ratio detector for target with no position uncertainty, generalized likelihood-ratio detector for target with position uncertainty specification 1, generalized likelihood-ratio detector for target with position uncertainty specification 2. Left panel is stripmap-mode operation; right panel is spotlight-mode operation.

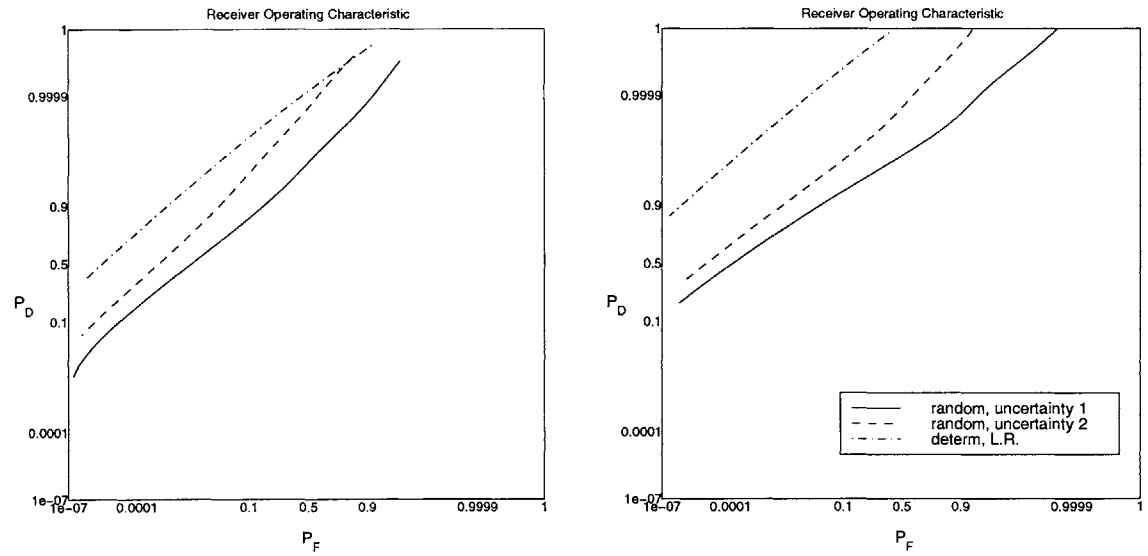

Figure 5.12 Receiver operating characteristics: 2 specular reflectors and 1 dihedral reflector; same arrangement as Figure 5.11.

scenario by building up from the 1-D radar model. The binary hypothesis for the scalar 1-D radar return in this case is the following. We observe

$$r(t) = w(t), \tag{5.67}$$

when the target is absent (hypothesis H_0), and we observe

$$r(t) = \sum_{m=1}^{M} A_k e^{i\phi_m} s_m(t - t_m) + w(t), \tag{5.68}$$

when the target is present (hypothesis H_1). In (5.67) and (5.68), the pulse delay time and the scattering amplitude of the m^{th} component, t_m and A_m, are random. The random variables t_1, ..., t_M are assumed mutually independent, and each t_m is uniformly distributed within $[t_m^0 - T_m/2, t_m^0 + T_m/2]$. The random variables A_1, ..., A_M are also assumed to be independent, and also uniformly distributed within $[A_1^{min}, A_1^{max}]$, ..., $[A_M^{min}, A_M^{max}]$. The randomness of target component positions models the variability or unavailability of exact knowledge about some aspects of the target constellation. The scattering-amplitude randomness models the variability or unavailability of exact knowledge about some aspects of target geometry and material constitution, such as the shape of scatterers and the distribution of dielectric constants within the scattering body.

5.4.1 Detection Scheme

Paralleling the work in Section 5.3.1, we can derive a generalized likelihood-ratio for this binary hypothesis problem. First, the likelihood ratio for the binary conditions described in (5.67) and (5.68), given a specific set of values for the parameters $t_1, ..., t_M, A_1, ...A_M$, can be obtained as a straightforward extension of (5.30):

$$l(\mathbf{r}; t_1, ..., t_M, A_1, ..., A_M) = \frac{p_{\mathbf{r}|H_1}(r_1, r_2, ..., r_M | H_1; t_1, ..., t_M, A_1, ..., A_M)}{p_{\mathbf{r}|H_0}(r_1, r_2, ..., r_M | H_0; t_1, ..., t_M, A_1, ..., A_M)}$$

$$= \prod_{m=1}^{M} e^{-A_m^2 E_m} I_0 \left(2A_m \left| \int_{-\infty}^{\infty} dt s_m^*(t - t_m) \cdot r(t) \right| \right), \tag{5.69}$$

where

$$E_m \equiv \int_{-\infty}^{\infty} dt s_m^*(t) \cdot s_m(t). \tag{5.70}$$

Second, the maximum-likelihood estimate of the parameters $t_1, ..., t_M, A_1, ...A_M$ is the set of values $\hat{t}_1, ..., \hat{t}_M, \hat{A}_1, ...\hat{A}_M$, that maximizes $l(\mathbf{r})$ in (5.69). Thus the generalized likelihood ratio, which is defined as the likelihood ratio when the maximum-likelihood estimate values are plugged in for the unknown parameters, is:

$$\begin{aligned}
\text{GLR} &= l(\mathbf{r}; \hat{t}_1, ..., \hat{t}_M, \hat{A}_1, ..., \hat{A}_M) \\
&= \max_{t_1,...,t_M,A_1,...,A_M} \prod_{m=1}^{M} e^{-A_m^2 E_m} I_0 \left(2A_m \left| \int_{-\infty}^{\infty} dt s_m^*(t - t_m) \cdot r(t) \right| \right) \\
&= \prod_{m=1}^{M} \max_{t_m, A_m} e^{-A_m^2 E_m} I_0 \left(2A_m \left| \int_{-\infty}^{\infty} dt s_m^*(t - t_m) \cdot r(t) \right| \right).
\end{aligned} \tag{5.71}$$

The second equality of (5.71) follows because t_m's an A_m's for different m's are independent of one another.

The values $\hat{t}_m$ and $\hat{A}_m$ that maximize

$$f(t_m, A_m) = e^{-A_m^2 E_m} I_0 \left(2A_m \left| \int_{-\infty}^{\infty} dt s_m^*(t - t_m) \cdot r(t) \right| \right)$$

can be obtained separately. It can be shown that

$$\hat{t}_m = \arg\max_{t_m} \left| \int_{-\infty}^{\infty} dt s_m^*(t - t_m) \cdot r(t) \right| \tag{5.72}$$

A necessary condition that $\hat{A}_m$ must satisfy is that the partial derivative of $f(t_m, A_m)$ with respect to A_m be zero. This condition is also sufficient, because $f(t_m, A_m)$ is unimodal in t_m. We thus have that

$$2\hat{A}_m E_m I_0 \left(2\hat{A}_m |\hat{r}_m| \right) - 2|\hat{r}_m| I_0' \left(2\hat{A}_m |\hat{r}_m| \right) = 0, \tag{5.73}$$

where

$$\hat{r}_m \equiv \int_{-\infty}^{\infty} dt s_m^*(t - \hat{t}_m) \cdot r(t), \tag{5.74}$$

and $I_0'(x) \equiv dI_0(x)/dx$.

Equation (5.73) does not have a simple analytic solution. One has to solve for $\hat{A}_m$ numerically for each input waveform $r(t)$. Thus it is quite involved to implement the strict generalized likelihood-ratio detector. To simplify the problem, we adopt the approximation

$$I_0\left(2\hat{A}_m|\hat{r}_m|\right) \approx e^{2\hat{A}_m|\hat{r}_m|} \tag{5.75}$$

which applies when the signal-to-noise-plus-clutter-ratio is high [36]. Applying (5.75), we obtain the simple expression for $\hat{A}_m$:

$$\hat{A}_m \approx \frac{|\hat{r}_m|}{E_m}. \tag{5.76}$$

Plugging (5,72) into (5.74) and (5.74) into (5.76), we have

$$\hat{A}_m \approx \frac{1}{E_m} \max_{t_m} \int_{-\infty}^{\infty} dt s_m^*(t - \hat{t}_m) \cdot r(t). \tag{5.77}$$

Substituting (5.72) and (5.77) into (5.71), the approximate expression of the generalized likelihood ratio becomes:

$$\text{GLR} \approx \prod_{m=1}^{M} \exp\left\{ \frac{1}{E_m} \max_{t_m} \left| \int_{-\infty}^{\infty} dt s_m^*(t - \hat{t}_m) \cdot r(t) \right|^2 \right\}. \tag{5.78}$$

The approximate generalized likelihood ratio in (5.78) can be easily extended to the case of 2-D polarimetric radar signal by replacing the single integrals in (5.70) and (5.78) with double integrals and the scalar radar signal waveforms and matched filter impulse responses with their polarimetric versions, The block diagram of the approximate generalized likelihood-ratio detector, given in (5.78), for multi-component targets with unknown phases, positions, and amplitudes is plotted in Figure 5.13. As indicated in the figure, the complex multi-resolution images after the whitening filter and the matched-filter bank are passed through square-law detectors, peak detectors, and energy ($1/E_m$) normalization prior to being added together at the input to a level detector with threshold θ.

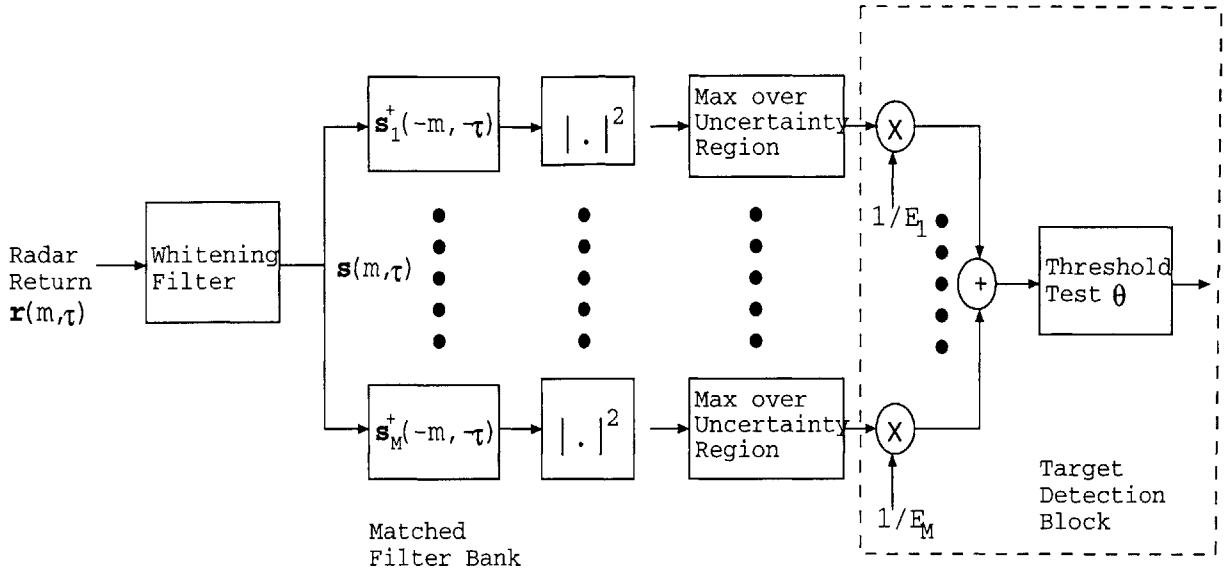

Figure 5.13 Generalized-likelihood-ratio detector for the multi-component target with unknown phases, positions, and amplitudes.

5.4.2 Performance Analysis

In this section, we calculate the receiver operating characteristic for the detector depicted in Section 5.4.1. First of all, we define

$$x_k \equiv \max_{m_k,\tau_k}\left[2\left|\sum_{m=-\infty}^{\infty}\int_{-\infty}^{\infty} d\tau \mathbf{s}_\mathbf{k}^\dagger(\mathbf{m}-\mathbf{m_k},\tau-\tau_\mathbf{k})\cdot\mathbf{r}(\mathbf{m},\tau)\right|\right]. \tag{5.79}$$

for each target component. Then the false-alarm probability of the approximate generalized likelihood-ratio detector for a given threshold θ is

$$P_F = \Pr\left\{\sum_{k=1}^{M}\frac{x_k^2}{4E_k} > \theta \mid H_0\right\}, \tag{5.80}$$

and the probability of detection is

$$P_D = \Pr\left\{\sum_{k=1}^{M}\frac{x_k^2}{4E_k} > \theta \mid H_1\right\}. \tag{5.81}$$

To calculate P_F, we apply the orthogonality condition to claim that when H_0 is true, the random variables x_1, x_2, ..., x_M are all independent of one another. So the joint probability

density function (pdf) can be expressed as the product of the individual pdf's, which gives a succinct representation of P_F:

$$P_F = 1 - \int_0^{\sqrt{4E_1\theta}} dx_1 p(x_1|H_0) \int_0^{\sqrt{4E_2[\theta-(x_1^2/4E_1)]}} dx_2 p(x_2|H_0)....$$

$$\times \int_0^{\sqrt{4E_M[\theta-(x_1^2/4E_1)-\cdots-(x_{M-1}^2/4E_{M-1})]}} dx_M p(x_M|H_0). \tag{5.82}$$

where the conditional pdf $p(x_k|H_0)$ is equal to the derivative of the level-crossing probability (5.63) or (5.64) in Section 5.3.2.3. Notice the parameters $u(0,0)$, β_x, and β_y are all determined by the impulse responses of the matched filters. In this section, their values are the same as those in Section 5.3.2.

To calculate P_D, we again apply the orthogonality condition to separate the joint conditional pdf. In addition, we use the same approximation as employed in Section 5.3.2.4, i.e., we assume that the probability the detector's output exceeds the threshold when a multi-component target with unknown phases, positions, and amplitudes is present is almost equal to the probability of exceeding the threshold when the same multi-component target with no position uncertainty is present. Thus we do not need to deal with the level-crossing theory of a non-stationary random field. The return-amplitude uncertainties, however, must be considered. This consideration is accomplished by weighting the probability of detection for a fixed amplitude target with the probability density functions for the return amplitudes and then integrating over all possible amplitude values. The result for P_D is given as follows:

$$P_D \approx 1 - \int dA_1 p(A_1) \int_0^{\theta} dy_1 e^{-y_1} e^{-A_1^2 E_1} I_0(A_1\sqrt{4E_1 y_1}) \times ...$$

$$\times \int dA_M p(A_M) \int_0^{\theta-u_1-\cdots-u_{M-1}} dy_M e^{-y_M} e^{-A_M^2 E_M} I_0(A_M\sqrt{4E_M y_M}), \tag{5.83}$$

where $p(A_k)$ is the pdf of amplitude factor A_k.

Numerical receiver operating characteristics results for some examples are presented below. The multi-component targets of concern are similar to those described in Section 5.3.3:

one contains three identical specular reflectors, and the other contains two specular reflectors and a dihedral reflector, whose orientations and geometries are specified in Section 5.2.2 and spatial distributions specified in Section 5.3.3. But here the multi-component targets have another degree of complexity: the amplitudes of the individual target-return components are random. In this section, we assume that all target-return components are scaled by independent identically distributed random variables that are uniformly distributed on a finite range.

Figure 5.14 plots the receiver operating characteristics of the likelihood-ratio detectors for the first example target. Figure 5.15 plots the receiver operating characteristics of the same detectors for the second example target. Results for stripmap-mode operation and spotlight-mode operation are included. There are three curves in each panel, which correspond to the detection performances of the likelihood-ratio detector for the multi-component target with no position uncertainty, the generalized likelihood-ratio detector for the multi-component target with position uncertainty specification 1 in Figure 5.10, and the approximate generalized likelihood-ratio detector for the multi-component target with amplitude uncertainty range $[0.7, 1.3]$ and the same position uncertainty specification. The numerical results in Figures 5.14 and 5.15 indicate that the detection performance for the target with amplitude uncertainty range $[0.7, 1.3]$ is inferior to the performance for the target without amplitude uncertainty for most P_D and P_F values. Notice that the effect of amplitude uncertainty is twofold. On the one hand, the lack of precise information degrades the detection performance. On the other hand, the uncertainty of amplitude may either enhance or decrease the SNCR value. These two trends compete with each other when the whole or part of the amplitude uncertainty range exceeds 1. For the first example in Figure 5.14, the trend of degrading detection performance dominates the trend of enhancing SNCR. For the second example in Figure 5.15, the trend of degrading detection performance dominates the trend of enhancing SNCR except when P_D and P_F are small.

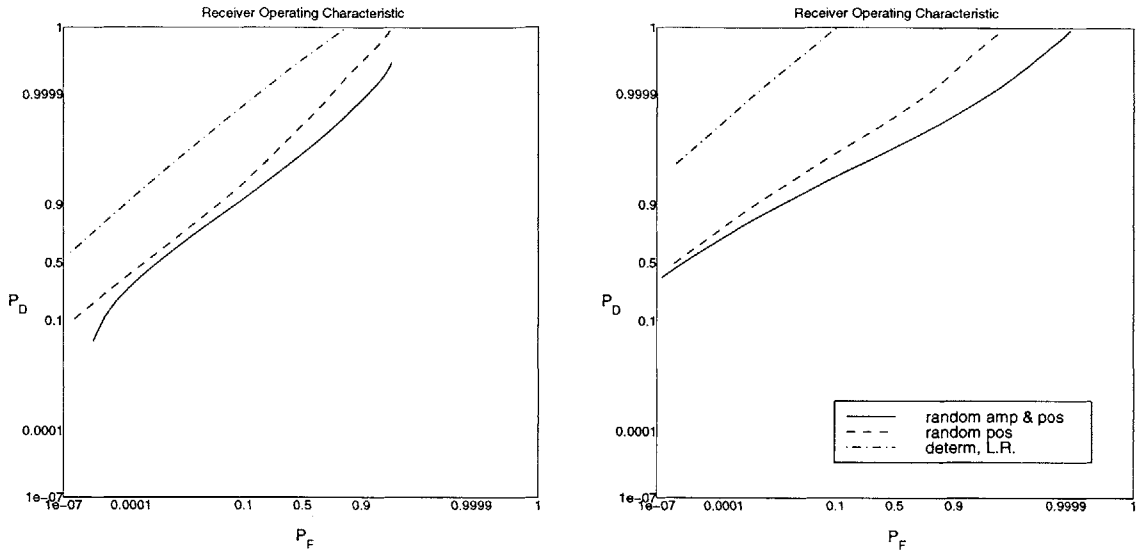

Figure 5.14 Receiver operating characteristics: 3 specular reflectors; likelihood-ratio detector for target with no position uncertainty, generalized likelihood-ratio detector for target with position uncertainty specification 1, and approximate generalized likelihood-ratio detector for the multi-component target with amplitude uncertainty range $[0.7, 1.3]$. Left panel is stripmap-mode operation; right panel is spotlight-mode operation.

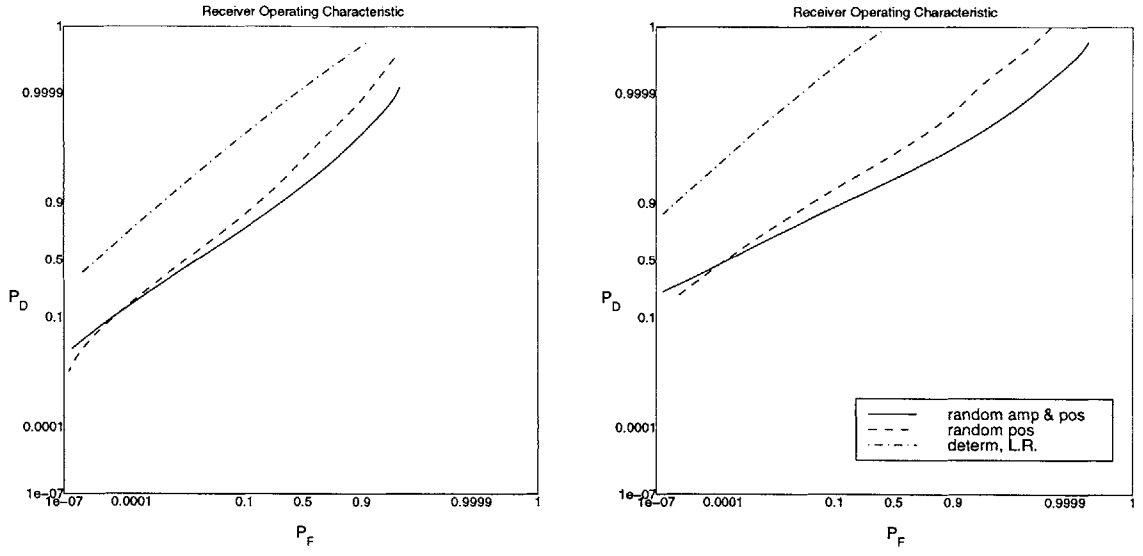

Figure 5.15 Receiver operating characteristics: 2 specular reflectors and 1 dihedral reflector; same arrangement as Figure 5.15.

5.5 Multi-Component Target Detection with Unknown Pose

Both Section 5.3 and Section 5.4 dealt with multi-component targets with position randomness. For those targets, the position randomness associated with individual target components were taken to be independent of one another. In radar signal processing, one often encounters another type of position randomness, which results from a random shift and/or rotation of a fixed target-component constellation. The locations of individual target components are still not fixed, but they are tied together to vary as a whole instead of varying independently. To generate different realizations of this position randomness is equivalent to randomly displacing or rotating the local coordinate system with respect to which the relative locations of all the individual components are fixed. In the practical sense, this model simulates a target that contains more than one scattering center and is subject to pose or location uncertainty. In this section, we choose to deal with a subset of this type of target: a multi-component target with random pose. To be more accurate, the locations of different target components rotate around a pose center on the 2-D image plane with a common random rotational angle.

5.5.1 Detection Scheme

Recognition problems for multi-component targets with different poses have been extensively studied. In [42], a computationally efficient approach based on the concept of mutual-information maximization is developed to do target matching and alignment. The automatic target classifier presented in [43] and [44] compares the data target with a bank of model hypothetical targets of different types, positions, and view angles via a vote-based approach for the similarities between extracted model target features and data target features. The target classifier in [45] also matches a feature vector extracted from SAR image chip data with a feature vector predicted from a hypothetical target class and pose by using

a Bayesian likelihood metric. Even though the definitions of match measure are different, all the works listed above are centered on a common concept: to recognize a model target with specific pose and location from the image data one should compare the data with a bank of hypothetical model targets. Incorporating this concept into the context of this thesis, the multi-component target detector for target with unknown pose can also be accomplished via such a comparative approach. In this section, we construct a generalized likelihood-ratio detector for the target with unknown pose. The generalized likelihood ratio maximizes the likelihood ratio with respect to a discrete subset of the pose angle ϕ within the overall uncertainty range: $\{\phi_1^u, \phi_2^u, ...\}$. In this sense, the generalized likelihood-ratio detector derived in this section is consistent with the basic concept of [42-45]. The only distinction is that here the measure of match is the likelihood ratio obtained in Section 5.2.

Before constructing the generalized likelihood-ratio detector for a target with unknown pose, we should have a clear definition for the target pose. For a multi-component with deterministic positions, the location of the ith component center (Δ_x^i, Δ_y^i) can be expressed in terms of the polar coordinate with respect to the pose center (x_0, y_0):

$$(\Delta_x^i, \Delta_y^i) = (x_0 + r_i \cos(\phi_i), y_0 + r_i \sin(\phi_i)), \tag{5.84}$$

where r_i is the distance between (Δ_x^i, Δ_y^i) and (x_0, y_0), and ϕ_i is the azimuthal angle of the vector connecting (x_0, y_0) to (Δ_x^i, Δ_y^i) with respect to $\hat{x}$ axis. When we incorporate a pose-angle uncertainty into the target model, the center location of component i becomes

$$(\Delta_x^i, \Delta_y^i) = (x_0 + r_i \cos(\phi_i - \phi), y_0 + r_i \sin(\phi_i - \phi)), \tag{5.85}$$

where ϕ is the random pose angle. The geometric constellation of a multi-component target with random pose is illustrated in Figure 5.16.

In Section 5.2, we have derived the likelihood ratio for a multi-component target with known component positions (see Eq. (5.12)) from which we see that the likelihood ratio

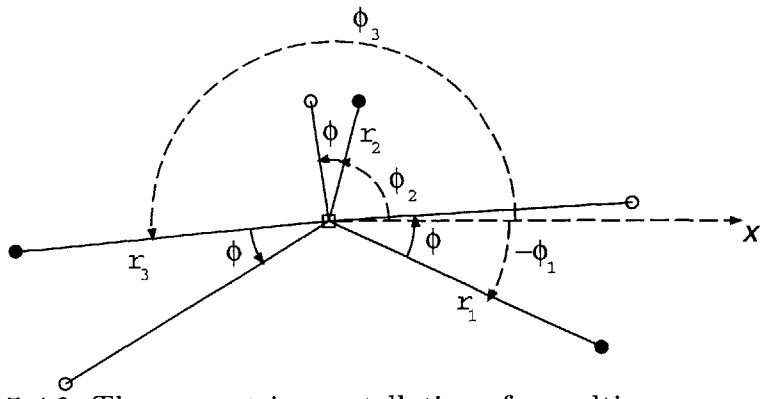

Figure 5.16 The geometric constellation of a multi-component target with random pose.

parameterized by the target pose angle is:

$$l(\mathbf{r};\phi) = \prod_{i=1}^{M} e^{-E_i} I_0\left(2\left|\sum_{m=-\infty}^{\infty}\int_{-\infty}^{\infty} d\tau\ \mathbf{s}_i^{\dagger}(m - m_i(\phi), \tau - \tau_i(\phi)) \cdot \mathbf{r}(m,\tau)\right|\right), \tag{5.86}$$

where

$$(m_i(\phi), \tau_i(\phi)) = ((x_0 + r_i\cos(\phi_i - \phi))/vT_s, 2(y_0 + r_i\sin(\phi_i - \phi))\cos(\psi)/c). \tag{5.87}$$

The generalized likelihood ratio is the maximum value of the likelihood ratio in (5.86) with respect to the pose angle ϕ within the uncertainty range:

$$\text{GLR} = \max_{\phi} \prod_{i=1}^{M} e^{-E_i} I_0\left(2\left|\sum_{m=-\infty}^{\infty}\int_{-\infty}^{\infty} d\tau\ \mathbf{s}_i^{\dagger}(m - m_i(\phi), \tau - \tau_i(\phi)) \cdot \mathbf{r}(m,\tau)\right|\right). \tag{5.88}$$

Even though the likelihood ratio in (5.86) is a continuous function of ϕ, the operation of maximization in (5.88) is easier to implement under a discrete basis; namely, the likelihood ratio is maximized over a discrete set of ϕ values $\{\phi_1^u, \phi_2^u, ...\}$ sampled from ϕ's uncertainty range. In this sense, a matched-filter bank followed by a 2-D sampler associated with a particular pose angle matches the data to a particular target model, and the measure of comparison is the overall likelihood ratio. Figure 5.17 depicts the block diagram of the generalized-likelihood-ratio detector for the multi-component target with unknown phases and pose.

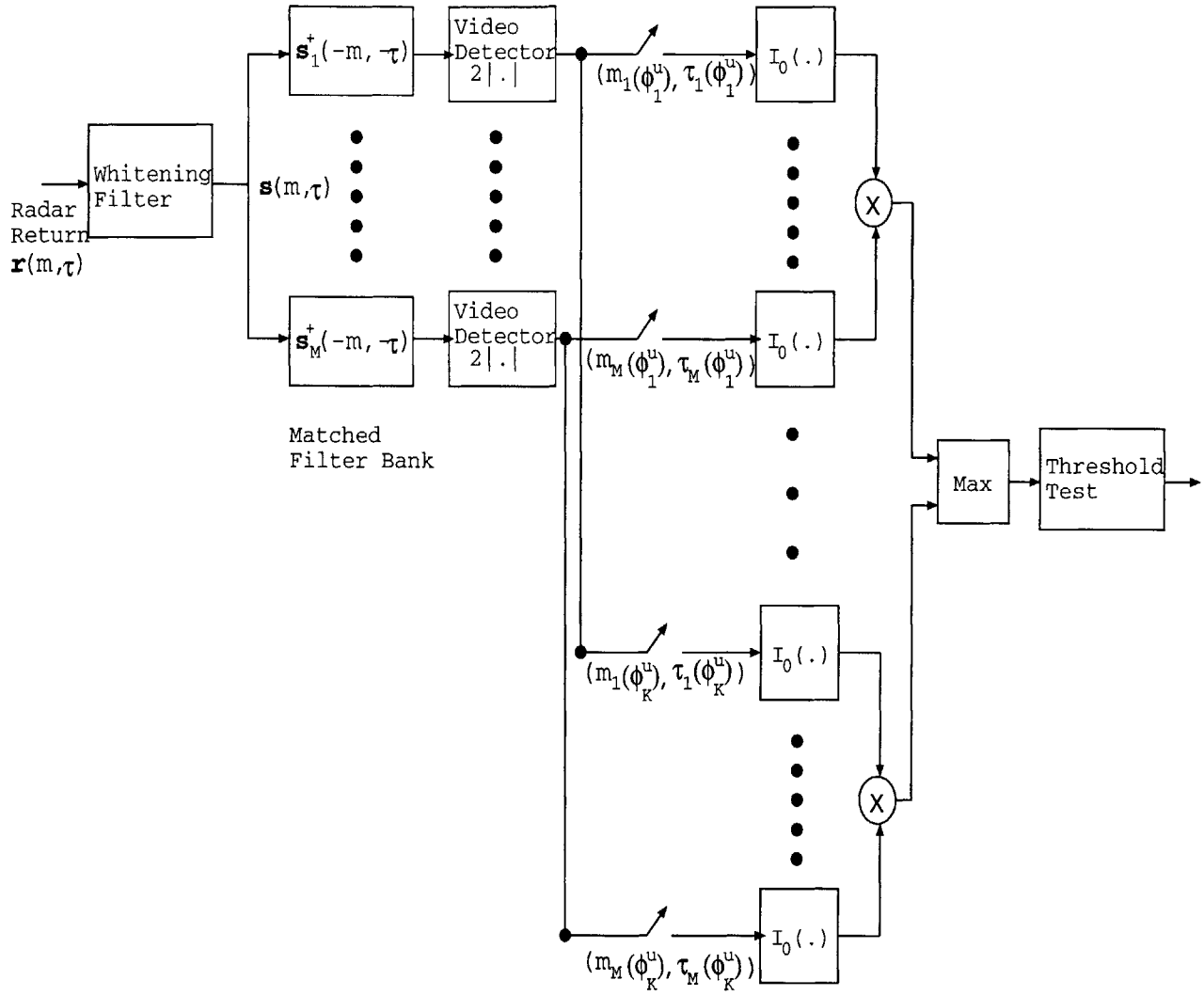

Figure 5.17 Generalized-likelihood-ratio detector for the multi-component target with unknown phases and pose.

5.5.2 Performance Analysis

In this section, we calculate the receiver operating characteristics of the generalized-likelihood-ratio detector for the multi-component target with unknown pose. First of all, under the same assumption used in Sections 5.3.2.4 and 5.4.2, the probability of detection P_D is approximately equal to the probability of detection when the target-component locations are exact and known, which is calculated in (5.16). So we only need to find the probability of false alarm P_F for the detector depicted in Figure 5.17.

It can be shown that for a given threshold γ, the probability of false alarm can be obtained as follows:

$$P_F = 1 - \Pr\left\{ \max_{\phi \in \{\phi_1^u, \phi_2^u, \ldots\}} \left[\prod_{i=1}^{M} I_0 \left(2 \left| \sum_{m=-\infty}^{\infty} \int_{-\infty}^{\infty} d\tau \; \mathbf{s}_i^{\dagger}(m - m_i(\phi), \tau - \tau_i(\phi)) \cdot \mathbf{w}(m, \tau) \right| \right) \right] \leq \gamma \right\} \tag{5.89}$$

where $\mathbf{w}(m, \tau)$ is the white random process of clutter-plus-noise. The generalized likelihood ratio in (5.89) is a stochastic function of ϕ, so apparently (5.88) can be solved by using the 1-D level-crossing theory presented in Section 5.3.2.1 with a slight modification from the continuous to the discrete case. But there is an obstacle that prohibits the direct application of the formula (5.46) to this new problem: the generalized likelihood ratio in (5.88) is not a stationary random process with respect to ϕ. Stationarity is the foundation of the whole level-crossing theory presented in Section 5.3.2.1. Thus the level-crossing formula for (5.89) cannot be easily derived from available results.

We can use the resolution-bin approximation in Section 5.3.2.3 to evaluate the approximate value of P_F. The process of calculation has two steps. First, in (5.88), the probability that the generalized likelihood ratio is smaller than a threshold for a discrete sampled set of the uncertain range of ϕ, $[\Phi_{min}, \Phi_{max}]$, is approximated by the probability that the generalized likelihood ratio is smaller than a threshold for the whole uncertain range of ϕ.

Namely,

$$P_F \approx 1-\Pr\left\{\max_{\phi\in[\Phi_{min},\Phi_{max}]}\left[\prod_{i=1}^{M} I_0\left(2\left|\sum_{m=-\infty}^{\infty}\int_{-\infty}^{\infty} d\tau\ \mathbf{s}_i^{\dagger}(m-m_i(\phi),\tau-\tau_i(\phi))\cdot\mathbf{w}(m,\tau)\right|\right)\right]\le\gamma\right\} \tag{5.90}$$

Second, this probability is approximated by the probability that the generalized likelihood ratio is smaller than a threshold for another discrete set of the uncertainty range of ϕ whose sampling interval is the resolution-bin size $\Delta\phi$. Since the level-crossing probabilities of the samples at different resolution bins are assumed independent, we have

$$\begin{aligned} P_F &\approx 1- \\ &\prod_{k=\Phi_{min}/\Delta\phi}^{\Phi_{max}/\Delta\phi}\Pr\left\{\left[\prod_{i=1}^{M} I_0\left(2\left|\sum_{m=-\infty}^{\infty}\int_{-\infty}^{\infty} d\tau\ \mathbf{s}_i^{\dagger}(m-m_i(k\Delta\phi),\tau-\tau_i(k\Delta\phi))\cdot\mathbf{w}(m,\tau)\right|\right)\right]\le\gamma\right\} \\ &= 1-\left\{\Pr\left\{\prod_{i=1}^{M}\left[I_0\left(2\left|\sum_{m=-\infty}^{\infty}\int_{-\infty}^{\infty} d\tau\ \mathbf{s}_i^{\dagger}(m-m_i(\phi),\tau-\tau_i(\phi))\cdot\mathbf{w}(m,\tau)\right|\right)\right]\le\gamma\right\}\right\}^{\frac{\Phi_{max}-\Phi_{min}}{\Delta\phi}} \end{aligned} \tag{5.91}$$

The angle ϕ in (5.91) could be any value within the uncertainty range because the probability within the product of second equality does not depend on ϕ at all. In contrast to (5.17), equation (5.91) can be easily expressed in terms of the P_F for the same multi-component target with known component positions, P_F^0,

$$P_F \approx 1-(1-P_F^0)^{\frac{\Phi_{max}-\Phi_{min}}{\Delta\phi}}. \tag{5.92}$$

There still remains the task of choosing the size of the pose-angle resolution bin, i.e., the problem of choosing $\Delta\phi$. Our idea for solving this problem is to come up with the sizes of linear resolution bins, x_{res} and y_{res}, when the regions of uncertainty for target components are 2-D and independent of one another, and then to use such sizes to determine the the size of angular resolution bins, $\Delta\phi$, from x_{res} and y_{res}. The procedures are as follows. (i) We obtain the average size of linear resolution-bins $x_{res}=y_{res}$ by fitting the 2-D level-crossing formula (5.63) with the resolution-bin approximation (5.64) at $P_F=0.1$ averaged over different sizes of uncertainty regions $X=Y$. (ii) There are eight possibilities in making a discrete

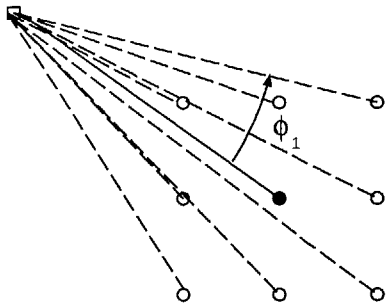

Figure 5.18 The geometry of angular increment with respect to linear resolution bins.

movement of a target component from the center point of its uncertainty region to the center of its adjacent resolution bin. Thus there are eight corresponding values for a discrete variation of the orientation angle of the line connecting the overall target center and a target component center (see Figure 5.18). We average such discrete angular variations over the eight possibilities. (iii) Finally, we average the angular increments obtained from procedure (ii) over different target components to obtain the average size of angular resolution bins $\Delta\phi$.

Figure 5.19 plots the receiver operating characteristics of the likelihood-ratio detectors for the first example target. Figure 5.20 plots the receiver operating characteristics of the same detectors for the second example target. Results from both stripmap-mode operation and spotlight-mode operation are shown. There are three curves in each panel, which correspond to the detection performances of the likelihood-ratio detector for the multi-component target with no position uncertainty, the generalized likelihood-ratio detector for the multi-component target with position uncertainty specification 1 in Figure 5.10, and the generalized likelihood-ratio detector for the multi-component target with a pose uncertainty where the range for the pose uncertainity region is 40° wide. The average sizes of linear resolution bins, the sizes of angular resolution bins for each target components, and the average angular-resolution-bin sizes corresponding to Figures 5.19 and 5.20 are listed in Table 5.1. The numerical results in Figures 5.19 and 5.20 indicate that when neither P_D

Scenario	$x_{res} = y_{res}$	$\Delta\phi$, comp. 1	$\Delta\phi$, comp. 2	$\Delta\phi$, comp. 3	ave. $\Delta\phi$
Spec. 1, Spotlight	0.62 m	10.3°	4.0°	4.6°	6.3°
Spec. 1, Stripmap	1.23 m	21.2°	8.6°	9.2°	13.2°
Spec. 2, Spotlight	0.55 m	10.3°	4.0°	4.0°	6.3°
Spec. 2, Stripmap	0.94 m	21.2°	8.6°	6.9°	12.0°

Table 5.1 Table of uncertainty cell sizes for target pose angles.

nor P_F is close to 1, the detection performance for target with pose uncertainty is superior to that for target with position uncertainty. This behavior can be intuitively explained by two facts: the pose uncertainty region for each individual component is 1-D (curve) whereas the position uncertainty region for each individual component is 2-D (square area), and that the pose uncertainties for all the components of a multi-component target are constrained whereas the position uncertainties for all the components of a multi-component target are independent. Thus the pose variation is less uncertain than the independent 2-D position variations, provided the target component traces swept via the pose variation do not greatly exceed the area of 2-D position uncertainty. In specification 1 of Figure 5.10, the maximum wedge angles between the lines connecting target center and the four corners of an uncertainty area are 139.4°, 83.7° and 42.3° for components 1, 2, and 3, respectively. Notice that the resolution-bin formula for 2-D position uncertainty, that is used to come up with the size of average annular resolution bin matches the analytical level-crossing formula at $P_F = 0.1$. Thus as both P_D and P_F approach 1, the pose-uncertainty ROC curves in Figures 5.19 and 5.20 become less accurate. So the fact that the ROC curves for uncertain pose and uncertain position cross in this region may be an artifact.

5.6 Multi-Component Target Detection: Conventional SAR Processors

The target detectors presented from Sections 5.2 through 5.5 are Neyman-Pearson op-

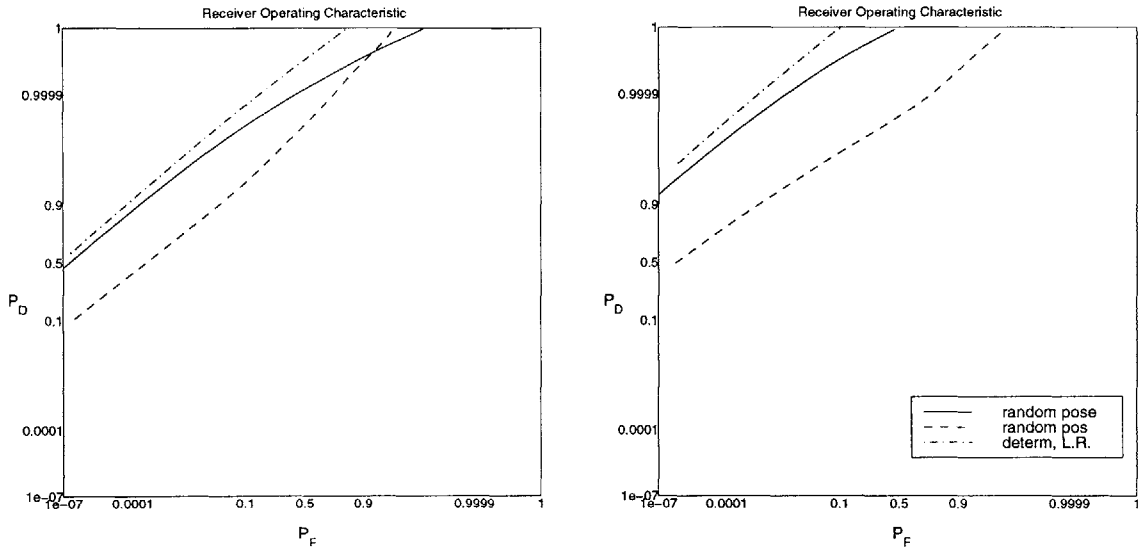

Figure 5.19 Receiver operating characteristics: 3 specular reflectors; likelihood-ratio detector for target with no position uncertainty, generalized likelihood-ratio detector for target with position uncertainty specification 1, and generalized likelihood-ratio detector for the multi-component target with a pose uncertainty where the uncertainty range for the pose angle is 40°. Left panel is stripmap-mode operation; right panel is spotlight-mode operation.

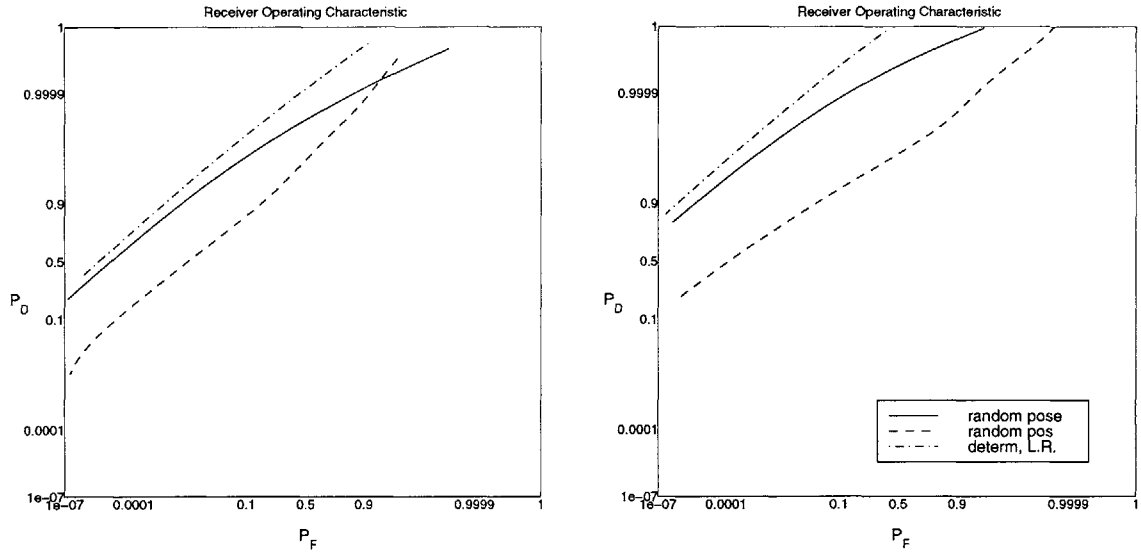

Figure 5.20 Receiver operating characteristics: 2 specular reflectors and 1 dihedral reflector; same arrangement as Figure 5.19.

timal, i.e., they optimally combine polarimetric, whitening-filter, and adaptive-resolution, processing. As in our early work on single-component target detection (presented in Chapters 3 and 4), the target detection performance of optimum multi-component target processors must exceed that of conventional SAR processors for such targets. In this section, we explicitly compare the receiver operating characteristics of the Neyman-Pearson processors with those of the conventional SAR processors to quantify the former's performance advantage.

In Chapter 3 and Chapter 4, we have introduced the conventional stripmap-mode SAR processor, which is a chirp-compression processor, and the conventional spotlight-mode SAR processor, which is a polar-format-Fourier-transform processor, for a single-component target. The conventional SAR processors for a multi-component target are straightforward extensions of these two schemes. Figure 5.21 sketches the block diagrams of the conventional SAR processor for a multi-component target with deterministic position and amplitude, with independent component position uncertainty, with position and amplitude uncertainties, and with pose uncertainty. In contrast to the Neyman-Pearson processors that possess a bank of matched filters, a conventional SAR processor has only one full-resolution ($\kappa = \nu = 1$) chirp-compression SAR imager for stripmap-mode operation, or one full-resolution ($\kappa = \nu = 1$) polar-format SAR imager for spotlight-mode operation. In addition, instead of the fully polarimetric signal dealt in the Neyman-Pearson processor, only one single polarization is considered in the conventional SAR processor (here we choose HH). The target detectors after the SAR imager are similar to their counterparts in Neyman-Pearson processors: they sample this output image according to the available information on target-component locations and calculate the likelihood ratio or generalized likelihood ratio.

In order to compute the receiver operating characteristics of the target detectors sketched in Figure 5.21, we have to obtain the statistics for the random part (clutter-plus-noise) of the radar return after SAR imager. The statistical models for clutter and noise under stripmap-mode and spotlight-mode operations are described in Sections 2.4, 2.5, and 4.2. The models

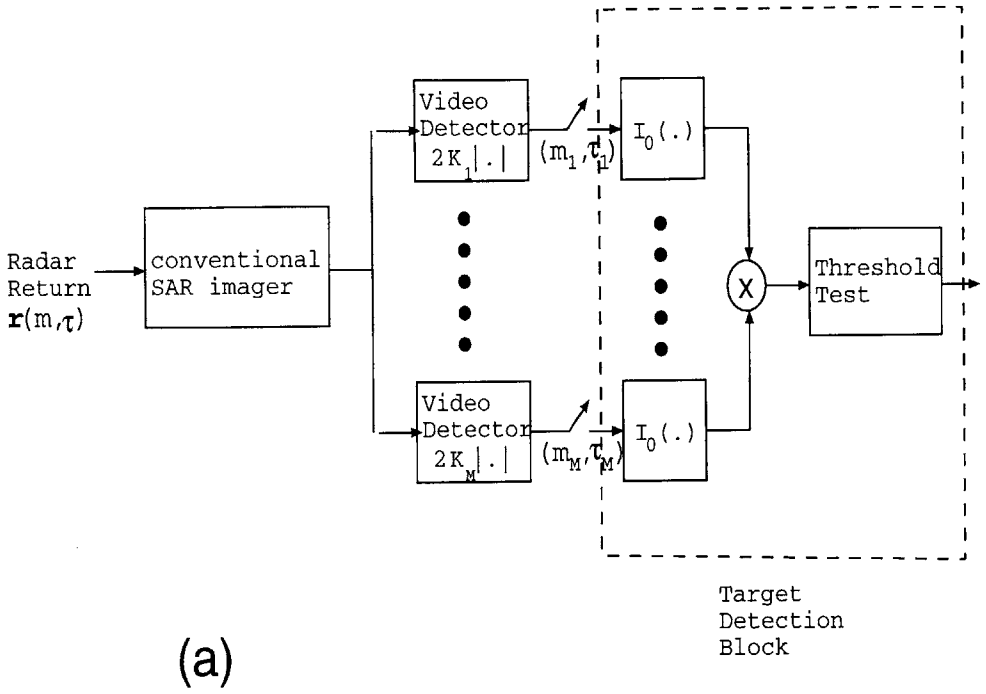
Radar
Return
r(m,τ)
conventional
SAR imager
Video
Detector
2K1|.|
Video
Detector
2KM|.|
(m1,τ1)
(mM,τM)
I0(.)
I0(.)
X
Threshold
Test
Target
Detection
Block

(a)

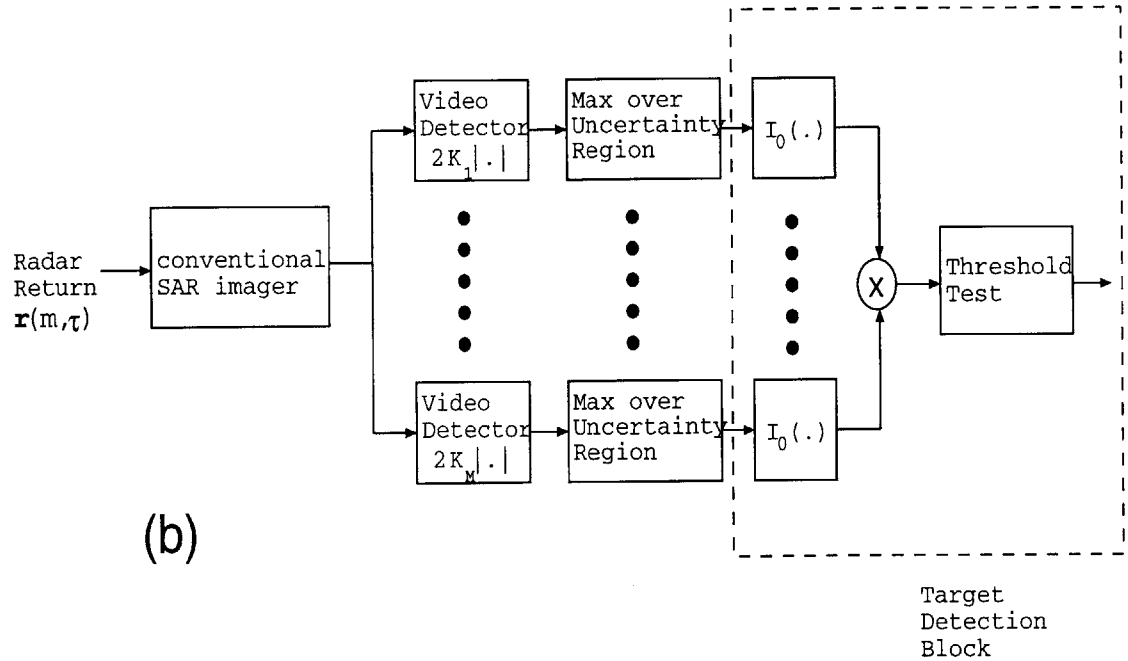
Radar
Return
r(m,τ)
conventional
SAR imager
Video
Detector
2K1|.|
Video
Detector
2KM|.|
Max over
Uncertainty
Region
Max over
Uncertainty
Region
I0(.)
I0(.)
X
Threshold
Test
Target
Detection
Block

(b)

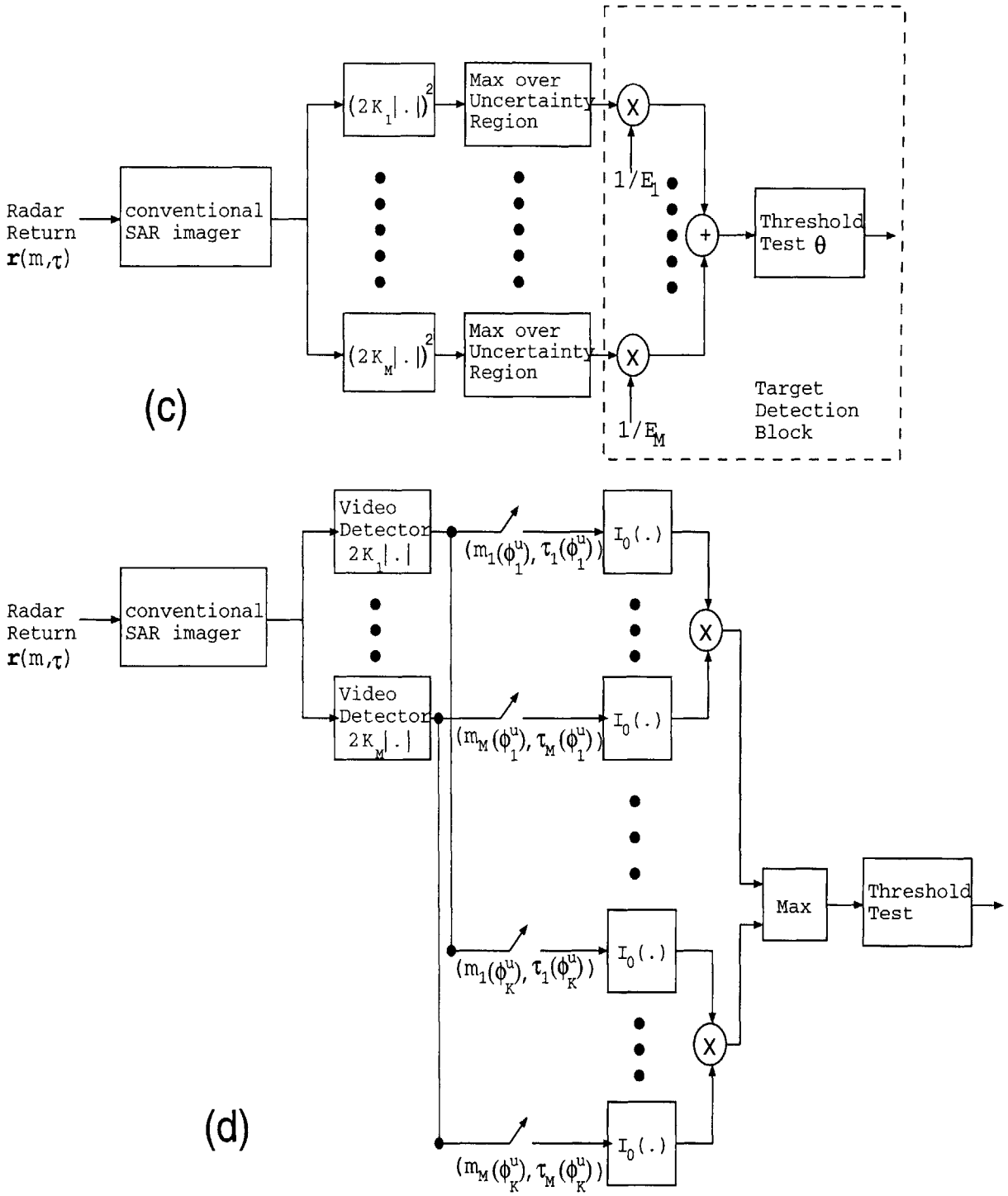

Figure 5.21 Conventional SAR processors for multi-component target detection; in order: (a) target with no position or amplitude randomness, (b) target with independent component position randomness, (c) target with independent component position and amplitude randomness, (d) target with pose randomness. The factor K_i equals $2\text{SNCR}_i/|S_i|$, where S_i is the sampled complex envelope of i^{th} component target return.

of conventional SAR imagers under stripmap-mode and spotlight-mode operations can be found in Sections 3.1.1 and 4.3.1. Combining the random radar return models with the conventional SAR imager models, we can obtain the statistics of the random radar signal after SAR imagers. It can be shown that the clutter and noise after the conventional SAR imagers are zero-mean and circulo-complex Gaussian random processes for both stripmap-mode and spotlight-mode operations. When we approximate the sum over cross-range index by an integral and replace a hard limit on integration by a Gaussian shaping function with equal width, the covariance functions for clutter output $\mathbf{l}_{\text{clutter}}$ and noise output $\mathbf{l}_{\text{noise}}$ can be derived with the following results.

For stripmap-mode operation, we find:

$$< \mathbf{l}_{\text{clutter}}(m_1,\tau_1)\cdot\mathbf{l}^{\dagger}_{\text{clutter}}(m_2,\tau_2) >\approx< \mathbf{l}_{\text{clutter}}(0,0)\cdot\mathbf{l}^{\dagger}_{\text{clutter}}(0,0) > e^{-(m_1-m_2)^2/2m_{\text{res}}^2}e^{-(\tau_1-\tau_2)^2/2\tau_{\text{res}}^2}, \tag{5.93}$$

$$< \mathbf{l}_{\text{noise}}(m_1,\tau_1)\cdot\mathbf{l}^{\dagger}_{\text{noise}}(m_2,\tau_2) >\approx< \mathbf{l}_{\text{noise}}(0,0)\cdot\mathbf{l}^{\dagger}_{\text{noise}}(0,0) > e^{-(m_1-m_2)^2/m_{\text{res}}^2}e^{-(\tau_1-\tau_2)^2/\tau_{\text{res}}^2}, \tag{5.94}$$

where

$$m_{\text{res}} = \frac{x_{\text{res}}}{vT_s}, \qquad \tau_{\text{res}} = \frac{2}{c}\cos(\psi)y_{\text{res}}. \tag{5.95}$$

The point-scatterer resolution lengths x_{res} and y_{res} in (5.95) are related to the parameters in Table 3.1 via (4.29) with $\kappa = \nu = 1$ and $\rho_t = 0$.

For spotlight-mode operation, we find:

$$< \mathbf{l}_{\text{clutter}}(x_1,y_1)\cdot\mathbf{l}^{\dagger}_{\text{clutter}}(x_2,y_2) >\approx< \mathbf{l}_{\text{clutter}}(0,0)\cdot\mathbf{l}^{\dagger}_{\text{clutter}}(0,0) > e^{-(x_1-x_2)^2/2x_{\text{res}}^2}e^{-(y_1-y_2)^2/2y_{\text{res}}^2}, \tag{5.96}$$

$$< \mathbf{l}_{\text{noise}}(x_1,y_1)\cdot\mathbf{l}^{\dagger}_{\text{noise}}(x_2,y_2) >\approx< \mathbf{l}_{\text{noise}}(0,0)\cdot\mathbf{l}^{\dagger}_{\text{noise}}(0,0) > e^{-(x_1-x_2)^2/x_{\text{res}}^2}e^{-2(y_1-y_2)^2/y_{\text{res}}^2}. \tag{5.97}$$

The point-scatterer resolution lengths x_{res} and y_{res} in (5.97) are related to the parameters in Table 3.1 via (4.31) with $\kappa = \nu = 1$ and $\rho_t = 0$. The intensities of covariance functions $< \mathbf{l}_{\text{clutter}}(0,0)\cdot\mathbf{l}^{\dagger}_{\text{clutter}}(0,0) >$ and $< \mathbf{l}_{\text{noise}}(0,0)\cdot\mathbf{l}^{\dagger}_{\text{noise}}(0,0) >$ have already been calculated in Chapters 3 and 4.

Equations (5.93), (5.94), (5.96), and (5.97) imply that if the separation between two sample points is appreciably larger than the resolution lengths of a point scatterer, then the correlation between these two sampled output clutter-plus-noise signals is very small. In other words, when different components of a target are all separated enough such that they are quite far away from the (point scatterer) resolution areas centered around each other, then the clutter-plus-noise image chips associated with different target components are independent identically distributed random fields whose spectra are prescribed by (5.93), (5.94), (5.96), and (5.97). Therefore, similar to the previous sections of this chapter, we can independently calculate the probability density function associated with each sampled output. So the formulae developed in Sections 5.2, 5.3, 5.4, and 5.5 for calculating P_D and P_F of the Neyman-Pearson processors are still valid for the conventional SAR processors after two modifications. First, we replace E_i, the output energy of component i, by the conventional-SAR-processor output SNCR of component i. Second, we replace the Neyman-Pearson processor output clutter-plus-noise spectrum with the conventional-SAR-processor output clutter-plus-noise spectrum, which was described in (5.93), (5.94), (5.96), and (5.97).

Figures 5.22 and 5.23 compare the receiver operating characteristics of the conventional SAR processor and of the Neyman Pearson processor when the target-component locations and radar-return amplitudes are exactly known. Figures 5.24 and 5.25 are the similar comparison when the target-component locations are independently random within 2-D uncertainty regions. Likewise, Figures 5.26 and 5.27 give the similar comparison when the target-component locations are independently random within 2-D uncertainty regions and the return amplitudes are independently random within uncertainty intervals. Finally, Figures 5.28 and 5.29 give the similar comparison when the target pose is random. It is clear in all cases from Figures 5.22 through 5.29, that the Neyman-Pearson processor has a better detection performance than the conventional SAR processor. Thus the motivation of studying the polarimetric, whitening-filter, adaptive-resolution processor is verified: we have

demonstrated from a first-principles approach that this kind of processor indeed outperforms the conventional full-resolution SAR processor in terms of not only single-component but also multi-component target detection.

The better target-detection performance of the Neyman-Pearson processors is the result of higher SNCR values corresponding to target components. There are three factors that give the Neyman-Pearson processors its higher SNCR values than the conventional SAR processors: the effect of the whitening filter, the polarimetric effect, and the adaptive-resolution effect. In the multi-component target examples we have considered so far, noise dominates over clutter. Thus the whitening filter does not have a major contribution. The polarimetric effect has a significant influence on the enhancement of SNCR: in a Neyman-Pearson processor, it can enhance the SNCR value of each component by a factor up to 2. The adaptive-resolution effect is not as significant as the polarimetric effect in the examples we have considered, but it still contributes somewhat. In addition, theoretically it could be very important when the size of reflector is much larger (stripmap-mode and spotlight-mode) or smaller (spotlight-mode) than the diameter of antenna aperture. Figures 5.22 through 5.29 also compare the receiver operating characteristics of conventional SAR processors and Neyman-Pearson processors when the radar signal of only one single polarization is available. They are actually equivalent to the comparison of adaptive-resolution and full-resolution processors. It can be observed that even though the Neyman-Pearson performance improvement is not as significant as those in Figures 5.27 through 5.29, there is still advantage to adaptive-resolution processing compared to the conventional full-resolution SAR processing. Figure 5.30 compares the receiver operating characteristics of the conventional SAR processor, the full-polarimetric Neyman-Pearson processor, and the scalar Neyman-Pearson processor for a different target scenario. In this case, the multi-component target consists of three specular reflectors with $\rho_t = 1.7$ m and the same known (Δ_x, Δ_y) positions as the one in Figure 5.22. The clutter-to-noise ratio is set to be 6.28×10^{-3}. The other parameters are identical

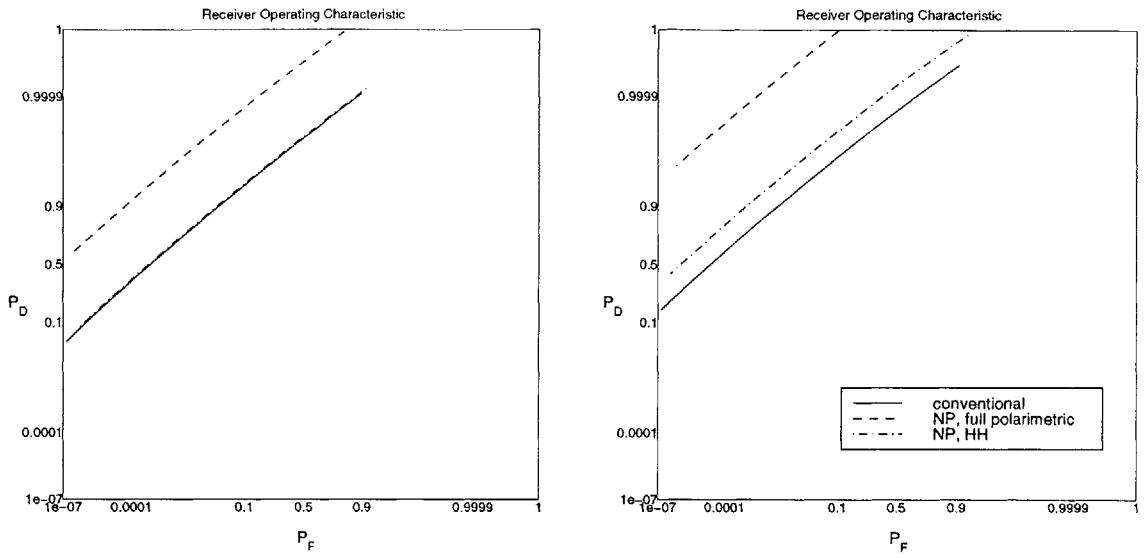

Figure 5.22 Receiver operating characteristics: Conventional SAR processor vs. polarimetric and non-polarimetric Neyman-Pearson processors, likelihood-ratio detector, multi-component target with random phases, 3 specular reflectors. Left panel is stripmap-mode operation; right panel is spotlight-mode operation.

to those used in Figures 5.22 through 5.29. It can be clearly observed in Figure 5.30 that the performance improvement of the Neyman-Pearson processor due to adaptive-resolution processing is as significant as that due to polarimetric synthesis.

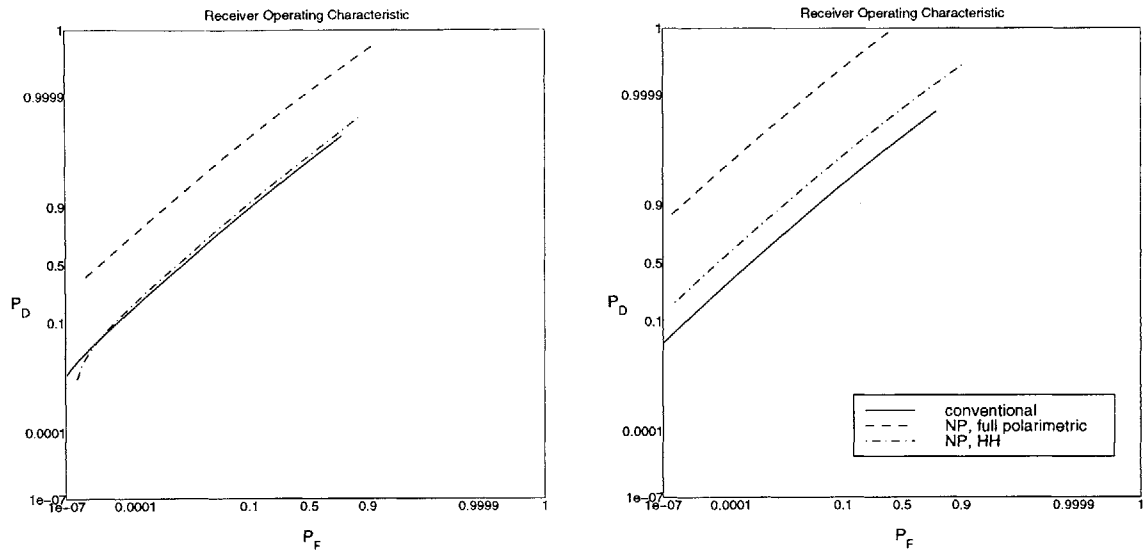

Figure 5.23 Receiver operating characteristics: Conventional SAR processor vs. polarimetric and non-polarimetric Neyman-Pearson processors, likelihood-ratio detector, multi-component target with random phases, 2 specular and 1 dihedral reflectors. Left panel is stripmap-mode operation; right panel is spotlight-mode operation.

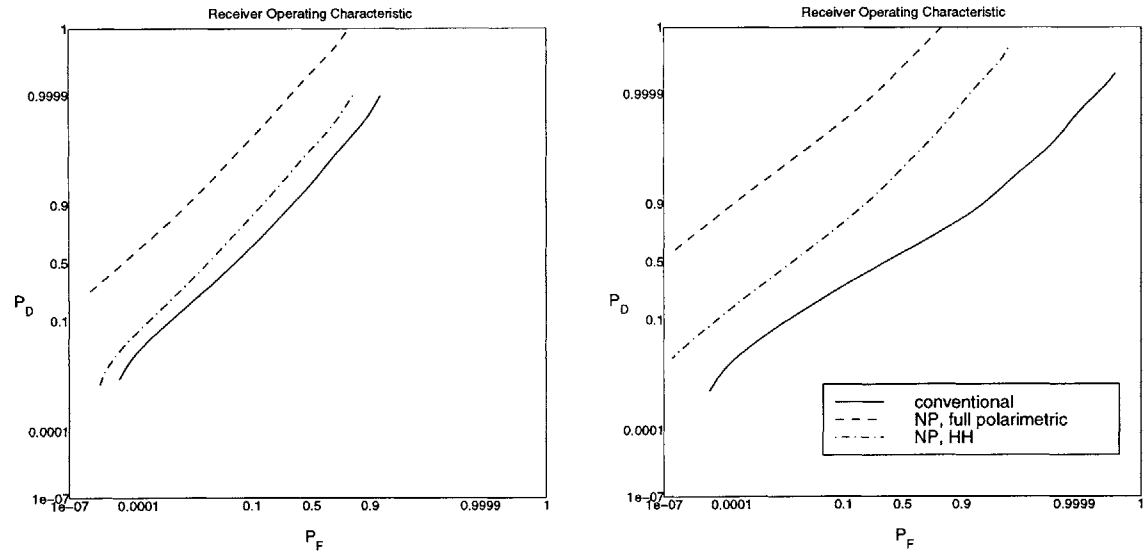

Figure 5.24 Receiver operating characteristics: Conventional SAR processor vs. polarimetric and non-polarimetric Neyman-Pearson processors, 3 specular reflectors; generalized likelihood-ratio detector for target with position uncertainty specification 2. Left panel is stripmap-mode operation; right panel is spotlight-mode operation.

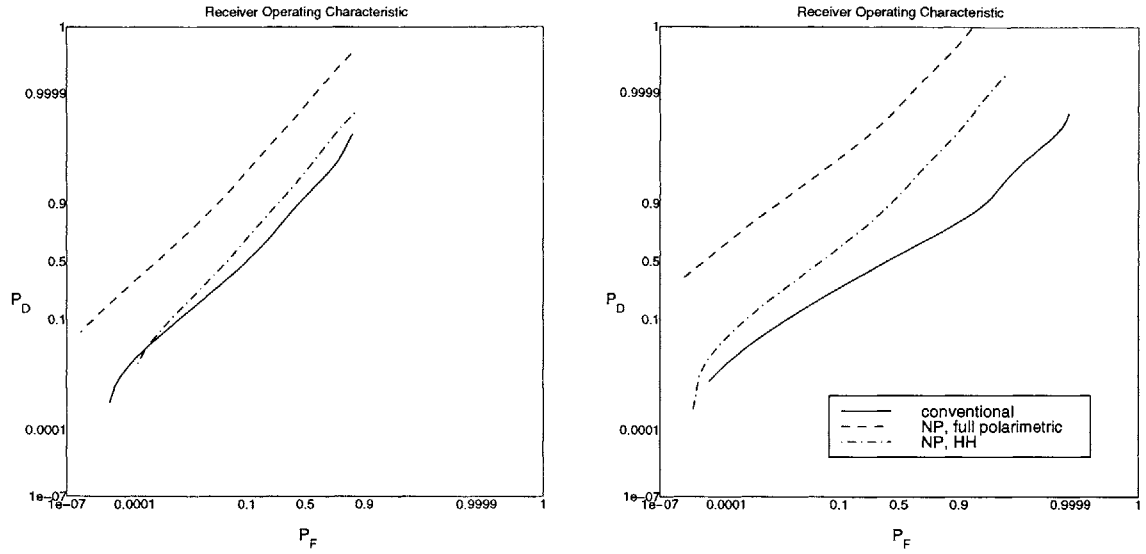

Figure 5.25 Receiver operating characteristics: 2 specular reflectors and 1 dihedral reflector; same arrangement as Figure 5.25.

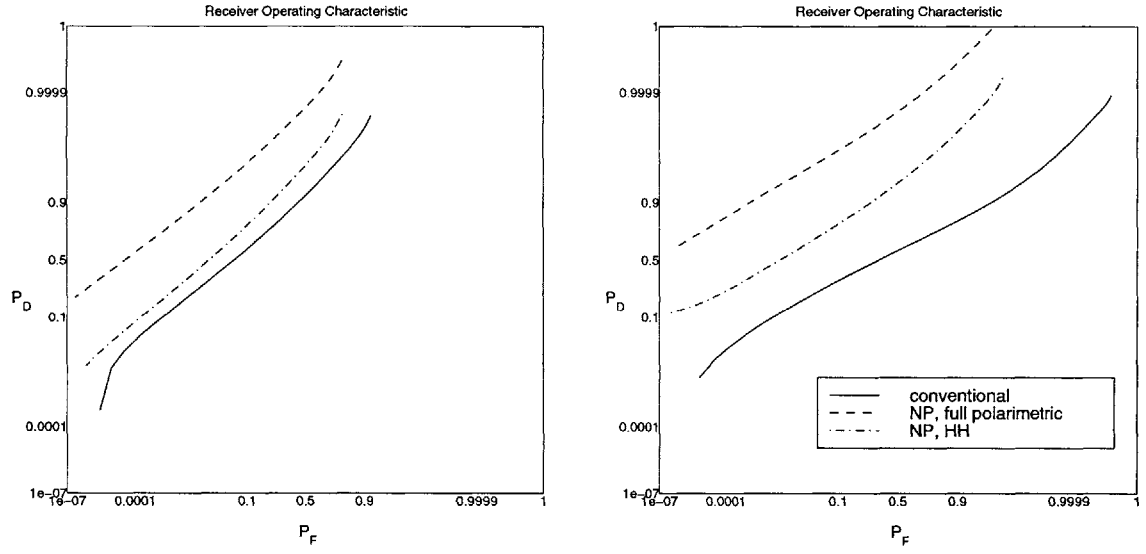

Figure 5.26 Receiver operating characteristics: Conventional SAR processor vs. polarimetric and non-polarimetric Neyman-Pearson processor, 3 specular reflectors, approximate generalized likelihood-ratio detector for the multi-component target with position uncertainty specification 2 and amplitude uncertainty range [0.7, 1.3]. Left panel is stripmap-mode operation; right panel is spotlight-mode operation.

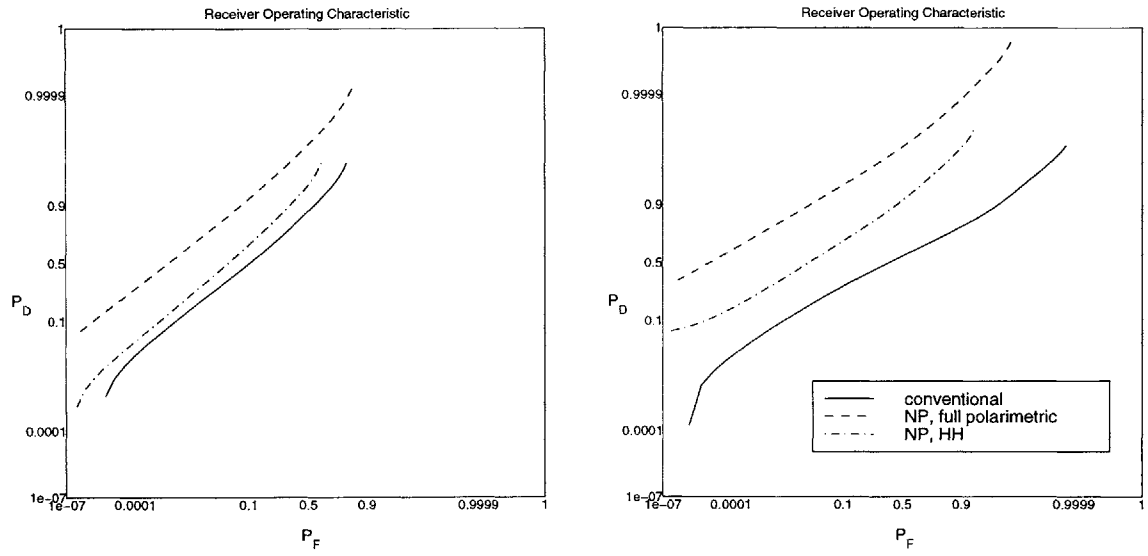

Figure 5.27 Receiver operating characteristics: 2 specular reflectors and 1 dihedral reflector; same arrangement as Figure 5.26.

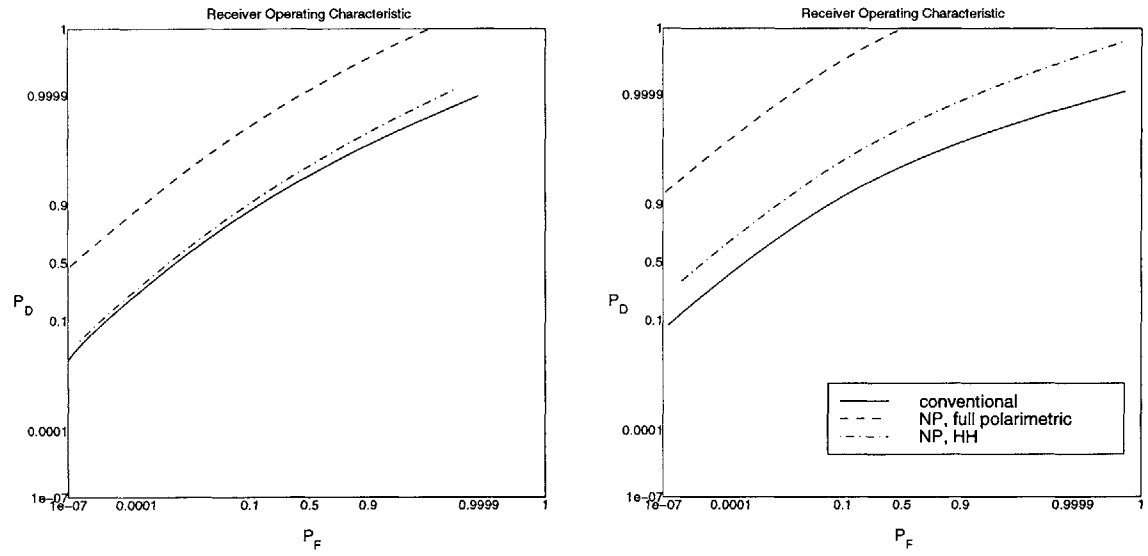

Figure 5.28 Receiver operating characteristics: Conventional SAR processor vs. polarimetric and non-polarimetric Neyman-Pearson processor, 3 specular reflectors, generalized likelihood-ratio detector for the multi-component target with a pose uncertainty where the uncertainty range for the pose angle is 40°. Left panel is stripmap-mode operation; right panel is spotlight-mode operation.

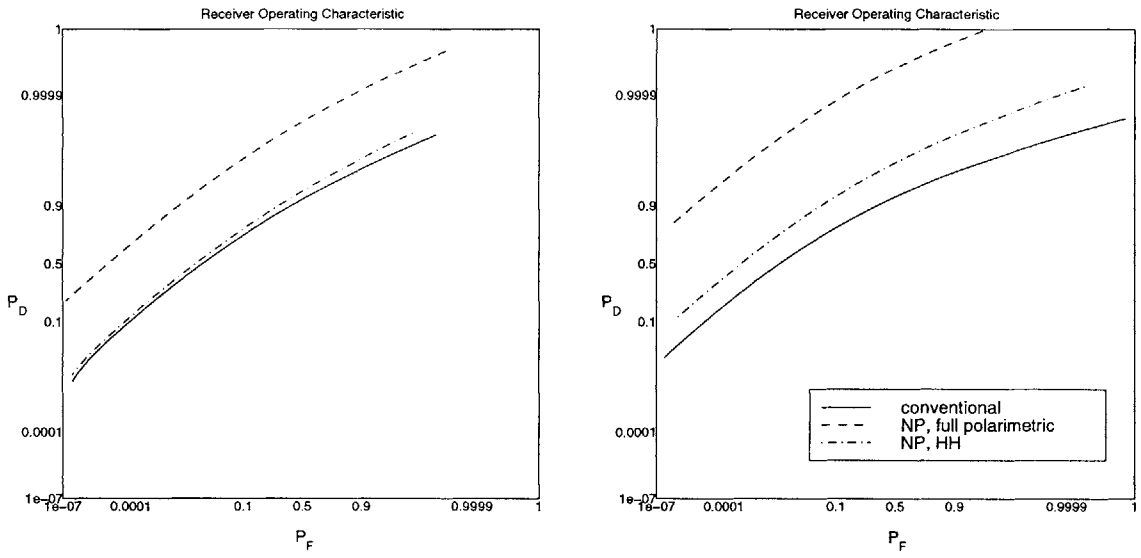

Figure 5.29 Receiver operating characteristics: 2 specular reflectors and 1 dihedral reflector; same arrangement as Figure 5.28.

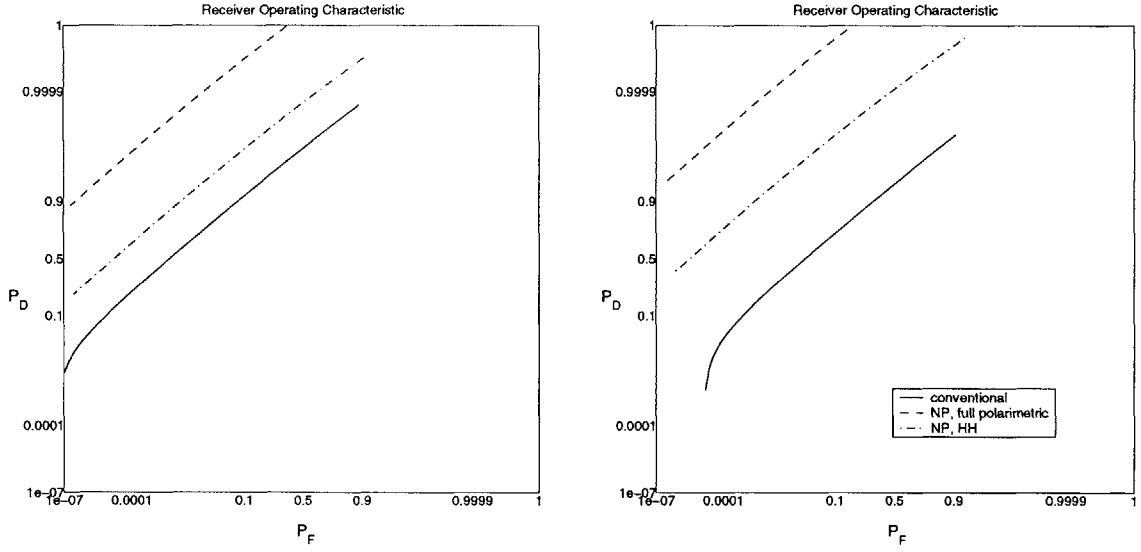

Figure 5.30 Receiver operating characteristics: Conventional SAR processor vs. polarimetric and non-polarimetric Neyman-Pearson processors. Multi-component target with random phases, 3 specular reflectors with $\rho_t = 1.7$ m; CNR $= 6.28 \times 10^{-3}$. Left panel is stripmap-mode operation; right panel is spotlight-mode operation.

Chapter 6

Multi-Component Target Classification Problems

From Chapter 2 through Chapter 5 we have dealt with target detection problems. Target detection is, in a sense, binary target recognition: is a particular target present or not. A normal automatic target recognition system must deal with an N-ary problem: of $N \geq 2$ target types, which one (if any) is present, based on radar return information. This problem is also known as classification. In this chapter, we extend our previous results for target detection problems to multi-component target classification problems. We will apply the Neyman-Pearson or conventional SAR target detectors we have already developed to form Neyman-Pearson or conventional SAR target classifiers. We will also come up with a simple method for assessing the performance of these classifiers.

6.1 Target Classification Problems and Schemes

We can formulate a multi-component target classification problem in a similar way to the multi-component target detection problem. We consider a scalar 1-D radar return $r(t)$ from a multi-component target and corrupted by a zero-mean unitary white Gaussian noise $w(t)$. Suppose the radar return contains a target return among N possible types. Then, if H_i denotes target i present, $r(t)$ can be written as follows:

$$\text{under } H_1: \quad r(t) = \sum_{m^1=1}^{M_1} e^{i\phi_{m^1}} s_{m^1}(t - t_{m^1}) + w(t),$$

.

.

$$\text{under } H_k: \quad r(t) = \sum_{m^k=1}^{M_k} e^{i\phi_{m^k}} s_{m^k}(t - t_{m^k}) + w(t),$$

$$\text{under } H_N: \quad r(t) = \sum_{m^N=1}^{M_N} e^{i\phi_{m^N}} s_{m^N}(t - t_{m^N}) + w(t). \tag{6.1}$$

The complex envelope $s_m^k(t)$ (for $k = 1$ to N) is the radar-return waveform from the m^k-th component of the k-th target when it is located at the scene center. The time delay t_m^k for this component is determined by its actual location. The phases ϕ_m^k are independent random variables that are uniformly distributed within $[0, 2\pi)$; they represent the incoherence of each target-component with respect to other components as well as the noise. A similar target classification formulation for a 2-D polarimetric radar return can also be easily obtained.

We can develop classifiers for a repertoire of multi-component targets based on the target detectors presented in Chapter 5. At the output stage of a target detector, a constant real signal level, which is equal to the likelihood ratio or generalized likelihood ratio, is compared with a threshold level in order to decide on the absence or presence of that target. When there can be more than one possible target type, we can pass the radar return through a bank of target detectors, one for each target type. The resulting real-valued output levels v_1, v_2, ..., v_N are the likelihood ratios or generalized likelihood ratios of conditions H_1, H_2, ..., H_N (target type $1, 2, ..., N$) with respect to condition H_0 (clutter and noise only). To carry out classification, we do not pass the $\{v_k\}$ through individual threshold comparators, but select their maximum value. If the p-th detector has maximum output, then the classifier decides the target to be type p. The classifier scheme proposed here is likelihood based. In other literature, the quantity chosen to compare in a target classifier may be vote-based, using radar return point features [43-45], or based on mutual information [42]. However, their front-stage architectures are quite similar: they all use matched-filter banks to extract the maximum amount of information pertinent to specific target types. Figure 6.1 plots the block diagram of a multi-component target classifier. The

first panel, as an example, sketches the details of a Neyman-Pearson classifier for a repertoire of multi-component targets with no position or amplitude randomness at all. Notice that in this architecture each individual detector output is weighted by the factor e^{-E} (E is the corresponding target-return energy) to compensate for the energy difference among different target types, which is slightly different from that in Figure 5.2. As indicated in (5.12), such factor also appears in the formulation of the likelihood ratio. For binary detection, the absence or presence of this factor does not change the performance at all. The second panel sketches the generic architecture of a target classifier with all possible scenarios: the targets of concern could have position, amplitude, or pose randomness.

6.2 Performance Analysis

The evaluation of target classification performance is not a straightforward extension of the target detection performance analysis presented in Chapter 5. The main reason is that the radar returns of different multi-component targets of concern often correlate with one another. For example, to calculate the probability of correct classification under H_i we need $\Pr[v_i > \max_{j \neq i} v_j \mid H_i]$, which cannot be found from just the marginal probability density functions of the individual random variables $\{v_1, ..., v_N\}$. One has to use the joint probability density function of all the random variables, which could have a dense correlation matrix. The calculation of such target-classification probability is computationally intensive. There are a couple of ways to reduce this computational complexity: we can proceed a preliminary analysis based on the marginal probability density functions of v_1, v_2, ... to observe the qualitative behaviors of classification probability; we can carry out Monte Carlo simulation for calculating the classification probability; or we can further reduce the complicated correlation matrix of v_1, v_2, ... for certain specific target-repertoire scenarios. In this section, we will present results from the first and the third approaches.

We first carry out a preliminary and qualitative analysis for the probability of target

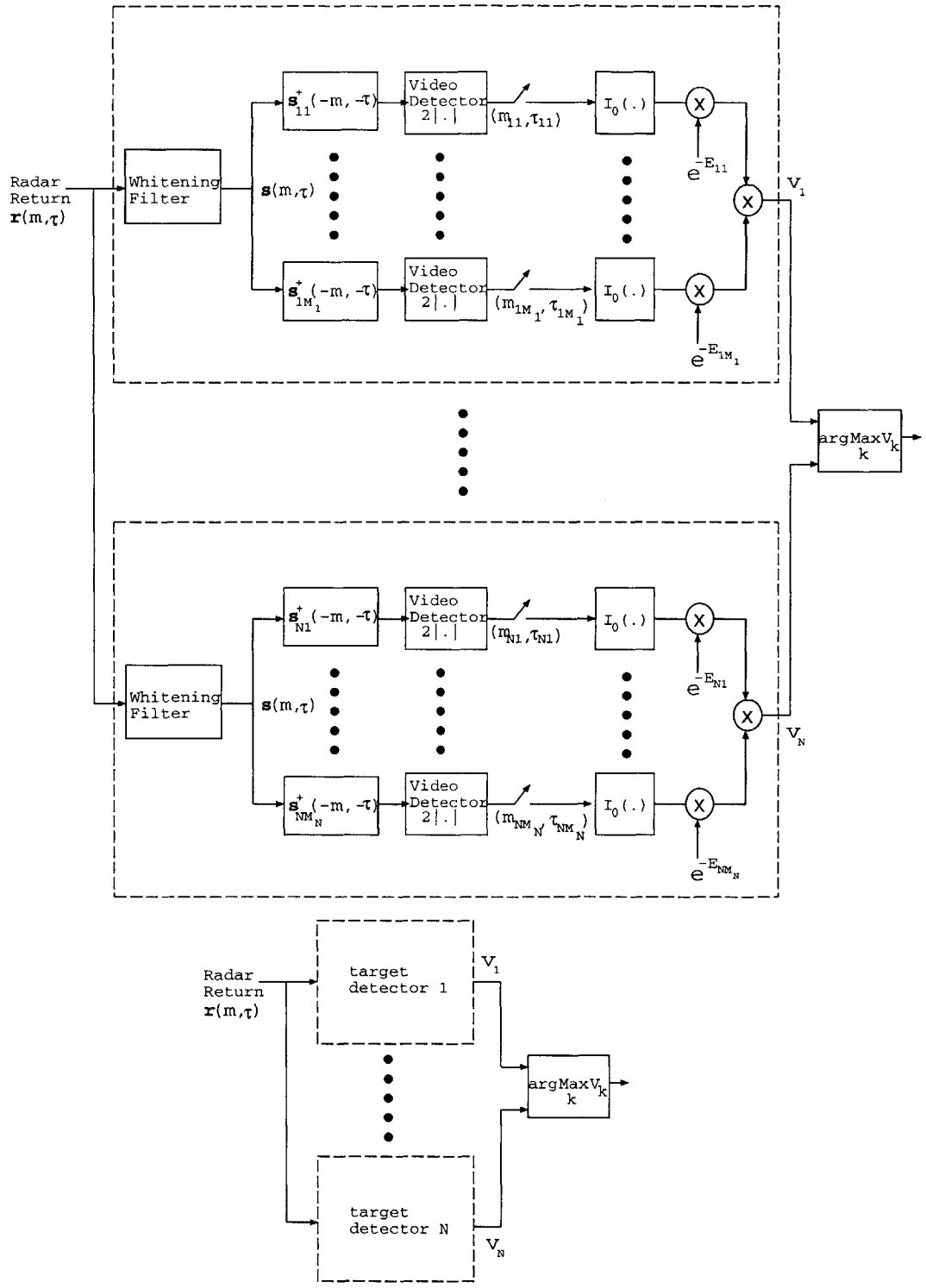

Figure 6.1 Multi-component target classifiers; in order: Neyman-Pearson classifier for targets with no position or amplitude randomness, and generic likelihood-ratio target classifier. In the second panel, each individual detector will be the one depicted in Figures 5.2, 5.5, 5.13, or 5.17, depending on the specific target scenario.

classification based on marginal probability density functions. Consider the i^{th} target detector in a classifier (see Figure 6.1). In a binary detection problem, its real output value v_i is compared with a threshold γ_i. When $v_i > \gamma_i$, target present is declared; otherwise target absent (H_0) is declared. In order to normalize the output random variables, let us choose the thresholds $\{\gamma_i\}$ to ensure that $P_F^{(i)}$ is equal to a constant α independent of target number i. The normalized detection variables are then defined to be $u_i \equiv v_i/\gamma_i$, for $1 \leq i \leq N$.

We now plot the conditional marginal probability density function $p_{u_i|H_j}(u_i|H_j)$ for a specific target-repertoire example. In this example, there are three possible multi-component targets. The first target contains three specular reflectors, the second one contains two specular reflectors plus one dihedral reflector, and the third one contains one specular reflector plus two dihedral reflectors. The radar-return amplitudes and the locations of all target components are deterministic and known. The detailed specifications are listed in Table 6.1. The flight and radar parameters are specified in Table 3.1, and the clutter-to-noise-ratio CNR $= 3.14 \times 10^{-2}$ (noise dominant). The detector block in use is the Neyman-Pearson (optimum) detector illustrated in Figure 5.2. The conditional probability density function $p_{u_i|H_i}(u_i|H_i)$ can be simply obtained from differentiating the probability of detection derived in Section 5.2. To derive the conditional probability density function $p_{u_i|H_j}(u_i|H_j)$ for $i \neq j$, we pass the j^{th} target return to the i^{th} filter bank, which does not match this target-return waveform, and then use the resulting output SNCR values to calculate the probability of "incorrect" detection. The conditional marginal probability density functions $p_{u_i|H_j}(u_i|H_j)$ of these three targets for stripmap-mode and spotlight-mode operations are plotted in Figures 6.2 and 6.3, respectively. In these figures, the probability of false alarm P_F is fixed at 0.00001.

The numerical results in Figures 6.2 and 6.3 indicate that when H_i is true the random variable u_i has a higher marginal probability density than u_j with $j \neq i$ in the above-threshold region. Notice that in both figures the horizontal axis is plotted in log scale. When

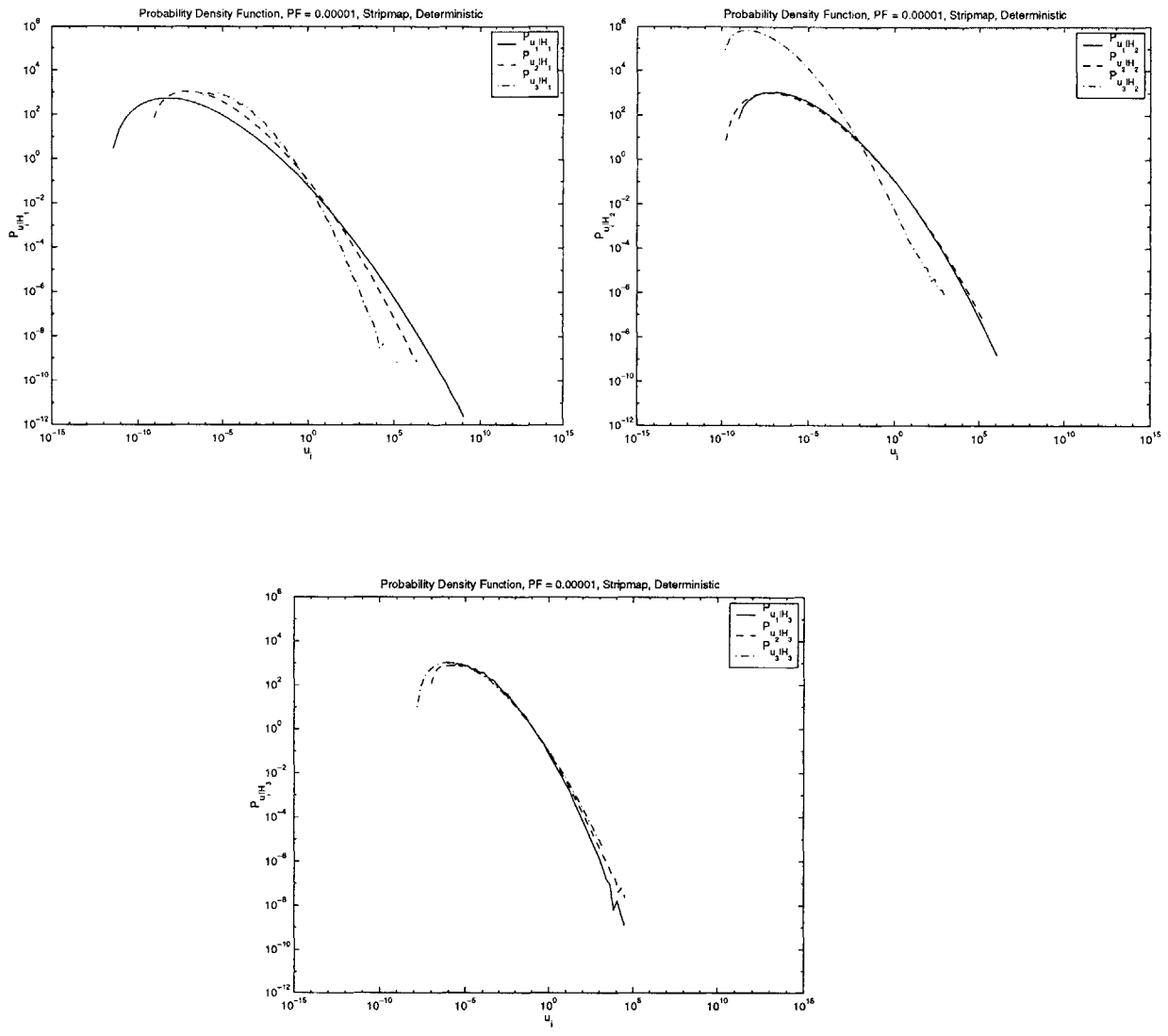

Figure 6.2 Conditional marginal probability density functions of the normalized random variable outputs u_1, u_2, u_3. The target scenario is specified in Table 6.1. The flight and radar parameters are specified in Table 3.1. The clutter-to-noise-ratio CNR $= 3.14 \times 10^{-2}$ (noise dominant). The detector block in use is the Neyman-Pearson (optimum) detector. The SAR operation mode is stripmap. The upper left, upper right, and lower panels correspond to condition H_1, H_2, H_3, respectively.

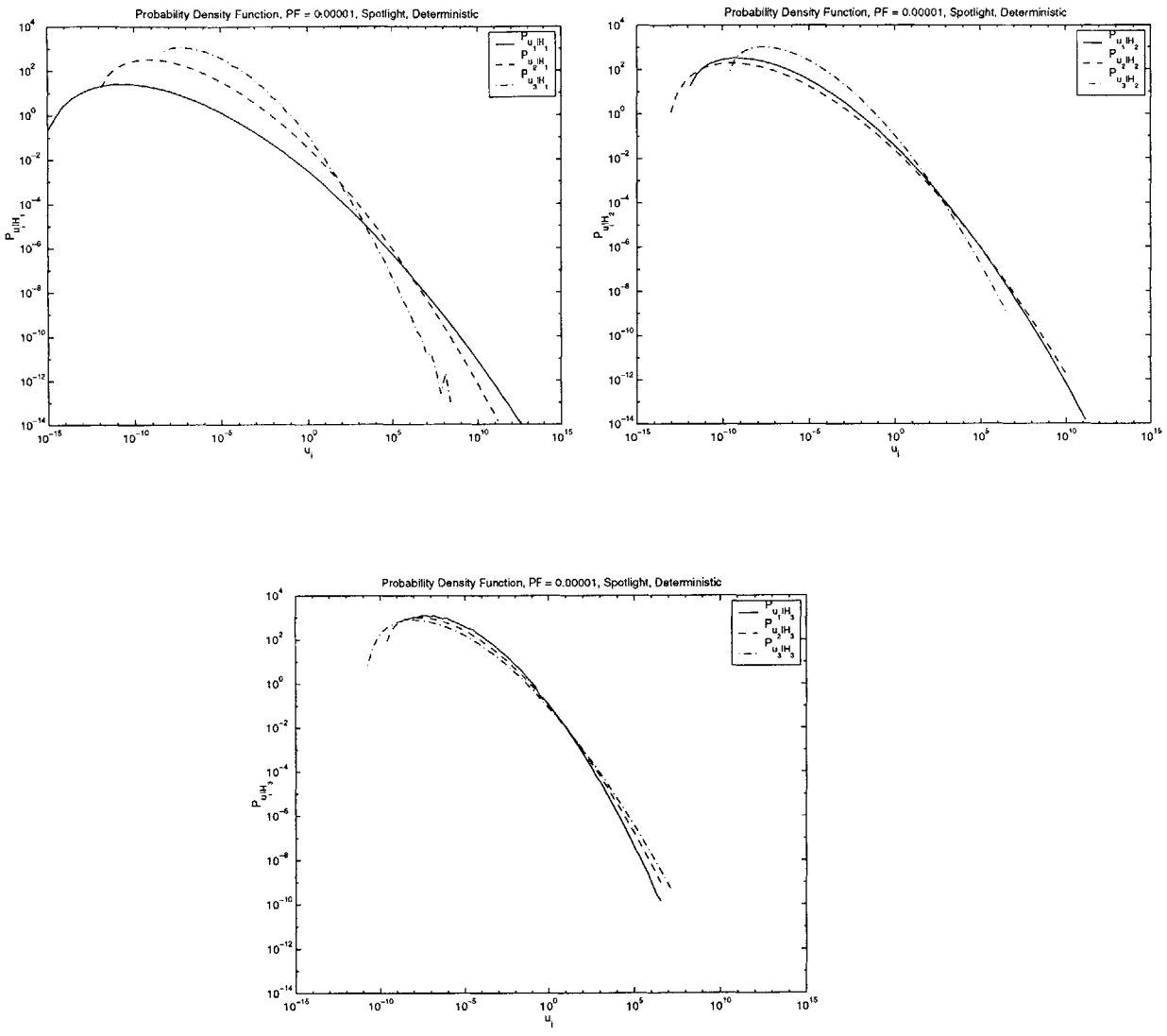

Figure 6.3 Conditional marginal probability density functions of the normalized random variable outputs u_1, u_2, u_3. The target scenario is specified in Table 6.1. The flight and radar parameters are specified in Table 3.1. The clutter-to-noise-ratio CNR $= 3.14 \times 10^{-2}$ (noise dominant). The detector block in use is the Neyman-Pearson (optimum) detector. The SAR operation mode is spotlight. The upper left, upper right, and lower panels correspond to condition H_1, H_2, H_3, respectively.

	Target 1	Target 2	Target 3
Component 1 type	specular	specular	specular
Component 1 (Δ_x, Δ_y)	(0 m, 0 m)	(0 m, 0 m)	(0 m, 0 m)
Component 1 ρ_t	0.5 m	0.5 m	0.5 m
Component 1 orientation	0°	0°	0°
Component 2 type	specular	specular	dihedral
Component 2 (Δ_x, Δ_y)	(-7 m, -3 m)	(-7 m, -3 m)	(-7 m, -3 m)
Component 2 ρ_t	0.5 m	0.5 m	0.5 m
Component 2 orientation	0°	0°	45°
Component 3 type	specular	dihedral	dihedral
Component 3 (Δ_x, Δ_y)	(5 m, -5 m)	(5 m, -5 m)	(5 m, -5 m)
Component 3 ρ_t	0.5 m	0.5 m	0.5 m
Component 3 orientation	0°	45°	45°

Table 6.1 Table of parameter values for SNCR calculations. Notice the orientation angle of a specular reflector refers to the angle between the slant range and the normal direction of the plate, the orientation angle of a dihedral reflector means the angle between the SAR flight path direction and the dihedral axis.

plotted in linear scale, the marginal probability density function of u_i under H_i is higher than those of u_j under H_i for $i \neq j$ for most possible threshold values larger than 1. This trend suggests that under H_i, for almost all threshold values larger than 1, the probability of correct detection of the i^{th} detector is higher than the probabilities of incorrect detection of the j^{th} detector for $j \neq i$. Such observation does not provide accurate information regarding the probability of correct classification. But it is still encouraging in the sense that when operated independently, the correct target detector outperforms the incorrect target detectors. Under the assumption that v_1, v_2, and v_3 are mutually independent, we can calculate the probability of correct classification for a specific condition H_i using marginal density functions:

$$\Pr\{\text{say}H_i|H_i\} = \Pr\{v_i > \max_{j\neq i} v_j|H_i\}$$

$$= \int_0^\infty dv_i p_{v_i|H_i}(v_i|H_i) \int_0^{v_i} dv_j p_{v_j|H_i}(v_j|H_i) \int_0^{v_i} dv_k p_{v_k|H_i}(v_k|H_i), \tag{6.2}$$

for distinct $\{i, j, k\}$, and therefore the average probability of correct classification

$$\begin{aligned} \text{PCC} &\equiv \Pr\{\text{say}H_1|H_1\}\Pr\{H_1\} + \Pr\{\text{say}H_2|H_2\}\Pr\{H_2\} + \Pr\{\text{say}H_3|H_3\}\Pr\{H_3\} \\ &= \frac{1}{3}[\Pr\{\text{say}H_1|H_1\} + \Pr\{\text{say}H_2|H_2\} + \Pr\{\text{say}H_3|H_3\}], \end{aligned} \tag{6.3}$$

where $\Pr\{H_1\}$, $\Pr\{H_2\}$, $\Pr\{H_3\}$ are assumed to be identical. Plugging the numerical results for the marginal probability density functions in Figures 6.2 and 6.3 into (6.2) and (6.3), we obtain the average probability of correct classification to be 0.578 ($\Pr\{\text{say}H_1|H_1\} = 0.735$, $\Pr\{\text{say}H_2|H_2\} = 0.514$, $\Pr\{\text{say}H_3|H_3\} = 0.486$) for spotlight-mode operation, and 0.534 ($\Pr\{\text{say}H_1|H_1\} = 0.709$, $\Pr\{\text{say}H_2|H_2\} = 0.494$, $\Pr\{\text{say}H_3|H_3\} = 0.411$) for stripmap-mode operation.

The independence assumption on v_1, v_2, and v_3 is not justifiable, because components of the different targets are very similar to one another in terms of both location and reflector type. To obtain an accurate numerical value for the probability of correct classification, we need the joint probability density function for $\{v_1, v_2, v_3\}$. As indicated before, this task is complicated and computationally intensive in general. Fortunately, for the target scenario specified in Table 6.1, the formulation for probability of correct classification can be significantly simplified. In the following paragraph, we derive upper and lower bounds on the probability of correct classification.

Consider first the H_1 condition, in which the target return contains three specular reflector components. Denote the output complex level from the sampler after the j^{th} component matched filter of the i^{th} detector as a_{ij}. We assume that the radar return from a reflector component is shift-invariant with respect to position. Thus the three real output levels from target detectors, v_1, v_2, and v_3, are

$$v_1 = e^{-3E_s} I_0(2|a_{11}|) I_0(2|a_{12}|) I_0(2|a_{13}|),$$

$$v_2 = e^{-2E_s - E_d} I_0(2|a_{21}|) I_0(2|a_{22}|) I_0(2|a_{23}|),$$

$$v_3 = e^{-E_s - 2E_d} I_0(2|a_{31}|) I_0(2|a_{32}|) I_0(2|a_{33}|), \tag{6.4}$$

where E_s is the SNCR of the specular reflector return, and E_d the SNCR of the dihedral reflector return. Due to the characteristics of the target scenario we have chosen, the nine random variables can be further simplified. The first components of the three targets are identical specular reflectors, the second components of the first and the second targets are also identical specular reflectors, and the third components of the second and the third targets are dihedral reflectors. Thus we have $a_{11} = a_{21} = a_{31}$, $a_{12} = a_{22}$, $a_{23} = a_{33}$. Second, because the location of the second component is far enough from that of the third component that the orthogonality condition holds, it can be shown that a_{13} is independent of a_{12} and a_{32}. Likewise, a_{23} is independent of a_{12} and a_{32}. Third, most of the energy from the specular reflector comes as a co-polarized return, whereas most of the energy for the dihedral comes as a cross-polarized return. The resolution lengths of these two returns are also different. So it can be shown that these two returns are approximately orthogonal to each other, which implies that a_{13} is independent of a_{23}, and a_{12} is independent of a_{32}. The above pairwise independence conditions guarantee that the four random variables a_{12}, a_{13}, a_{23}, and a_{32} are independent of one another. Based on these facts, we can express the four complex random variables as follows:

$$\begin{aligned} a_{13} &\approx w_{13} + e^{i\phi_3} E_s, \\ a_{23} &\approx w_{23}, \\ a_{12} &\approx w_{12} + e^{i\phi_2} E_s, \\ a_{32} &\approx w_{32}, \end{aligned} \tag{6.5}$$

where ϕ_2 and ϕ_3 are independent random variables uniformly distributed within $[0, 2\pi)$, and w_{13}, w_{23}, w_{12}, w_{32} are mutually independent complex Gaussian random variables:

$$w_{13} \sim N(0, E_s),$$

$$w_{23} \sim N(0, E_d),$$

$$w_{12} \sim N(0, E_s),$$

$$w_{32} \sim N(0, E_d). \tag{6.6}$$

Moreover, we can express v_1, v_2, and v_3 in terms of random variables $\{a_{11}, a_{12}, a_{13}, a_{23}, a_{32}\}$:

$$v_1 = e^{-3E_s} I_0(2|a_{11}|) I_0(2|a_{12}|) I_0(2|a_{13}|),$$

$$v_2 = e^{-2E_s - E_d} I_0(2|a_{11}|) I_0(2|a_{12}|) I_0(2|a_{23}|),$$

$$v_3 = e^{-E_s - 2E_d} I_0(2|a_{11}|) I_0(2|a_{32}|) I_0(2|a_{23}|), \tag{6.7}$$

Notice that the a_{11} dependence is common to v_1, v_2, and v_3. So in order to obtain the probability of correct classification, it is not necessary to have the distribution of a_{11}.

According to (6.5) through (6.7), the probability of correct classification for target 1 is

$$\begin{aligned}\Pr\{\text{say}H_1|H_1\} &= \Pr\{v_1 > v_2 \ \&\ v_1 > v_3|H_1\} \\ &= \Pr\{e^{-E_s} I_0(2|a_{13}|) > e^{-E_d} I_0(2|a_{23}|) \\ &\quad \&\ e^{-2E_s} I_0(2|a_{12}|) I_0(2|a_{13}|) > e^{-E_d} I_0(2|a_{32}|) I_0(2|a_{23}|)|H_1\}.\end{aligned} \tag{6.8}$$

The computation of probability $\Pr\{\text{say}H_1|H_1\}$ in (6.7) is still time-consuming since the second condition $e^{-2E_s} I_0(2|a_{12}|) I_0(2|a_{13}|) > e^{-E_d} I_0(2|a_{32}|) I_0(2|a_{23}|)$ specifies an intertwined integration domain in four dimensions. To simplify the calculation, we will bound this probability from above and below, rather than work on an exact evaluation. Combining the second condition with the first condition in (6.8), it can be shown that

$$\begin{aligned}&\Pr\{e^{-E_s} I_0(2|a_{13}|) > e^{-E_d} I_0(2|a_{23}|) \ \&\ e^{-2E_s} I_0(2|a_{12}|) > e^{-E_d} I_0(2|a_{32}|))|H_1\} \\ &\leq \Pr\{\text{say}H_1|H_1\} \leq \Pr\{e^{-E_s} I_0(2|a_{13}|) > e^{-E_d} I_0(2|a_{23}|)|H_1\}.\end{aligned} \tag{6.9}$$

Moreover, from the fact that a_{13} and a_{23} are approximately independent of a_{12} and a_{32}, we can express these bounds on $Pr\{\text{say}H_1|H_1\}$ in (6.9) as follows:

$$\Pr\{e^{-E_s} I_0(2|a_{13}|) > e^{-E_d} I_0(2|a_{23}|) \mid H_1\} \times \Pr\{e^{-2E_s} I_0(2|a_{12}|) > e^{-E_d} I_0(2|a_{32}|)) \mid H_1\}$$

$$\leq \Pr\{\text{say}H_1|H_1\} \leq \Pr\{e^{-E_s}I_0(2|a_{13}|) > e^{-E_d}I_0(2|a_{23}|) \mid H_1\}. \tag{6.10}$$

By plugging the statistics in (6.6) and (6.7) into (6.10), we can obtain the exact numerical values for the upper and lower bounds on $\Pr\{\text{say}H_1|H_1\}$. Define

$$Q_1 \equiv \int\int_{e^{-E_s}I_0(2\sqrt{E_s x})>e^{-E_d}I_0(2\sqrt{E_d y})} dx\ dy\ e^{-x}e^{-y}e^{-E_s}I_0(2\sqrt{E_s x}). \tag{6.11}$$

Then (6.10) is equivalent to:

$$Q_1^2 \leq \Pr\{\text{say}H_1|H_1\} \leq Q_1. \tag{6.12}$$

From similar arguments, we can also obtain the exact value for the probability of correct classification for target 2, and upper and lower bounds for the probability of correct classification for target 3. Define

$$Q_2 \equiv \int\int_{e^{-E_d}I_0(2\sqrt{E_d x})>e^{-E_s}I_0(2\sqrt{E_s y})} dx\ dy\ e^{-x}e^{-y}e^{-E_d}I_0(2\sqrt{E_d x}). \tag{6.13}$$

It can be shown that

$$\Pr\{\text{say}H_2|H_2\} = Q_1Q_2, \tag{6.14}$$

and

$$Q_2^2 \leq \Pr\{\text{say}H_3|H_3\} \leq Q_2. \tag{6.15}$$

From (6.12), (6.14), and (6.15), we can obtain the bounds for the average probability of correct classification PCC:

$$\frac{1}{3}(Q_1^2 + Q_1Q_2 + Q_2^2) \leq \text{PCC} \leq \frac{1}{3}(Q_1 + Q_1Q_2 + Q_2), \tag{6.16}$$

where equally likely hypotheses have been assumed.

For the target scenario given in Table 6.1, clutter-to-noise-ratio CNR $= 3.14 \times 10^{-2}$, radar and flight parameters given in Table 3.1, the probability of average correct classification (calculated by using (6.16)) is between 0.9949 and 0.9966 for spotlight-mode operation, and between 0.8907 and 0.9260 for stripmap-mode operation. These values are higher than

the values obtained from the independent-v_i assumption (0.578 for spotlight-mode operation and 0.534 for stripmap-mode operation). Thus, the marginal probability densities for the detector-bank outputs alone are not adequate to evaluate the probability of correct classification. Figure 6.4 plots the upper and lower bounds for the average probability of correct classification with respect to clutter-to-noise-ratio. In the figure, the quantity 1/CNR measures the intensity of noise level with respect to a fixed clutter level. The larger 1/CNR is, the higher the noise level is. As indicated in the figure, both the upper bound and the lower bound for the probability of correct recognition decrease with increasing noise level. This is consistent with our intuition: when the noise intensity is higher, the target classifier performance is more seriously degraded. However, neither the upper bound nor the lower bound for the probability of correct classification decreases indefinitely with increasing noise intensity. Instead, they converge asymptotically to constant values (0.41 for upper bound and 0.25 for lower bound). Such asymptotic behavior can be explained as follows. At very high noise level, the target-return signatures in the radar signal are totally obscured by the additive random noise. The radar returns from different types of targets cannot be distinguished, in this limit, by the target classifier. Therefore the classification operation simply becomes a blind guess, which has a 1/3 probability of being correct for the three-target example. Interestingly, 1/3 is the mean of the asymptotic upper bound 0.41 and lower bound 0.25.

The above theory of classification performance analysis is for deterministic targets. The formulation (6.16) can be easily extended to the case of targets with unknown positions. Consider the same three targets, but let each component of each target have an uniformly random uncertainty designated by specification 2 of Figure 5.10. By replacing the probability density functions of a_{23} and a_{32} in (6.5) (which are complex Gaussian random variables) with the level-crossing probability density function developed in Section 5.3.2.3, we can use the same approach embodied by (6.4) through (6.16) to evaluate the upper and lower bounds for

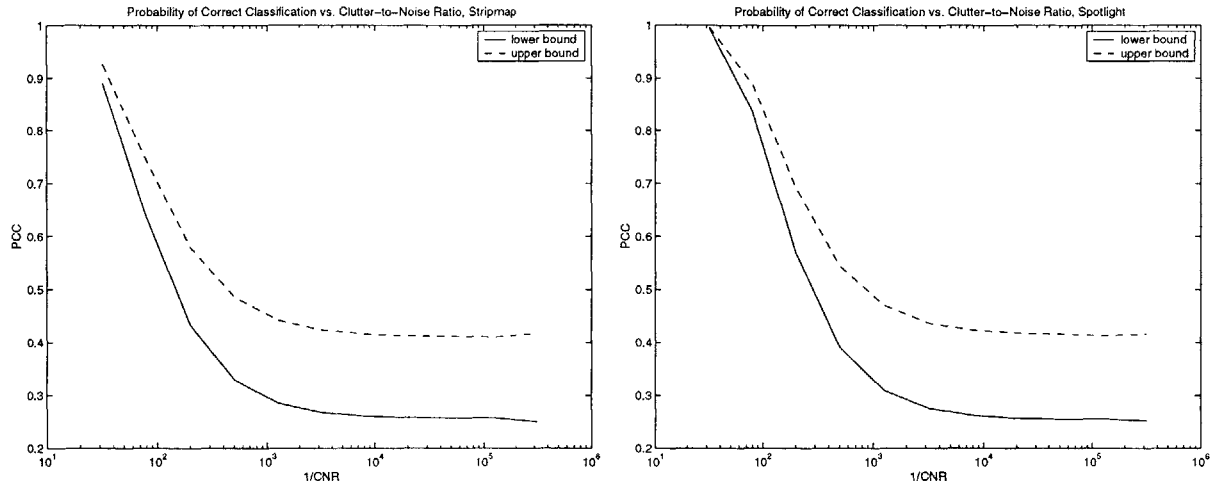

Figure 6.4 Upper and lower bounds for probability of correct recognition versus clutter-to-noise-ratio (CNR). The target scenario is specified in Table 6.1. The flight and radar parameters are specified in Table 3.1. The Neyman-Pearson-detector-based classifier is used. The left panel corresponds to stripmap-mode operation and the right panel corresponds to spotlight-mode operation. The solid and the dashed curves correspond to the PCC lower bounds and upper bounds, respectively.

the average probability of correct classification. For spotlight-mode operation, the average probability of correct classification is between 0.797 and 0.858; for stripmap-mode operation, the average probability of correct classification is between 0.694 and 0.783. Naturally, these values are smaller than their deterministic-target counterparts.

A conventional SAR target classifier can be similarly constructed by paralleling the conventional SAR target detectors associated with the target types of concern. By following the procedures similar to those used in Eqs. (6.4) through (6.16), we can also calculate an upper bound and a lower bound for the conventional SAR classifier's performance for the three targets specified in Table 6.1. There are, however, some differences in the performance-calculation procedure for conventional SAR classifier compared to that for the Neyman-Pearson classifier. First, as a result of Figure 5.21 (a), the three output levels from

conventional SAR detectors, v_1', v_2', and v_3', are (cf. (6.4))

$$v_1' = e^{-3E_s} I_0(2K_{11}|a_{11}'|) I_0(2K_{12}|a_{12}'|) I_0(2K_{13}|a_{13}'|),$$

$$v_2' = e^{-2E_s - E_d} I_0(2K_{21}|a_{21}'|) I_0(2K_{22}|a_{22}'|) I_0(2K_{23}|a_{23}'|),$$

$$v_3' = e^{-E_s - 2E_d} I_0(2K_{31}|a_{31}'|) I_0(2K_{32}|a_{32}'|) I_0(2K_{33}|a_{33}'|), \tag{6.17}$$

where $K_{ij} = 2\text{SNCR}_{ij}/|S_{ij}|$, SNCR_{ij} is the SNCR of the j^{th} component of target i, S_{ij} is the sampled target-return complex envelope of the j^{th} component of target i after conventional SAR imaging, E_s and E_d are the SNCRs of specular-reflector and dihedral-reflector returns, respectively.

Second, the complex samples a_{ij}' of the conventional SAR classifier have different behavior from their counterparts a_{ij} of the Neyman-Pearson processor. For example, under H_1 condition, we can express a_{12}', a_{13}', a_{23}', and a_{32}' as follows:

$$a_{13}' \approx w_3 + e^{i\phi_3} G_s,$$

$$a_{23}' \approx w_3 + e^{i\phi_3} G_s,$$

$$a_{12}' \approx w_2 + e^{i\phi_2} G_s,$$

$$a_{32}' \approx w_2 + e^{i\phi_2} G_s, \tag{6.18}$$

where G_s is the sampled target-return complex envelope of the specular reflector. w_2 and w_3 are independent zero-mean Gaussian random variables with identical variances. Unlike (6.5), here: (i) the specular target-return is also present in a_{23}' and a_{32}'; and (ii) the random parts of the (a_{13}', a_{23}') pair or (a_{12}', a_{32}') pair, are identical (w_3 or w_2) rather than independent of each other. These differences are due to the fact that the conventional SAR classifier uses a common imager rather than distinctive matched filters for specular-reflector and dihedral-reflector returns.

Applying (6.17) and (6.18) to the procedures from (6.8) through (6.16), we can calculate the upper bound and the lower bound for the probability of correct classification for the conventional SAR classifier. The results are as follows:

$$\frac{1}{3}(Q_1'^2 + Q_1'Q_2' + Q_2'^2) \leq \text{PCC} \leq \frac{1}{3}(Q_1' + Q_1'Q_2' + Q_2'), \tag{6.19}$$

where

$$Q_1' \equiv \int_{e^{-E_s} I_0(2\sqrt{E_s x}) > e^{-E_d} I_0(2\sqrt{E_d x})} dx\ e^{-x} e^{-E_s} I_0(2\sqrt{E_s x}), \tag{6.20}$$

$$Q_2' \equiv \int_{e^{-E_d} I_0(2\sqrt{E_d x}) > e^{-E_s} I_0(2\sqrt{E_s x})} dx\ e^{-x} e^{-E_d} I_0(2\sqrt{E_d x}). \tag{6.21}$$

Figure 6.5 compares the Neyman-Pearson classifier's and conventional SAR classifier's PCC upper and lower bounds as functions of the clutter-to-noise-ratio. The target-scenario parameters are specified in Table 6.1. It is clear in the figure that both the PCC upper bound and lower bound of the conventional SAR classifier are lower than those of the Neyman-Pearson classifier. We see that the conventional SAR processor has a PCC upper bound that is lower than the Neyman-Pearson processor's PCC lower bound for $1/\text{CNR} > 100$ in stripmap-mode operation and $1/\text{CNR} > 300$ in spotlight-mode operation. In this good-performance region, we have thus proven that the Neyman-Pearson processor is better than the conventional SAR processor, even though we did not obtain exact performance results for either.

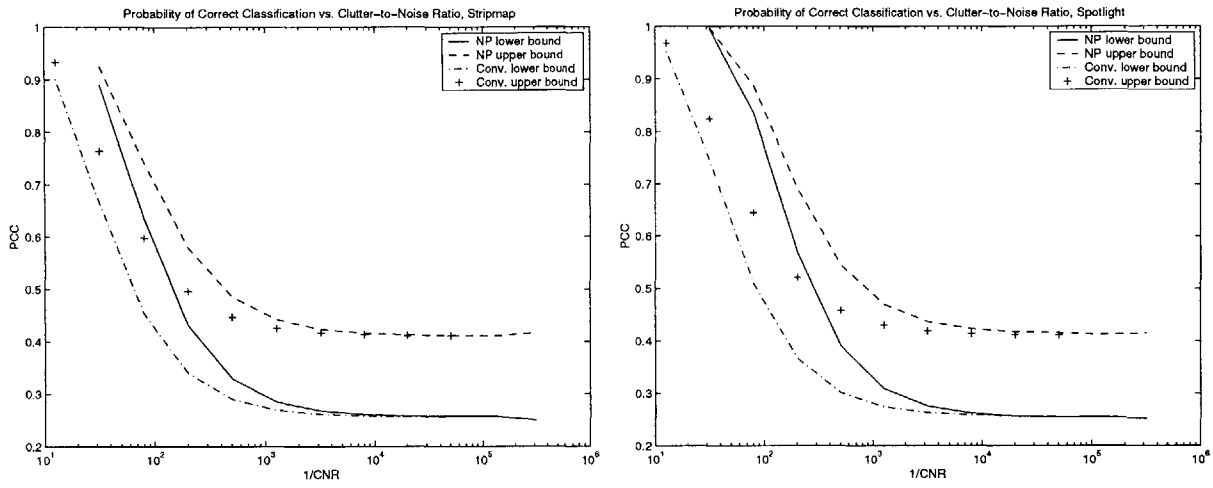

Figure 6.5 Upper and lower bounds for probability of correct recognition versus clutter-to-noise-ratio (CNR). The parameter specification is identical to the one in Figure 6.4. Both conventional SAR classifier and Neyman-Pearson classifier are considered. The left panel corresponds to stripmap-mode operation and the right panel corresponds to spotlight-mode operation. The solid, dashed, dashed-dot, and cross curves correspond to the PCC lower bounds of the Neyman-Pearson classifier, the PCC upper bounds of the Neyman-Pearson classifier, the PCC lower bounds of the conventional SAR classifier, and the PCC upper bounds of the conventional SAR classifier classifier, respectively.

Chapter 7

Conclusions

This thesis developed a physics-based target recognition theory for synthetic aperture radar (SAR) images. The basic idea was to construct radar return signatures from electromagnetic scattering theory, and to apply conventional SAR processors, adaptive-resolution processors, and Neyman-Pearson processors to perform detection or recognition based on these radar signatures. The contribution of this study is not one of new efficient or powerful processing schemes for real radar data or complicated target signatures generated from CAD models. Instead, it seeks to theoretically quantify the target-recognition performance improvement of adaptive-resolution, polarimetric, or whitening-filter processing, and to provide physical interpretations for such advantages. Each individual chapter in this thesis is a construction block for this overarching framework.

In Chapter 2, we derived the radar return models for 2-D stripmap-mode SAR signatures. The radar return was assumed to have three components: single-component target return, clutter, and noise. To construct target return and clutter, the sensor (transmitter/receiver) model, electromagnetic wave propagation model from sensor to scatterers and vice versa, and the electromagnetic scattering model, were employed. A repertoire of simple reflectors were listed as the candidates for the single-component target. To calculate their scattering effects, we applied the physical optics or geometric optics approximation to the electromagnetic scattering theory. Clutter was assumed to be the radar return from a random rough surface. To obtain its statistics, we combined the Kirchhoff approximation for rough-surface scattering and a semi-empirical statistical model for the localized reflection coefficients.

In Chapter 3, we presented processor/detector schemes for 2-D stripmap-mode SAR images with a single-component target. The processors of concern included a full-resolution,

conventional 2-D stripmap SAR processor which consists of the chirp-compression filters along cross-range and range directions, an adaptive-resolution chirp-compression processor with variable processing durations for both filters, and a whitening-filter, Neyman-Pearson optimum processor. Performance analysis indicated that the variations of the cross-range image resolution lengths of an adaptive-resolution processor with respect to processing duration are different for different types of targets. We also observed that in order to have maximum signal-to-noise-plus-clutter ratio (SNCR), the cross-range processing duration of the adaptive-resolution processor should be shorter than that of the conventional SAR processor. The polarimetric effect and frequency-dispersion effect of electromagnetic scattering were observed from the SNCR behavior of a dihedral with respect to its orientation angle and the SNCR behavior of a dielectric volume with respect to the range processing duration. By comparing the SNCR values of the Neyman Pearson optimum processor and the optimized adaptive-resolution processor, it was shown that: (i) when noise dominates over clutter, these two processors are approximately identical, regardless of polarimetric factor; (ii) unlike the conclusion obtained from 1-D SAR work [6][23], the optimized adaptive-resolution processor cannot approximate the Neyman-Pearson optimum processor when clutter dominates over noise, no matter how large the target dimension is.

In Chapter 4, we presented processor/detector schemes for 2-D spotlight-mode SAR images with a single-component target. The processors of concern included a full-resolution, conventional 2-D spotlight SAR processor which consists of the de-chirped compensation, polar formatting, and Fourier transformation blocks, an adaptive-resolution chirp-compression processor with variable Fourier-transformation durations for both dimensions, and a whitening-filter, Neyman-Pearson optimum processor. Performance analysis indicated that the variations of both cross-range and range image resolution lengths for the same target repertoire are different between spotlight-mode and stripmap-mode operations. The advantage of adaptive-resolution processing in enhancing SNCR was also observed in spotlight-mode op-

eration; the optimum cross-range processing duration is different from that of the stripmap-mode, though. Except for certain minor differences, the spotlight-mode SNCR behaviors with respect to processing durations, target orientations, and in terms of comparison of the optimum Neyman-Pearson processor and the optimized adaptive-resolution processor, are quite similar to those of the stripmap-mode case.

In Chapter 5, the single-component SAR target detection theory developed in previous chapters was extended to detection problems for multi-component targets. Four target scenarios were considered: a target with random component phases; a target with random component phases and positions; a target with random component phases, positions, and radar-return amplitudes; and a target with random pose. For the first scenario, we derived the likelihood-ratio detector, sum-amplitude detector, and sum-amplitude-square detector associated with Neyman-Pearson processor (whitening-filter plus adaptive-resolution matched filter), the conventional SAR processor, and the Neyman-Pearson processor with no polarimetric factor. For the other three scenarios, we developed the generalized likelihood-ratio detector or approximate generalized likelihood-ratio detector. To evaluate the detection performance for a multi-component target with position randomness, we proposed an approximate 2-D level-crossing theory based on the analytic 1-D level-crossing formula as well as 1-D resolution-bin approximation, and we verified this theory with Monte Carlo simulations. Performance analysis indicated that as the degree of randomness increases, target detection performance degrades. Furthermore, it was seen that the performance improvement of the Neyman-Pearson processor over the conventional SAR processor which is due to the adaptive-resolution effect, the polarimetric effect, or their combination of both could be very significant.

In Chapter 6, we developed a multi-component target classification scheme based on the detection schemes in Chapter 5. Such classifier contains a bank of target detectors that calculate the likelihood ratio of a specific target condition with respect to the clutter-plus-

noise condition, and a selector that picks the maximum among the individual-detector output levels. A preliminary performance analysis of this target classifier was given for a specific target repertoire. The marginal probability density functions associated with the detection block outputs were compared, and upper and lower bounds for the average probability of correct classification pertinent in this specific target scenario were derived.

A couple of future directions can be exploited based on this research. First, a comprehensive and rigorous performance analysis for the target classifiers in Chapter 6 is lacking. The analysis scheme and results in Chapter 6 provide reasonable heuristic understanding of the performances of Neyman-Pearson and conventional SAR likelihood-ratio target classifiers, but more precise information regarding the probability of correct recognition (PCR) [43-45] is needed. It is both theoretically and computationally involved to calculate the PCR for a repertoire of spatially overlapped targets, because the classifier output signals from the detector bank are then correlated with one another. To work on a comprehensive classification performance, one has to come up with a simplification scheme for this issue.

The other direction is consideration of the layover problem. Synthetic aperture radars map the geometric constellation of 3-D space onto a 2-D plane. That means two different points in physical space may be mapped into the same point on the image plane. For a ground-looking radar, layover occurs when an object elevated from the ground level, but still within the radar beamwidth, is registered in image space over a point on the ground plane. Layover casts radar returns at positions where they are not supposed to be. In this sense, it may be regarded as a kind of clutter. One can use the physics-based approach in this thesis to understand the characteristics of layover signals, and try to develop useful schemes to suppress them. One of the primary issues will be to identify whether a radar return is due to layover. From previous studies [46-48], it is known that layover can only be identified and its exact characteristics (such as the height of the scatterer) be retrieved via radar returns from two or more observation directions. Based on this perspective, spotlight-mode SAR

that collects the complete radar-return phase history of a fixed region from a wide range of viewing angles may be a potential tool for the further dealing with the layover phenomenon. A demonstration of this potential appears in [46]. At different viewing angles the high-rising scatterer is laid over different points on the ground, the spotlight phase history of its return signature after registration is not stationary within a limited region, which is different from the radar return of a scatterer on the ground.

The multi-component target articulation problem is also a worthwhile topic to pursue. In this thesis, the target-component position uncertainties we considered were either mutally independent or bound together as a whole such that only one degree of freedom was left. In the real world, some multi-component targets have a more complicated arrangement for position uncertainties. In such arrangement, target components are divided into several groups. The components in each group are bound together and may have a pose uncertainty. But the pose uncertainities of different groups are mutually independent. An example for this type of target is a tank with a rotatable turrent. The analytical tools developed in this thesis are able to deal with this problem, even though we have to construct a more elaborate generalized likelihood ratio detector that takes all the independent pose uncertainities into account.

Appendix A

Dihedral Scattering

The bistatic scattering tensor of a right-angle dihedral reflector is obtained by calculating the scattered field for a given incident plane wave. For convenience, we will start in the local coordinate system defined by the orientation of the dihedral reflector.

A.1 Scattering Tensor of a Dihedral Reflector

As indicated in Figure A.1, the local rectangular coordinates for the right-angle dihedral reflector as defined by the dihedral axis $\hat{z}_b$, and two directions $\hat{x}_b$ and $\hat{y}_b$ corresponding to the wedge formed by its two plates. Plate 1 is on the plane defined by $\hat{x}_b$ and $\hat{z}_b$, and plate 2 is on the plane defined by $\hat{y}_b$ and $\hat{z}_b$. The edge lengths of the dihedral along $\hat{x}_b$, $\hat{y}_b$, and $\hat{z}_b$ directions are l_x, l_y and l_z, respectively.

Suppose the incident electric field is a monochromatic plane wave with the phasor

$$\bar{\bar{E}}_i(\bar{r}) = \bar{E}_{i0} e^{ik\hat{k}_i \cdot \bar{r}}, \tag{A.1}$$

where

$$-\hat{k}_i = \hat{x}_b \sin(\theta_i)\cos(\phi_i) + \hat{y}_b \sin(\theta_i)\sin(\phi_i) + \hat{z}_b \cos(\theta_i), \tag{A.2}$$

and θ_i and ϕ_i are measured with respect to the local coordinates. Similar to [26], we only include the single-scattering terms and double-scattering terms in the expression for the overall scattered field $\bar{\bar{E}}_s(\bar{r})$. Hence

$$\bar{\bar{E}}_s(\bar{r}) \approx \bar{\bar{E}}_1(\bar{r}) + \bar{\bar{E}}_2(\bar{r}) + \bar{\bar{E}}_{12}(\bar{r}) + \bar{\bar{E}}_{21}(\bar{r}). \tag{A.3}$$

In this expression, $\bar{\bar{E}}_1$ is the single-scattering field from the surface current on plate 1, which is directly induced by the incident field $\bar{\bar{E}}_i$; $\bar{\bar{E}}_2$ is the single-scattering field from the surface

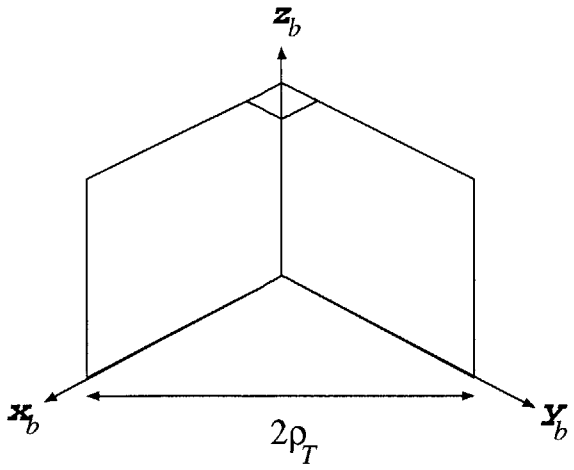

Figure A.1 The right-angle dihedral reflector.

current on plate 2, which is directly induced by the incident field $\bar{\bar{E}}_i$; $\bar{\bar{E}}_{12}$ is the double-scattering field from the surface current on plate 2, which is induced by the single-scattering field from plate 1; and $\bar{\bar{E}}_{21}$ is the double-scattering field from the surface current on plate 1, which is induced by the single-scattering field from plate 2.

The single-scattering term $\bar{\bar{E}}_1$ is obtained from the physical optics approximation:

$$\begin{aligned}\bar{\bar{E}}_1(\bar{r}_s) &\approx i\mu_0\Omega(\bar{\bar{I}} - \hat{r}_s\hat{r}_s)\cdot\frac{e^{ikr_s}}{4\pi r_s}\int\int_I d\bar{r}' 2\hat{n}_1 \times \bar{H}_i(\bar{r}')e^{-ik\hat{r}_s\cdot\bar{r}'} \\ &= \frac{i\mu_0\Omega}{2\pi\eta}\frac{e^{ikr_s}}{r_s}\exp\{-ik[(\sin(\theta_i)\cos(\phi_i)+\sin(\theta_s)\cos(\phi_s))l_x/2+(\cos(\theta_i)+\cos(\theta_s))l_z/2]\} \\ &\quad\times(\bar{\bar{I}} - \hat{r}_s\hat{r}_s)\cdot[\hat{k}_i\hat{y}_b - (\hat{k}_i\cdot\hat{y}_b)\bar{\bar{I}}]\; l_x l_z\;\mathrm{sinc}[k(\sin(\theta_i)\cos(\phi_i)+\sin(\theta_s)\cos(\phi_s))l_x/2] \\ &\quad\times\mathrm{sinc}[k(\cos(\theta_i)+\cos(\theta_s))l_z/2]\cdot\bar{E}_{i0}, \qquad (A.4)\end{aligned}$$

where $\bar{H}_i = \hat{k}_i \times \bar{E}_i/\eta$ is the incident magnetic field, and the normal direction of plate 1 $\hat{n}_1 = \hat{y}_b$. The surface integral in (A.4) was evaluated by substituting in the expression for $\bar{H}_i$, shifting the local coordinate center of $\bar{r}'$ to the center of plate 1, and integrating the result.

Similar to $\bar{\bar{E}}_1$, the single-scattering term $\bar{\bar{E}}_2$ is also obtained from the physical optics approximation. The result is

$$\bar{\bar{E}}_2(\bar{r}_s) \approx \frac{i\Omega\mu_0}{2\pi\eta}\frac{e^{ikr_s}}{r_s}\exp\{-ik[(\sin(\theta_i)\sin(\phi_i)+\sin(\theta_s)\sin(\phi_s))l_y/2+(\cos(\theta_i)+\cos(\theta_s))l_z/2]\}$$
$$\times(\bar{\bar{I}}-\hat{r}_s\hat{r}_s)\cdot[\hat{k}_i\hat{x}_b-(\hat{k}_i\cdot\hat{x}_b)\bar{\bar{I}}]\; l_y l_z\;\mathrm{sinc}[k(\sin(\theta_i)\sin(\phi_i)+\sin(\theta_s)\sin(\phi_s))l_y/2]$$
$$\times\mathrm{sinc}[k(\cos(\theta_i)+\cos(\theta_s))l_z/2]\cdot\bar{E}_{i0}, \tag{A.5}$$

To calculate the double-scattering term $\bar{\bar{E}}_{12}$, we first obtain the (single) scattered field $\bar{\bar{E}}_{r1}$ from plate 1, and then use it as the incident field to calculate the scattering field from plate 2. Based on the argument in [26], the field $\bar{\bar{E}}_{r1}$ is obtained from geometric optics. Assuming that the wavelength of the electromagnetic wave is much smaller than the size of plate 1, $\bar{\bar{E}}_{r1}$ can be modeled as the reflected field of the incident plane wave $\bar{\bar{E}}_i$ from an infinitely-large, perfectly-conducting plane. Thus we have

$$\bar{\bar{E}}_{r1}(\bar{r}) \approx (-\hat{h}_{r1}\hat{h}_{i1}+\hat{v}_{r1}\hat{v}_{i1})\cdot\bar{E}_{i0}e^{ik\hat{k}_{r1}\cdot\bar{r}}, \tag{A.6}$$

where

$$\hat{h}_{i1} = \frac{\hat{k}_i\times\hat{y}_b}{|\hat{k}_i\times\hat{y}_b|} \tag{A.7}$$

$$\hat{v}_{i1} = \hat{k}_i\times\hat{h}_{i1} \tag{A.8}$$

$$\hat{k}_{r1} = -\hat{x}_b\sin(\theta_i)\cos(\phi_i)+\hat{y}_b\sin(\theta_i)\sin(\phi_i)-\hat{z}_b\cos(\theta_i), \tag{A.9}$$

$$\hat{h}_{r1} = \hat{h}_{i1} \tag{A.10}$$

$$\hat{v}_{r1} = \hat{k}_{r1}\times\hat{h}_{r1} \tag{A.11}$$

However, no matter how much larger plate 1 is compared to the electromagnetic wavelength, it is not truly infinite. From geometric optics, the collection of all the rays reflected from a finite plate does not permeate all of space, but rather forms a conical bundle. Hence it is probable that the reflected rays from plate 1 do not irradiate all of plate 2. From ray

tracing, we find that the area on the $\hat{y}_b$-$\hat{z}_b$ plane that is irradiated by the reflected field $\bar{\bar{E}}_{r1}$ is a parallelogram with corner points $(y_b, z_b) = (0,0)$, $(0, l_z)$, $(l_x \tan(\phi_i), -l_x \cot(\theta_i)\sec(\phi_i))$, and $(l_x \tan(\phi_i), l_z - l_x \cot(\theta_i)\sec(\phi_i))$.

The double-scattering field $\bar{\bar{E}}_{12}$ induced by the field $\bar{\bar{E}}_{r1}$ on plate 2 is calculated from the physical optics approximation. The incident field that induces surface current on plate 2 is expressed in (A.6), but the domain over which the surface integral is carried out is the irradiated area of plate 2 rather than the whole plate. This area turns out to be a trapezoid bounded by the corner points: $(y_b, z_b) = (0,0)$, $(0, l_z)$, $(\min[l_y, l_x \tan(\phi_i)]$, $\max[0, -l_x \cot(\theta_i)\sec(\phi_i)])$, and $(\min[l_y, l_x \tan(\phi_i)], l_z - \min[0, -l_x \cot(\theta_i)\sec(\phi_i)])$. Therefore the double-scattering term $\bar{\bar{E}}_{12}(\bar{r})$ is

$$\bar{\bar{E}}_{12}(\bar{r}_s) \approx \frac{i\Omega\mu_0}{2\pi\eta}\frac{e^{ikr_s}}{r_s}\exp\{ik[(\sin(\theta_i)\sin(\phi_i) - \sin(\theta_s)\sin(\phi_s))l_y/2 - (\cos(\theta_i) + \cos(\theta_s))l_z/2]\}$$

$$\times(\bar{\bar{I}} - \hat{r}_s\hat{r}_s)\cdot[\hat{k}_{r1}\hat{x}_b - (\hat{k}_{r1}\cdot\hat{x}_b)\bar{\bar{I}}]\cdot(-\hat{h}_{r1}\hat{h}_{i1} + \hat{v}_{r1}\hat{v}_{i1})$$

$$\times\{\ \frac{1}{ik_z}\exp\left[ik_z\left(\beta - \alpha\frac{\beta - \frac{l_z}{2}}{\alpha + \frac{l_y}{2}}\right)\right]\frac{\exp\left[i\left(k_y + k_z\frac{\beta-\frac{l_z}{2}}{\alpha+\frac{l_y}{2}}\right)\alpha\right] - \exp\left[i\left(k_y + k_z\frac{\beta-\frac{l_z}{2}}{\alpha+\frac{l_y}{2}}\right)(-\frac{l_y}{2})\right]}{i\left(k_y + k_z\frac{\beta-\frac{l_z}{2}}{\alpha+\frac{l_y}{2}}\right)}$$

$$-\frac{1}{ik_z}\exp\left[ik_z\left(\gamma - \alpha\frac{\gamma + \frac{l_z}{2}}{\alpha + \frac{l_y}{2}}\right)\right]\frac{\exp\left[i\left(k_y + k_z\frac{\gamma+\frac{l_z}{2}}{\alpha+\frac{l_y}{2}}\right)\alpha\right] - \exp\left[i\left(k_y + k_z\frac{\gamma+\frac{l_z}{2}}{\alpha+\frac{l_y}{2}}\right)(-\frac{l_y}{2})\right]}{i\left(k_y + k_z\frac{\gamma+\frac{l_z}{2}}{\alpha+\frac{l_y}{2}}\right)}\ \}$$

$$\cdot\bar{E}_{i0}, \qquad (A.12)$$

for $\cot(\theta_i)\sec(\phi_i) > -l_z/l_x$ and $\sin(\theta_i)\cos(\phi_i) > 0$, where

$$k_y = k[\sin(\theta_i)\sin(\phi_i) - \sin(\theta_s)\sin(\phi_s)], \qquad (A.13)$$

$$k_z = -k[\cos(\theta_i) + \cos(\theta_s)], \qquad (A.14)$$

$$\alpha = \min[l_y, l_x \tan(\phi_i)] - l_y/2, \qquad (A.15)$$

$$\beta = -\min[0, -l_x \cot(\theta_i)\sec(\phi_i)] + l_z/2, \qquad (A.16)$$

$$\gamma = \max[0, -l_x \cot(\theta_i)\sec(\phi_i)] - l_z/2, \qquad (A.17)$$

For $\cot(\theta_i)\sec(\phi_i) \leq -l_z/l_x$ or $\sin(\theta_i)\cos(\phi_i) \leq 0$, we get $\bar{\bar{E}}_{12}(\bar{r}_s) \approx 0$.

Similar to $\bar{\bar{E}}_{12}$, the double-scattering term $\bar{\bar{E}}_{21}$ can also be obtained from the geometric optics and physical optics approximations. The result is

$$\bar{\bar{E}}_{21}(\bar{r}_s) \approx \frac{i\Omega\mu_0}{2\pi\eta}\frac{e^{ikr_s}}{r_s}\exp\{ik[(\sin(\theta_i)\cos(\phi_i) - \sin(\theta_s)\cos(\phi_s))l_x/2 - (\cos(\theta_i) + \cos(\theta_s))l_z/2]\}$$

$$\times(\bar{\bar{I}} - \hat{r}_s\hat{r}_s)\cdot[\hat{k}_{r1}\hat{y}_b - (\hat{k}_{r1}\cdot\hat{y}_b)\bar{\bar{I}}]\cdot(-\hat{h}_{r2}\hat{h}_{i2} + \hat{v}_{r2}\hat{v}_{i2})$$

$$\times\{\ \frac{1}{ik_z}\exp\left[ik_z\left(\beta' - \alpha'\frac{\beta' - \frac{l_z}{2}}{\alpha' + \frac{l_x}{2}}\right)\right]\frac{\exp\left[i\left(k_x + k_z\frac{\beta' - \frac{l_z}{2}}{\alpha' + \frac{l_x}{2}}\right)\alpha'\right] - \exp\left[i\left(k_x + k_z\frac{\beta' - \frac{l_z}{2}}{\alpha' + \frac{l_x}{2}}\right)(-\frac{l_x}{2})\right]}{i\left(k_x + k_z\frac{\beta' - \frac{l_z}{2}}{\alpha' + \frac{l_x}{2}}\right)}$$

$$-\frac{1}{ik_z}\exp\left[ik_z\left(\gamma' - \alpha'\frac{\gamma' + \frac{l_z}{2}}{\alpha' + \frac{l_x}{2}}\right)\right]\frac{\exp\left[i\left(k_x + k_z\frac{\gamma' + \frac{l_z}{2}}{\alpha' + \frac{l_x}{2}}\right)\alpha'\right] - \exp\left[i\left(k_x + k_z\frac{\gamma' + \frac{l_z}{2}}{\alpha' + \frac{l_x}{2}}\right)(-\frac{l_x}{2})\right]}{i\left(k_x + k_z\frac{\gamma' + \frac{l_z}{2}}{\alpha' + \frac{l_x}{2}}\right)}\ \}$$

$$\cdot\bar{E}_{i0}, \tag{A.18}$$

for $\cot(\theta_i)\csc(\phi_i) > -l_z/l_y$ and $\sin(\theta_i)\sin(\phi_i) > 0$, where

$$\hat{h}_{i2} = \frac{\hat{k}_i \times \hat{x}_b}{|\hat{k}_i \times \hat{x}_b|} \tag{A.19}$$

$$\hat{v}_{i2} = \hat{k}_i \times \hat{h}_{i2} \tag{A.20}$$

$$\hat{k}_{r2} = \hat{x}_b\sin(\theta_i)\cos(\phi_i) - \hat{y}_b\sin(\theta_i)\sin(\phi_i) - \hat{z}_b\cos(\theta_i), \tag{A.21}$$

$$\hat{h}_{r2} = \hat{h}_{i2} \tag{A.22}$$

$$\hat{v}_{r2} = \hat{k}_{r2} \times \hat{h}_{r2} \tag{A.23}$$

$$k_x = k[\sin(\theta_i)\cos(\phi_i) - \sin(\theta_s)\cos(\phi_s)], \tag{A.24}$$

$$\alpha' = \min[l_x, l_y\cot(\phi_i)] - l_x/2, \tag{A.25}$$

$$\beta' = -\min[0, -l_y\cot(\theta_i)\csc(\phi_i)] + l_z/2, \tag{A.26}$$

$$\gamma' = \max[0, -l_y\cot(\theta_i)\csc(\phi_i)] - l_z/2, \tag{A.27}$$

For $\cot(\theta_i)\csc(\phi_i) \leq -l_z/l_y$ or $\sin(\theta_i)\sin(\phi_i) \leq 0$, we get $\bar{\bar{E}}_{21}(\bar{r}_s) \approx 0$.

Based on (2.17), the overall bistatic scattering tensor of a dihedral reflector is obtained from the scattered fields in (A.4), (A.5), (A.12) and (A.18).

A.2 Dihedral Orientation in a 2-D SAR Scenario

The orientation of a dihedral is defined by two mutually orthogonal vectors: the dihedral axis $\hat{z}_b$, and the bisecting direction of the 90° wedge, $(\hat{x}_b+\hat{y}_b)/\sqrt{2}$. These two vectors form a right-angle pair which can be arbitrarily pointed. In Chapter 2, we only considered a set of special cases in which the bisecting direction $(\hat{x}_b+\hat{y}_b)/\sqrt{2}$ is identical to the radar's nominal direction $\hat{z}'$. Even so, the dihedral axis $\hat{z}_b$ can be rotated on the $x-y'$ plane. Using ϕ to denote the angle between $\hat{z}_b$ and $\hat{x}$, we have that

$$\hat{x}_b = \frac{1}{\sqrt{2}}[\hat{z}' + \hat{y}'\cos(\phi) - \hat{x}\sin(\phi)], \tag{A.28}$$

$$\hat{y}_b = \frac{1}{\sqrt{2}}[\hat{z}' - \hat{y}'\cos(\phi) + \hat{x}\sin(\phi)], \tag{A.29}$$

$$\hat{z}_b = \hat{z}'. \tag{A.30}$$

Suppose the target on the ground is located at the nominal center, namely, the slant direction at $m=0$, from (2.14) and (A.2) the direction of the incident plane wave is then

$$\begin{aligned}\hat{k}_i &= -\hat{x}_b\sin(\theta_i)\cos(\phi_i) - \hat{y}_b\sin(\theta_i)\sin(\phi_i) - \hat{z}_b\cos(\theta_i)\\ &= \hat{r}_i \approx -\hat{z}' + \hat{x}mvT_s/L'.\end{aligned} \tag{A.31}$$

From (A.28), (A.29), (A.30), and (A.31), we can calculate θ_i, ϕ_i, θ_s and ϕ_s as follows:

$$\theta_i = \cos^{-1}(-\hat{k}_i\cdot\hat{z}_b) = \cos^{-1}(mvT_s\cos(\phi)/L'), \tag{A.32}$$

$$\phi_i = \cos^{-1}(-\hat{k}_i\cdot\hat{z}_b/\sin(\theta_i)) = \cos^{-1}\left[\frac{1/\sqrt{2}(1-mvT_s\sin(\phi)/L')}{\sqrt{1-\cos^2(\phi)(mvT_s/L')^2}}\right], \tag{A.33}$$

$$\theta_s = \theta_i, \quad \phi_s = \phi_i. \tag{A.34}$$

By plugging the results for θ_i, ϕ_i, θ_s, and ϕ_s from (A.32), (A.33) and (A.34) into (A.4), (A.5), (A.12) and (A.18), we obtain the scattering tensor when the dihedral is observed at the antenna locations determined by the 2-D SAR scenario. Notice when $l_x = l_y$ and the antenna position is close to $m = 0$ (i.e., $mvT_s/L' << 1$), we get

$$\bar{\bar{S}}_{12} \approx \bar{\bar{S}}_{21} \approx -\frac{i\mu_0\Omega}{2\sqrt{2}\pi\eta} \exp[-ikl_z \cos(\phi)(mvT_s/L')]$$

$$\times[(\hat{x}\cos(\phi) + \hat{y}'\sin(\phi))(\hat{x}\cos(\phi) + \hat{y}'\sin(\phi)) - (\hat{x}\sin(\phi) - \hat{y}'\cos(\phi))(\hat{x}\sin(\phi) - \hat{y}'\cos(\phi))]$$

$$l_x l_z \ \mathrm{sinc}[kl_z \cos(\phi)(mvT_s/L')], \tag{A.35}$$

$$\bar{\bar{S}}_1 \approx \bar{\bar{S}}_2 \approx 0 \tag{A.36}$$

Furthermore, in the Fraunhofer limit $kl_z \cos(\phi)/L' << 1$, the sinc function in (A.37) can be approximated by a Gaussian function $\exp[-(kl_z \cos(\phi)/L')^2(mvT_s)^2]$. This outcome, which is consistent with the radar return model for a dihedral in [23], implies that the footprint size of the radar return from the dihedral target varies with its orientation angle ϕ. When the aircraft flight path is perpendicular to the dihedral axis, namely at $\phi = 90°$, the dwell time for the target return is the largest.

Finally, from Figure 2.3, $l_x = l_y = l_z = \sqrt{2}\rho_t$.

Appendix B

Dielectric Volume Scattering

This appendix calculates the scattering tensor of a dielectric volume. As indicated in Figure 2.3, the dielectric volume is a homogeneous, rectangular body with thickness d and square top-bottom faces of edge length $2\rho_t$. Similar to the case of dihedral scattering, the bistatic scattering tensor of a dielectric volume is obtained by calculating the scattered field for a given incident plane wave. The volume scattering from a dielectric body can be conceived as a re-radiating process. For a monochromatic plane wave with the phasor $\bar{\bar{E}}_i(\bar{r}) = \bar{E}_{i0}e^{ik\hat{k}_i\cdot\bar{r}}$ incident upon the dielectric body V, a volume current density $\bar{\bar{J}}_{\text{ind}}(\bar{r})$ is induced within the scatterer. This induced current then produces the radiation field $\bar{\bar{E}}_s(\bar{r})$, in which

$$\bar{\bar{E}}_s(\bar{r}_s) = i\mu_0\Omega\int\int\int_V d\bar{r}'\bar{\bar{G}}(\bar{r},\bar{r}')\cdot\bar{\bar{J}}_{\text{ind}}(\bar{r}') \approx i\mu_0\Omega(\bar{\bar{I}}-\hat{r}_s\hat{r}_s)\cdot\frac{e^{ikr_s}}{4\pi r_s}\int\int\int_V d\bar{r}'e^{-ik\hat{r}_s\cdot\bar{r}'}\bar{\bar{J}}_{\text{ind}}(\bar{r}'). \tag{B.1}$$

The approximation shown holds in the far-field region $kr_s >> 1$. From [49], the induced current density $\bar{\bar{J}}_{\text{ind}}(\bar{r})$ has the following relationship with the electric field within the dielectric volume $\bar{\bar{E}}_{\text{int}}(\bar{r})$:

$$\bar{\bar{J}}_{\text{ind}}(\bar{r}) = -i\Omega(\epsilon_s-\epsilon_0)\bar{\bar{E}}_{\text{int}}(\bar{r}), \tag{B.2}$$

where ϵ_s is the permittivity of the dielectric body.

The internal field $\bar{\bar{E}}_{\text{int}}$ includes the incident field $\bar{\bar{E}}_i$ and the field radiated by the $\bar{\bar{E}}_i$-induced current density. In a rigorous approach, this quantity should be treated as an unknown in the radiation equation (B.1), which is an integral equation, and solved for via numerical methods such as the Method of Moments [49]. In this thesis, we adopt

an approximate analytical approach to avoid the complication of numerical methods: the infinite-layer approximation [27].

To calculate the internal field, the infinite-layer approximation assumes that the dielectric volume is a homogeneous horizontal layer bounded by free space at the top and the bottom. Defining the normal direction to the top-bottom planes of dielectric volume to be $\hat{z}_b$, we express the incident k-vector as

$$\bar{k}_i = k\hat{k}_i = \hat{\rho}_b k_{i\rho} - \hat{z}_b k_{iz}, \tag{B.3}$$

where

$$k_{i\rho}^2 + k_{iz}^2 = \Omega^2 \mu_0 \epsilon_0, \tag{B.4}$$

and $\hat{\rho}_b$ is the unit vector along the projection of $\bar{k}_i$ onto the surface perpendicular to $\hat{z}_b$.

For a plane wave incident upon such three-layer (free space-dielectric-free space) structure, the electromagnetic field inside the dielectric layer contains downgoing and upgoing plane waves whose propagation directions are determined by phase-matching conditions [25]. These directions are

$$\bar{k}_s = k\hat{k}_i = \hat{\rho}_b k_{i\rho} - \hat{z}_b k_{sz}, \tag{B.5}$$

$$\bar{K}_s = k\hat{k}_i = \hat{\rho}_b k_{i\rho} + \hat{z}_b k_{sz}, \tag{B.6}$$

where

$$k_{i\rho}^2 + k_{sz}^2 = \Omega^2 \mu_0 \epsilon_s. \tag{B.7}$$

Thus the internal electric field $\bar{\bar{E}}_{\text{int}}$ is [25][27]

$$\bar{\bar{E}}_{\text{int}}(\bar{r}) = \{(\hat{h}_A \hat{h}_i A_h + \hat{v}_A \hat{v}_i \sqrt{\epsilon_0/\epsilon_s} A_v) e^{i\bar{k}_s \cdot \bar{r}} + (\hat{h}_B \hat{h}_i B_h + \hat{v}_B \hat{v}_i \sqrt{\epsilon_0/\epsilon_s} B_v) e^{i\bar{K}_s \cdot \bar{r}}\} \cdot \bar{E}_{i0}, \tag{B.8}$$

where

$$A_h = \frac{2\left(1 + \frac{k_{iz}}{k_{sz}}\right) e^{-i(k_{iz}+k_{sz})d/2}}{\left(1 + \frac{k_{iz}}{k_{sz}}\right)\left(1 + \frac{k_{sz}}{k_{iz}}\right) e^{-ik_{sz}d} + \left(1 - \frac{k_{iz}}{k_{sz}}\right)\left(1 - \frac{k_{sz}}{k_{iz}}\right) e^{ik_{sz}d}}, \tag{B.9}$$

$$B_h = \frac{2\left(1-\frac{k_{iz}}{k_{sz}}\right)e^{-i(k_{iz}-k_{sz})d/2}}{\left(1+\frac{k_{iz}}{k_{sz}}\right)\left(1+\frac{k_{sz}}{k_{iz}}\right)e^{-ik_{sz}d}+\left(1-\frac{k_{iz}}{k_{sz}}\right)\left(1-\frac{k_{sz}}{k_{iz}}\right)e^{ik_{sz}d}}, \tag{B.10}$$

$$A_v = \frac{2\left(1+\frac{\epsilon_s k_{iz}}{\epsilon_0 k_{sz}}\right)e^{-i(k_{iz}+k_{sz})d/2}}{\left(1+\frac{\epsilon_s k_{iz}}{\epsilon_0 k_{sz}}\right)\left(1+\frac{\epsilon_0 k_{sz}}{\epsilon_s k_{iz}}\right)e^{-ik_{sz}d}+\left(1-\frac{\epsilon_s k_{iz}}{\epsilon_0 k_{sz}}\right)\left(1-\frac{\epsilon_0 k_{sz}}{\epsilon_s k_{iz}}\right)e^{ik_{sz}d}}, \tag{B.11}$$

$$B_v = \frac{2\left(1-\frac{\epsilon_s k_{iz}}{\epsilon_0 k_{sz}}\right)e^{-i(k_{iz}-k_{sz})d/2}}{\left(1+\frac{\epsilon_s k_{iz}}{\epsilon_0 k_{sz}}\right)\left(1+\frac{\epsilon_0 k_{sz}}{\epsilon_s k_{iz}}\right)e^{-ik_{sz}d}+\left(1-\frac{\epsilon_s k_{iz}}{\epsilon_0 k_{sz}}\right)\left(1-\frac{\epsilon_0 k_{sz}}{\epsilon_s k_{iz}}\right)e^{ik_{sz}d}}, \tag{B.12}$$

The vector $\hat{h}_i$ in (B.8) is the horizontal polarization of the incident plane wave, which is orthogonal to the plane determined by $\hat{z}_b$ and $\hat{k}_i$, the vector $\hat{v}_i$ in (B.8) is the vertical polarization of the incident plane wave, which is equal to $\hat{k}_i \times \hat{h}_i$, and

$$\hat{h}_A = \hat{h}_B = \hat{h}_i, \tag{B.13}$$

$$\hat{v}_A = \hat{k}_s \times \hat{h}_A, \quad \hat{v}_B = \hat{K}_s \times \hat{h}_B. \tag{B.14}$$

Plugging the internal field in (B.8) into (B.2), and plugging the induced current density in (B.2) into (B.1), we can perform the volume integral over V, where $V = \{(x', y', z') | -\rho_t \leq x' \leq \rho_t, -\rho_t \leq y' \leq \rho_t, -d/2 \leq z' \leq d/2\}$, to obtain the following expression for the scattered field:

$$\bar{\bar{E}}_s(\bar{r}_s) \approx \mu_0 \Omega^2 (\epsilon_s - \epsilon_0)(\bar{\bar{I}} - \hat{r}_s \hat{r}_s) \cdot \frac{e^{ikr_s}}{4\pi r_s} 4\rho_t^2 \, \mathrm{sinc}(k\alpha_{xb}\rho_t) \, \mathrm{sinc}(k\alpha_{yb}\rho_t)$$
$$\{(\hat{h}_A \hat{h}_i A_h + \hat{v}_A \hat{v}_i \sqrt{\epsilon_0/\epsilon_s} A_v) \, d \, \mathrm{sinc}(k\beta_1 d/2) + (\hat{h}_B \hat{h}_i B_h + \hat{v}_B \hat{v}_i \sqrt{\epsilon_0/\epsilon_s} B_v) \, d \, \mathrm{sinc}(k\beta_2 d/2)\}, \tag{B.15}$$

where

$$\alpha_{xb} = (\hat{k}_i - \hat{r}_s) \cdot \hat{x}_b, \tag{B.16}$$

$$\alpha_{yb} = (\hat{k}_i - \hat{r}_s) \cdot \hat{y}_b, \tag{B.17}$$

$$k\beta_1 = -k_{sz} - k(\hat{z}_b \cdot \hat{r}_s), \tag{B.18}$$

$$k\beta_2 = k_{sz} - k(\hat{z}_b \cdot \hat{r}_s). \tag{B.19}$$

Again, based on (2.17), the overall bistatic scattering tensor of a dielectric volume can be obtained from the scattered field in (B.15). To apply this result to the 2-D SAR problem, we only have to specify the orientation of the target normal direction $\hat{z}_b$ with respect to the radar scenario, and determine the incident and scattering directions $\hat{k}_i$ and $\hat{r}_s$ from the radar antenna location. When the target on the ground is located at the nominal center, $\hat{k}_i = -\hat{r}_s$ can be obtained via (2.14).

Appendix C

Backpropagation Formulation for the Pulse Radar Signal

The backpropagation formulation for the radar signal model is based on the reciprocity of free space. For a continuous-wave radar signal waveform, the derivation of the backpropagation formulation in [23] from the reciprocity theorem in [25] is straightforward. In this appendix, we will demonstrate that for the non-monochromatic condition, provided the radar signal bandwidth is not too large compared to the carrier frequency, the backpropagation formulation is approximately valid.

Suppose there are two surfaces S_b and S_c in free space with center locations $\bar{r}_b^0$ and $\bar{r}_c^0$, respectively. On these two surfaces electric and magnetic currents are distributed. Without loss of generality, we assume that there are only electric surface current densities $\bar{K}_b(\bar{r},t)$ and $\bar{K}_c(\bar{r},t)$. Both $\bar{K}_b(\bar{r},t)$ and $\bar{K}_c(\bar{r},t)$ have angular carrier frequency Ω_c. However, they are not monochromatic in general. Therefore the time-dependent phasors, $\bar{\tilde{K}}_b(\bar{r},t)$ and $\bar{\tilde{K}}_c(\bar{r},t)$, of the surface current densities $\bar{K}_b(\bar{r},t)$ and $\bar{K}_c(\bar{r},t)$ are:

$$\bar{K}_p(\bar{r},t) = \mathrm{Re}\left\{\bar{\tilde{K}}_p(\bar{r},t)e^{-i\Omega_c t}\right\}, \tag{C.1}$$

for $p = b,\ c$. We will express the surface current densities in terms of their frequency components,

$$\bar{K}_p(\bar{r},t) = \mathrm{Re}\left\{\int_{-\infty}^{\infty}\frac{d\Omega}{2\pi}\bar{\tilde{\mathrm{K}}}_p(\bar{r},\Omega)e^{-i(\Omega_c+\Omega)t}\right\}, \tag{C.2}$$

for $p = b,\ c$, where $\bar{\tilde{\mathrm{K}}}_p(\bar{r},\Omega)$ is the Fourier transform of $\bar{\tilde{K}}_p(\bar{r},t)$.

From (C.2), the electric field $\bar{E}_p(\bar{r},t)$ induced by the surface current density $\bar{K}_p(\bar{r},t)$ on

the surface S_p can be represented in terms of Green's function,

$$\bar{E}_p(\bar{r},t) = \mathrm{Re}\left\{\int_{-\infty}^{\infty}\frac{d\Omega}{2\pi}\int\int_{S_p} d\bar{r}_p i(\Omega_c+\Omega)\mu_0\bar{\bar{G}}(\bar{r},\bar{r}_p;\Omega_c+\Omega)\cdot\bar{\bar{K}}_p(\bar{r}_p,\Omega)e^{-i(\Omega_c+\Omega)t}\right\}, \quad (C.3)$$

for $p = b,\ c$, where $\bar{\bar{G}}(\bar{r},\bar{r}_p;\Omega_c+\Omega)$ is the free-space Green's function at (angular) frequency $\Omega_c+\Omega$.

We are interested in the induced electric field only within a restricted region. To be more specific, we only need to know $\bar{E}_b(\bar{r},t)$ for $\bar{r}\in S_c$, and $\bar{E}_c(\bar{r},t)$ for $\bar{r}\in S_b$. Suppose that: (i) every point $\bar{r}_b$ on S_b is in the far-field region of $\bar{K}_c(\bar{r}_c,t)$ on S_c for all of its frequency components, and vice versa; and (ii) $|\bar{r}_b^0-\bar{r}_c^0|$ is much larger than the diameters of S_b and S_c. Then the Green's function can be approximated as follows:

$$\bar{\bar{G}}(\bar{r}_p,\bar{r}_q,\Omega_c+\Omega)\approx e^{i(\Omega/c)|\bar{r}_b^0-\bar{r}_c^0|}\bar{\bar{G}}(\bar{r}_p,\bar{r}_q,\Omega_c), \quad (C.4)$$

for $(p,q) = (b,c),\ (c,b)$. Plugging (C.4) into (C.3), and assuming that the bandwidth of $\bar{K}_p(\bar{r},t)$ is much smaller than the carrier frequency Ω_c, we get

$$\bar{\bar{E}}_p(\bar{r}_q,t)\approx\int\int_{S_p} d\bar{r}_p i\Omega_c\mu_0\bar{\bar{G}}(\bar{r}_q,\bar{r}_p;\Omega_c)\cdot\bar{\bar{K}}_p(\bar{r}_p,t-|\bar{r}_b^0-\bar{r}_c^0|/c). \quad (C.5)$$

Following the notation in [25], we define

$$<p,q>(t) = \int\int_{S_p} d\bar{r}_p\bar{\bar{E}}_q(\bar{r}_p,t)\cdot\bar{\bar{K}}_p(\bar{r}_p,t) \quad (C.6)$$

for $(p,q) = (b,c),\ (c,b)$. Plugging (C.5) into (C.6), we obtain

$$<p,q>(t) = \int\int_{S_p} d\bar{r}_p\int\int_{S_q} d\bar{r}_q\bar{\bar{K}}_p(\bar{r}_p,t)\cdot i\Omega_c\mu_0\bar{\bar{G}}(\bar{r}_p,\bar{r}_q;\Omega_c)\cdot\bar{\bar{K}}_q(\bar{r}_q,t-|\bar{r}_b^0-\bar{r}_c^0|/c). \quad (C.7)$$

Paralleling the radar scenario discussion in Chapter 2, we see that S_b can be taken to be the target/clutter surface, S_c the receiver antenna aperture, $\bar{K}_b$ the induced current density on the target/clutter surface due to the incident radar transmitting pulse, and $\bar{\bar{K}}_c$ the conjugate of the complex envelope of the local oscillator current density on the receiver

antenna aperture. Hence the moment $< c, b >= \int\int_{S_c} d\bar{r}_c \bar{\bar{E}}_b(\bar{r}_c, t) \cdot \bar{\bar{K}}_c(\bar{r}_c, t)$ is exactly the complex envelope of the radar return signal in (2.25). Referring to (C.5), we define the backpropagation electric field $\bar{E}_c^b$ induced by the surface current density $\bar{K}_c$ on S_c, with the time-dependent phasor around S_b to be

$$\bar{\bar{E}}_c^b(\bar{r}_b, t) \approx \int\int_{S_c} d\bar{r}_c i\Omega_c \mu_0 \bar{\bar{G}}(\bar{r}_b, \bar{r}_c; \Omega_c) \cdot \bar{\bar{K}}_c(\bar{r}_c, t + |\bar{r}_b^0 - \bar{r}_c^0|/c). \tag{C.8}$$

The name "backpropagation field" is derived from the time-reversal propagation characteristics revealed in (C.8). For example, when the source current $\bar{K}_c$ at S_c emits a pulse at $t = 0$, the forward-propagation field around S_b is a pulse at $t = |\bar{r}_b^0 - \bar{r}_c^0|/c$. However, from (C.8), the backpropagation field $\bar{E}_c^b$ around S_b is a pulse at $t = -|\bar{r}_b^0 - \bar{r}_c^0|/c$.

Define

$$< b, c^b > (t) = \int\int_{S_b} d\bar{r}_b \bar{\bar{E}}_c^b(\bar{r}_b, t) \cdot \bar{\bar{K}}_b(\bar{r}_b, t). \tag{C.9}$$

Then from (C.7), (C.8), (C.9), and the reciprocity of the free-space Green's function,

$$\bar{\bar{G}}(\bar{r}_p, \bar{r}_q; \Omega_c) = \bar{\bar{G}}^T(\bar{r}_q, \bar{r}_p; \Omega_c), \tag{C.10}$$

it can be shown that

$$< c, b > (t) =< b, c^b > (t - |\bar{r}_b^0 - \bar{r}_c^0|/c), \tag{C.11}$$

which is the backpropagation formulation for the radar return signal.

References

[1] D. C. Munson, J. D. O'Brien, and W. K. Jenkins, "A tomographic formulation of spotlight-mode synthetic aperture radar," *Proceedings of the IEEE*, Vol. 71, No. 8, pp. 917 - 925, 1983.

[2] D. C. Munson, R. L. Visentin, "A signal-processing view of strip-mapping synthetic aperture radar," *IEEE Transactions on Acoustics, Speech, and Signal Processing*, Vol. 37, No. 12, pp. 2131 - 2147, 1989.

[3] D. Park, *High-Resolution Laser Radar Performance Analysis,* Ph.D. thesis, Department of Electrical Engineering and Computer Science, MIT, 1988.

[4] D. Park, and J. H. Shapiro, "Performance analysis of optical synthetic aperture radars," *Proceedings of SPIE*, Vol. 999, pp. 100 - 116, 1988.

[5] W. G. Carrara, R. S. Goodman, and R. M. Majewski, *Spotlight Synthetic Aperture Radar: Signal Processing Algorithms,* Artech House, Boston, 1995.

[6] G. Leung, and J. H. Shapiro, "Toward a fundamental understanding of multiresolution SAR signatures," *Proceedings of SPIE*, Vol. 3070, pp. 100 - 109, 1997.

[7] L. M. Novak, S. D. Halversen, G. J. Owirka, and M. Hiett, "Effects of polarization and resolution on the performance of a SAR automatic target recognition system," *The Lincoln Laboratory Journal*, Vol. 8, No. 1, pp. 49 - 68, 1995.

[8] H. R. Park, J. Li, and H. Wang, "Polarization-space-time domain generalized likelihood ratio detection of radar targets," *Signal Processing*, Vol. 41, pp. 153 - 164, 1995.

[9] M. W. Tu, I. J. Gupta, and E. K. Walton, "Application of maximum likelihood estimation to radar imaging," *IEEE Transactions on Antennas and Propagation*, Vol. 45, No. 1, pp. 20 - 27, 1997.

[10] T. Soni, J. R. Zeidler, and W. H. Ku, "Performance evaluation of 2-D adaptive prediction filters for detection of small objects in image data," *IEEE Transactions on Image Processing*, Vol. 2, No. 3, pp. 327 - 340, 1993.

[11] W. Irving, R. B. Washburn, and W. E. L. Grimson, "Bounding performance of peak-based target detectors," *Proceedings of SPIE*, Vol. 3070, pp. 245 - 257, 1997.

[12] J. S. Lee, and K. Hoppel, "Principal components transformation of multifrequency polarimetric SAR imagery," *IEEE Transactions on Geoscience and Remote Sensing*, Vol. 30, No. 4, pp. 686 - 696, 1992.

[13] L. M. Novak, M. C. Burt, R. D. Chaney and G. J. Owirka "Optimal processing of polarimetric synthetic-aperture radar imagery," *The Lincoln Laboratory Journal*, Vol. 3, No. 2, pp. 273 - 290, 1990.

[14] X. Yu, L. E. Hoff, I. S. Reed, A. M. Chen, and L. B. Stotts, "Automatic target detection and recognition in multiband imagery: a unified ML detection and estimation approach," *IEEE Transactions on Image Processing*, Vol. 6, No. 1, pp. 143 - 156, 1997.

[15] S. Krishnamachari, and R. Chellapa, "Multiresolution Gauss-Markov random field models for texture segmentation," *IEEE Transactions on Image Processing*, Vol. 6, No. 2, pp. 251 - 267, 1997.

[16] A. H. S. Solberg, T. Taxt, and A. K. Jain, "A Markov random field model for classification of multisource satellite imagery," *IEEE Transactions on Geoscience and Remote Sensing*, Vol. 34, No. 1, pp. 100 - 113, 1996.

[17] W. W. Irving, L. M. Novak and A. S. Willsky, "A multiresolution approach to discriminating targets from clutter in SAR imagery," *Proceedings of SPIE*, Vol. 2487, pp. 272 - 299, 1995.

[18] R. D. Chaney, A. S. Willsky, and L. M. Novak, "Coherent aspect-dependent SAR image formation," *Proceedings of SPIE*, Vol. 2230, pp. 256 - 274, 1994.

[19] N. S. Subotic, B. J. Thelen, J. D. Gorman, and M. F. Reiley, "Multiresolution detection of coherent radar targets," *IEEE Transactions on Image Processing*, Vol. 6, No. 1, pp. 21 - 35, 1997.

[20] N. Nandhakumar, and J. K. Aggarwal, "Physics-based integration of multiple sensing modalities for scene interpretation," *Proceedings of the IEEE*, Vol. 85, No. 1, pp. 147 - 163, 1997.

[21] R. L. Moses, E. Erten, and L. C. Potter, "Performance analysis of anisotropic scattering center detection," *Proceedings of SPIE*, Vol. 3070, pp. 235 - 244, 1997.

[22] L. C. Potter, and R. L. Moses, "Attributed scattering centers for SAR ATR," *IEEE Transactions on Image Processing*, Vol. 6, No. 1, pp. 79 - 91, 1997.

[23] G. Leung, *Synthetic Aperture Radar Discrimination of Diffuse and Specular Target Returns,* M.Eng. thesis, Department of Electrical Engineering and Computer Science, MIT, 1997.

[24] L. Tsang, J. A. Kong, and R. T. Shih, *Theory of Microwave Remote Sensing,* John Wiley and Sons, New York, 1985.

[25] J. A. Kong, *Electromagnetic Wave Theory,* Wiley, New York, 1990.

[26] M. A. Richards, and K. D. Trott, "A physical optics approximation to the range profile signature of a dihedral corner reflector," *IEEE Transactions on Electromagnetic Compatibility*, Vol. 37, No. 3, pp. 478 - 481, 1995.

[27] K. Pimsamarn, *Electromagnetic Scattering Model for Saline Ice Covered with Frost Flowers,* M.Eng. thesis, Department of Electrical Engineering and Computer Science, MIT, 1997.

[28] J. C. Henry, "The Lincoln Laboratory 35 GHz airborne SAR imaging radar system," in *Proceedings of IEEE National Telesystems Conference*, pp. 353 - 358, Atlanta, Georgia, USA, 1991.

[29] H. L. Van Trees, *Detection, Estimation and Modulation Theory: Part III,* Wiley, New York, 1971.

[30] M. D. Desai, and W. K. Jenkins, "Convolution backprojection image reconstruction for spotlight mode synthetic aperture radar," *IEEE Transactions on Image Processing*, Vol. 1, No. 4, pp. 505 - 517, 1992.

[31] C. W. Helstrom, *Statistical Theory of Signal Detection,* Pergamon Press, 1968.

[32] M. G. Bello, *Centralized and Decentralized Map Updating and Terrain Masking Analysis,* Ph.D. thesis, Department of Electrical Engineering and Computer Science, MIT, 1981.

[33] A. J. F. Siegert, "On the first passage time probability problem," *Physical Review*, Vol. 81, pp. 617 - 623, 1951.

[34] S. O. Rice, "Distribution of the duration of fades in radio transmission," *Bell System Technology Journal*, Vol. 37, pp. 581 - 635, 1958.

[35] V. I. Tikhonov, "The Markov nature of the envelope of quasiharmonic oscillations," *Radio Engineering and Electronic Physics*, Vol. 6, pp. 961 - 971, 1961.

[36] C. W. Helstrom, "A note on a Markov envelope process," *Transactions of Institute of Radiation Engineers*, Vol. 1, pp. 139 - 140, 1959.

[37] S. O. Rice, "The mathematical analysis of random noise," *Bell System Technology Journal*, Vol. 23, pp. 282 - 332, 1944, Vol. 24, pp. 46 - 156, 1945.

[38] H. M. Taylor and S. Karlin, *An Introduction to Stochastic Modeling*, Academic Press, 1984.

[39] J. H. Shapiro, R. W. Reinhold, and D. Park, "Performance analyses for peak-detecting laser radars," *Proceedings of SPIE*, Vol. 663, pp. 38 - 56, 1996.

[40] R. J. Adler and A. M. Hansofer, "Level crossings for random fields," *The Annals of Probability*, Vol. 4, pp. 1 - 12, 1976.

[41] D. A. Kessler and I. Freund, "Level-crossing densities in random wave fields," *Journal of Optical Society of America A-Optics and Image Science*, Vol. 15, pp. 1608 - 1618, 1998.

[42] P. A. Viola, *Alignment by Maximization of Mutual Information,* Ph.D. thesis, Department of Electrical Engineering and Computer Science, MIT, 1995.

[43] M. Boshra and B. Bhanu, "Bounding SAR ATR performance based on model similarity," to appear in *Proceedings of SPIE*, Vol. 3721, 1999.

[44] M. Boshra and B. Bhanu, "Performance prediction and validation for object recognition," to appear in *Proceedings of SPIE*, Vol. 3721, 1999.

[45] H. C. Chang and R. L. Moses, "ATR performance prediction using attributed scattering features," to appear in *Proceedings of SPIE*, Vol. 3721, 1999.

[46] M. Desai, "High accuracy and synthetic aperture radar image layover," *Proceedings of SPIE*, Vol. 1630, pp. 2 - 14, 1992.

[47] W. G. Kropatsch, and D. Strobl, "The generation of SAR layover and shadow maps from digital elevation models," *IEEE Transactions on Geoscience and Remote Sensing*, Vol. 28, No. 1, pp. 98 - 107, 1990.

[48] D. G. Tilley, and K. S. Bonwit, "Reduction of layover distortion in SAR imagery," *Remote Sensing and Environment*, Vol. 27, pp. 211 - 220, 1989.

[49] D. E. Livesay, and K. M. Chen, "Electromagnetic fields induced inside arbitrarily shaped biological bodies," *IEEE Transactions on Microwave Theory and Techniques*, Vol. MTT - 22, No. 12, pp. 1273 - 1280, 1974.